Durability of bonded crack retarders for aerospace

Thesis

The Open University

Faculty of Mathematics, Computing & Technology

Department of Engineering and Innovation

Materials Engineering Group

Durability of Bonded Crack Retarders for Aerospace

by

Abdul Khadar Syed

June 2014

A THESIS SUMMITTED TO THE DEPARTMENT OF ENGINEERING AND INNOVATION OF THE OPEN UNIVERSITY FOR THE DEGREE OF DOCTOR OF PHILOSOPHY

ORIGINAL COPY TIGHTLY BOUND

Abstract

The increase in demand for aircraft focuses the structural designers and manufacturers towards the reduction of manufacturing cost and structural weight while maintaining high safety, damage tolerance, and structural integrity. These weight savings can be achieved by using large integral structures. However, large integral structures show reduced performance with respect to damage tolerant design due to lack of physical barriers that can arrest a growing crack such as presently exist in structures joined with rivets and bolts.

Fibre metal laminates such as Glass Laminated Aluminium Reinforced Epoxy (GLARE) have been proven effective as bonded crack retarders (BCR) in reducing the fatigue crack growth rate and improving the life of metallic aircraft structures. A major problem associated with bonded crack retarders is the development of thermal residual stresses which may have negative impact on the performance of the structure. Hence, the objectives of this research are to investigate the thermal residual stress developed during the strap bonding process and the fatigue durability of bonded crack retarders.

Extensive research performed in this dissertation covers the detailed investigation of thermal residual stresses and the fatigue durability of GLARE bonded crack retarders when incorporated onto different structural coupons and on an aircraft mock-up panel. Thermal residual stresses developed during the strap bonding process are very low and the application of a bonded crack retarder improved the fatigue performance of the specimen.

The experimental data on residual stress measurements and fatigue testing provides information for researchers and aircraft structural designers to improve the performance and life of critical aircraft structures and the possibilities of incorporating the bonded crack retarder concept in the initial design and fabrication stages.

Acknowledgement

First and foremost, I would like to express my sincere gratitude to my supervisors Prof. Michael E. Fitzpatrick and Dr. James E Moffatt for their continuous support during my research, for their patience, motivation, enthusiasm, and immense knowledge. Their guidance helped me in all the time of research, discussions, and writing of this thesis. I could not have imagined having better advisors for my Ph.D. study. I would like to express my special appreciation to Mike Fitzpatrick for his continuous encouraging and invaluable guidance. You have been a tremendous supervisor and will be an inspiration.

I would also like to thank Prof. Philip Irving, Dr, Xiang Zhang and Jeremy Doucet from Cranfield University for their help and support during the sample preparations and for their valuable discussions in the research. My sincere thanks to Markus Heinimann, Bernard De Mestral, Gerriet Feyen from Alcoa, and Robert Maziarz and Luigi Castelletti from Airbus, UK for material supply and for their valuable discussions during the project and in review meetings.

I greatly acknowledge the UK Technology Strategy Board and the Lloyd's Register Foundation (LRF), a UK registered charity that helps to protect life and property by supporting engineering-related education, public engagement and the application of research, for funding this project.

I would like to acknowledge all beam line scientists of the diffraction facilities in UK and across the Europe: Dr. Shu Yan Zhang, Dr. Joe Kelleher and Dr. Saurabh Kabra from ENGIN-X, ISIS, UK; Dr. Thilo Pirling from SALSA, ILL, France and Dr. Steven Van Petegam and Dr. Vadim Davydov from POLDI, PSI, Switzerland.

My sincere thanks to the support staff in the materials engineering department: Stan Hiller, Pete Ledgard, Damian Flack, Gordon Imlach, Ian Norman and Charles Snelling. Especially, this work would not have been completed without the expertise and help of

Stan, Pete and Damian during my testing, sample preparation and for their patience during my discussions. My special thanks to three of you for your numerous support during this research.

I owe my special thanks to all the current and previous research students, with whom I enjoyed this long journey of Ph.D. Without your constant motivation, support and the fun time we had in the office and outside, this journey was not so easy. I would like to thank current and previous technical staff and research associates. I also like to thank my friends in India and in the rest of the world for being there for me through this journey.

I would like express my heartfelt thanks to my family, my mother, and father, my wife, my son and my sister (deceased) for all of the sacrifices that you have made on my behalf. Your prayer for me was what sustained me thus far. Without your sacrifices, this thesis was impossible. Finally, I would like to dedicate this thesis and my future success to my wife.

July, 2014

Abdul Khadar Syed

Milton Keynes, UK

Preface

This thesis is submitted for the degree of Doctor of Philosophy at The Open University, United Kingdom. The work described in this thesis was carried out in the Department of Materials Engineering, Faculty of Mathematics, Computing, and Technology, between November 2010 and June 2014, under the supervision of Prof. Michael Edward Fitzpatrick, and Dr. Jim Moffatt.

It is entirely the work of the author except where clearly referenced. None of this work has been submitted for a degree or other qualification at this or any other university. Some of the results of this work have been published or about to be published in academic journals, conference proceedings and as oral or poster presentations as listed below:

[1]. **Abdul Khadar Syed**, Michael E Fitzpatrick, James E Moffatt, Jeremy Doucet, Isidro Durazo-Cardenas, *Effect of impact damage on fatigue durability of structures reinforced with GLARE bonded crack retarder*, Composite structures **(Submitted).**

[2]. **Abdul Khadar Syed**, Michael E Fitzpatrick, James E Moffatt, *Evolution of residual stress during fatigue crack growth in an aluminium specimen with a bonded crack retarder*, Composite Structures 117, pp. 12-16, 2014.

[3]. **Abdul Khadar Syed**, Michael E Fitzpatrick, James E Moffatt, *Effect of thermal residual stresses on bonded structures containing cold expanded and bolted holes*, Advanced Materials Research, Vol 996, pp. 682-687, 2014.

[4]. M. B. Heinimann, R. Maziarz, L. Castelletti, V. Naik, P. E. Irving, D. Figueroa, J. Doucet, X. Zhang, M. Boscolo, M. E Fitzpatrick, **A. K. Syed**, J. E. Moffatt, C. D. M. Liljedahl, *Use of Bonded Crack Retarders to Improve Damage Tolerance of Wing Covers*, AEROMAT 25-The Latest World in Aerospace Materials, Orlando, Florida, 16-19 June, 2014 **(Abstract accepted).**

Abdul Khadar Syed,
Milton Keynes, UK

Table of contents

List of figures

List of tables

Chapter 1 : Introduction

The aviation industry has experienced rapid development since the Second World War. Besides the global economy, the technology of air transport has grown tremendously to its present state. The aircraft industry became very conservative in adopting new designs and technologies. A major breakthrough occurred in 1930 when Boeing introduced all metal aircraft, which was a decisive moment for the aviation industry and led to a huge growth in air traffic. This technology breakthrough was required in order to reach the increase in demand for aircraft and to meet the challenges of future mass air transportation. Since then aircraft designers and engineers have developed new technologies and sophisticated manufacturing methods to make the aircraft lighter, fail-safe, fuel-efficient, and economical. The innovation of new materials for structural applications allows reduction of the operating cost of aircraft by means of reducing weight, fuel consumption, and maintenance. On the other hand, safety and damage tolerance are two critical aspects in incorporating these new materials into the design process.

In the past few decades, designers and engineers have been successful in adopting new materials such as composites and Fibre Metal Laminates (FML) in aircraft structural applications. The development of new materials in the aviation industry takes many years where designers must understand the new materials in terms of mechanical properties (yield strength, fatigue resistance etc.), durability (corrosion, impact damage, material degradation to severe environments etc.), physical and chemical properties (weight, thermal expansion etc.) and technological properties (machinability, repairability etc.) when adopting new manufacturing methods. In addition to this aircraft designers and manufacturers have to achieve high durability, high efficiency, and an acceptable level of economy in this competitive market.

The structural weight of the aircraft plays an important role in its performance and also on the economy. Figure 1.1 shows the direct operating cost (DOC) of an aircraft. It can be seen that 40-50% of direct operating cost is the ownership cost and the remaining 50-60% direct operating cost is operational expenses to the airlines. Furthermore, 40-50% of the ownership cost is covered by the recurring production cost. The lighter the aircraft the lower the fuel consumption and fuel load, so increasing the payload of the aircraft. Operating efficiency and economy with passenger comfort are paramount in commercial transport aircraft. Reduced airframe weight pays off in fuel economy and, therefore, reduces direct operating costs for the operators. Therefore the primary objective of the future aircraft design should focus on the following [1-3].

- Structures with high damage tolerance and fail safety
- Structures with low weight
- Low operating cost and
- Low maintenance with improved durability

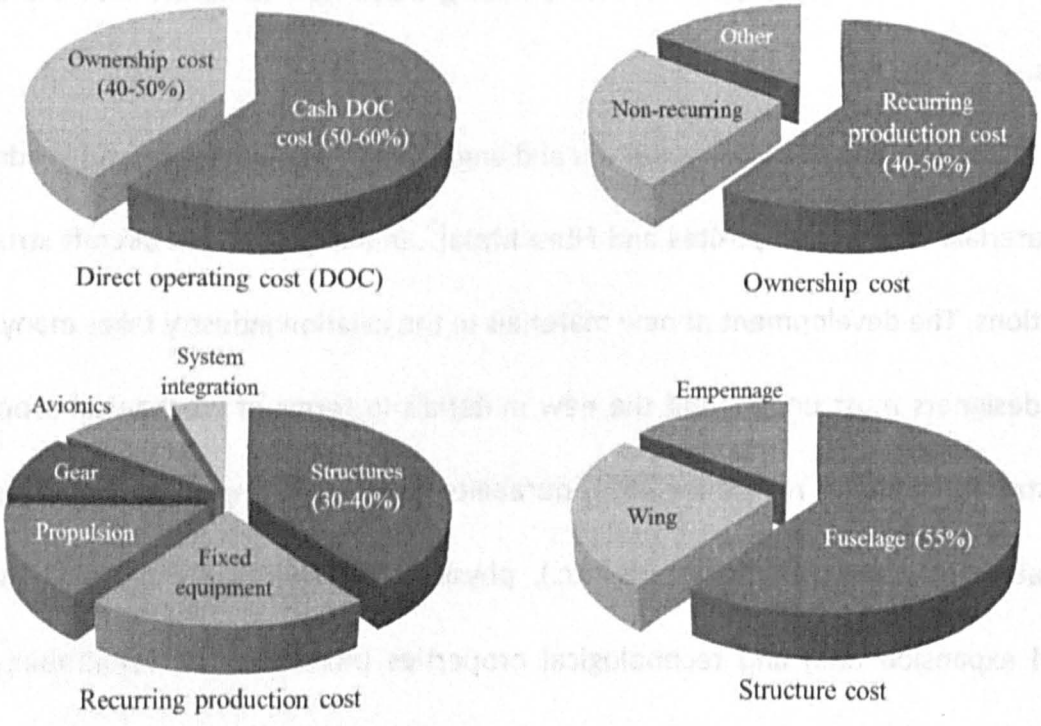

Figure 1.1. Direct operating cost of aircraft [1]

The aircraft structure in service will experience an extensive spectrum of cyclic loads that can result in fatigue crack initiation, propagation, and eventually structural failure. For

several important structures within the airframe, fatigue is the limiting design parameter. In general, aircraft structures are composed of a large number of riveted and bolted joints with a number of geometrical discontinuities, which act as stress concentration areas, that leads to crack initiation and subsequently crack growth during the service. Because of the complexity in aircraft structures it is impossible to reduce the size of these geometrical notches.

After crack initiation, the structure is still safe to be in service if the crack can be detected and monitored before it reaches its critical size which will cause failure. In this case, the inspection intervals should be frequent enough to ensure safety. This approach will increase the maintenance cost, which is not favourable. One accident that occurred because of fatigue cracking is the 'Aloha accident' [4]. On April 28, 1988, a Boeing 737-200 series aircraft operated by Aloha Airlines experienced a structural failure at 24,000 feet altitude when travelling from Hilo to Honolulu, Hawaii. The flight was safely landed at Kahului Airport on the Island of Maui with one dead and serious injuries to several passengers. Figure 1.2 shows the image after landing and during the emergency evacuation.

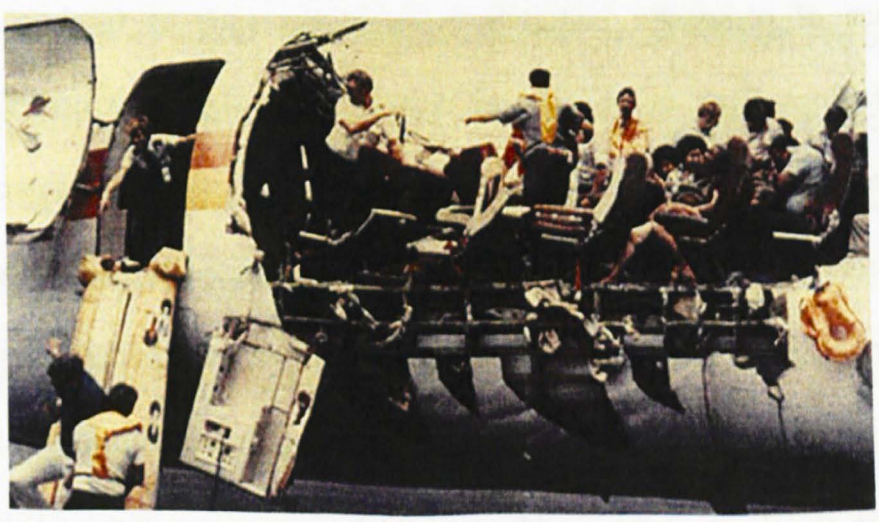

Figure 1.2. Aloha airlines flight after landing during emergency evacuation [5]

After thorough investigation, The National Transportation Safety Board (NTSB) released a report, which determined the cause of the incident. It was concluded that the presence of

multiple fatigue cracking of the skin adjacent to rivet holes along the lap joint and significant degradation of the adhesive due to environmental conditions resulted in disbonding of the upper and lower fuselage skin.

Conventional metallic built-up structures have been used for more than 60 years and the design and manufacturing process have been optimised. Presently, the bulk of an aircraft construction consists of different aluminium alloys but conventional alloys show only moderate fatigue performance [6]. In addition to reducing the weight of the aircraft, the primary goal of the development of new materials is to reduce fatigue, hence increasing the damage tolerance and fail safety. For these reasons hybrid materials are receiving considerable attention for use in new generation aircraft due to their low weight, high specific strength, stiffness, and superior durability in aerospace applications. Besides the improvements in metals through new alloys and manufacturing processes, the use of composites has increased. However the extensive use of composite materials in aircraft structures is limited due to their complex failure mechanisms [7].

The first use of composite material in commercial aircraft structures was in 1983 when Airbus introduced the first all composite rudder for the Airbus A300 and A310 [6]. Later, the use of composite materials in structures such as fuselage belly skins, fin/fuselage fairings, flaps, etc. has increased [6, 7]. The significant use of fibre metal laminates in aircraft structural components has increased in the last two decades. These hybrid structures have been successfully employed as bonded crack retarders (BCR) in aircraft repair technology. A fibre metal laminate consists of alternating thin layers of metal sheets and fibre reinforced epoxy resin. The most promising fibre metal laminate is Glass Laminated Aluminium Reinforced Epoxy (GLARE), which is made up of alternate thin aluminium layers and fibres of glass embedded in an epoxy prepreg. These hybrid structures exhibit many advantages over monolithic aluminium alloys. GLARE combines

desirable properties of both metal and fibrous composite materials such as high strength and stiffness, good fatigue resistance, high corrosion resistance, good residual and blunt notch strengths and flame resistance. On the other hand, the delamination properties are a drawback.

As the technology has matured design engineers are now interested to use fibre metal laminates in the initial design and manufacturing process to replace the conventional methods of joining (rivets and bolts) aircraft structures, to reduce the weight of the aircraft and increase the fuel efficiency. Nevertheless, the most crucial element in a bonded crack retarder is the adhesive joint between the fibre metal laminate and metal substrate.

During the bonding process the adhesive needs to cure at high temperature which leaves residual stresses in the structure because of the differences in coefficient of thermal expansion (CTE) between the fibre metal laminate and metal substrate. These residual stresses can affect the fatigue behaviour of the aircraft structure. When the aircraft experiences its operating temperature range (typically −60°C to +70°C) these residual stresses may have a significant effect on the fatigue performance of the structure when reinforced with a bonded crack retarder. Another important factor to be considered is the delamination behaviour of the adhesive when exposed to the aircraft working environment. Delamination can cause disbonding of the metal sheets from the prepreg which leads to failure of the structure.

1.1 The project scope

The possible use of bonded crack retarding technology to improve the damage tolerance and fail safety of the aircraft has been investigated. This project is an extension of previous studies [8-17] made in bonded crack retarding technology research which involved The Open University, Cranfield University, Airbus, and Alcoa. A multi-disciplinary

programme was carried out by these partners where they investigated different adhesive bonding processes and different crack retarding materials and their performance on fatigue crack growth. The objectives of this investigation were to quantify the thermal residual stresses developed in the reinforced structure due to different adhesive bonding processes. In addition to this, the effect of different strap materials, stiffness ratios, and applied stress ratios on the performance of the bonded crack retarders was investigated.

From previous research [9] it was concluded that the major parameters influencing the retardation behaviour of different strap materials are the thermal residual stresses and the global stiffness ratio. The high temperature adhesive curing process developed thermal residual stresses, which are tensile in nature, in the reinforced structure. The strap material having the closest coefficient of thermal expansion mismatch to the reinforced structure produced low thermal residual stresses. Aluminium and GLARE straps were found to have a closest coefficient of thermal expansion mismatch. Aluminium strap was showed poor performance whereas GLARE was shown to be superior.

This project now moves to the next stage where the performance of GLARE as a bonded crack retarder when bonded onto small coupon specimens and mock-up aircraft panels will be studied. The project is funded by a grant from the UK Technology Strategy Board and includes The Open University, Cranfield University, Airbus, and Alcoa. The material is supplied by Airbus, Alcoa, and Cytec and specimens were prepared at Cranfield University. The project is divided into four distinct and related parts:

1. Characterisation of thermal residual stresses developed in the reinforced structure due to GLARE bonding in different coupon specimens, in structural joints and finally on a mock-up aircraft panel. This work was performed by The Open University.

2. To quantify the retardation behaviour of GLARE by using mechanical testing of coupon specimens. This work is performed by The Open University.
3. To validate the finite element models by the results obtained from mechanical testing. This work is performed by Cranfield University.
4. Testing of the mock-up aircraft panel and validate with the theoretical models. This work is performed by Cranfield University.

The author's study mainly focuses on the first two objectives and will be discussed in detail in the next section.

1.2 Objectives

For any new material, its application requires development studies of various technological and design requirements involved. For bonded crack retarders it is very important to study the residual stresses generated during the bonding process and delamination behaviour of the adhesive when subjected to aircraft service temperature. Residual stresses play a significant role on the fatigue performance of the bonded crack retarder. Hence it is important to study the fatigue performance of the bonded crack retarder when residual stresses are present. Residual stresses will always be present in aircraft structures, regardless of the bonding curing temperature, as the working temperatures experienced by aircraft structure range from about -60°C at altitude to +70°C on the ground during hot sunny days.

In order to investigate the properties of bonded crack retarders when incorporated into different structural components, the following studies were undertaken. Fatigue testing was carried at three different temperatures i.e. at room temperature, +70°C and -60°C which bounds to aircraft service temperatures. The objectives are sectioned into two main areas of investigation; residual stress measurements in structures and coupon specimens reinforced with bonded crack

retarders, and fatigue life improvement of coupon specimens reinforced with bonded crack retarders.

Residual stress measurements:

1. Characterisation of residual stresses generated in a middle crack tension (M(T)) coupon specimen reinforced with a bonded crack retarder.
2. Characterisation of residual stresses in a coupon specimen reinforced with a bonded crack retarder and containing a cold expanded hole and a bolted hole.
3. Investigate the residual stresses developed in a single edge notch tension (SEN(T)) coupon specimen reinforced with a bonded crack retarder. Also to investigate the residual stresses developed in a SEN(T) coupon specimen when subjected to a low velocity impact.
4. Investigate the residual stresses developed in an aircraft manhole coupon specimen reinforced with a bonded crack retarder and containing cold expanded and bolted holes.
5. Characterisation of residual stresses in a butt strap coupon specimen reinforced with a bonded crack retarder and containing cold expanded and bolted holes.
6. Characterisation of residual stresses in a mock-up aircraft panel assembly reinforced with bonded crack retarders.

Fatigue properties:

To quantify the fatigue life improvement associated with bonded crack retarders the following mechanical testing was performed. All the testing was carried out on small coupon specimens and the data obtained can be used to predict the behaviour of large structures with different geometry.

1. Characterisation of fracture toughness and delamination properties of the adhesive used in this research to bond the crack retarder to the structural elements. This

characterisation was performed by using double cantilever beam (DCB) tests at room temperature, +70°C and -60°C.

2. Investigation of fatigue life improvement at room temperature, +70°C and -60°C by the M(T) coupon specimens reinforced with bonded crack retarders.
3. The effect of thermal cycling on fatigue life improvement and delamination properties of M(T) coupon specimens reinforced with bonded crack retarders.
4. Investigation of fatigue life improvement of a single edge notch tension (SEN(T)) coupon specimen reinforced with a bonded crack retarder when tested at room temperature.
5. The effect of low velocity impact damage on fatigue life improvement and delamination behaviour of SEN(T) coupon specimens reinforced with bonded crack retarders.
6. Effect of cold expanded and bolted hole on the fatigue life improvement of SEN(T) coupon specimens reinforced with a bonded crack retarder.

The conclusions from this research will have a major impact on the initial design and manufacturing process of light weight aircraft structures and provide information on thermal residual stresses, fatigue durability, and failure mechanisms associated with bonded crack retarders.

1.3 Structure of the thesis

The research presented in this thesis includes experimental analysis of residual stresses and fatigue durability of bonded crack retarders. In Chapter 2, a detailed literature review on the development of GLARE, the main characteristics of GLARE and literature on the research of bonded crack retarders are presented in detail.

In chapter 3, the theoretical framework of residual stresses is presented. Residual stresses origin, types, measurement techniques and the various neutron diffraction

instruments used in this research are described in detail. In chapter 4, the theoretical framework of fracture mechanics and fatigue is presented. Linear elastic fracture mechanics, stress intensity factor, characterisation of fatigue crack growth and various parameters affecting crack growth and fatigue life are discussed in detail.

In Chapter 5, the experimental materials, material characterisation, specimen geometries, specimen preparation, and experimental procedures are presented in detail. In Chapter 6, experimental results on residual stress measurements on various coupon specimens will be presented and discussed in detail.

In Chapter 7, experimental results and discussions on the characterisation of fatigue durability of various coupon specimens reinforced with bonded crack retarders is presented. In addition to this critical strain energy release rate of adhesive used to bond the straps onto the coupon specimens is presented.

In Chapter 8, the conclusions based on this research will be drawn and possible future work that could be done will also be discussed in this chapter.

1.4 References

[1]. J. Munroe, K. Wilkins, and M. Gruber, *Integral Airframe Structures (IAS)-Validated Feasibility Study of Integrally Stiffened Metallic Fuselage Panels for Reducing Manufacturing Costs, Technical Report NASA/CR-2000-209337*, NASA Langley Technical Report Server, Seattle, Washington, May 2000.

[2]. M. Boscolo, *A finite element analysis of bonded crack retarders for integral aircraft structures*, Ph.D. thesis, Department of Aerospace Engineering, Cranfield University, 2009.

[3]. R. B. Deo, J. H. Starnes, and R. C. Holzwarth, *Low-Cost Composite Materials and Structures for Aircraft Applications, Paper presented at the RTO AVT Specialists meeting on Low Cost Composite Structures*, held in Loen, Norway, 7-11 May 2001, and published in RTO-MP-069(II), 2001.

[4]. A. Asundi and A. Choi, *Fiber metal laminates: an advanced material for future aircraft, Journal of Materials Processing Technology*, vol. 63, pp. 384–394, 1997.

[5]. *http://www.airlinepilotchatter.com/2011/04/southwest-holes-and-american-wire.html*, Accessed on 10th January, 2014.

[6]. R. Marissen, *Fatigue Crack Growth Predictions in Aramid Reinforced Aluminum Laminates (ARALL)*, Journal of Aircraft, vol. 25, no. 2, pp. 135–140, 1988.

[7]. A. A. Baker, S. Dutton, and D. W. Kelly, *Composite Materials for Aircraft Structures*, American Institute of Aeronautics and Astronautics, 2004.

[8]. X. Zhang, M. Boscolo, D. Figueroa-Gordon, G. Allegri, and P. E. Irving, *Fail-safe design of integral metallic aircraft structures reinforced by bonded crack retarders*, Engineering Fracture Mechanics, vol. 76, no. 1, pp. 114–133, 2009.

[9]. P. Irving, X. Zhang, D. Figueroa-Gordo, M. Boscolo, and D. Cartie, *Bonded reinforcement and crack retarders in integral aluminium aircraft structures*, An internal report, Cranfield University, 2010.

[10]. M. Garratt, M. Heinimann, R. Bucci, and M. Kulak, *Improving damage tolerance of aircraft structures through the use of selective reinforcement*, 23rd symposium of international committee on aeronautical fatigue, ICAF-2005, Hamburg, pp. 197–208, 2005.

[11]. C. D. M. Liljedahl, M. E. Fitzpatrick, and L. Edwards, *Evolution of residual stresses with fatigue crack growth in integral structures with crack retarders*, Materials Science and Engineering: A, vol. 523, no. 1–2, pp. 152–159, 2009.

[12]. C. D. M. Liljedahl, M. E. Fitzpatrick, and L. Edwards, *Distortion and residual stresses in structures reinforced with titanium straps for improved damage tolerance*, Materials Science and Engineering: A, vol. 486, no. 1–2, pp. 104–111, 2008.

[13]. C. D. M. Liljedahl, M. E. Fitzpatrick, and L. Edwards, *Residual stresses in structures reinforced with adhesively bonded straps designed to retard fatigue crack growth*, Composite Structures, vol. 86, no. 4, pp. 344–355, 2008.

[14]. C. Liljedahl, M. Fitzpatrick, O. Zanellato, and L. Edwards, *Effect of Temperature on the Residual Stresses in an Integral Structure with a Crack-Retarding Patch*, Strain, vol 47, pp. 1–6, 2011.

[15]. X. Zhang, P. Irving, M. Boscolo, G. Allegri, and D. Figueroa-Gordon, *Improving fail-safety of aircraft integral structures through the use of bonded crack retarders,* in 24th Symposium of International Committee of Aeronautical Fatigue, Naples, Italy, 2007.

[16]. P. Irving and D. Figueroa, *Routes to improved damage tolerance; Prediction of damage tolerant performance of high strength and hybrid structures*, First International Conference on Damage Tolerance of Aircraft Structures. The Netherlands, 2007.

[17]. P. E. Irving, X. Zhang, J. Doucet, D. Figueroa-Gordon, M. Boscolo, M. Heinimann, G. Shepherd, M. E. Fitzpatrick, and D. Liljedahl, *Life Extension Techniques for Aircraft Structures – Extending Durability and Promoting Damage Tolerance through Bonded Crack Retarders* ,in 26th Symposium of International Committee of Aeronautical Fatigue, Montreal, Canada, pp. 753–770, 2011.

Chapter 2 : Fibre metal laminates

The development of new materials for the aircraft industry that makes the aircraft stronger, lighter, and more fuel-efficient is intensifying. Introducing new material involves time, money, and economic risks. Recent decades have shown that some potential materials to replace aluminium, such as steel, wood, and thermoplastics have been unsuccessful [1]. Innovations in composites and advanced aluminium alloys led researchers to build new materials with the combined properties of both metal and composites which resulted in the development of fibre-metal laminates. This new generation hybrid composite material has overcome the disadvantages of both metals and polymers. A brief historical development of fibre metal laminates will be discussed in this section.

2.1 Historical development of fibre metal laminates

There is a trend in aircraft manufacture towards the use of large integral structures produced by composite materials which will replace conventional monolithic aluminium alloys and also replace conventional fabrication methods such as riveting, welding, casting, forging and high speed machining processes. However, integral structures show reduced performance with respect to the damage tolerant design due to a lack of physical barriers as they are essentially one-piece construction. The presence of physical barriers which presently exists in structures joined with rivets and bolts can arrest a growing crack [2, 3].

One of the spectacular in-service failures of modern aircraft (Aloha airlines in 1988, discussed in chapter 1) [4] has focused engineers towards improving the damage tolerance and fail safety of the aircraft. In service aircraft structures will experience significant fatigue loadings. As the aircraft ages, the maintenance cost will increase in proportion to the increasing amount of damage. Damaged sections have to be replaced

or repaired. Both approaches are well established but will cause high cost and aircraft down times [5]. For this reason novel crack retarding features have to be incorporated in the initial design and manufacturing process. These features will increase the fatigue life of the structures, reduce the maintenance thereby reducing the maintenance cost and reducing the overall weight of the aircraft by limiting the number of mechanical fasteners.

During the 1980s an important development in the materials used in aerospace was made at Delft University of Technology (DUT), The Netherlands. It was found that the fatigue properties of thick monolithic aluminium sheets can be improved by replacing them with a built up laminate of thin aluminium sheets bonded with an adhesive. The laminate structure is advantageous over monolithic aluminium sheet material as if a crack starts in one aluminium layer of the laminate the remaining uncracked sheets will reduce the crack growth in the cracked sheet by crack bridging and stiffening [4-7].

Another breakthrough was made in the development of materials used in aerospace with the improvement of the fatigue performance of these built up laminates. It was found that incorporating high strength fibres into the adhesive used for bonding the metallic sheet laminate will provide better fatigue performance. These laminates are known as Fibre Metal Laminates (FML). The first fibre metal laminate was Aramid Reinforced Aluminium Laminate (ARALL) built up with Aramid fibres. ARALL consists of three main components: thin high-strength aluminium alloy sheets (about 65% in volume, 80% in weight), a structural adhesive (about 17% in volume, 10% in weight), and high strength aramid fibres (about 17% in volume, 10% in weight) [4-7].

Figure 2.1 shows the schematic representation of fibre metal laminate. The mechanism of fatigue resistance in ARALL is that loads in the cracked metal layers are transmitted to the fibres via the adhesive and hinder the crack opening, subsequently reducing the stress intensity factor in the aluminium layers. This effect is called fibre

bridging [4]. Two different grades of ARALL were developed, ARALL 1 was a variant with aluminium alloy 7075 layers and aramid fibres and ARALL 2 was a variant of aluminium alloy 2024 layers and was used in the as-cured condition.

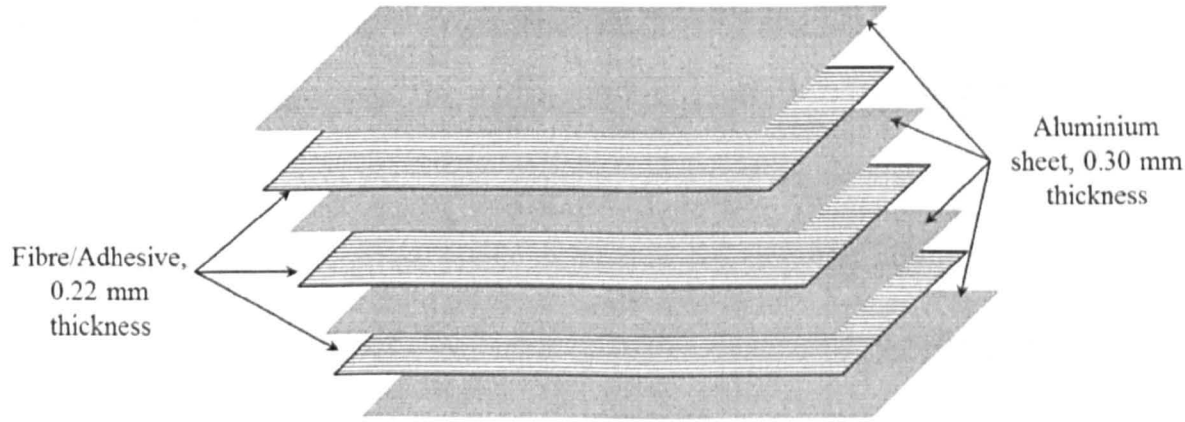

Figure 2.1: Schematic representation of Fibre Metal Laminates

In 1985 two patents were accepted and the production of ARALL was started by Alcoa [8]. The properties of these fibre metal laminates can be easily altered and optimal properties of the laminate can be achieved by increasing the volume fraction of the fibres, tailoring the fibre orientation in the main loading axis, and by decreasing the thickness of the individual aluminium layers. It has been shown that crack growth in thin sheet materials is lower than thick sheets or plate due to the plane stress effect.

This new class of material combines both the properties of the monolithic aluminium alloy with high fatigue resistance and weight saving potential. However, ARALL showed some disadvantages, such as [4, 9]:

- Aramid fibre yielded too low residual strength for a cross-ply laminate.
- Fibre failure occurred during flight simulation fatigue tests at elevated stress levels which resulted in poor performance.
- The adhesive layer absorbed moisture and was sensitive to environmental degradation. Furthermore, the aramid fibres behaved weakly under compression load.

Later, a much stiffer fibre metal laminate consisting of carbon fibres instead of aramid fibres, the CARALL laminate was investigated at Delft University of Technology [4, 5]. Research has shown that CARALL laminates also have fibre failure during flight-simulation fatigue tests at elevated stress levels, which resulted in poor performance. The limited failure strain of the carbon fibres (0.5-2%) was thought to be a disadvantage. However, the fatigue performance of these laminates was notch sensitive due to the galvanic corrosion between the aluminium sheet and carbon fibres [10, 11]. In 1987 a third generation of fibre metal laminates was developed at DUT with the name of GLARE [12], in which aramid fibres were replaced with much stiffer glass fibres. Figure 2.2 shows the classifications of fibre metal laminates. Fibre metal laminates were also developed with titanium and magnesium alloys. However, fibre metal laminates with aluminium alloys are preferred owing to the high production cost associated with titanium and magnesium alloys fibre metal laminates [4, 5, 12].

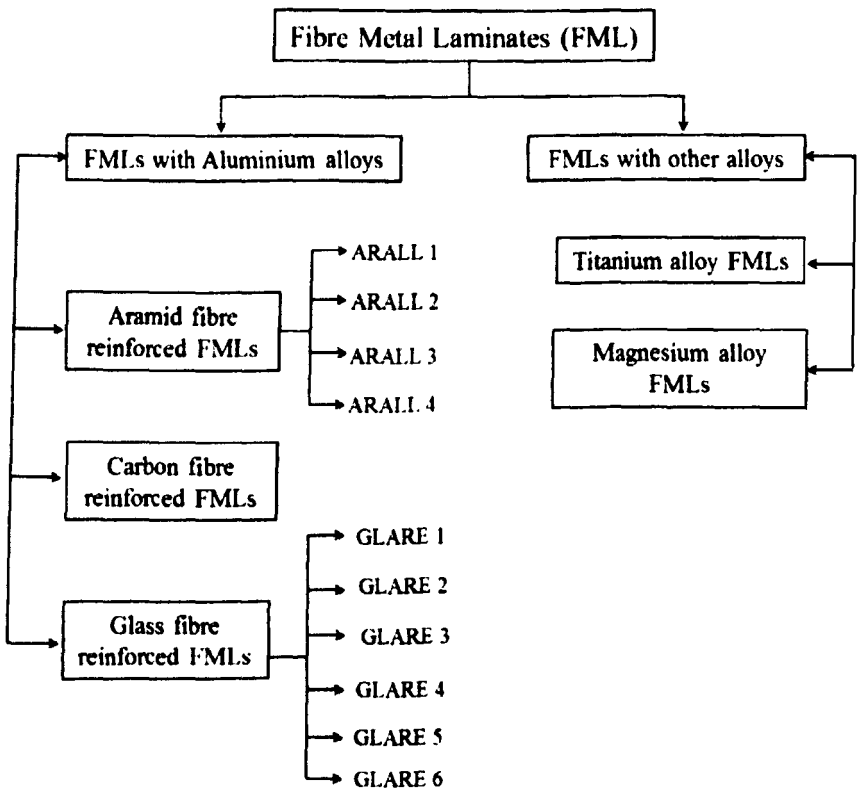

Figure 2.2: Classification of Fibre Metal Laminates [10]

2.2 Glare

GLARE is a composite structure made of aluminium layers of 0.3 to 0.5 mm thickness and fibre reinforced composite layers of 0.25 to 0.5 mm thickness. These fibres are impregnated in epoxy resin. Fibre orientation plays an important role in the final mechanical properties of the structure and can be aligned in different directions with respect to the rolling direction of the aluminium layers. Figure 2.3 shows both unidirectional and cross-ply GLARE laminates. The number of metal and adhesive layers is limited in the layered structure and the ratio between them is expressed as $(n+1)/n$, where n represents the number of glass fibre layers and $n+1$ is the number of aluminium layers. The properties of GLARE can be tailored and used for different applications by changing the thickness of the aluminium sheet, the fibre orientation, the fibre volume fraction, and the aluminium alloy type. Commercially available different GLARE laminates are summarized in table 2.1.

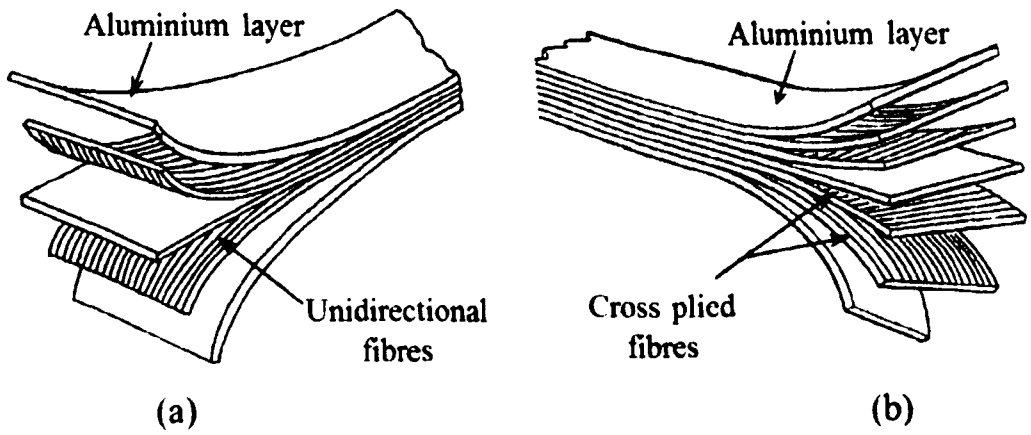

Figure 2.3: Build-up of GLARE laminates (a) unidirectional fibres and (b) cross-plied fibres [13]

GLARE laminates are manufactured by bonding together alternate layers of glass fibres impregnated in epoxy resin and unclad aluminium sheets. The glass fibre epoxy and aluminium sheets are stacked in the required orientation and cured in an autoclave. The adhesive system in which glass fibres are impregnated determines the bonding strength and can significantly affect the performance of the laminate.

During the curing process, the GLARE will be heated to a curing temperature of typically 120°C and then cooled to room temperature. The difference in the thermal expansion coefficients of aluminium sheets and glass fibre adhesive layers results in residual stresses in the laminate after curing. At 120°C the glass fibre adhesive layers starts to solidify by building cross-links in the material. After cooling from the curing temperature to room temperature, the aluminium sheets shrink more than the glass fibres. This contraction is restrained which results in tension in the aluminium sheets and compression in fibres. This stress system is unfavourable for the fatigue performance of the aluminium and has an influence on the fatigue behaviour and fail safety of the structure. This unfavourable stress system can be reversed by a post-cure stretching process which will produce beneficial compressive stresses in the aluminium layers. This process will increase the production cost and it is not possible to post stretch large aircraft panels [3, 9].

Grade	Aluminium layers		Fiber layers		Density (g/cm^3)	Beneficial characteristics
	Alloy	Thickness (mm)	Orientation	Thickness (mm)		
GLARE 1	7475-T76	0.3 – 0.4	Unidirectional	0.25	2.52	Fatigue, strength
GLARE 2A	2024-T3	0.2 – 0.5	0°/0°	0.25	2.52	Fatigue, strength
GLARE 2B	2024-T3	0.2 – 0.5	90°/90°	0.25	2.52	Fatigue, strength
GLARE 3	2024-T3	0.2 – 0.5	0°/90°	0.25	2.52	Fatigue, impact
GLARE 4	2024-T3	0.2 – 0.5	0°/90°/0°	0.375	2.45	Fatigue, strength
GLARE 5	2024-T3	0.2 – 0.5	0°/90°/90°/0°	0.5	2.38	Impact
GLARE 6	2024-T3	0.2 – 0.5	+45°/-45°	0.25	2.52	Shear, off-axis properties

Table 2.1: Different types of commercially available GLARE [5]

The orientation of glass fibres will vary between different grades of GLARE. For GLARE 1, GLARE 2A, GLARE 2B, GLARE 4, and GLARE 5 unidirectional glass fibre layers are stacked symmetrically between two aluminium layers. For GLARE 3 a glass-fibres-epoxy layer is laid along the rolling direction of the aluminium sheet, and the next glass-fibres-epoxy

layer will be placed perpendicular to the aluminium sheet rolling direction. For GLARE 6 a glass-fibres-epoxy layer is laid at +45° to the aluminium sheet rolling direction and the next glass-fibres-epoxy layer will be placed –45° to the aluminium sheet rolling direction [12].

In addition to the orientation of the glass fibres, the bonding strength of the layers will have a significant effect on the properties of GLARE laminates. To optimise this, aluminium layers are surface treated and primed prior to bonding. Surface treatment modifies the surface of aluminium sheets and increases the bond strength by stabilising the thermochemical-mechanical environment on the aluminium surface. There are various surface treatment technologies available such as:

a) Mechanical treatments (abrasion and grit blasting)

b) Chemical treatments (acid etchings)

c) Electrochemical treatments (anodizing)

d) Coupling agent treatments

e) Dry surface treatments

Among these, electro chemical treatments, in particular chromic acid anodizing (CAA) and phosphoric acid anodizing (PAA), are currently the preferred surface treatment techniques in the aerospace industry [14]. The pre-treatment for aluminium sheets involves alkaline degreasing, pickling in chromic sulphuric acid, chromic acid anodization or phosphoric acid anodizing, and priming with BR 127 which is a modified epoxy phonolic primer with corrosion inhibiting properties [15].

Chromic acid anodizing and phosphoric acid anodizing processes involve the use of hexavalent chromium and phosphorous. Chromic acid anodizing is found to give relatively thick oxide layers on the surface ranging from 1.5-3 μm with cell wall thickness ~30nm which are highly porous. A newer anodizing process, phosphoric acid anodizing, which

can produce a much thinner oxide layer was developed by Boeing and is currently the preferred surface treatment for aluminium alloys. The surface oxide is thinner, ranging from 400-800 nm including ~100 nm small protruding fibrils. The oxide is highly porous with a cell wall thickness of ~40 nm which is thicker than chromic acid anodizing. The phosphate component of the oxide makes it highly moisture-resistant which leads to clearly better joint durability. In addition the surface fibrils produced by phosphoric acid anodizing can act as a part of the fibre reinforced matrix and the subsequent application of primers will result in good long term performance of the bonding interface [16, 17].

2.3 Characteristics of GLARE

The layered structure in GLARE offers different mechanical properties and failure modes depending on the layup of constituents. GLARE laminates are suitable for various machining processes such as drilling, milling, etc. and also can sustain bending operations if performed with particular care. The constituents and composition of the laminate dominate the formability of the GLARE. The formability of GLARE is not as great as monolithic aluminium due to its laminated structure and limited failure strains (glass fibres 4%) of the fibres, and the multiple failure modes that occur. However, this limited formability is adequate in some structural elements such as stringers. Stringers or profiled shapes are produced by bending processes. The fibre orientation in the stringers is only in the longitudinal direction which is favourable for bending in the transverse direction. The bend lines are parallel to the fibres and applied strain are perpendicular to the fibres which allows manufacturing stringers from flat laminates just like metal sheets Figure 2.3 shows different cross sections of profiles and stringers [18].

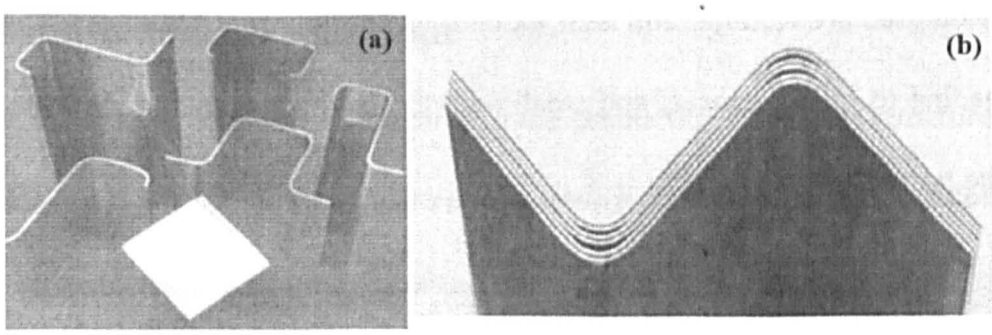

Figure 2.4: (a) Different cross sections of profiles and stringers (b) build-up stringer [17]

Stringers and profiles are made in a wide variety of shapes. The bend radiuses of these structures are of the same magnitude as those fabricated with metal alloy. Thick stringers or profiles are made by a combination of forming and lay-up processes. In this case, the thin laminates are assembled in thick stringers by bonding of the profiles with an adhesive [18].

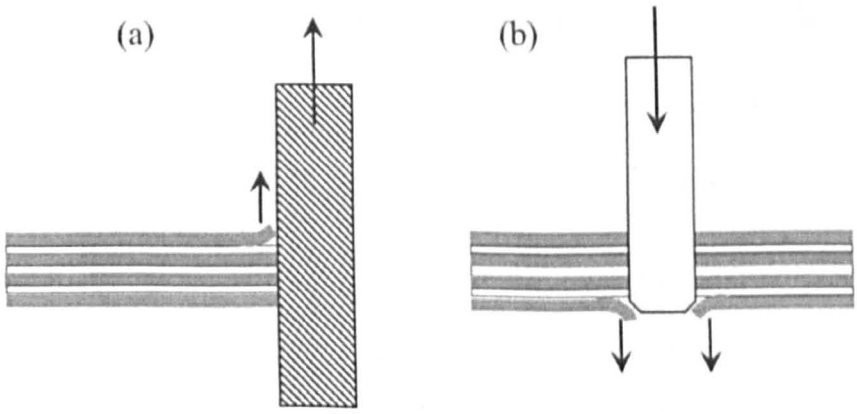

Figure 2.5: Mechanism of GLARE damage due to machining

Most machining operations on GLARE can be carried out after the complete structure is prepared. During machining processes peel forces are induced perpendicular to the laminate. The most common machining processes used are edge milling and drilling holes for riveting and bolting of the assembly. The presence of glass fibres leads to considerable damage to the tool. In addition, during machining GLARE can experience edge delamination. Figure 2.5 shows the mechanisms of delamination in GLARE during machining. The peel forces induced during drilling are enough to cause delamination during the exit of the drill. Hence it is essential to limit the applied forces during machining of GLARE laminates. Besides milling and drilling other machining processes

that may be used are waterjet and laser jet cutting. These processes will introduce rough edges leading to fatigue cracks, and small heat affected zones in the cutting area that impair the properties [18].

2.3.1 Impact behaviour

Improved damage tolerance and weight reduction are two important advantages of GLARE. It has other favourable characteristics which are superior to monolithic aluminium.

- Impact properties of GLARE with biaxial fibre layers are better than that of monolithic aluminium.
- The impact resistance of GLARE can be optimized by increasing the volume fraction of glass fibres in the adhesive, which resulted in a special variant called GLARE 5 which has been in use as a cargo floor in the Boeing 777.
- Quasi-isotropic layup configuration of laminates will provide better impact resistance than unidirectional layups.
- At low velocity impact damage, GLARE has higher cracking energy and smaller damaged area than monolithic aluminium which is attributed to the stronger glass fibres and the laminate structure [19-21].

Impact damage on aircraft structures mostly occurs by sources such as runway debris, hail, collision between service vehicles, cargo, bird strikes, and heavy tool drops during servicing. Impact damage in GLARE can result in damage to the aluminium and glass fibre layers in the interior which makes it difficult to detect and increases the safety concerns for the aircraft structure. Impact damage on GLARE results in plastic deformation of the aluminium layers and glass fibre breakage. This may reduce the performance of the structure by reducing the strength and stiffness of the laminate [22-24].

2.3.2 Environmental behaviour

Aluminium is the most widely used material in the production of aircraft structures. Long exposures to severe environments will cause material damage due to corrosion which may affect the structural performance of the metal. On the other hand GLARE offers good protection against corrosion by preventing through thickness corrosion. The prepreg layers present in between the aluminium layers in the GLARE act as moisture barriers, whereas the aluminium layers protect the fibre/epoxy layers from picking up moisture. The aluminium sheets used in GLARE have significantly more corrosion resistance than thicker aluminium plate, which is attributed to the much faster quench followed by rolling of aluminium sheets; this results in strained grain boundaries and makes the material corrosion resistant [25].

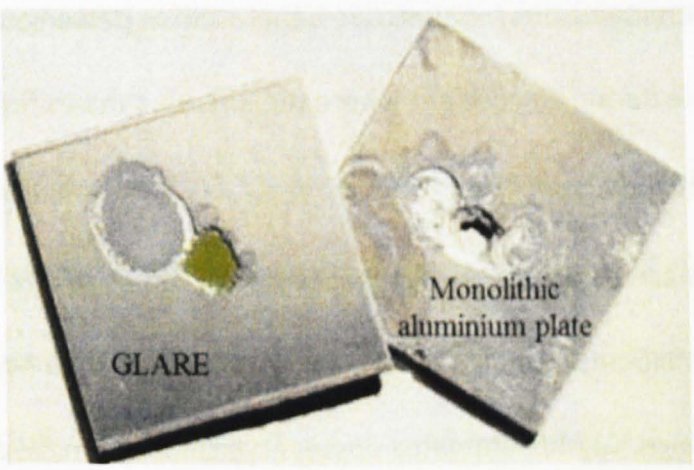

Figure 2.6: Corrosion in GLARE and monolithic aluminium plate [25]

Moisture absorption is very limited due to the laminated structure. The aluminium sheet offers protection to the glass-fibre-epoxy layers through degradation due to moisture. The aluminium sheets used in the production of GLARE are anodized and primed with a corrosion-inhibiting primer which further increases the corrosion resistance. Figure 2.6 shows the difference in corrosion behaviour of GLARE and monolithic aluminium plate. The laminated structure of the GLARE will prevent through thickness corrosion. From figure 2.6 it can be seen that only the first layer of aluminium sheet was affected by

corrosion in the GLARE and the epoxy layer, which is a non-corroding material, prevented further damage to the structure. In contrast to the GLARE, through thickness corrosion can be observed in the monolithic aluminium plate. However, GLARE is susceptible to stress corrosion cracking [4, 9, 15].

2.3.3 Fire resistance

In addition to the excellent impact damage properties, GLARE has superior fire resistance than conventional aluminium. A typical burn-through resistance test is used to characterise the fire resistance properties of GLARE. Fire resistance performed at 1200°C showed that the GLARE prevented fire from penetrating for more than fifteen minutes and relatively low temperatures were maintained on the other side of the GLARE. The outer aluminium layer quickly melted but the next layers were able to withstand the temperature. This improved fire resistance is beneficial for passenger aircraft in view of the short escape time during an accident where the aircraft catches fire [4, 9].

2.3.4 Mechanical behaviour

Aerospace materials are designed for optimal performance in severe conditions. GLARE combines both metallic and composite properties which lead to improvement in the aircraft structural design. GLARE laminates possess typical mechanical properties superior to the monolithic aluminium which are listed in table 2.2.

Material	Ultimate tensile strength (MPa)		0.2% Tensile yield strength (MPa)		Tensile elastic modulus (GPa)		Tensile ultimate strain (%)	
	L	T	L	T	L	T	L	T
2024-T351	455	448	359	324	72	72	19	19
GLARE 1	1282	352	545	333	65	50	4.2	7.7
GLARE 2	1214	317	360	228	66	50	4.7	10.8
GLARE 3	717	716	305	283	58	58	4.7	4.7
GLARE 4	1027	607	352	255	57	50	4.7	4.7
GLARE 5	683	681	297	275	59	59	4.7	4.7

Table 2.2: Tensile properties of GLARE laminate [15]

Typically GLARE exhibits strongly directional properties with respect to the orientation of the glass fibres in the laminate. GLARE laminates exhibit inelastic behaviour under tension due to plasticity of the aluminium layers. The fibres contribute to the strength and modulus in the direction along which they are aligned whereas aluminium sheet layers contribute to control the tensile properties in the transverse direction [15, 26-28].

The elastic modulus of GLARE is lower than the monolithic aluminium due to the presence of the epoxy/glass layers. Tensile properties of GLARE are superior than the aluminium alloys in the fibre aligned direction. However the transverse properties of GLARE are lower than aluminium alloys, though this can be improved by cross-ply (+45°/–45°) orientation of the glass fibres. The use of cross-plied laminates produces similar properties in both longitudinal and transverse directions of the GLARE. These types of laminates are most widely used in structures where high damage tolerance is required [15, 26-28].

Experimental, analytical, and finite element modelling [29-32] were developed to predict the in-plane tensile properties and stress-strain response of different GLAREs. The results indicated that the tests and predictions are in good agreement. The inelastic behaviour of GLARE in tension should be considered to accurately predict its tensile response [32].

Properties	Test direction	2024-T3, 1.6 mm thickness	GLARE 1	GLARE 2	GLARE 3	GLARE 4	GLARE 5
0.2% compressive yield strength (MPa)	Longitudinal	304	447	390	319	349	283
	Transverse	345	427	253	318	299	280
Compressive elastic modulus (GPa)	Longitudinal	74	63	69	63	62	61
	Transverse	74	56	56	62	57	61

Table 2.3: Compressive properties of GLARE laminate [15]

Compressive properties of different GLARE materials are listed in table 2.3. It can be seen that the compressive yield strength of different GLAREs, except for GLARE 5, are higher in the longitudinal direction (0° orientation of glass fibres) and lower in the transverse direction, except for GLARE 1, which is attributed to the fibre orientation. However the tensile and compressive elastic moduli (see. table 2.2) in different GLAREs are nearly equal due to the fact that the modulus of glass fibres is dominant during compression [33].

Sadighi et al [34] studied the effect of fibre orientation, laminates sequencing on the mechanical properties of GLARE, and concluded that GLARE with 0° fibre orientation resulted in higher tensile strength than the GLARE with 90° fibre orientation due to its low load resistance and fibre matrix failure. Impact energy absorption of GLARE with 45° fibre orientation is higher than the 0° and 90° fibre orientation. Increasing the number of aluminium layers will result in increased impact, tensile and bending strengths.

2.4 Bonded crack retarders for metallic aircraft structures

Metallic aircraft structures are susceptible to fatigue cracking during service. A continuing challenge in the aviation industry is to maintain the damage tolerance and structural integrity of aircraft structures which might be subjected to fatigue loading. Replacing cracked components is expensive and results in high operating cost. Traditional methods of repairing cracked components such as bolted or riveted metallic patches are inefficient due to a number of reasons [35]. Formation of new and additional fastener holes for the repair causes additional stress concentration areas in the structure from where cracks can develop. These repairs have to be performed in situ which might be increasing the risk of damaging other parts such as hydraulic and electrical systems and introducing swarf into the structure. Application of metallic patches may alter the stress distribution in the

surrounding structures, resulting in cracking. Additionally, poor mechanical fastening procedures result in poor contact surfaces. When aircraft experience aggressive environments and fatigue loads the relative motion of the contacting surfaces may introduce fretting corrosion or fretting damage which further reduces the performance of the repaired structure [6, 35, 36].

Work performed by the Australian aeronautical research laboratories resulted in the development of a new aircraft structural repair process which overcomes the above mentioned disadvantages and proved to be cost effective and successful. This new process is based on adhesively bonding composite patches onto the repaired structure. This method has proven effective when compared to the repair by mechanical fastening, by reducing the stress concentration areas. The major advantage in the composite patch is the ability to tailor the directional stiffness of the patch which allows applying the patches specifically in the desired direction of cyclic loading. Application of the composite patch repair method has proven to be fast, relatively cheap, and very efficient in load transfer. The high formability of the composite material allows producing complex shapes such as curved shapes in critical locations. The low electric conductivity of boron/epoxy facilitates the use of eddy current non-destructive techniques for monitoring cracks below the patch. Additionally, the use of adhesive bonding repair instead of bolted and riveted produces a sealed interface which reduces the possibility of fretting corrosion [35, 36-40].

The disadvantage of composite patch bonding is their relatively low coefficient of thermal expansion (CTE) compared to the metallic aluminium alloys. The bonding process requires temperatures typically ranging from 80°C–120°C which results in the development of thermal residual stress and distortion in the repaired structure [38]. The size of the residual stress will depend on the mismatch of coefficient thermal expansion

between substrate and strap material. However the bonded composite patches can be used for a wide range of applications which have been successfully exploited and are listed below [37, 40].

Composite patch as crack retarder

- can reduce stress intensity factors in fatigue crack regions,
- can reduce stress intensity factors in the regions affected by stress corrosion cracking (SCC),
- can increase damage tolerance and fail-safety.

Composite patches as stiffeners

- to increase fatigue, static and buckling strengths,
- can reduce deflection.

Composite patches to restore residual strength or stiffness

- after corrosion removal,
- after flaw or crack removal,
- after expiration of nominal fatigue life,
- after reshaping to reduce stress concentration,
- in regions with widespread cracking.

Over the past few decades numerous efforts have been placed to successfully apply the crack retarding technology to aging aircraft, which increases the life of the aircraft with associated economic benefits. Table 2.4 summarises the successful application of crack retarding technology undertaken in the 20th century [41, 42].

Aircraft	Problem	Repair	Remarks
C 130	Stress corrosion cracked stiffeners in wing, aluminium alloy 7075, 3 mm thick	Unidirectional boron/epoxy patch, 0.4 mm thick structural film adhesive	Over 3000 repairs. No growth in 19 years of service. Estimated savings $67M
Macchi	Fatigue cracking in magnesium alloy (MSRB) landing wheel	As above, 0.3 mm patch	Life doubled, estimated savings $2M

Mirage III	Fatigue cracking in lower wing skin, aluminium alloy AU4SG, 3.5 mm thick	As above, 0.7 mm patch	180 wings repaired or reinforced. Estimated savings $28M
F111-C	Secondary bending in wing pivot fittings leading to a fatigue problem. Steel D6ac, 7 mm thick, with risers fastened to aluminium alloy wing skin	As above, 20 mm thick, doubler	Produces over 30% strain reduction in critical region. Eighteen aircraft reinforced to date
F111-C	Stress corrosion cracking in weapon longeron flange, aluminium alloy 7075-T6	Graphite cloth patch (wet layup with EA 9394 resin) and epoxy paste adhesive	More than 10 aircraft repaired. No problems experienced after 5 years of operation
C-141 (USAF)	Fatigue cracking in wing riser weep holes, 7075T6	B/Ep patch (0°,±20° plies), structural film epoxy	55 aircraft repaired by Helitech/CTI, over 260 patches applied
F/A-18	Fatigue cracking in fatigue test bulkhead, aluminium alloy 7050, 6 mm thick	As above, 1 mm thick, doubler	Doubler withstood over 10,000 hours of severe cyclic loading. Strain reduction over 23%
Bell 206	Demonstration repair to blade near tip	B/Ep repair with structural film epoxy	Helicopter operates in tropical environment; over 1400 hours of operation some minor erosion of adhesive at leading edge
Boeing 747	Simulated repairs to several regions including fuselage lap-joint, wing leading edge, trailing edge flap and engine thrust reverser cowl	Structural film epoxy or toughened acrylic adhesives used	Demonstrator repairs; 12600 flying hours, 2660 landings with no problems
Boeing 767	Corrosion damage in fuselage keel beam; aluminium alloy 7150 T6511, 6.6 mm thick	As above, 1.5 mm thick doubler	Demonstrator repair experienced, 8300 flying hours, 5900 landings with no problems
Boeing 727	Simulated damage in fuselage lap seam region, 2024 T3, 1 mm thick	As above, 0.5 mm thick patch	Recent demonstrator repair as part of extensive test program; 5570 flying hours, 4670 landings with no problems
Airbus A340 (Test fuselage Munich)	Repairs to saw cuts in lap seam joint which were made to represent multi-site damage. Saw cuts were 170 mm and 220 mm long	Two B/Ep patches 0.76 mm thick applied with structural film epoxy	Patches have survived over 28,000 pressurisation cycles to date with no disbonds or crack growth
Boeing 747-400 series (Test fuselage-Seattle)	Repairs to fatigue cracks in a range of locations in the forward fuselage, including a shear tie, door skin and fuselage skin	B/Ep patch and structural film epoxy	Repairs (other than one frame) withstood over 20,000 pressurisation cycles with no crack growth or disbonds

Table 2.4: Applications of bonded boron/epoxy repairs to metallic aircraft structure [41, 42]

The use of bonded crack retarders relies on various factors such as the type of material for the crack retarder, geometry, location of the repair and the type of adhesive system used to achieve the desired strength. Work reported in [35, 38, 39], in which carbon fibre reinforced polymer (CFRP) and boron fibre reinforced polymer (BFRP) composites were

used as crack retarders showed that due to the high elastic modulus and the galvanic corrosion boron fibre reinforced polymer was preferred to carbon fibre reinforced polymer.

In 1990, Schijve [43] investigated various crack retarding materials made of aluminium alloy, 2024-T3, 7075-T6 and Ti-6Al-4V and Aramid reinforced aluminium laminate. The effect of different ways of joining the straps on to the skin and its effect on the performance of the crack retarder was also investigated. The main outcome of this investigation was that the adhesive bonding is more effective in reducing the crack growth in the repaired structure when compared to riveting. Amongst all crack retarding materials aramid reinforced aluminium laminate and titanium alloys performed better with aramid reinforced aluminium laminate being the best when applied on the pressurised fuselage. Moreover, aramid reinforced laminate straps have closer thermal expansion coefficient to the substrate material than that of the titanium alloy which reduces the thermal residual stresses in the reinforced structure. Aramid fibres are electrically neutral which means that galvanic corrosion is not expected when they are used in combination with aluminium [43, 44].

The hybrid concept of crack retarders led researchers to perform extensive experimental investigation to select the optimal materials for aircraft integral structures. Heinimann et al. [45] studied the effect of different reinforcement materials (GLARE, AA7075-T762, and carbon- epoxy in a fibre-metal laminate) on the fatigue life of aluminium panels. The reinforcements were adhesively bonded to the aluminium panel, which may result in the development of stresses in the panel. For this reason, the crack retarders were pre-stretched to reduce the effect of thermal residual stresses generated during the bonding process. In the stretched crack retarder straps, the aluminium layers are under compressive residual stress, which contributes to the excellent fatigue

behaviour of this material. The application of reinforcements on the thinnest panels resulted in life improvement of more than 300%. Heinimann et al. also investigated the effect of aluminium reinforcements on integrally stiffened panels and observed 50% life improvement.

As mentioned, the main disadvantage of composites as a crack retarder results from their relatively low coefficient of thermal expansion compared to the parent or repaired material which results in the development of thermal residual stresses in the parent material [40, 46-56]. The tensile nature of the thermal stresses induced in the reinforced substrate may have a negative impact on the crack initiation and crack propagation behaviour, and thereby reduce the fatigue life improvement effects during service. Aerospace structures experience a range of temperatures at different altitudes and environments. At higher altitudes the low temperatures experienced by aerospace structures can increase the residual stresses significantly over that seen at room temperature [57]. The residual stresses generated during patch bonding will affect the stress/strain state of the structure and can result in a significant shift in the stress intensity factor range for a growing fatigue crack. This shift in the stress intensity factor will vary through the thickness of the bonded structure being higher at the unbonded side [58, 59]. The amount of residual stresses developed depends on the curing temperature of the adhesive and thermal expansion coefficient of strap and reinforced structure. The magnitude of the stress can be defined by [58]:

$$\sigma_{res} = \frac{\Delta T(\alpha_s - \alpha_r)E_s E_r}{(E_s t_s + E_r t_r)} t_r \qquad \text{Equation 2.1}$$

Where σ_{res}= Residual stresses generated due to bonding

ΔT= Temperature change

α_s = CTE of substrate

α_r = CTE of reinforced strap

E_s= Elastic modulus of substrate

E_r= Elastic modulus of reinforced strap

t_s= Thickness of substrate

t_r= Thickness of reinforced strap

Djokic *et al.* [49] studied the development of thermal residual stresses during the composite bonding process and suggested that by lowering the curing temperature of the adhesive the stresses generated during the bonding process can be reduced. But lowering the curing temperature will result in longer processing cycles which increases the production cost and also reduces the glass transition temperature of the adhesive. Due to the drawbacks of low temperature curing, high temperature curing adhesive is preferred and the stresses developed during the high temperature curing can be altered by selecting a similar thermal expansion coefficient for the substrate and reinforcing material which will be discussed later. Liljedahl et al. studied various strap materials (CFRP, titanium, GFRP and GLARE) bonded to the aluminium alloy 7085-T7651 and concluded that GLARE produced low residual stresses when compared to other strap materials [51-54]. Figure 2.7 shows the residual stress distribution of various strap materials.

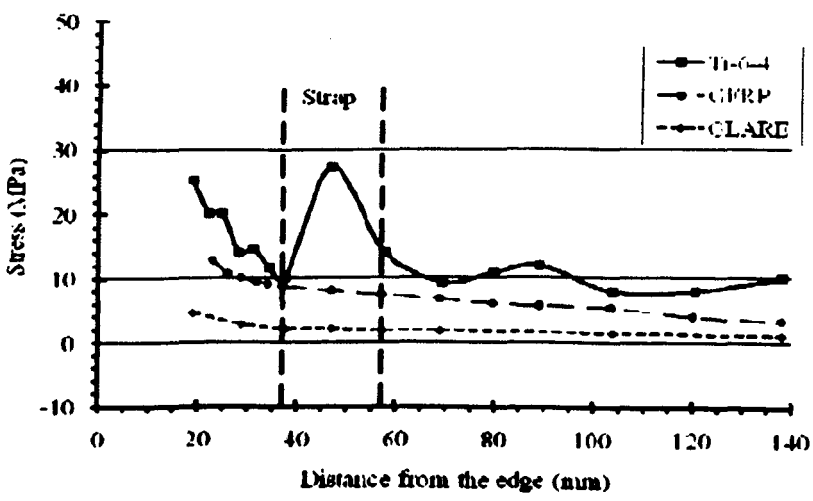

Figure 2.7: Residual stress distribution of various strap materials [54]

Apart from the type of reinforced strap material, geometry will play a vital role in the performance of the strap. The structures can be reinforced or repaired in two ways: by bonding the strap on one side of the panel or two sides of the panel. Figure 2.8 shows the schematic representation of single and double sided strap bonding. The former method is called single sided bonding and the latter called double sided bonding.

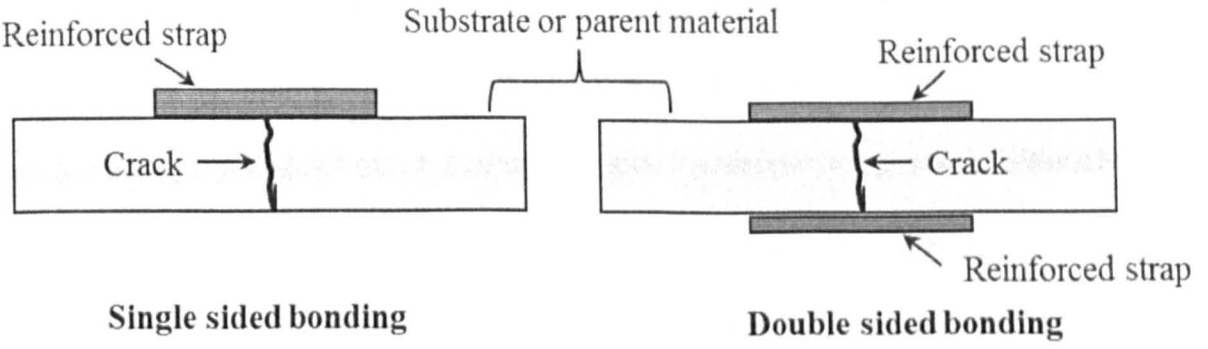

Figure 2.8: Schematic representation of single and double sided bonding

Double sided bonding is more preferred and effective than single side bonding due to its symmetric reinforcement [61]. Unfortunately single sided bonding is the most widely used technique due to the design requirements of the repaired structure. Asymmetric single-sided bonding will result in in-plane deflection of the structure which causes high stress intensity factors on the unbonded side and may affect the crack propagation [53, 55, 61, 63]. Another important aspect which affects the performance of the crack retarder is the stiffness ratio which is defined as the ratio of the strap stiffness to the overall assembly stiffness and given by [64, 54]

$$\mu = \frac{\sum E_{strap} A_{strap}}{(E_{Al} A_{Al}) + \sum (E_{strap} A_{strap})}$$ Equation 2.2

Where E_{strap} = Elastic modulus of strap material

E_{Al}= Elastic modulus of substrate material

A_{strap} = Cross sectional area of strap and

A_{Al}= Cross sectional area of substrate

Unfortunately there is little literature present on the bonded crack retarder concept. As mentioned earlier, The Open University and Cranfield University have been heavily involved in the bonded crack retarder concept to increase the damage tolerance and fail safety of aircraft structures for a number of years. In 2007, Zhang et al. [62] investigated the effect of stiffness ratio on the fatigue life improvement of aluminium alloy 7085-T7651. GLARE was used as the reinforcing material with 1.8 and 5.4 mm thickness. A substrate with 1.8 mm thick GLARE strap showed a reduction in fatigue life compared to a substrate without any strap, whereas a substrate with 5.4 mm thick GLARE strap showed an 86% life improvement due to the reduction in crack growth which is attributed to the stiffness ratio. This investigation shows the need to perform further research to study the effect of stiffness ratio on the fatigue life improvement.

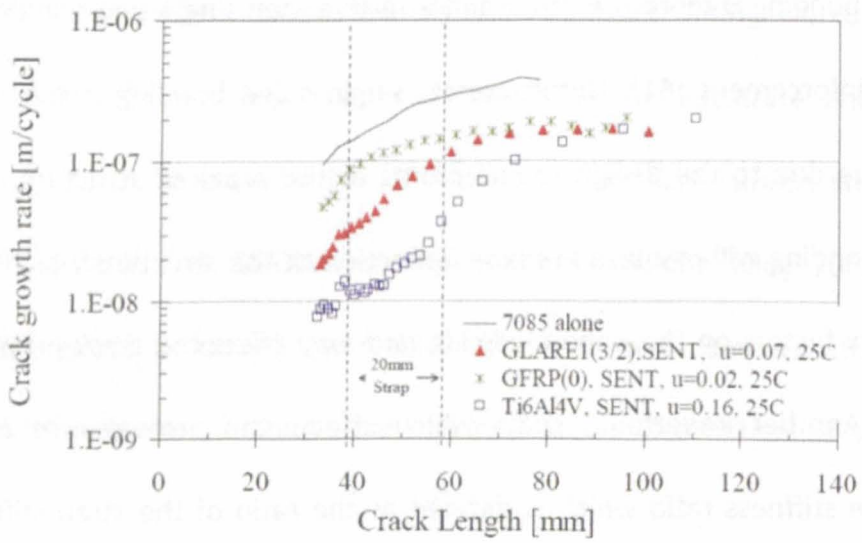

Figure 2.9: Effect of stiffness ratio on crack growth rates of different strap materials [60]

Further research performed by Irving et al [54] investigated titanium, GLARE and GFRP straps with different stiffness ratios ranging from 0.02–0.16. The results are shown in figure 2.9. In comparison with the unstrapped substrate, titanium strap with 0.16 stiffness ratio showed better performance by greatly reducing the crack growth under the strap whereas a GLARE strap with 0.07 stiffness ratio showed lower performance than the

titanium strap. From this research it was concluded that the fatigue life improvement is also dependent on the stiffness ratio.

Irving et al [60] also performed investigation on the effect of thermal residual stresses on the crack growth behaviour of aluminium alloy 7085-T7651 when bonded with different strap materials. Figure 2.10 shows the comparison of crack growth rates of different strap materials. It can be seen that the optimum retardation behaviour is exhibited by the aluminium strap which is attributed to the absence of thermal residual stresses due to the similar thermal expansion coefficient of strap and substrate material. Furthermore a GLARE strap performed better than titanium and GFRP straps which is attributed to the low (10-15 MPa) thermal residual stresses compared to thermal residual stresses developed by GFRP straps (40-50 MPa). Titanium and GFRP straps showed similar crack growth rates and it was found that they have similar residual stress fields which are greater than the stresses induced by GLARE bonding.

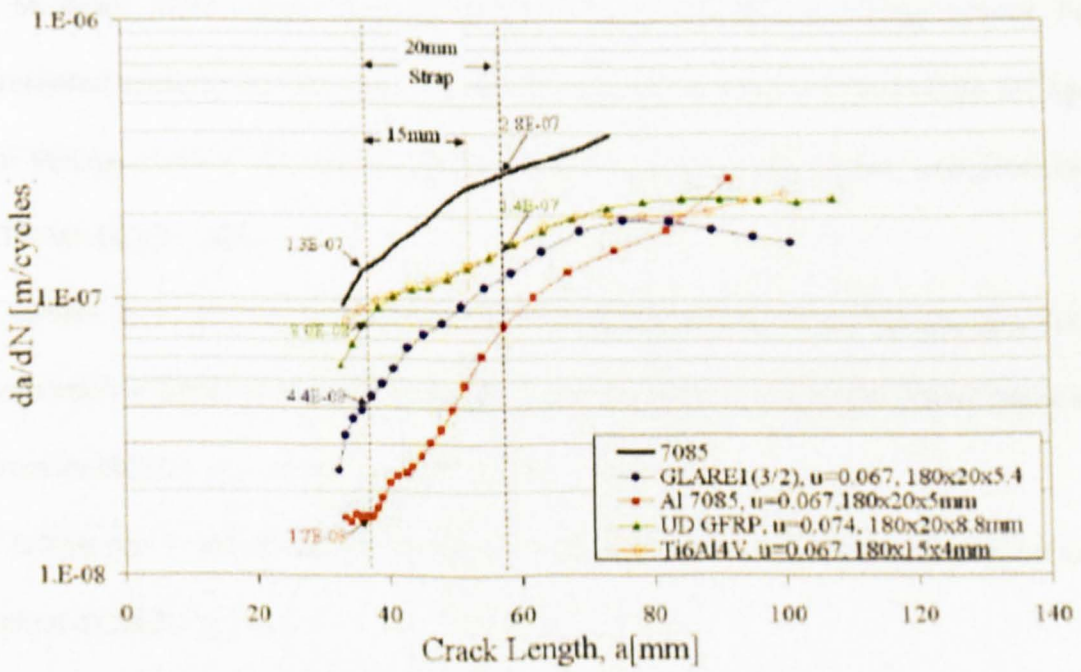

Figure 2.10: Comparison of crack growth rates of different strap materials [60]

From the extensive research performed on bonded crack retarders over the last few years, it has been shown that the major parameter influencing the performance of the strap material is the magnitude of thermal residual stresses and the global stiffness ratio.

Amongst all the strap materials investigated, GLARE has shown low stresses and better retardation behaviour even with high temperature curing of the adhesive which makes it the optimum material as reinforcing straps.

2.5 Summary

This chapter presents a detailed literature review on history and development of fibre metal laminates. A brief history of GLARE, the characteristics of GLARE and different variants in GLARE are discussed in detail. Further, the early research on the application of bonded crack retarders and the results are discussed in detail. The detailed literature review presented in this chapter shows that the use of bonded crack retarders can provide significant life improvement in fatigue crack growth and residual strength for aerospace structural applications.

2.6 References

[1]. J. Schijve, *Development of fibre-metal laminates, ARALL and GLARE, new fatigue resistant materials,* internal Report LR-715, Aerospace Engineering, Delft University of Technology 1993.

[2]. H. J. Schmidt and B.B. Schmidt, *Damage tolerance design and analysis of current and future aircraft structure*, in International air and space symposium and exposition, pp. AIAA 2003–2784, 2003.

[3]. X. Zhang, M. Boscolo, D. Figueroa-Gordon, G. Allegri, and P. E. Irving, *Fail-safe design of integral metallic aircraft structures reinforced by bonded crack retarders*, Engineering Fracture Mechanics, vol. 76, no. 1, pp. 114–133, 2009.

[4]. L. B. Vogelesang and A. Vlot, *Development of fibre metal laminates for advanced aerospace structures*, Journal of Materials Processing Technology, vol. 103, no. 1, pp. 1–5, 2000.

[5]. A. Vlot. and G. J. Willem, *Fibre Metal Laminates: An Introduction*. Kulwer academic publishers, 2001.

[6]. J. M. Baker, Alan, Richard Chester, *Bonded Repair Technology for Aging Aircraft*, Paper presented at the RTO AVT Specialists meeting on Life Management Techniques for Ageing Air Vehicles, held in Manchester, United Kingdom, 8-11 October 2001, and published in RTO-MP-079 (II), 2001.

[7]. J. Schijve, H. T. M. Van Lipzig, G. F. J. A. Van Gestel, and A. H. W. Hoeymakers, *Fatigue properties of adhesive-bonded laminated sheet material of aluminum alloys*, Engineering Fracture Mechanics, vol. 12, no. 4, pp. 561–579, 1979.

[8]. J. Schijve and L. Vogelesang, *Laminate of aluminium sheet material and aramid fibres*, US patent 4500589, A, 1985.

[9]. M. Hagenbeek, *Characterisation of Fibre Metal Laminates under Thermo-mechanical Loadings*, Ph.D. thesis, Aerospace engineering, Delft University of Technology, 2005.

[10]. T. Sinmazçelik, E. Avcu, M. Ö. Bora, and O. Çoban, *A review: Fibre metal laminates, background, bonding types and applied test methods*, Materials and Design, vol. 32, no. 7, pp. 3671–3685, 2011.

[11]. E. Hombergsmeier, *Development of advanced laminates for aircraft structures*, in ICAS, 2006, pp. 1–10.

[12]. A.Vlot, *Glare, history of the development of a new aircraft material*, Kulwer academic publishers, 2001.

[13]. A. Asundi and A. Choi, *Fiber metal laminates: an advanced material for future aircraft*, *Journal of Materials Processing Technology*, vol. 63, pp. 384–394, 1997.

[14]. S. Y. Park, W. J. Choi, H. S. Choi, H. Kwon, and S. H. Kim, *Recent Trends in Surface Treatment Technologies for Airframe Adhesive Bonding Processing: A Review (1995–2008)*, The Journal of Adhesion, vol. 86, no. 2, pp. 192–221, 2010.

[15]. G. Wu and J. Yang, *The mechanical behavior of GLARE laminates for aircraft structures*, Journal of the Minerals, Metals and Materials Society, vol. 57, no. 1, pp. 72–79, 2005.

[16]. G. W. Critchlow and D. M. Brewis, *Review of surface pre-treatments for aluminium alloys*, International Journal of Adhesion and Adhesives, vol. 16, no. 4, pp. 255–275, 1996.

[17]. A. Bjørgum, F. Lapique, J. Walmsley, and K. Redford, *Anodising as pre-treatment for structural bonding*, International Journal of Adhesion and Adhesives, vol. 23, no. 5, pp. 401–412, 2003.

[18]. J. Sinke, *Manufacturing of GLARE Parts and Structures*, Applied Composite Materials, vol. 10, no. 4, pp. 293–305, 2003.

[19]. B. Liaw, Y. Liu, and E. Villars, *Impact damage mechanisms in fiber-metal laminates*, in Proceedings of the SEM Annual Conference on Experimental and Applied Mechanics, pp. 536–539, 2001.

[20]. M. Krull and A. Vlot, *Impact Damage Resistance of Various Fibre Metal Laminates*, Journal de Physica IV France, vol. 7, pp. 1045–1050, 1997.

[21]. A. Vlot, *Impact loading on fibre metal laminates*, International Journal of Impact Engineering, vol. 18, no. 3, pp. 291–307, 1996.

[22]. M. Sadighi, R. C. Alderliesten, and R. Benedictus, *Impact resistance of fiber-metal laminates: A review*, International Journal of Impact Engineering, vol. 49, pp. 77–90, 2012.

[23]. A. Vlot, E. Kroon, and G. La Rocca, *Impact Response of Fiber Metal Laminates*, Key Engineering Materials, vol. 141–143, pp. 235–276, 1997.

[24]. A. Fahr, C. E. Chapman, D. S. Forsyth, C. Poon, and J. F. Lalibert, *Non-destructive evaluation methods for damage assessment in fiber-metal laminates*, Polymer Composites, vol. 21, no. 4, pp. 568–575, 2000.

[25]. C. A. J. R. Vermeeren, *An Historic Overview of the Development of Fibre Metal Laminates*, Applied Composite Materials, vol. 10, no. 4–5, pp. 189–205, 2003.

[26]. J. W. Gunnink, J. W. Boud, and Laurens, *Aerospace Arall The Advancement in Aircraft Materials*, in 35th International SAMPE Symposium, 1990, pp. 1708–1721.

[27]. J. W. Gunnink and B. Vogelesang, *Aerospace Arall-A challenge for the aircraft designer*, in 36th International SAMPE Symposium, 1991, pp. 1509–1522.

[28]. R. J. Bucci, L. N. Muller, L. B. Vogelesang, and J. W. Gunnik, *Aluminum Alloys-Contemporary Research and Applications*, vol. 31, pp. 295–322, 1989.

[29]. M. Hagenbeek and C. Van Hengel, *Static properties of fibre metal laminates*, Applied Composite Materials, pp. 207–222, 2003.

[30]. G. Wu and J.-M. Yang, *Analytical modelling and numerical simulation of the nonlinear deformation of hybrid fibre–metal laminates*, Modelling and Simulation in Materials Science and Engineering, vol. 13, no. 3, pp. 413–425, 2005.

[31]. M. Kawai, M. Morishita, S. Tomura, and K. Takumida, *Inelastic behavior and strength of fiber-metal hybrid composite: GLARE*, International Journal of Mechanical Sciences, vol. 40, pp. 183–198, 1998.

[32]. H. Esfandiar, S. Daneshmand, and M. Mondali, *Analysis of Elastic-Plastic Behavior of Fiber Metal Laminates Subjected to In-Plane Tensile Loading*, International Journal of Advanced Design and Manufacturing Technology, vol. 5, no. 1, pp. 61–69, 2012.

[33]. J. Verolme, *The compressive properties of GLARE*, Internal report LR-666, Faculty of Aerospace Engineering, Delft University of Technology, 1991.

[34]. M. Sadighi and S. Dariushi, *An experimental study of the fibre orientation and laminate sequencing effects on mechanical properties of Glare*, Journal of Aerospace Engineering, vol. 222, no. 7, pp. 1015–1024, 2008.

[35]. A. Baker, *Repair of cracked or defective metallic aircraft components with advanced fibre composites—an overview of Australian work*, Composite Structures, vol. 2, pp. 153–181, 1984.

[36]. A. A. Baker, *Evaluation of Adhesives for Fibre Composite Reinforcement of Fatigue-cracked Aluminium Alloys*. Vol 97, Metallurgy report: Aeronautical Research Laboratories, Australia, 1975.

[37]. A. A. Baker, *A summary of work on applications of advanced fibre composites at the Aeronautical Research Laboratories, Australia*, Composites, vol. 9, no. 1, pp. 11–16, 1978.

[38]. A. A. Baker, *Fibre composite repair of cracked metallic aircraft components — practical and basic aspects*, Composites, vol. 18, no. 4, pp. 293–308, 1987.

[39]. A. Baker, *Bonded composite repair of fatigue-cracked primary aircraft structure*, Composite Structures, vol. 47, no. 1-4, pp. 431-443, 1999.

[40]. A. A. Baker, L. R. F. Rose, and R. Jones, *Advances in the Bonded Composite Repair of Metallic Aircraft Structure*. Elsevier, 2003.

[41]. A. Baker and R. Jones, *Bonded Repair of Aircraft Structures*. Springer, 1988.

[42]. A. Baker, L. Rose, K. Walker, and E. Wilson, *Repair substantiation for a bonded composite repair to F111 lower wing skin*, Applied Composite Materials, pp. 251–267, 1999.

[43]. J. Schijve, *Crack stoppers and arall laminates*, Engineering Fracture Mechanics, vol. 37, no. 2, pp. 405–421, 1990.

[44]. R. Marissen, *Fatigue crack growth in ARALL-A hybrid aluminium-aramid composite material; Crack growth mechanisms and quantitative predictions of the crack growth rates*, Ph.D. thesis, Delft University of technology, 1988.

[45]. M. Garratt, M. Heinimann, R. Bucci, and M. Kulak, *Improving damage tolerance of aircraft structures through the use of selective reinforcement*, 23rd symposium of international committee on aeronautical fatigue, ICAF-2005, Hamburg, pp. 197–208, 2005.

[46]. A. Vlot, T. Soerjanto, I. Yeri, and J. Schelling, *Residual thermal stresses around bonded fibre metal laminate repair patches on an aircraft fuselage*, Internal report IR-799, Aerospace Engineering, Delft University of Technology, 1995.

[47]. S. Güngör, *Residual stress measurements in fibre reinforced titanium alloy composites*, Acta Materialia, vol. 50, pp. 2053–2073, 2002.

[48]. P. Hofslagare, *Residual Stress Measurement on Fibre-metal-laminates*, Journal of Neutron Research, vol 11, no. 4, pp. 215-220, 2003.

[49]. D. Djokic, A. Johnston, A. Rogers, P. Lee-Sullivan, and N. Mrad, *Residual stress development during the composite patch bonding process: measurement and modelling*, Composites Part A: Applied Science and Manufacturing, vol. 33, no. 2, pp. 277–288, 2002.

[50]. R. Kaye and M. Heller, *Finite element-based three-dimensional stress analysis of composite bonded repairs to metallic aircraft structure*, International Journal of Adhesion and Adhesives, vol. 26, no. 4, pp. 261–273, 2006.

[51]. C. D. M. Liljedahl, M. E. Fitzpatrick, and L. Edwards, *Evolution of residual stresses with fatigue crack growth in integral structures with crack retarders*, Materials Science and Engineering: A, vol. 523, no. 1–2, pp. 152–159, 2009.

[52]. C. D. M. Liljedahl, M. E. Fitzpatrick, and L. Edwards, *Distortion and residual stresses in structures reinforced with titanium straps for improved damage tolerance*, Materials Science and Engineering: A, vol. 486, no. 1–2, pp. 104–111, 2008.

[53]. C. D. M. Liljedahl, M. E. Fitzpatrick, and L. Edwards, *Residual stresses in structures reinforced with adhesively bonded straps designed to retard fatigue crack growth*, Composite Structures, vol. 86, no. 4, pp. 344–355, 2008.

[54]. P. E. Irving, X. Zhang, J. Doucet, D. Figueroa-Gordon, M. Boscolo, M. Heinimann, G. Shepherd, M. E. Fitzpatrick, and D. Liljedahl, *Life Extension Techniques for Aircraft Structures – Extending Durability and Promoting Damage Tolerance through Bonded Crack Retarders* ,in 26th Symposium of International Committee of Aeronautical Fatigue, Montreal, Canada, pp. 753–770, 2011.

[55]. Z. Wang, J. Xiao, D. Jiang, J. Zeng, and F. Yang, *Thermal Residual Stresses in Single-sided Bonded Composite Patching*, Journal of Reinforced Plastics and Composites, vol. 28, no. 5, pp. 587–599, 2008.

[56]. D. Daverschot, A. Vlot, and H. Woerden, *Thermal residual stresses in bonded repairs*, Applied Composite Materials, viol 9, no. 3, pp. 179–197, 2002.

[57]. C. Liljedahl, M. Fitzpatrick, O. Zanellato, and L. Edwards, *Effect of Temperature on the Residual Stresses in an Integral Structure with a Crack-Retarding Patch*, Strain, vol 47, pp. 1–6, 2011.

[58]. V. Sabelkin, S. Mall, M. A. Hansen, R. M. Vandawaker, and M. Derriso, *Investigation into cracked aluminum plate repaired with bonded composite patch*, Composite Structures, vol. 79, no. 1, pp. 55–66, 2007.

[59]. G.-C. Tsai and S. B. Shen, *Fatigue analysis of cracked thick aluminum plate bonded with composite patches*, Composite Structures, vol 64, no. 1, pp. 79–90, 2004.

[60]. P. Irving, X. Zhang, D. Figueroa-Gordo, M. Boscolo, and D. Cartie, *Bonded reinforcement and crack retarders in integral aluminium aircraft structures*, An internal report, Cranfield University, 2010.

[61]. A. Albedah, B. B. Bouiadjra, R. Mhamdia, F. Benyahia, and M. Es-Saheb, *Comparison between double and single sided bonded composite repair with circular shape*, Materials & Design, vol 32, no. 2, pp. 996–1000, 2011.

[62]. X. Zhang, P. Irving, M. Boscolo, G. Allegri, and D. Figueroa-Gordon, *Improving fail-safety of aircraft integral structures through the use of bonded crack retarders*, in 24th Symposium of International Committee of Aeronautical Fatigue, Naples, Italy, 2007.

[63]. J. Klug and C. Sun, *Large deflection effects of cracked aluminum plates repaired with bonded composite patches*, Composite Structures, vol 42, no. 3, pp. 291–296, 1998.

[64]. P. Irving and D. Figueroa, *Routes to improved damage tolerance; Prediction of damage tolerant performance of high strength and hybrid structures*, First International Conference on Damage Tolerance of Aircraft Structures. The Netherlands, 2007.

Chapter 3 : Residual stresses

Residual stresses are those which are essentially generated from incompatibilities between different regions in a material: in other words stresses present in the material in the absence of any external loads. They are difficult to foresee and play a significant role in component failure in combination with applied stress. They can be introduced into structural components during manufacturing and during use. Residual stresses may arise from differences in thermal expansion (e.g. welding and adhesion), plastic deformation (e.g. metal shaping) and misfits between different regions, different parts, and different phases. In actual practice it is unlikely to produce a component which is free from residual stresses because they will arise in the material during manufacturing [1]. For any material or structural component that contains residual stresses and is externally loaded the actual stress state comprises the external loading stress and the residual stresses. Therefore, it is essential to determine the residual stresses to maintain structural integrity and fail safety of the material and structure.

Residual stresses are either beneficial or detrimental depending on the behaviour of the material and the residual stress state. In general residual stresses which can act opposite to the applied loading are beneficial. Tensile residual stresses are harmful and often cause fatigue failure or stress corrosion cracking in a part or a structural components experiencing cyclic or fatigue loads in tension. On the other hand, compressive residual stresses are beneficial and can prevent initiation and propagation of fatigue crack growth, hence increasing the life of the part or structural element. For this reason manufacturing processes are preferred to leave beneficial compressive stresses in structures that can inhibit the failure [2].

3.1 Types of residual stresses

Residual stresses in a body are those which are not necessary to maintain equilibrium between the body and its environment. All engineering components that are manufactured and fabricated by inhomogeneous deformation of polycrystalline materials experience misfit between different regions within a body resulting in residual stresses. They are categorized into different groups by the scale over which they self-equilibrate and by cause (e.g. thermal residual stresses) [3]. Most of their origins may be generalised as mechanical, thermal, or a combination of two. Residual stresses may be categorized in several ways:

- By cause, such as thermal or elastic misfits.
- By the scale on which they self-equilibrate: Type I (macrostresses), Type II (microstresses II) and Type III (microstresses III).

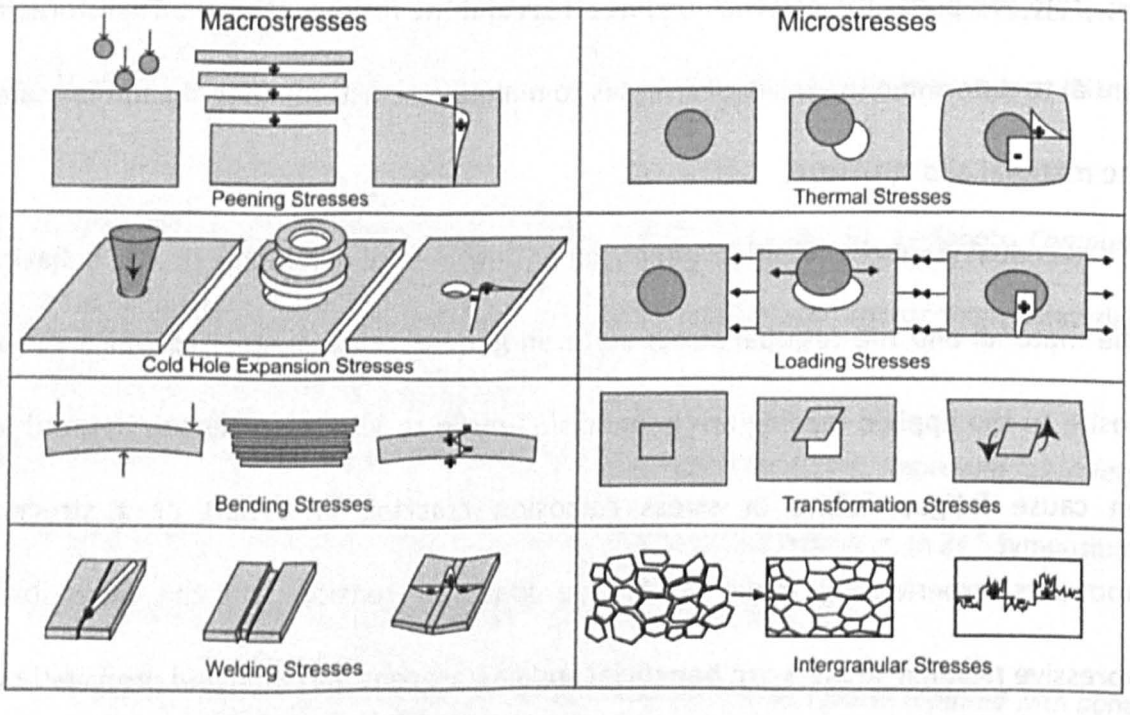

Figure 3.1: An example of different types of residual macro and micro stresses [4]

A widely accepted classification of residual stresses is the scale on which the stress varies or over which the stress self-equilibrates. Figure 3.1 shows the schematic illustration of examples of residual stresses over a length scale [4].

- Type I residual stresses are often termed as macrostresses as they are assumed to be continuous from grain to grain or phase to phase. The internal forces related to these stresses are balanced in all planes and their respective moments will be equal to zero in all axes.
- Type II stresses are generated due to stress mismatch from grain to grain or phase to phase. They are discontinuous from grain to grain and usually extent over a scale of a few tens of microns. They are homogeneous within crystal domains and internal forces related to these stresses balance between different grains or phases.
- Type III residual stresses are often termed microstresses. They arise due to misfits such as crystal defects, due to incoherency at interfaces and dislocation stress fields. They are homogeneous over the smallest crystal domains of the material. Type II and Type III stresses are collectively termed as microstresses [4, 5].

3.2 Residual stress measurement techniques

Residual stresses can have beneficial or detrimental effect depending on the loading direction and the stress state. Hence it is important to quantify and qualify the residual stresses to predict the service life of a structure and to determine the likelihood of failure. Residual stress measurement techniques are categorized according to the measurement depth into the component, the spatial resolution, the cost of the method, the number of stress components measured (1D, 2D or 3D stress state) and the state of the sample after measurement (destructive and non-destructive). In most publications, the state of the sample after measurement is considered for classification into destructive and non-destructive methods. All the destructive and non-destructive techniques are based on the measurement of strains and good understanding of the elastic and plastic behaviour of the material will enable the strains to be converted into stress.

Destructive methods of measuring residual stresses involve removing a section of material from the component that contains residual stresses and the resulting deformation is measured. In destructive techniques material removal process can be classified into three categories, mechanical (cutting, drilling, etc.), chemo-mechanical (chemical milling), and electro-chemical (electro polishing). Only residual stresses of type I (macrostresses) can be measured by destructive techniques. Type II and type III residual stresses cannot be determined as the microstresses balance to zero over the typical volume of material removed. The most common type of destructive techniques are compliance, curvature [3], hole drilling [6], and the contour method [7].

The advantage of the destructive techniques is their availability and the measured results are proven to agree well with other measurement techniques. There are now several verified destructive techniques [3, 6, 7] which are widely used depending on the stress state and the geometry of the specimen. On the other hand, the disadvantage of these techniques is that the specimen is damaged and is no longer available for repeat measurements. Also, this technique is confined to measure only macrostresses.

Non-destructive methods of residual stress measurement depend on the response of intrinsic properties of a crystalline material, such as atomic spacing, magnetic properties or velocity of ultrasonic waves passing through the material to be measured [8]. The major advantage of non-destructive method is the specimen is not damaged and the measurements can be repeated. Therefore, these measurement methods do not affect the mechanical properties of components or its serviceability. There are number of non-destructive techniques available which are mainly categorized as follows:

1. Diffraction methods
    - Conventional X-ray diffraction
    - Neutron diffraction

- Synchrotron X-ray diffraction

2. Ultrasonic methods
3. Magnetic methods
4. Raman spectroscopy
5. Optical methods

3.2.1 Diffraction methods

Diffraction methods are well known non-destructive techniques for residual stress measurements. These mainly apply to polycrystalline materials. Diffraction methods are based on Bragg's law of diffraction [4, 5] where interatomic spacing (d) of lattice planes in crystalline materials is determined from radiation of known wavelength (λ) as a function of location and direction within the sample. The measured lattice spacing is used to compute the strain thereby stress by the use of appropriate lattice constants.

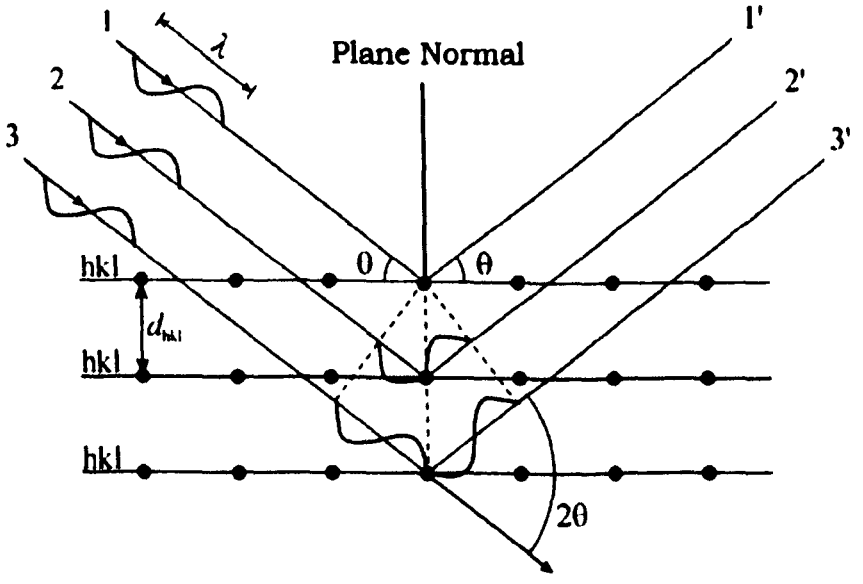

Figure 3.2: Schematic representation of Bragg's law

Bragg's law was discovered by W.L. Bragg in 1912. Figure 3.2 shows the schematic representation of Bragg's law. The diffraction results in the change in path of the incident beam which will be equal to an integer multiple of the wavelength, *n*. The relationship between wavelength and path difference can be expressed as Bragg's equation [4, 5]:

$$n\lambda = 2d\sin\theta \qquad \text{Equation 3.1}$$

Where n = multiple integer

λ = wavelength of X-rays

θ = incident angle and

d = Interplanar distance or lattice spacing

The diffraction methods are sub-categorized into three according to their depth of penetration and spatial resolution as conventional X-ray diffraction, synchrotron X-ray diffraction and neutron diffraction [4, 5].

3.2.1.1 Conventional X-ray diffraction

Conventional X-ray diffraction (XRD) is the most widely used non-destructive technique to measure residual stresses in a material, due to its availability and low operating cost. Conventional X-rays are strongly absorbed and can penetrate only a few microns (~100 μm) into most materials due to the energy level of the X-rays used. Strain measurements by X-ray diffraction are restricted to surface regions due to electromagnetic interaction between X-rays and electron cloud around the nuclei. X-ray radiation can be obtained from a variety of target metals, Cr K-α or Cu K-α are the most commonly used.

The surface elastic stress in this method is determined by the conventional $\sin^2\psi$ technique where the lattice spacing of any crystallographic planes in a direction is determined at several inclination angles and the stress is determined from the d-spacing vs.$\sin^2\psi$ plot. The overwhelming challenge faced by this technique is the presence of heavy texture and coarse grain effects which often exists in components for engineering application and which severely affects the peak shape and in turn the statistical quality of the data. The localized information from the surface with little depth penetration makes conventional X-ray diffraction unsuitable for our studies [9, 10].

3.2.1.2 Synchrotron X-ray diffraction

Synchrotron X-ray diffraction or hard X-ray diffraction is also based on Bragg's law. Synchrotron X-ray diffraction is a rapidly developing technique which allows fast internal

strain mapping with very high spatial resolution. Synchrotron X-rays are differentiated from laboratory X-rays by their high energy and intense photon flux which increases penetratability to a few millimetres compared to few microns by laboratory X-rays. The synchrotron radiation is obtained from low energy electrons whose energies will be increased by accelerating in a circular motion in a synchrotron ring. The electron beam is guided into the synchrotron ring in a straight path through so-called insertion devices consisting of an array of magnets (dipole, quadrupole, and hexapole magnets). The electron beam is then forced to follow a sinusoidal path through insertion devices. During this passage synchrotron radiation emits and the electron beam is radially accelerated by a dipole magnet which leads to further synchrotron radiation. Energy lost during synchrotron radiation emission will be compensated by radio frequency cavities. The resulting synchrotron beam has a wide range of energies ranging from 10^{-12} to 10^{3} keV and is directed to different beam lines for different types of application according to the user's specifications [5, 11].

Most synchrotron X-ray diffraction experiments are performed with monochromatic, narrow width radiation. Selection of wavelength and bandwidth of X-rays relies on a monochromator which is usually made out of one or more perfect crystals of silicon or germanium [5]. By adjusting the incident angle of the monochromator, a particular energy level is selected by Bragg diffraction which is used as an incident synchrotron X-ray beam. However, strain measurements can also be performed by using a polychromatic beam of synchrotron X-rays where the energy peak is identified by special detectors which can differentiate between photons of different energies [12]. Owing to their high energy, synchrotron X-rays produce very narrow intense X-rays of wavelength of magnitude less than the interatomic spacing. This makes the diffraction angle much smaller compared to conventional X-ray diffraction.

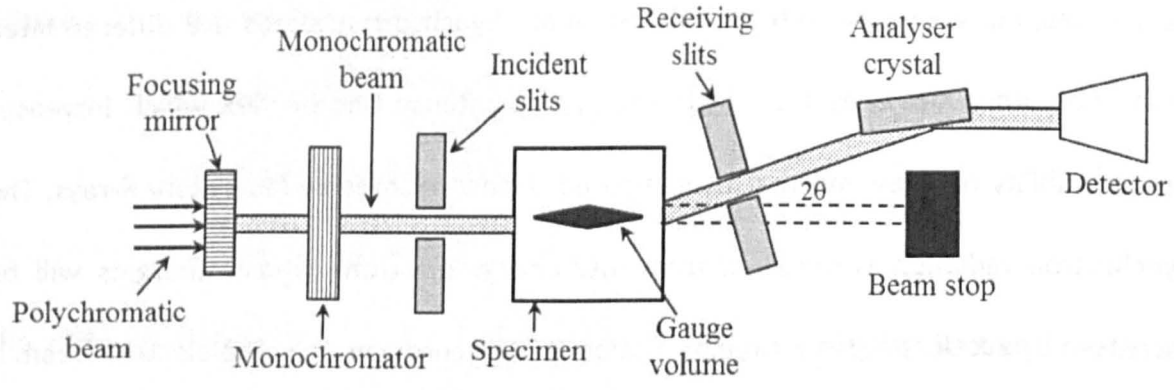

Figure 3.3: Schematic representation of experimental set-up with monochromatic synchrotron X-ray beam at European Synchrotron Radiation Facility [13]

Figure 3.3 shows the schematic representation of synchrotron X-ray diffraction. The polychromatic synchrotron X-ray beam from the storage ring is first passed through the focussing mirrors. The beam is then passed through the monochromator where the beam is collimated and a monochromatic beam with single wavelength is selected according to the user's requirement. The incident beam is then passed through a slit system which controls the incident beam spot size. Due to very high energy and low wavelength, the diffraction angle of synchrotron X-rays is very low. The low diffraction angle causes significant elongation of the gauge volume along the direction of the incident beam. The vertical opening of the incoming and receiving beam slits determine the gauge volume [12, 13].

The diffracted beam from the sample is passed through an analyser crystal. Analyser crystals are single crystals which effectively define the diffraction angle. The diffracted beam is then collected by the detectors. In a typical experimental hutch at a synchrotron source, detectors are mounted on a circular table known as the omega table. The sample is mounted on a positioner which is placed on a smaller circular table concentric with the omega table. The θ-2θ diffraction geometry is maintained by individual movement of the two tables. The sample holder is fitted with a translational motor which can move the sample across the gauge volume and strain maps can be obtained rapidly [12, 13].

3.2.1.3 Gauge volume

For residual stress measurements in any engineering component, it is essential to know where the measurements have been taken, which is defined by the gauge volume. The geometric definition of the gauge volume is the region of the incident beam viewed by the detector [5]. Figure 3.4 shows the schematic representation of gauge volume. The gauge volume defines the spatial resolution of the measured volume inside a material. The geometry and the dimensions of the gauge volume are particularly important and have a significant effect on the residual stress measurements. The gauge volume is depending on the incident beam, slits, or the diffracted beam receiving slits.

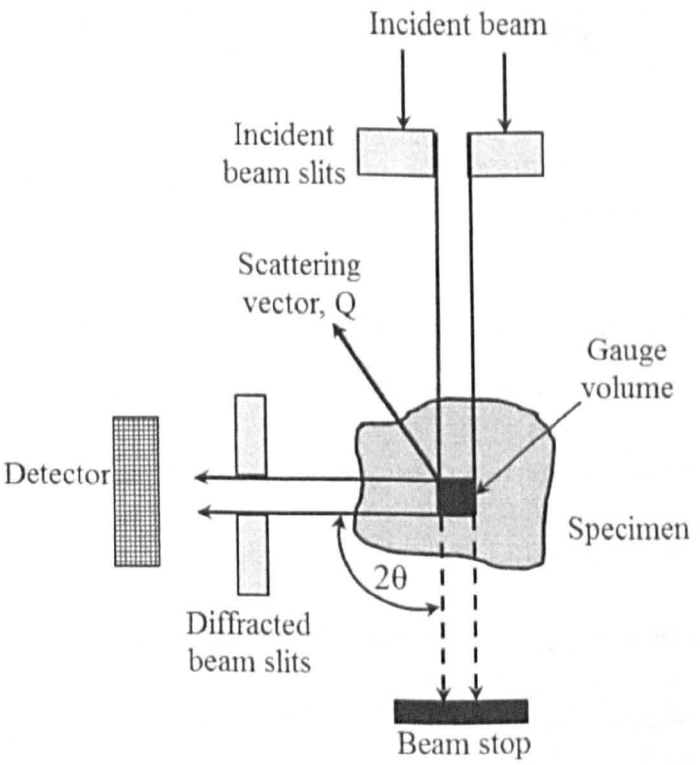

Figure 3.4: Schematic representation of gauge volume definition

Assuming the incident beam is following perfect, parallel transmitted paths through the incident and diffracted slits, the gauge volume is perfectly cuboid and often termed as the nominal gauge volume (NGV). The centroid of the nominal gauge volume is the geometric center of this volume, and is coincident with the nominal measurement position of the diffractometer.

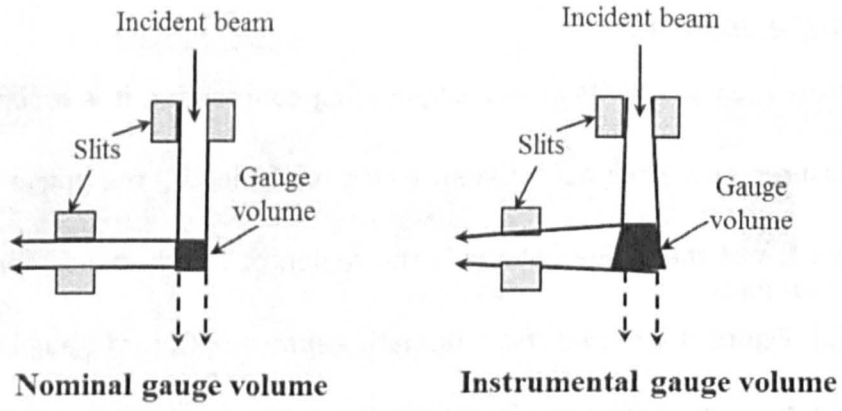

Figure 3.5: Schematic representation of nominal and instrumental gauge volume

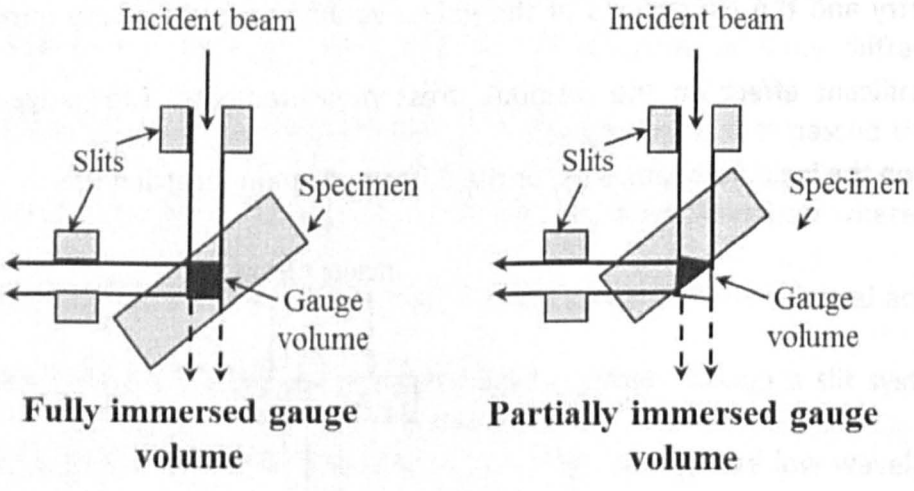

Figure 3.6: Schematic representation of fully and partially immersed gauge volumes

The sample gauge volume is not an instrumental constant and varies according to the sample being measured. A partially filled gauge volume has a great effect on the strain measurements. Figure 3.6 shows the schematic representation of a partially filled gauge volume. A partially-filled gauge volume introduces two main errors [5].

- When the gauge volume is not fully immersed (figure 3.6), the defined gauge volume by the slits does not coincide with the centroid of the actual measured region. Therefore, the centroid of the actual measured region has to be corrected by finding the centre of gravity of the actual gauge volume.
- If the gauge volume is not fully immersed, geometrical pseudo-strains arise in the measurements. The contributors to pseudo-strains are the wavelength effect, peak clipping effect and the geometric effect.

3.2.1.4 Neutron diffraction

Neutron diffraction is a well-established technique to determine strains within metallic structures. The neutron diffraction method is one of the most popular diffraction techniques which is very similar to the conventional X-ray diffraction (Bragg's law) as it relies on elastic deformation within a polycrystalline material that causes changes in the spacing of the lattice planes. The advantage of neutron diffraction over conventional X-ray diffraction is its larger penetration depth. For neutron diffraction, neutrons can be produced in two different ways, by the fission (steady state) reactor process and by a spallation (pulsed) process [4, 5, 14].

Neutron produced by either reactor processes or spallation processes are very fast, having short wavelengths and high energy in the range of MeV. These high energy, short wavelength neutrons are not suitable for strain measurements. Therefore, the high energy neutrons will pass through moderators to reduce their energy. The high energy neutron will make numerous collisions with the atoms in the moderator and release some of their energy. These low energy neutrons, thermodynamically in equilibrium with the medium at ambient temperature, have a wavelength in the order of 1.5Å, close to the interplanar spacing of most crystalline materials [4, 5].

Neutron diffraction is capable of measuring residual strains throughout the volume of a specimen i.e. mapping of strains [15]. A sample measured with neutron diffraction is bombarded either with a multiple wavelengths or single wavelength neutron beam and the resulting diffracted neutrons will be collected and recorded. The interplanar distance is then determined by using Bragg's law as mentioned earlier. The direct strain (ε) in the material in the measured direction can be calculated if both the interplanar distances of stresses (d_σ) and unstressed or stress free reference (d_0) sample are measured by the following equation [4, 5]

$$\varepsilon\,(x,y,z) = \frac{d_\sigma(x,y,z) - d_0}{d_0}$$ Equation 3.2

When three principal directional strains are known, the corresponding principal stresses can be computed by Hooke's law and are given by [4, 5]

$$\sigma_x = \frac{E}{(1+\nu)(1-2\nu)}\left[(1-\nu)\varepsilon_x + \nu\left(\varepsilon_y + \varepsilon_z\right)\right]$$ Equation 3.3

Where ν is the Poisson's ratio.

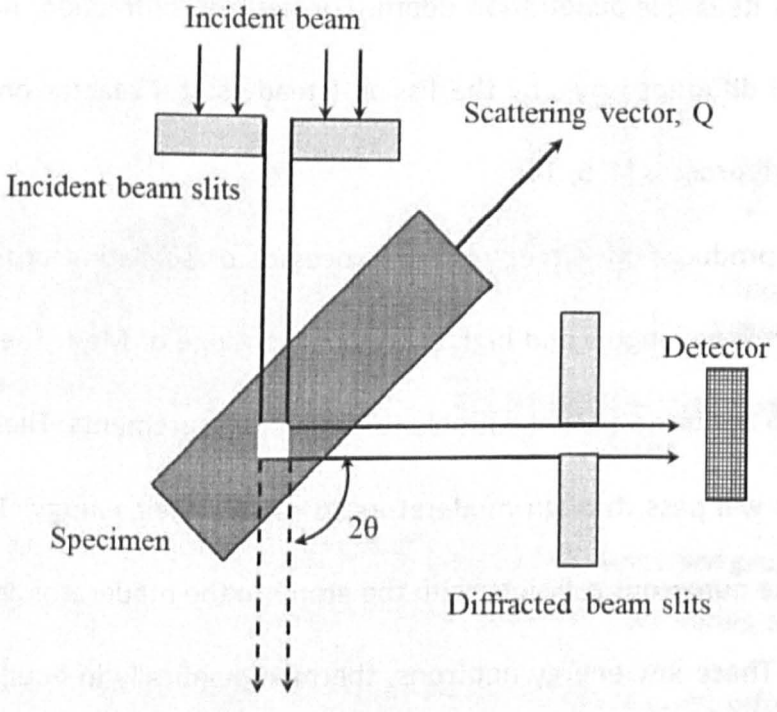

Figure 3.7: Principle of strain mapping using neutron diffraction

Figure 3.7 shows the principle of strain mapping using neutron diffraction. The measurement volume or gauge volume over which the data is averaged is determined by the width of incident beam slits and the width and height of the receiving slits or collimators. The scattering vector Q represents the direction of measurement. Divergence of the beam will affect the measuring volume and is influenced by the distance between the slits and the specimen.

In neutron diffraction residual stress measurements it is preferable to have a cubic measuring volume i.e. the same gauge volume dimensions in all three orthonormal directions [5, 16-21]. The obtained diffraction spectrum is further analysed to determine

the lattice parameters used for computing strains. This will be discussed later in this chapter. As mentioned earlier, there are two different types of neutron sources that are used for neutron diffraction measurements, reactor source or constant wavelength source, and spallation source.

3.2.1.5 Constant wavelength neutron diffractometer

In a constant wavelength neutron or reactor source diffractometer, neutrons are produced by a fission process. Most of the present neutron sources are fission reactors. The core of a fission reactor is very compact and typically is powered by enriched Uranium. Modern fission reactors are designed to produce maximum flux. The fast neutrons produced by the fission process are passed through a moderator in order to make them suitable for strain measurements. In a constant wavelength neutron diffractometer a polychromatic beam will emanate from the reactor source. The neutron beam will pass along a neutron guide and impinge on a crystal monochromator. For strain measurements, a wavelength is chosen to get a diffraction peak for the plane and the 2θ of interest by filtering out the neutrons of other wavelengths using the monochromator. The monochromator is typically a Si or Ge single crystal cut parallel to a known crystallographic plane. The wavelength distribution of the neutron beam is depends on the characteristics of the monochromator [4, 5].

The filtered beam generated by the monochromator is relatively wide (~4 cm) which is narrowed down to a few millimetres by slits placed before the specimen. Similarly, the diffracted beam is confined by another slit placed just after the sample and together the slits define the gauge volume. Neutrons scattered from the sample are recorded as a function of the diffraction angle by a detector. Stress mapping over the entire sample is done by moving the sample with respect to the gauge volume [5].

3.2.1.6 Spallation or pulsed source neutron diffractometer

In a spallation neutron source, high energy sharp pulses of protons accelerated in a synchrotron hit a target of high atomic mass (Pb, W, Ta or U). The pulsed photon beam results in spallation reactions and produces high energy sharp pulses of neutrons. A spallation neutron diffractometer uses a polychromatic neutron beam to measure the lattice parameter from different lattice planes of the material. Approximately 15 neutrons are produced for each proton and these neutrons are moderated to energies in the range 1-1000 MeV in order to use for scattering experiments [5].

Neutrons with different wavelengths will strike the specimen. Different wavelength neutrons will arrive at different times at the detector. The time taken for neutrons to reach the detector from the moderator is known as the time-of-flight (TOF). The detectors will record neutron count and time-of-flight. The initial flight from the source to the sample spreads out the neutrons in velocity and hence wavelength. Incident flight paths are typically between 20 and 100 meters; the greater the length, the higher the accuracy, but the lower the intensity. The time of flight is used to determine the wavelength of the neutron beam precisely [4, 5].

By knowing the time of flight, diffraction angle 2θ and the path lengths (L), the lattice spacing for a particular lattice plane can be determined. A time of flight diffractometer uses a wide range of wavelength typically from 0.5-5Å which enables the recording of multiple diffraction peaks from different lattice planes in the material. These diffraction peaks may be analysed separately or together. In a time of flight diffractometer different neutron energies arrive at different times at the detector resulting in the following advantages:

- The range of neutron energies results in multiple diffraction peaks allowing measurement of complex systems.

- High energy resolution of the incident energy results in high precision data allowing important detail in the scattering pattern to be resolved.
- Low background between the pulses with good signal-to-noise ratio allows observing more subtle effects with less effort [22, 23].

Both spallation and reactor source diffractometers are widely used. The neutron diffraction experiments in this dissertation were conducted at four places:

1. ENGIN-X, ISIS, UK (Time of flight)
2. POLDI, PSI, Switzerland (Time of flight)
3. SALSA, ILL, France (Constant wavelength)
4. STRESS-SPEC, FRM-II, Germany (Constant wavelength)

3.2.1.7 ENGIN-X, time of flight diffractometer

ENGIN-X is a time of flight (spallation source) diffractometer [24] where multiple reflections can be measured at once. It consists of a collimated incident pulsed neutron beam, a large *x, y, z* and *ω* positioner, two radial collimators and two neutron detector banks.

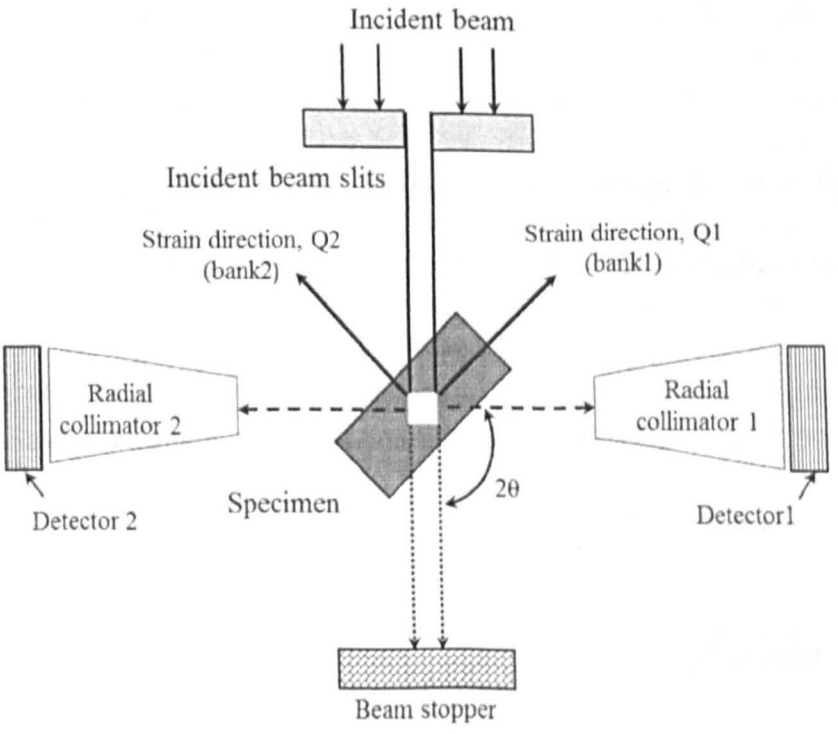

Figure 3.8: Plan view of ENGIN-X diffractometer at ISIS, UK

Detector banks are placed at ± 90° to the incident beam which allows measuring two strain components at once. 0.5, 1, 2, 3 and 4 mm collimators are available. A schematic representation of ENGIN-X is shown in figure 3.8. A pulsed beam of neutrons with wide energy spectrum is incident on to the sample. The height and width of the incoming neutron beam can be defined by incident beam slits. The beam will interact with the specimen and a small fraction of the beam is scattered into the two detectors at an angle of 2θ. Assuming elastic scattering the wavelength *(λ)* of the detected neutrons is defined by its time-of-flight, *t* and given by:

$$\lambda = \frac{h}{m(L_1 + L_2)t}$$ Equation 3.4

where *h* is Planck's constant, *m* is the mass of neutron, L_1 and L_2 the are primary and secondary flight paths respectively. The primary flight path is the distance between the moderator and the detector and the secondary flight path is the distance between the centroid of the gauge volume and the detector. The diffraction pattern consists of multiple reflections. Rather than fitting each reflection, Rietveld or Pawley fitting will be used which gives good approximation when determining the engineering elastic strain in a component [25]. In Rietveld refinement a complete diffraction spectrum is fitted and the average lattice parameter is determined. It is also possible to fit individual diffraction peaks which gives the d-spacing for each lattice plane [25]. The *ENGIN-X Script Based Analysis* (EX-SBA) software is used for the data analysis and to determine the lattice plane's spacing.

Diffraction peaks correspond to a family of lattice planes and using Bragg's law and *d*-spacing can be obtained by

$$d_{hkl} = \frac{h}{2\sin\theta\, m(L_1 + L_2)}t$$ Equation 3.5

where d_{hkl} is the lattice parameter and the strain in each principal direction can be determined by

$$\varepsilon = \frac{d - d_0}{d_0} \; or \; \frac{t - t_0}{t_0} \qquad \text{Equation 3.6}$$

where d and d_0 are the stressed and unstressed lattice parameters of the sample and t and t_0 are the time of flight of diffraction peaks in the stressed and unstressed samples. The direct stress in each principal direction can be computed by using Hooke's law (equation 3.3). EX-SBA is also capable of estimating the fitting error (Δa) for lattice spacing which can be used to determine the strain error as follows

$$\Delta\varepsilon = \sqrt{\left(\frac{\partial\varepsilon}{\partial a}\cdot\Delta a\right)^2 + \left(\frac{\partial\varepsilon}{\partial a_0}\cdot\Delta a_0\right)^2} \qquad \text{Equation 3.7}$$

The error in stress induced by the peak fitting error will be estimated in an equivalent manner.

3.2.1.8 POLDI, time of flight diffractometer

POLDI (Pulse-Overlap Diffractometer) is based at a continuous spallation neutron source where overlapping neutron pulses are used to determine the residual stresses [26, 27]. The neutron flux is comparable to a medium flux reactor. Figure 3.9 shows the plan view of the POLDI diffractometer at the Paul Scherrer Institut (PSI), Switzerland. In a pulsed overlap diffractometer, the beam chopper is one of the important components which defines the performance of the diffractometer. The chopper at POLDI is 700 mm in diameter and rotates at 15,000 rpm. The distance between the chopper and the specimen is 11.8 meters. The total length of the flight path is about 14 meters.

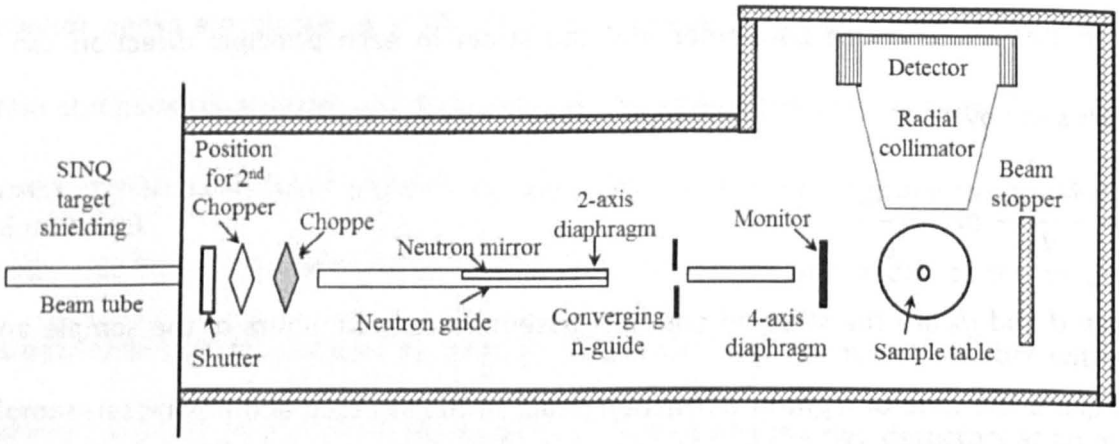

Figure 3.9: Plan view of POLDI diffractometer at PSI, Switzerland [22]

POLDI has one radial collimator (with 0.6, 1.5 and 4 mm resolution), placed at 90° to the incident beam. The neutron beam from the chopper is directed to the specimen through a neutron guide. The length of the neutron guide is about 10 meters. Neutron mirrors or optics are integrated into the neutron guide which divided into three subsections. Optics in-between the chopper and the specimen minimize losses and maintain the neutron density at the specimen which was present at the chopper. Two adjustable diaphragms are used to define the incident beam size: the diaphragm placed away (approximately 3 meters from the sample) from the specimen is fixed and used to restrict the divergence of the beam, and a diaphragm close to the specimen is adjustable and determines the incident beam size.

POLDI works on a similar principle to ENGIN-X, where a neutron beam of wide energy is incident onto the specimen and a small fraction of the beam is scattered into the detector at an angle of 2θ. At a time of flight diffractometer all reflections that are sufficiently strong can be used. At POLDI Pawley refinement is not used, but it allows fitting all the peaks independently. A weighted average lattice parameter of the four to six strongest diffraction planes will be used to determine the lattice parameter.

$$\langle a \rangle = \frac{\sum_{hkl} \frac{a_{hkl}\sqrt{h^2+k^2+l^2}}{\Delta a^2{}_{hkl}}}{\sum_{hkl} \frac{1}{\Delta a^2_{hkl}}}$$ Equation 3.8

Where $\langle a \rangle$ is the weighted average lattice parameter, and Δa_{hkl} is the error in measured a_{hkl}. Assuming elastic scattering, the weighted average lattice parameter of each diffraction peak can be used to determine strain in each principal direction by equation 3.8.

3.2.1.9 SALSA, constant wavelength diffractometer

SALSA (Strain Analyser for Large and Small scale engineering Applications) is a monochromatic strain diffractometer commissioned at the ILL continuous flux reactor source and dedicated to large engineering applications. Figure 3.10 shows the schematic representation of SALSA. It is equipped with a six axis Hexapod as the sample manipulator. The load capacity of 500 kg and the translation and tilt range of 600 mm and 30° respectively allow SALSA to manipulate both small and large specimens precisely. The position accuracy of each cylinder in the Hexapod is 2 μm which leads to a positioning error at the sample position of less than 50 μm [28].

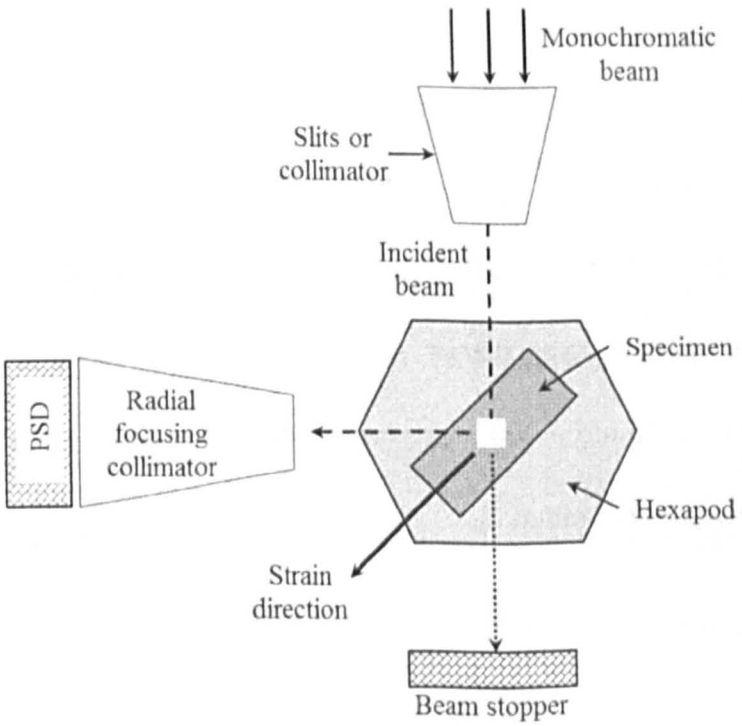

Figure 3.10: Schematic representation of the SALSA diffractometer at ILL

A silicon monochromator is used to filter the polychromatic neutron beam. The silicon monochromator can produce high intensity, narrow diffraction peaks with high

resolution. SALSA uses a position sensitive detector which can cover 4° in 2θ at a typical distance of 1 meter [28].

A neutron beam is delivered through a double focusing monochromator consisting of 39 variably bent silicon crystals which change the horizontal curvature and take-off angle of the beam. This allows a high intensity neutron beam at SALSA ranging from 1.30 Å to 3 Å which is suitable for the investigation of most engineering applications [28].

A monochromatic beam of the chosen wavelength is incident onto the specimen and a small fraction of the beam is scattered into the detector at an angle of 2θ. The chosen wavelength of the beam is dependent on the type of material being investigated and the measured lattice plane. In this research all the specimens were manufactured with aluminium which is face centred cubic (FCC) and the {311} lattice plane was chosen for the measurements because of its high multiplicity factor (24 for {311}). Also the elastic response of the 311 plane closely reflects the macroscopic elastic response of aluminium [25].

The diffracted beam from the specimen will pass through the radial focusing collimators placed perpendicular to the incident beam and collected by the position sensitive detector. The data collected by the detector are analysed by using a computer based programme called LAMP (Large Array Manipulation Programme). From the analysed data, we can obtain the *2θ* for the measured lattice plane and the lattice spacing *(d)* and strain (ε) can be determined by

$$d = \frac{\lambda}{2\sin\theta} \qquad \text{Equation 3.9}$$

$$\varepsilon = \frac{d_\sigma - d_0}{d_0} \qquad \text{Equation 3.10}$$

where d_σ is the lattice spacing of the stressed component and d_0 is the lattice spacing of unstressed material. The direct stress in each principal direction can be computed by using equation 3.3.

3.2.1.10 STRESS-SPEC, constant wavelength diffractometer

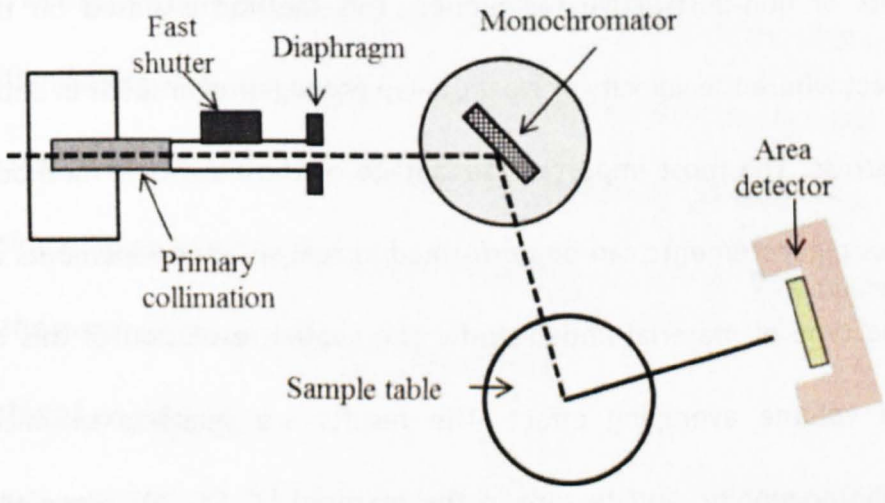

Figure 3.11: Schematic representation of the STRESS-SPEC diffractometer

STRESS-SPEC (figure 3.11) is a constant wavelength diffractometer located at a thermal beam port at the FRM-II neutron source, Germany. It comprises a highly flexible monochromator using three different crystals: Ge (511), bent silicon Si (400) and pyrolitic graphite PG (002). The take-off angles at the monochromator can be varied from 35° to 110° which allows one to obtain different wavelengths of the beam depending on the type of material and application. The wavelength of the incident beam can vary from 1Å to 2.4 Å [29].

The instrument consists of two slit systems, primary and secondary which are connected to the sample table in such a way that the center remains constant in all conditions. Therefore new alignment is not necessary for any sample or wavelength change. A two dimensional position sensitive detector is placed perpendicular to the incident beam. A sample table which can accommodate a maximum weight of 250kg with accuracy in positioning of 10μm is placed in between the incident beam and the detector.

It works on a principle similar the SALSA diffractometer. The strains, stresses, and fitting errors were computed as for the SALSA diffractometer.

3.2.2 Ultrasonic methods

Residual stress measurement by using the ultrasonic method is one of the promising developments of non-destructive techniques. This method is based on the acoustic-elasticity effect where the velocity of elastic wave propagation in solids in depends on the mechanical stress. The most important advantage of the ultrasonic method is that the residual stress measurements can be performed in real structural elements and it is not limited to the type of material under study. The spatial resolution of this technique is limited by a volume averaging effect. The results are sensitive to microstructure, inclusions, inhomogeneity, and texture in the material [3, 14, 30]. Since the materials investigated in this research have residual stress gradients within them, this method is not suitable to be used. Also, specimens investigated in this research are bonded with GLARE straps which make this method unsuitable due to the reflections from different layers in the GLARE produce unreliable measurements.

3.2.3 Magnetic methods

The magnetic method is of particular interest because of its potential as an industrial tool for non-destructive measurements. A magnetic method works on magnetostriction where each magnetic domain is magnetised along the easy axes of the crystallographic magnetisation direction. If a ferromagnetic material is magnetised, it would elongate in the direction of magnetisation. The magnetic Barkhausen noise method is the most popular of the magnetic methods [14]. The major advantage of this technique is that it is fast and portable. However, the method is only applicable for ferromagnetic materials and not suitable for this research as the aluminium alloy is non-ferromagnetic material.

3.2.4 Raman spectroscopy

Residual stress measurements by using Raman spectroscopy work on the Raman effect where inelastic scattering of light is employed. When light interacts with matter, most of the photons are elastically scattered and have the same energy (frequency and wavelength) as the incident photons. However, a small portion of the photons will scatter by an excitation having different energy from those elastically scattered and are known as inelastically-scattered photons. The inelastically scattered photons can be used to measure residual stresses in a material. This method has very fine spatial resolution (~1μm), but the penetration depth is very limited [3].

3.2.5 Optical methods

The elastic deformation of a material causes small changes in temperature and these thermal variations give an indication of the variation in the stresses. It is possible to map these thermal variations by using an appropriate infrared camera. The thermoelastic constant describes the dependence of temperature on stress and allows one to determine the hydrostatic stress component [3].

3.3 Diffraction instruments used in this research

In this research, only neutron diffraction has been used for residual stress measurements. Table 3.1 shows the number of visits to each diffractometer during this Ph.D. research.

Diffractometer	Source	Type	Number of visits
ENGIN-X	ISIS, UK	TOF	5
POLDI	PSI, Switzerland	TOF	2
SALSA	ILL, France	Constant λ	4
STRESS-SPEC	FRM-II, Germany	Constant λ	1

Table 3.1: Number of times visited at each diffractometer used in this research

3.4 Summary

In this chapter, residual stress and residual stress measurement techniques were discussed in detail. In this research, neutron diffraction has been used to investigate the residual stresses developed during the strap bonding process. Instruments working on the principle of both spallation and reactor source are used and the detailed description of the working principle of each diffraction instrument is discussed. The experimental results of residual stress measurements will be given in Chapter 6.

3.5 References

[1]. P. J. Withers and H. K.D. H. Bhadeshia, *Residual stress. Part 2–Nature and origins*, Materials Science and Technology, vol 17, no. 4, pp. 366-375, 2001.

[2]. P. J. Withers, *Residual stress and its role in failure*, Reports on Progress in Physics, vol. 70, no. 12, pp. 2211–2264, 2007.

[3]. P. J. Withers and H. K. D. H. Bhadeshia, *Residual stress; Part 1 – Measurement techniques*, Materials Science and Technology, vol. 17, no. 5, pp. 355–365, 2001.

[4]. M. Hutchings, P. Withers, T. Holden, and T. Lorentzen, *Introduction to the Characterization of Residual Stress by Neutron Diffraction*. CRC Press, 2005.

[5]. M .E. Fitzpatrick, A. Lodini, *Analysis of Residual Stress by Diffraction using Neutron and Synchrotron Radiation*. CRC Press, 2003.

[6]. E. Procter and E. Beaney, *The trepan or ring core method, centre-hole method, Sach's method, blind hole methods, deep hole technique*, Advances in surface treatments, vol. 4, pp. 165–198, 1987.

[7]. M. Prime, *Cross-sectional mapping of residual stresses by measuring the surface contour after a cut*, Journal of Engineering Materials and Technology, vol. 123, pp. 162–168, 2001.

[8]. P. J. Withers, M. Turski, L. Edwards, P. J. Bouchard, and D. J. Buttle, *Recent advances in residual stress measurement*, International Journal of Pressure Vessels and Piping, vol. 85, no. 3, pp. 118–127, 2008.

[9]. J. Pineault, M. Belassel, and M. Brauss, *X-Ray Diffraction Residual Stress Measurement in Failure Analysis, Failure Analysis and Prevention*, ASM Handbook, Vol 11. ASM International, pp. 484–497, 2002.

[10]. M. E. Fitzpatrick, A. T. Fry, P. Holdway, F. A. Kandil, J. Shackleton, and L. Suominen, *Determination of residual stresses by X-ray diffraction*, A national measurement good practice guide 52, National Physical Laboratory,2005.

[11]. P. J. Withers and P. J. Webster, *Neutron and Synchrotron X-ray Strain Scanning*, Strain, vol. 37, no. 1, pp. 19–33, 2001.

[12]. R. Owen, *Synchrotron Strain Mapping: Aerospace Application*, Ph.D. Thesis, University of Manchester, 2002.

[13]. Supriyo Ganguly, *Non-Destructive Measurement of Residual Stresses in Welded Aluminium 2024 Airframe Alloy*, PhD Thesis, Materials engineering, The Open University, 2004.

[14]. N. S. Rossini, M. Dassisti, K. Y. Benyounis, and A. G. Olabi, *Methods of measuring residual stresses in components*, Materials & Design, vol. 35, pp. 572–588, 2012.

[15]. K. Kozaczek and C. Hubbard, *Diffraction techniques in engineering applications*, Materials Science Forum, vol 210-213, pp. 703-710, 1996.

[16]. X.L. Wang, *The Application of Neutron Diffraction to Engineering Problems*, Journal of the Minerals, Metals and Materials Society, vol. 58, no. 3, pp. 52–57, 2006.

[17]. A.N. Ezeilo and G. A. Webster, *Advances in Neutron Diffraction for Engineering Residual Stress Measurements*, Textures and Microstructures, vol. 33, no. 1–4, pp. 157–171, 1999.

[18]. M. I. Ripley, *Residual stresses measurement using neutrons*, Materials Forum, vol. 30, pp. 219–224, 2006.

[19]. A. Pyzalla, *Determination of the residual stress state in components using neutron diffraction*, Journal of Neutron Research, vol. 8, pp. 187–213, 2000.

[20]. A. Allen and M. Hutchings, *Neutron diffraction methods for the study of residual stress fields*, Advances in Physics, vol. 34, no. 4, pp. 445–473, 1985.

[21]. T. M. Holden, J. H. Root, R. A. Holt, and M. Hayashi, *Neutron-diffraction measurements of stress*, Physica B: Condensed Matter, vol. 213–214, pp. 793–796, 1995.

[22]. D. L. Price and J. J. Rush, *Neutron sources and Applications*, Report of review, DOE/ER-0607P, 1992.

[23]. G. A. Webster and R. C. Wimpory, *Non-destructive measurement of residual stress by neutron diffraction*, Journal of Materials Processing Technology, vol. 117, no. 3, pp. 395–399, 2001.

[24]. J. R. Santisteban, M. R. Daymond, J. A. James, and L. Edwards, *ENGIN-X: a third-generation neutron strain scanner*, Journal of Applied Crystallography, vol. 39, no. 6, pp. 812–825, 2006.

[25]. M. R. Daymond, M. A. M. Bourke, R. Von Dreele, B. Clausen, and T. Lorentzen, *Use of Rietveld refinement for elastic macrostrain determination and for evaluation of plastic strain history from diffraction spectra*, Journal of Applied Physics, vol. 82, no. 4, pp. 1554-1562, 1997.

[26]. U. Stuhr, *Time-of-flight diffraction with multiple pulse overlap. Part I: The concept*, Nuclear Instruments and Methods in Physics Research Section A: Accelerators, Spectrometers, Detectors and Associated Equipment, vol. 545, no. 1–2, pp. 319–329, 2005.

[27]. U. Stuhr, H. Spitzer, J. Egger, A. Hofer, P. Rasmussen, D. Graf, A. Bollhalder, M. Schild, G. Bauer, and W. Wagner, *Time-of-flight diffraction with multiple frame overlap Part II: The strain scanner POLDI at PSI*, Nuclear Instruments and Methods in Physics Research Section A, vol. 545, no. 1–2, pp. 330–338, 2005.

[28]. T. Pirling, G. Bruno, and P. J. Withers, *SALSA—A new instrument for strain imaging in engineering materials and components*, Materials Science and Engineering: A, vol. 437, no. 1, pp. 139–144, 2006.

[29]. M. Hofmann, R. Schneider, G. A. Seidl, J. Rebelo-Kornmeier, R. C. Wimpory, U. Garbe, and H. G. Brokmeier, *The new materials science diffractometer STRESS-SPEC at FRM-II*, Physica B: Condensed Matter, vol. 385–386, no. 2, pp. 1035–1037, 2006.

[30]. T. Leon-Salamanca and D. F. Bray, *Residual stress measurement in steel plates and welds using critically refracted longitudinal (LCR) waves*, Research in Nondestructive Evaluation, vol. 7, no. 4, pp. 169–184, 1996.

Chapter 4 : Fracture mechanics and fatigue

Over the decades, fatigue and fracture have been the major contributors to structural failure. All engineering components and structures contain geometrical discontinuities, such as holes, keyways in shafts, windows in aircraft fuselages, etc. The size and shape of these discontinuities typically determine the strength of the structure. The complex physical process of material failure includes the combination of a number of parameters related to the type of material and its properties, residual and mean stress, structural geometry, etc. For any new material in an engineering application it is necessary to understand the fracture mechanics involved in the failure of the structure. Hence, for better understanding of the basic principles and the experimental methods performed in this research, this chapter will focus on the theoretical framework of fracture mechanics and fatigue, and will provide a quick guide to discuss the experimental methodologies applied in this research.

4.1 Fracture mechanics

Fracture is a major issue in most engineering materials, influenced by mechanical, metallurgical, and environmental factors. Among these, mechanical factors, which include structural geometry and loading conditions, are the most important. Structural geometry and loading conditions are not only required for stress analysis, but also contribute to how and when structural failure will occur [1]. There are increasing problems in structural design as a result of the increase in complex technologies in engineering applications. However, fracture mechanics have helped to better an understanding of complex structures and offset some of the potential failures. The field of fracture mechanics has matured in the past few decades and is considered as an established engineering discipline for better understanding of practical problems in structural integrity and damage tolerance in the aircraft industry [2].

Fracture mechanics is a set of theories describing the behaviour of structures with geometrical discontinuities. The applicability of fracture mechanics plays a vital role in industries such as automobile, aircraft, and nuclear power, where structural integrity and damage tolerance is required. The application of fracture mechanics to predict and understand failures is pre-eminent, especially in the aerospace industries. Fracture mechanics is based on the assumption that all engineering materials contain flaws or cracks, where the applied stress will concentrate, and from which failure starts. The estimation of remaining life of a structural component requires better understanding of the stress distribution around a crack in conjunction with crack growth conditions [3].

Griffith studied the quantitative connection between fracture stress and flaw or crack size and concluded that a crack becomes unstable when the change in the strain energy from crack growth is sufficient to overcome the surface energy of the material [4]. Since Griffith's model assumes the fracture is dependent exclusively on the surface energy of the material, it is applicable only to brittle materials. Irwin developed [5, 6] Griffith's model and work performed by Westergaard [7] derived a pioneered crack tip characterising parameter which is known as stress intensity factor which was more useful to solve fracture mechanics issues. Later, researchers [8-10] developed fracture mechanics and succeeded in prevention of structural failure by its application. In 1960, Paris applied fracture mechanics principles to fatigue crack growth where they studied the effect of stress state at the crack tip [11].

Fracture mechanics can be broadly categorised into two classifications, Linear Elastic Fracture Mechanics (LEFM) and Elastic Plastic Fracture Mechanics (EPFM). Linear elastic fracture mechanics relies on the small size of the plastic region at the crack tip, whereas elastic plastic fracture mechanics allows a large plastic region at the crack tip.

The majority of materials and loading conditions in the aerospace industry lie in the linear elastic fracture mechanics regime, hence this chapter will only focus on this.

4.2 Linear elastic fracture mechanics (LEFM)

Linear elastic fracture mechanics is based on the assumption that the material is isotropic and elastically linear. In reality a loaded cracked body is accompanied by inelastic deformation and nonlinear effects at the crack tip. This is not true for ideally brittle materials. However, the extent of inelastic deformation and nonlinear effects are small relative to the linear dimensions of the cracked body, crack size and the crack itself. In such cases, linear theory is adequate to describe the stress distribution in the cracked body. The theory of linear elastic fracture mechanics is developed by using two approaches, stress intensity factor (SIF), K, and strain energy release rate (K_c).

4.2.1 Notches and stress concentration

Structural elements often have sudden discontinuities in the geometry. Under loads, at these structural discontinuities the local stress can be magnified and cause the structure to fail. Discontinuities such as holes, threads, notches, grooves, etc. are examples of stress raisers. The localization of high stress field is called stress concentration. Stress concentration, which represents the severity of a notch or hole, is a dimensionless factor known as a stress concentration factor (K_T), defined as the ratio of the maximum stress at the root of a notch or hole to the nominal applied load.

$$K_T = \frac{\sigma_{max}}{\sigma_{\min}} = 1 + 2\sqrt{\frac{D}{\rho}} \qquad \text{Equation 4.1}$$

Where D and ρ are the notch depth (or half crack length) and notch root radius respectively. Stress concentration factor is inversely proportional to the notch root radius. Hence, for brittle materials the presence of a notch or crack is crucial to its performance. For a notched component, stress concentration factor is strictly not constant but varies

with notch depth. In brittle materials a negligible amount of energy is absorbed by plastic flow, whereas in a ductile material plastic flow of material is higher, and hence higher energy absorption. Thus ductile materials are less susceptible to notch sensitivity [12].

4.2.2 Stress intensity factor approach

Prior to discussing the stress intensity factor approach, it is important to discuss the different displacement modes that are possible when a cracked body is subjected to loading.

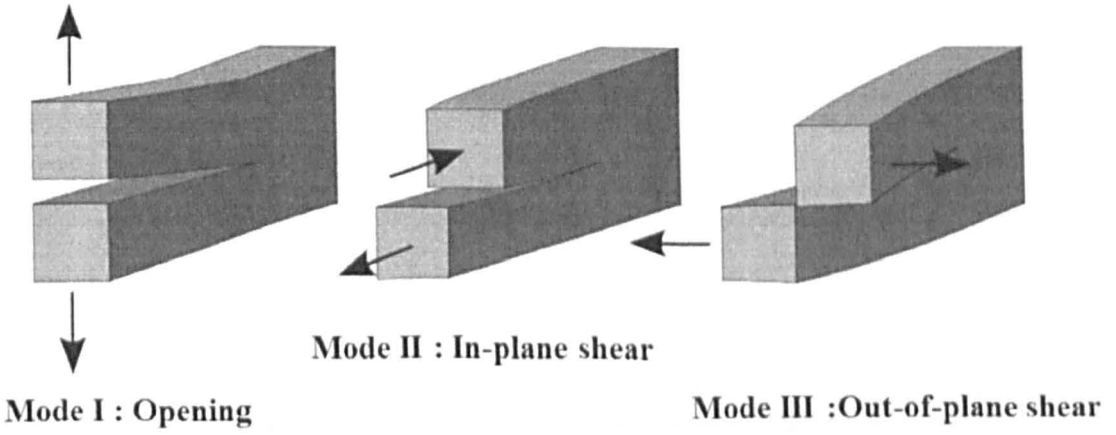

Figure 4.1: The three modes of crack surface displacements [2]

In geometrical structures, notches such as holes cause inhomogeneous stress distribution due to abrupt geometrical changes which act as stress concentration areas. The stress system in the vicinity of a crack tip may be divided into three, depending on the mode of crack surface displacement. Figure 4.1 shows the three different types of crack loading modes.

In service, if a crack grows perpendicular to the applied tensile stress this is referred to as Mode I or opening mode crack displacement. Mode II crack displacement is referred to as sliding mode, where two crack surfaces move in opposite directions along the length of the crack body. Mode III or tearing crack displacement mode is defined as when the two-crack surfaces move in opposing directions perpendicular to the length of the crack body. This mainly occurs due to shear loads. The crack initiation period followed

by crack growth period depends on the type of crack displacement mode and stresses around the crack tip. Most engineering structures will experience Mode I crack displacement. Hence this research is focused only on Mode I crack displacement.

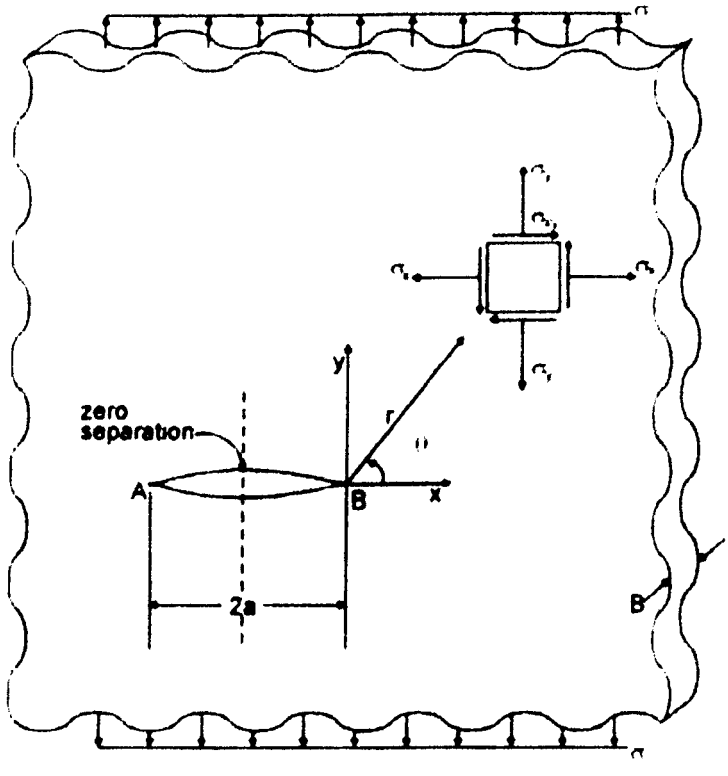

Figure 4.2: Stress state coordinate system at the crack tip [2]

Engineering structures, in particular aircraft structures, consist of numerous stress concentration areas which are prone to crack initiation. Stress concentration and stress intensity factor are two major factors that affect the crack initiation and growth period respectively. As mentioned earlier, Irwin [5, 6] developed the stress intensity factor approach which will describe the intensity of the stress in the vicinity of a crack tip. The coordinate system of the stress state in a wide plate in the vicinity of the crack tip is shown in figure 4.2. Figure 4.2 shows a crack of length 2a parallel to the x-direction is present under uniaxial stress σ. The applied stress is perpendicular (y-direction) to the crack length. The stress state at the crack tip with respect to the polar coordinates θ and r is given by [2, 13-15]:

$$\sigma_x = \frac{K_I}{\sqrt{2\pi r}}\cos\left(\frac{\theta}{2}\right)\left[1+\sin\left(\frac{\theta}{2}\right)\sin\left(\frac{3\theta}{2}\right)\right]+\ldots \qquad \text{Equation 4.2}$$

$$\sigma_x = \frac{K_I}{\sqrt{2\pi r}}\cos\left(\frac{\theta}{2}\right)\left[1-\sin\left(\frac{\theta}{2}\right)\sin\left(\frac{3\theta}{2}\right)\right]+\ldots \quad \text{Equation 4.3}$$

$$\sigma_x = \frac{K_I}{\sqrt{2\pi r}}\cos\left(\frac{\theta}{2}\right)\sin\left(\frac{\theta}{2}\right)\cos\left(\frac{3\theta}{2}\right)+\ldots \quad \text{Equation 4.4}$$

Where K_I= Stress intensity factor (SIF) and v=Poisson's ratio

For thin plates, a plane stress condition exists where $\sigma_z = 0$ and for thick plates, a plane strain condition exists where $\sigma_z = v(\sigma_x + \sigma_y)$ and $\tau_{yz} = \tau_{zx} = 0$ for $\varepsilon_z = 0$

Equations 4.2-4.4 are asymmetrically correct for a crack with small radius r. Figure 4.3 shows the relation between crack tip radius and stress at the crack tip. It can be observed that the crack tip radius can control the stress state at crack tip. The stress distribution increases with $1/\sqrt{r}$.

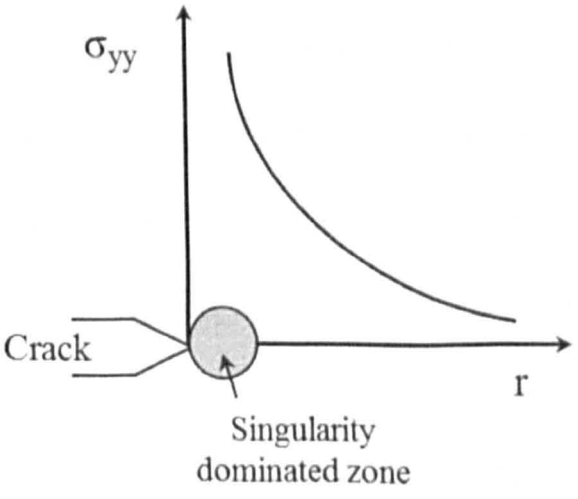

Figure 4.3: Relation between crack tip radius and stress at a crack tip

Consider a crack subjected to Mode I loading on a crack plane where θ=0, the applied stress is in the y-direction and the stress distribution given by [2, 13-15]:

$$\sigma_x = \sigma_y = \frac{K_I}{\sqrt{2\pi r}} \quad \text{Equation 4.5}$$

In linear elastic fracture mechanics, as r becomes zero the stress tends to infinity where a mathematical singularity exists only at the crack tip. Similarly, as r increases, the stress approaches zero. Therefore, it is more suitable to express the stress field at the crack tip in terms of stress intensity factor [16]. Stress intensity factor is an indication of likely crack

growth rate. For this one must be able to determine K_I from remote loads and geometry [2].

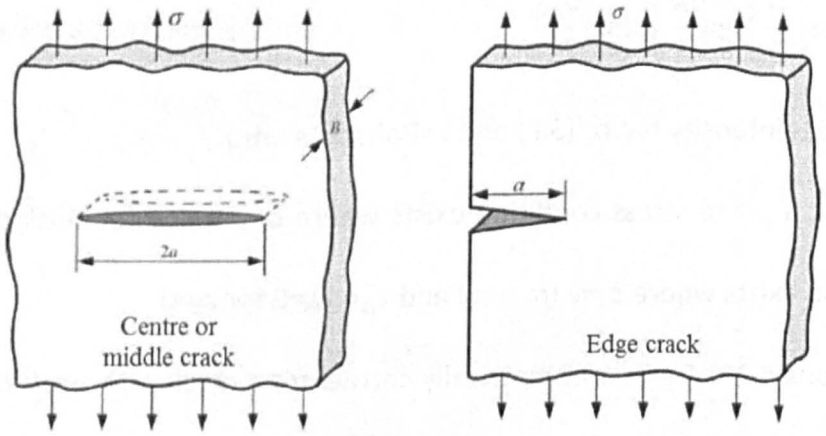

Figure 4.4: Crack in semi-infinite plate subjected to remote stress [2]

Figure 4.4 shows the Mode I crack displacement in a semi-infinite plate for centre crack and edge crack specimens. Anderson [2] suggested a closed-form solution for an infinite plate with a centre crack subjected to Mode I remote stress. The crack tip singularity for centre crack and edge crack configurations are proportional to the remote stress and square root of the crack length and the stress intensity factor is given by:

$K_I = \sigma\sqrt{\pi a}$ for centre crack Equation 4.6

$K_I = 1.12\sigma\sqrt{\pi a}$ for edge crack Equation 4.7

Where a is half crack length and σ is the applied stress. Stress intensity factor is a similitude parameter, i.e. two different cracked structures made of the same material but with different crack loads and crack lengths with the same stress intensity factor should behave the same way. For a given material in plane strain condition, failure occurs always at the same value of stress intensity factor [14-16].

So far, we have discussed stress intensity factor for an infinite plate. The stress distribution will be different in a finite cracked plate as illustrated in figure 4.5. In an infinite plate with a through crack, the lines of force at a distance W from the crack

centreline will have force components parallel (F_x) and perpendicular (F_y) to the crack growth direction.

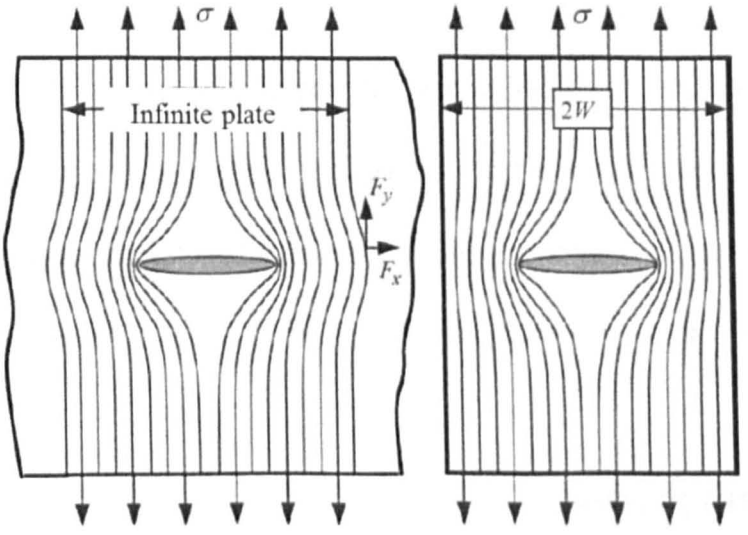

Figure 4.5: Stress concentration effect at a crack tip in infinite and finite cracked plates [2]

If the plate is of finite width, the force component parallel to the crack growth direction will become zero on the free edge which causes the lines of force to be compressed and results in a higher stress intensification at the crack tip [2]. In this scenario, a geometry factor (β) will be introduced to determine stress intensity factor in finite plate. The value of β is dependent on specimen geometry and presented in [2, 14, 15]. For a finite plate with through crack stress intensity factor with β is given by

$$K_I = \beta\sigma\sqrt{\pi a} \qquad \text{Equation 4.8}$$

$$\beta = \sqrt{\sec\frac{\pi a}{W}} \qquad \text{Equation 4.9}$$

A similar solution derived for a semi-infinite plate with a small edge crack present perpendicular to the remote stress and stress intensity factor is given by

$K_I = 1.12\sigma\sqrt{\pi a}$ as shown in figure 4.4 Equation 4.10

This is similar to equation 4.6. The factor β =1.12 represents a 12% increase in K_I for an edge crack specimen which is due to the different boundary conditions present at the crack tip. For the same remote stress, an edge crack opens more because it is less

restrained whereas a centre crack will form an elliptical shape when loaded [2, 13-15]. K_I is a similitude parameter and is the basis for the failure criteria. Two different cracked structures made of the same material but with different crack lengths, with different loads and with the same K_I, should behave the same way. Various solutions of β factor for different specimen geometries are presented in [2, 13-15]. At this point, it is important to mention that this research involves testing of only centre crack or middle crack (M(T)) and edge crack or single edge notch tension (SEN(T)) specimens with Mode I loading condition.

4.2.3 Crack tip plasticity

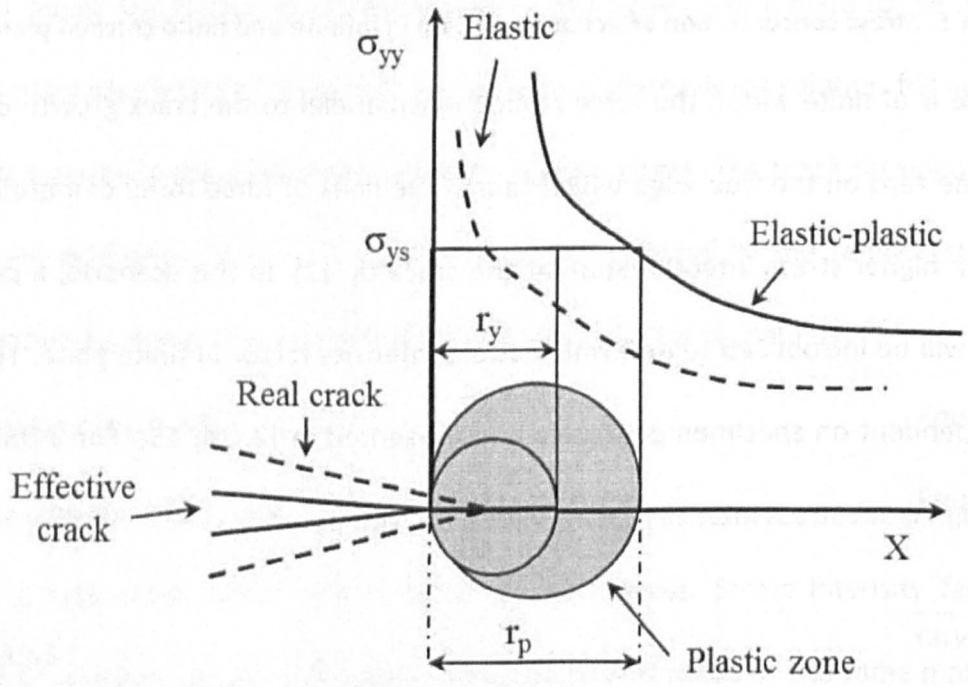

Figure 4.6: First (elastic) and second-order (elastic-plastic) estimates of plastic zone size [14]

As discussed earlier, linear elastic fracture mechanics is based on the assumption that a sharp crack predicts an infinite stress at the crack tip. In the presence of load, structural materials deform plastically above the yield stress and in reality there will be a small plastic zone surrounding the crack tip. The size of the crack tip plastic zone can be estimated by two methods: by the Irwin approach and by the strip-yield model. The Irwin approach is the most popular and is discussed as follows [14].

Irwin [6] made the first attempt to predict the size of the plastic zone in front of a crack and proposed a circular plastic zone size around the crack tip as shown in figure 4.6. According to Irwin, the presence of a plastic zone at a crack tip makes the crack behave as if it is longer than the actual crack and can be viewed as a real crack having a notional tip distance r_y ahead of the effective crack tip. A first order estimation of plastic zone size can be expressed as [12, 14, 15]:

$$r_y = \frac{1}{2\pi}\left(\frac{K}{\sigma_{ys}}\right)^2 \qquad \text{Equation 4.11}$$

where σ_{ys} is the yield stress of the material.

Beyond the plastic zone, the K corresponding to the real crack size describes the elastic stress distribution. This elastic stress distribution takes over from the yield stress at a distance of r_y from the effective crack tip. For materials with the same yield stress and K values, the plastic zone size will be same. Irwin proposed a second order, or elastic-plastic, plastic zone size by using simple force balance theory, given by [12, 14, 15]:

$$r_p = \frac{1}{\pi}\left(\frac{K}{\sigma_{ys}}\right)^2 \qquad \text{Equation 4.12}$$

The extent of the plastic zone estimated by equations 4.11 and equation 4.12 will typically be considerably smaller than the geometrical features of the component. Most structural problems of interest to the aerospace community can be characterized by linear elastic fracture mechanics parameters because the extent of yielding is contained within a small region around the crack tip [17, 18,]. Crack tip plasticity is important in linear elastic fracture mechanics to determine the stress state (plane strain or plane stress) relative to the specimen dimensions and the crack size. The increased stress state at the crack tip results in Poisson's contraction at the crack tip. The material thickness and amount of yielding at the crack tip affects the amount of Poisson's contraction. In linear

elastic fracture mechanics material yielding can be categorized into two: free yielding (plane stress) and constrained yielding (plane strain).

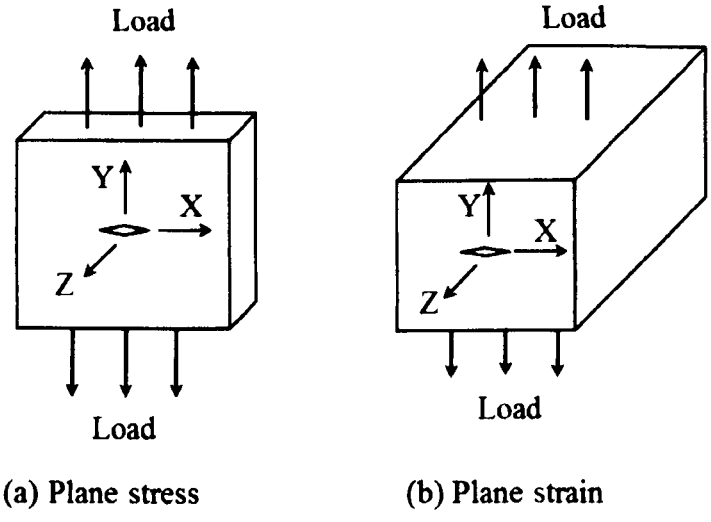

Figure 4.7: Plane stress and plane strain states in a cracked body

The stress state in the structure defines the fracture plane. When a thin plate with a crack is loaded parallel to its plane, it develops plastic strain near the crack tip and plane stress conditions exist. In this, material within the crack tip stress field and close to the free surface (z-direction, figure 4.7) can deform laterally. A biaxial stress state develops and the material will fracture in a ductile characteristic with a 45° shear lip at each free surface. Plane stress occurs in relatively thin bodies where the stress through the thickness cannot vary appreciably [19]. In plane stress conditions stress components σ_z, τ_{zx} and τ_{zy} are zero and σ_x, σ_y and τ_{xy} are the only non-zero components.

Plane strain exists in thick plates. In a thick plate, material within the crack tip and away from the free surfaces deforms laterally as it is constrained by the surrounding material. In this condition a triaxial stress state exists and no strain is present perpendicular to the stress axis on the direction of crack propagation. Under plane-strain conditions, materials behave essentially elastically until the fracture stress is reached and then rapid fracture occurs. In plane strain condition there are three non-zero strain components ε_x, ε_y and γ_{xy} and three zero components ε_z, γ_{xz} and γ_{yz}.

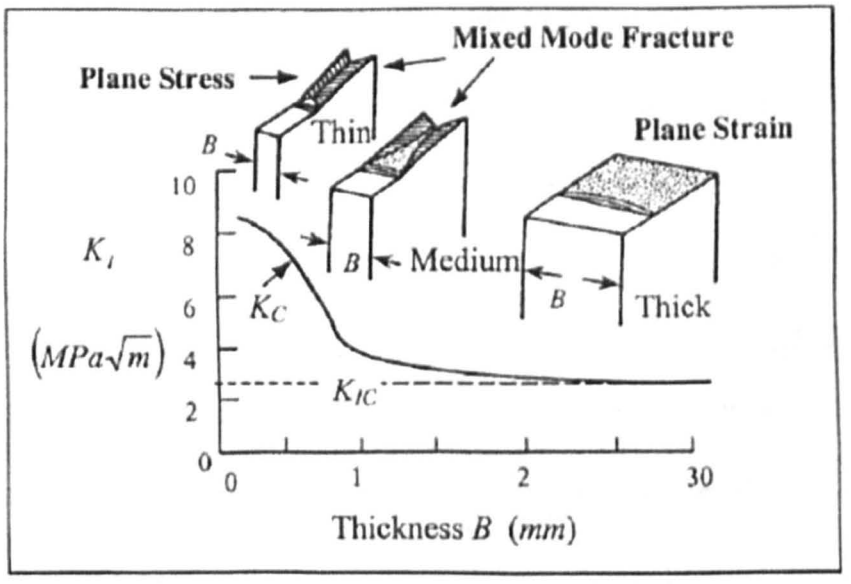

Figure 4.8: Relation between fracture toughness and material thickness [20]

For a given material in plane strain, failure occurs always at the same value of stress intensity factor. This value is called plane-strain fracture toughness and is denoted by K_{IC}. Fracture toughness measures the resistance of a material to crack propagation and depends on the thickness of the plate. Figure 4.8 shows the relation between the fracture toughness and the thickness of material. In the case of plane stress condition the critical stress intensity factor can be derived by an empirical fitting law of the graph shown in figure 4.8. In general, neither plane stress nor plane strain states can be fully achieved but the stress condition is always three dimensional [20].

4.2.4 Strain energy release rate or the energy approach

The energy approach developed by Griffith [4] is based on the first law of thermodynamics. He noted that, when a crack is introduced in a material there is a balance between the decrease in potential energy and increase in surface energy resulting from the presence of the crack. If the energy decreases or remains constant, a crack can form or an existing crack can grow. Later Irwin [5, 6] formulated Griffith's model in a form that is more convenient for solving linear elastic fracture mechanics problems, and defines energy release rate (G) which is a measure of energy required to initiate crack

propagation. For an infinite plate with a centre crack length of 2a the energy release rate is given by:

$$G = \frac{\pi\sigma^2 a}{E} = \frac{K_I^2}{E}$$ Equation 4.13

4.3 Fatigue

The fatigue phenomenon is often referred to as a process of progressive, localized, and permanent structural damage that occurs in a material undergoing fluctuating loading under stresses or strains that have nominal value less than the yield strength of the material. In general, fatigue damage is caused by the three simultaneous actions of cyclic stress, tensile stress, and localised plastic strain. Absence of any one of these would not initiate the fatigue mechanism. Cyclic stress results in plastic strain and hence initiates a fatigue crack, and tensile stresses will promote further crack propagation. Compressive loads may result in localized tensile stresses but they will not damage the material by fatigue [20]. The fatigue failure occurs in different stages as follows [20, 21]:

- Substructural and microstructural changes (creation of nucleation sites for fatigue crack initiation).
- Initiation of one or more micro cracks forming nucleation sites.
- The propagation and coalescence of micro cracks to form dominant cracks.
- Propagation of dominant cracks.
- Structural instability or final failure.

The fatigue life until failure mainly consists of two stages, crack initiation, and crack growth. Fatigue crack initiation and crack growth are a consequence of cyclic slip. As a crack initiates, it will act as a stress concentration and leads to aggressive crack growth and then final failure. Crack growth resistance will depend upon the bulk properties of the material. Once the crack has initiated, it is no longer a surface phenomenon. The gap

between the crack initiation and crack growth stages plays a significant role in the fatigue life of the structure because several surface conditions affect the crack initiation period but not the crack growth [22]. Hence, it is very important to understand the effect of various parameters on fatigue crack growth and fatigue life of the structure. The flow chart in figure 4.9 shows the fatigue mechanisms and various parameters controlling them.

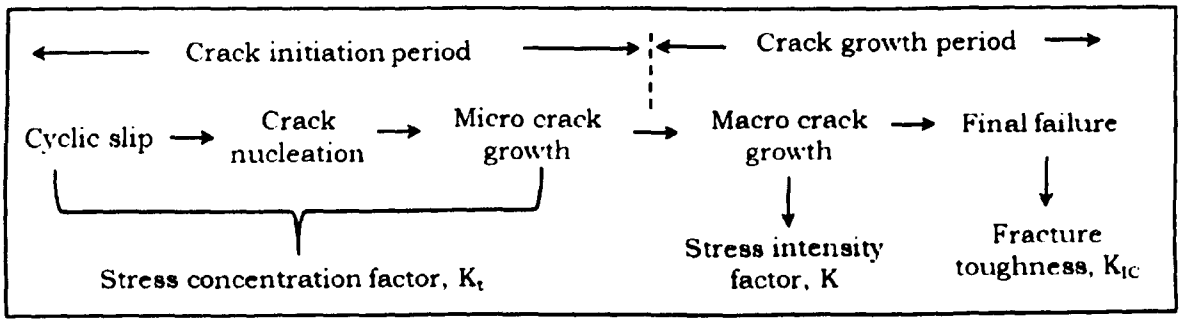

Figure 4.9: Different phases of fatigue failure and relevant factors [22]

The major part of the fatigue life of a structure is often covered by a crack initiation period. The stress concentration factor is the driving force to initiate cracks. At low amplitudes, the nucleation stage can occupy the majority of the lifetime. At high amplitudes, nucleation is usually accomplished within a small fraction of the fatigue life. Under the action of cyclic loads, cracks can initiate because of cyclic plastic deformation.

The stress concentration factor mainly depends on the type of structure, manufacturing process and the working environment of the structure. A high stress at the material surface can be observed if the structure contains high, sharp notches which will affect the crack initiation period. Microscopic investigations on specimens of aluminium alloys at relatively high stress levels have shown a fairly large number of microcracks in different surface grains [23, 24]. However, if the applied stress/load is well below the yield stress of the material the stress concentration results in crack initiation.

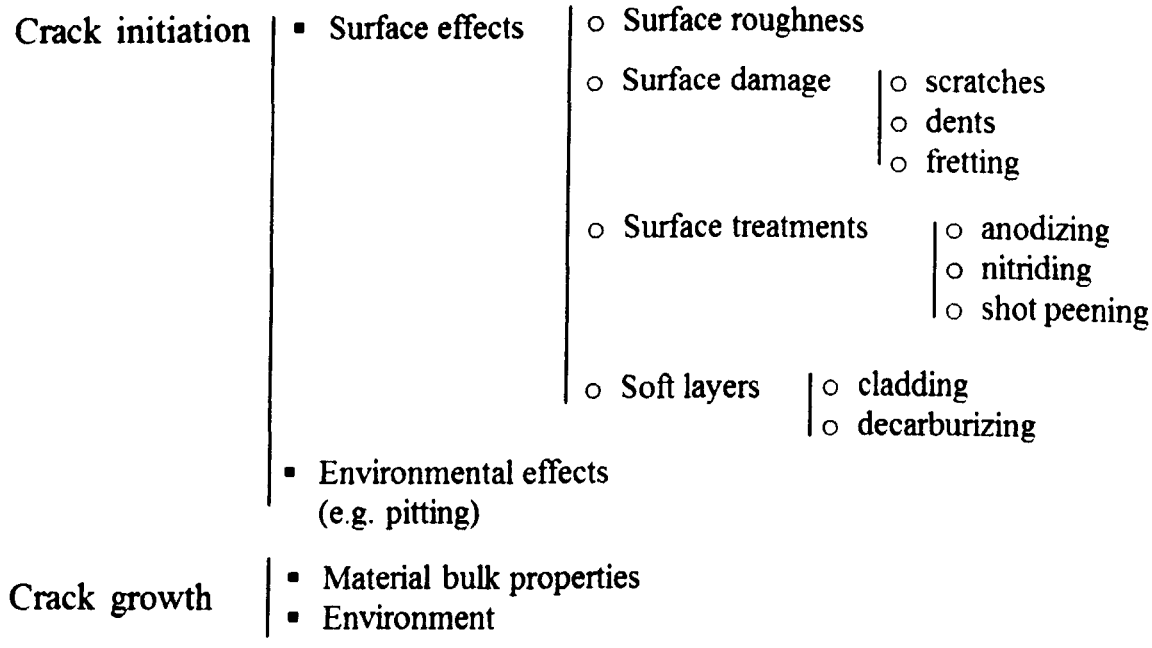

Figure 4.10: Various effects on the fatigue crack initiation and growth period [22]

Figure 4.10 shows various well-known effects on the crack initiation and crack growth period. The purpose of this discussion here is to reveal general aspects related to the fatigue process in terms of the crack initiation and crack growth periods. When the crack reaches a critical crack length, crack growth mechanisms become dominant and the material surface conditions are no longer contributors. The crack growth is then a material bulk properties phenomenon.

Usually in symmetric specimens with uniaxial loading conditions, the crack growth direction is macroscopically perpendicular to the loading direction. After the crack has grown away from the free surface, material located on the plane of highest shear stress results in slip plastic deformations which will occur on more than one slip plane. These planes are normally at an angle to the crack plane due to the bi-and tri-axial stress states that exist in plane-stress and plane-strain conditions respectively. During loading the crack will open due to the slip deformation and cause crack extension. The slip deformations are not fully reversible due to strain hardening. Slip plastic deformation will result in a ridge of microplastic deformation which collectively are known as striations [2].

The environment plays a vital role on the crack initiation and crack growth. An aggressive environment can result in corrosion of the structure which can be harmful for the fatigue life of the structure. This type of fatigue is known as corrosion fatigue. Corrosion fatigue can be cycle dependent, time dependent or a combination of both. Cycle dependent corrosion fatigue corresponds to a simple acceleration of the fatigue crack growth that is insensitive to the loading frequency. Time dependent corrosion fatigue can be modelled by a simple superposition of the inert fatigue crack growth rate with the environmental cracking rate. However, in most materials environment combinations exhibit both cycle-dependent and time-dependent behaviour [22]. In this dissertation fatigue tests are performed by using only constant amplitude (CA) fatigue, therefore the discussions in the following sections concentrate on constant amplitude fatigue testing.

4.3.1 Characterisation of fatigue crack growth

Damage tolerance analysis assumes the pre-existence of an initial crack or defect in the component. Crack-tip conditions are uniquely defined by a single loading parameter such as the stress intensity factor. The stress intensity factor concept can be used to correlate the externally applied cyclic load on the component with the fatigue crack growth. In the case of a stationary crack, two components will fail at the same critical stress intensity factor value, provided an elastic singularity zone exists at the crack tip. Under certain conditions, fatigue crack growth can be characterized by the stress-intensity factor approach. Over the past few decades numerous fatigue crack growth laws have been derived based on the stress intensity factor approach.

It is practically impossible to discuss every available fatigue crack growth model because of the large number in the literature. Therefore, the remainder of this section discusses the models which are most promising and/or commonly used. Different fatigue crack growth models reconfirm the fact that there is no standard methodology to

perform fatigue crack growth life predictions for structures. The main goal of the crack propagation models is to relate the material damage to the cyclic loads applied. However, due to the number and complexity of the mechanisms involved in this problem, there are almost as many equations as there are researchers in the field. Though many models have been developed, each model can only account for one or a small number of phenomenological factors [25].

In 1920 Griffith [26] investigated the theoretical and experimental strength of materials and discovered that microscopic cracks or defects exist in materials. These cracks or defects will be present in most materials regardless of the manufacturing process. These microscopic cracks results in lower strength of the material because under applied load, high stress concentrations occur at these cracks, which magnifies the stress at the crack tip. Under a loading condition, these cracks will grow more quickly causing the material to fail long before it reaches its theoretical strength. Figure 4.11 shows the typical relationship between crack growth rate *(da/dN)* and stress intensity factor range, ΔK defined as

$$\Delta K = K_{max} - K_{min} \qquad \text{Equation 4.14}$$

K_{max} and K_{min} are the maximum and minimum stress intensity factors corresponding to the externally applied maximum and minimum load or stress.

The sigmoidal plot shown in figure 4.11 is divided into three regions. In **Region I** crack propagation will be extremely slow with very low ΔK values reaching the threshold point ΔK_{th} or threshold region. The threshold region indicates that ΔK values below this value are too low to cause crack growth. Experimental validation of the threshold point is difficult but generally taken as crack growth rates $<10^{-8}$m/cycle. Knowledge of ΔK_{th} permits the calculation of permissible crack lengths and/or applied stresses in order to avoid fatigue crack growth [2, 14].

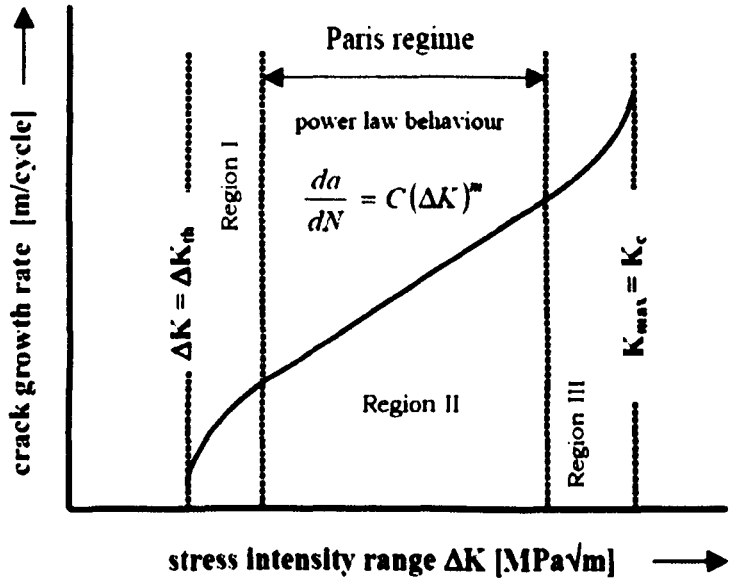

Figure 4.11: Different regions of fatigue crack propagation [2]

Region II is where crack growth rates are in between 10^{-8} to 10^{-6} m/cycle. This mid region is a stable crack growth region indicated as a straight line on a logarithmic scale and most structural components operate in this region, where macro crack growth can be observed. **Region III** is characterised by rapid and unstable crack growth. Crack growth rates accelerate (>10^{-6}m/cycle) as the stress intensity factors approaches the fracture toughness of the material. The transition from Region II and Region III behaviour is dependent on the stress intensity factor, stress ratio (R) and the yield strength of the material. In many engineering applications this region will be ignored as it will not affect the total crack propagation life [2, 14].

A number of researchers [11, 26-33] have developed equations that model all or part of the sigmoidal da/dN and ΔK relationship. The applicability of each model varies from case to case, there is no general agreement among the researchers to select any fatigue crack growth model in relation to the concept of fatigue crack behaviour. Hence, three different models, namely, the Paris-Erdogan, Forman and modified Forman and NASGRO models, which are most popular, are discussed in this section. Each model has its own capabilities and limitations. These models only consider the region III and take into

account the main properties, such as crack closure, plane stress and plain strain, threshold, and mean stress.

During 1960, Paris [11, 26] postulated that the stress intensity factor range might characterise sub-critical crack growth under fatigue loading. Paris and Erdogan were the first to discover the power law or Paris law (equation 4.15) relationship for fatigue crack growth in region II. The Paris law is accepted for a wide range of materials which show sigmoidal crack propagation behaviour. According to Paris and Erdogan, crack growth rate can be related to stress intensity factor range by:

$$\frac{da}{dN} = C\Delta K^m \qquad \text{Equation 4.15}$$

where **C** and **m** are material constants that depend on microstructure, fatigue loading sequence, mean stress, temperature and environment. The Paris law is capable of describing only the region II in the sigmoidal plot. The Paris-Erdogan equation does not consider the effect of the stress ratio, the existence of a fatigue threshold, and the accelerated fatigue crack growth rate when the K_{max} approaches the material fracture toughness. Moreover, it does not adequately describe if the data exhibits a threshold (region I) or an accelerated growth (region III) and it tends to overestimate region I, but underestimates region III fatigue crack growth rates. However, the Paris-Erdogan equation is still very popular and used in engineering applications.

In 1967 Forman [27] proposed a modified version of the Paris law which defines the relationship for region II and region III. Equation 4.16 details Forman's law.

$$\frac{da}{dN} = \frac{C\Delta K^m}{(1-R)K_c - \Delta K} \qquad \text{Equation 4.16}$$

Where R is the stress ratio = $\sigma_{min}/\sigma_{max}$

Later a modified version of Forman's equation was developed taking into consideration the ΔK_{th}. ΔK_{th} greatly depends on the stress ratio and material. The

modified Forman's law (equation 4.17) provided a better relationship for region II, III and as well as for slower crack growth in region I. It is also capable of representing data of various stress ratios for regions II and III. But, this law is based on the assumption that the region III behavior is caused by a superposition of fracture and fatigue rather than plastic zone effects. In region III, at high stress intensities, the plastic zone size will become large compared to the dimension of the crack and the plasticity starts influencing the crack growth rate.

$$\frac{da}{dN} = \frac{C(\Delta K - \Delta K_{th})}{(1-R)K_c - \Delta K} \qquad \text{Equation 4.17}$$

Where ΔK_{th} is the crack growth threshold mean stress intensity factor.

The Forman equation is capable of representing the data for different stress ratios. It has given good results for crack growth in aluminium alloys and steels but not in many other materials. The material constants *C* and *m* will play a vital role in the crack growth rate prediction.

Another recent development in empirical crack growth laws to development of the so-called NASGRO equation by taking into account the retardation due to underloads. It represents the most comprehensive growth law formulation comprising the mean stress effect, threshold, fast fracture and crack closure. The NASGRO equation can be expressed as

$$\frac{da}{dN} = C\left[\left(\frac{1-f}{1-R}\right)\Delta K\right]^n \frac{\left(1-\frac{\Delta K_{th}}{\Delta K}\right)^p}{\left(\frac{1-K_{max}}{K_{crit}}\right)^q} \qquad \text{Equation 4.18}$$

Where *C* and *n* are the empirical parameters describing the linear region (region II) of the sigmoidal curve. *p* and *q* are the empirical parameters describing the curvature near threshold region (region I) and at instability region (region III) in the sigmoidal curve respectively. *f* is the crack opening function.

4.3.2 Parameters influencing the fatigue crack growth

Understanding the concept of fatigue crack growth behaviour, from an initial flaw to final failure, and various parameters affecting it, is essential to design materials and structures with respect to damage tolerance. Crack growth in a material is a function of stress intensity factor. This stress intensity factor is shown to explicitly depend upon time and various material constants. However, crack growth rate is affected by several other parameters which are divided into intrinsic (materials mechanical properties) and extrinsic (loading conditions and environmental factors) parameters. Although these parameters are not going to be the focus of this dissertation it is important to have the knowledge and therefore they will be discussed further in this section.

4.3.2.1 Influence of material

Fatigue life is closely related to the surface treatment. In general, compressive stresses at the surface have a positive impact on fatigue life. Cold rolling and shot peening, especially for low stress high-cycle fatigue, are the most widely used surface treatments to generate beneficial compressive stresses at the surface. The type of microstructure, the grain size and material texture influence the mechanical properties of a material. In general, the smaller the grain size the higher the fatigue limit. But often threshold ΔK is larger for a material with large grain size. Grains oriented perpendicular to the crack growth direction will act as barriers and decrease the fatigue crack growth rate. Higher yield strength materials have higher threshold values for nonferrous alloys. Another factor which influences the fatigue life is thermal fatigue which occurs when mismatch of thermal expansion coefficients between two mating parts induces thermal strains when temperature changes. Thermal fatigue will also occur when the changes of temperature are severe and/or frequent [20-22].

4.3.2.2 Influence of environment

An aggressive environment can result in corrosion that is harmful for the fatigue life of the structure. Corrosion fatigue is undesirable and unacceptable in damage tolerant design. Usually corrosion prevention is considered as the selection of a corrosion resistant material and/or applying some corrosion protective layers. However, despite corrosion protection, fatigue cracks may arise in the aluminium due to moisture and exposing to aggressive environment. It occurs mainly as transgranular crack growth [22]. Stefanie studied the influence of air humidity on the near threshold fatigue crack growth in 2024-T3 aluminium alloy and concluded that the material tested in high humidity produced a higher threshold stress intensity range compared to laboratory air. This might be attributed to environmentally generated debris on the crack faces bridging the crack at low loading and crack-opening-displacement conditions [22, 34, 35].

4.3.2.3 Influence of stress ratio and residual stresses

A fatigue load cycle is generally defined by any two of the four stress parameters, which are minimum stress (σ_{min}), maximum stress (σ_{max}), mean stress (σ_m) and amplitude (σ_a). It is generally accepted that the fatigue crack growth propagation not only depends on the material and stress intensity factor range but also on the stress ratio (R-ratio). Amongst the parameters which influence the crack growth, stress ratio and residual stresses are the most important. Figure 4.12 shows the effect of stress ratio on crack growth. Under the same stress intensity factor range, increasing the R-ratio has a tendency to increase the crack growth rates. From Figure 4.12 it can be observed that the effect of increase in R-ratio is less significant in the Paris regime than the threshold and final failure regimes. When a larger mean stress is present it tends to open microcracks or macrocracks resulting in shorter fatigue life and a lower fatigue limit [36, 37].

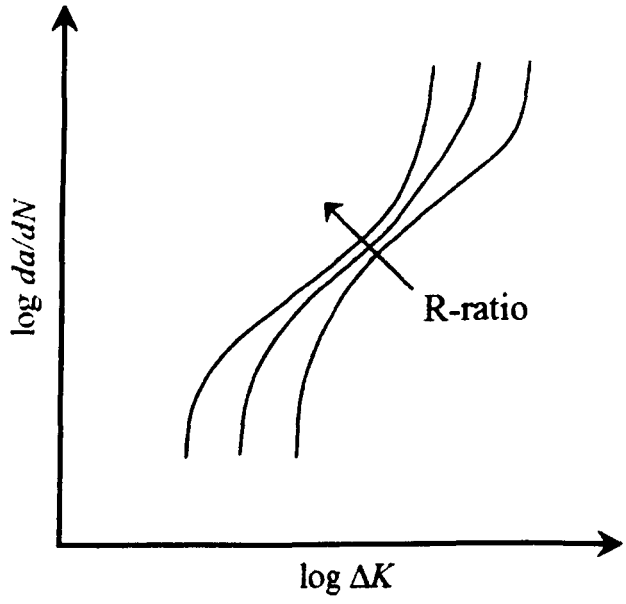

Figure 4.12: Effect of R-ratio on fatigue crack growth

Fatigue life prediction of structural components is a critical action in the aerospace industry. Better understanding of the fracture mechanics allows designing complex structures that operate with statistical reliability. However, large uncertainty can be observed in the performance of structures when residual stresses are present. As discussed in chapter 3, residual stresses are always present in a material as they derive from the manufacturing process itself. Thus, they are present in the material in different magnitudes which will affected by the environment, material, and load history. The presence of residual stresses changes the effective mean stress experienced by a structure during fatigue cycling and hence affects both crack initiation and crack growth. The presence of tensile residual stresses will add to applied stress levels and lead to fracture at lower loads than might be expected; whereas compressive stresses at the surface are beneficial, as they are a source of crack closure and effectively increase the crack initiation period [36, 37].

4.3.3 Crack closure

Crack closure is a phenomenon where a crack will remain closed even when an external load is present. Elber [38] discovered the crack closure phenomenon and reported that fatigue cracks are closed for a significant portion of a tensile load cycle, probably owing to

residual plastic deformation left in the wake of a growing crack. The crack faces are subjected to considerable compressive stresses. Elber called this phenomenon plasticity-induced crack closure.

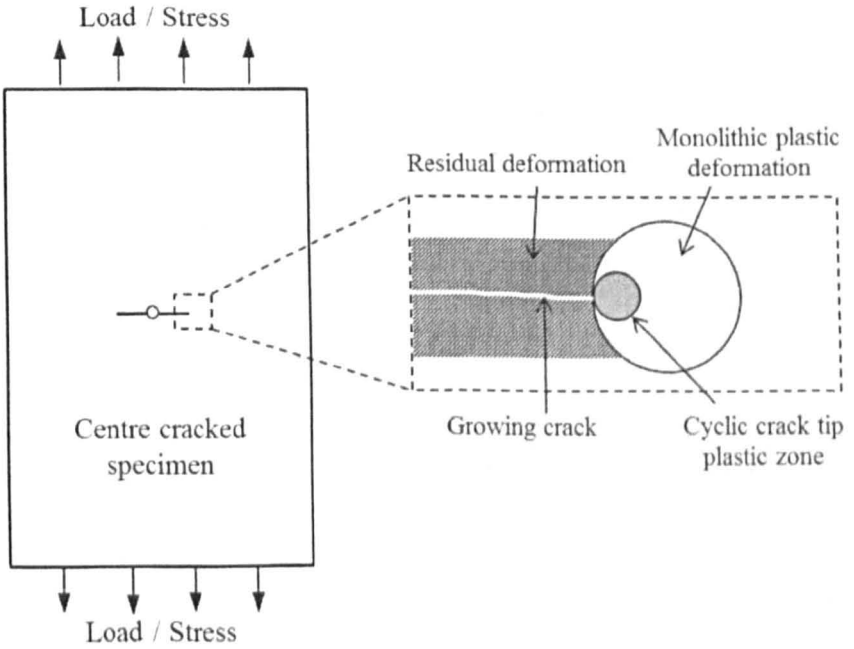

Figure 4.13: Plastic zones of a growing crack in a centre cracked specimen

During cyclic loading, plastic deformation occurs at the crack tip and the deformation zone will be elongated in the loading direction. During unloading, a much smaller reverse plastic deformation will occur at the crack tip. This reverse plastic deformation is known as monotonic plastic deformation and approximately one-quarter of the size of the plastic zone created during loading. It occurs in every loading cycle and the crack is thus growing through plastic zones of previous cycles. Figure 4.13 shows zones of plastic deformation in the vicinity of a growing crack [2, 14, 22, 38-41].

Elber postulated that crack closure decreases the fatigue crack growth by reducing the stress intensity factors at the crack tip. Figure 4.14 illustrates the closure concept. When a specimen is cyclically loaded between K_{max} and K_{min}, the crack faces are in contact below K_{op}, the stress intensity at which the crack opens. Elber assumed that the portion of the cycle that is below K_{op} does not contribute to fatigue crack growth because there is no change in crack-tip strain during cyclic loading of a closed crack. He observed the

occurrence of crack closure by crack opening displacement (COD). He also observed that specimen with a saw cut instead of a fatigue crack does not have a plastic wake field [2, 22]

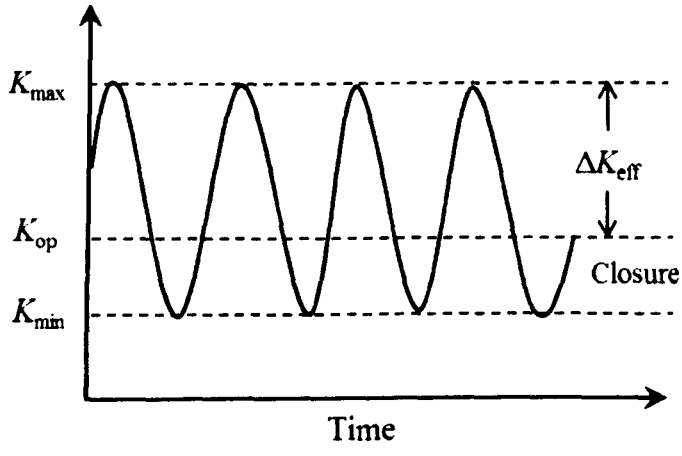

Figure 4.14: Plastic zones of growing crack in a centre cracked specimen

K_{max}, K_{min}, K_{op}, are the maximum, minimum, and crack opening stress intensity factors corresponding to σ_{max}, σ_{min}, σ_{op} maximum, minimum, and crack opening applied stress respectively.

From figure 4.14 it can be observed that when a specimen is subjected to cyclic loading, crack closure occurs if $\sigma_{min}<\sigma_{op}$. The crack is partly or fully closed at σ_{min}. During loading, the crack tip is fully open when $\sigma = \sigma_{max}$. Upon unloading, the crack is open until crack closure starts at the crack tip. It should be noted that the stress singularity, which is defined by the stress intensity factor, is present as long as the crack is open. As soon as the crack is closed the stress singularity will be nullified. In addition to this, experiments performed on aluminium alloy 2024-T3 show that σ_{op} was approximately constant during the fatigue test and implies that σ_{op} was independent of the crack length and dependent on the applied cyclic stress. Furthermore, the crack closure occurs more at material surface where plane stress conditions are relevant and less at mid thickness of the material where plane strain conditions prevail [22, 42].

4.3.4 Fatigue in fibre metal laminates

To improve the fatigue performance of monolithic aluminium alloys the fibre-metal laminate (ARALL and GLARE) concept was developed by research on fatigue of laminated sheet material without fibres. Schijve studied the fatigue properties of adhesively bonded sheet material of aluminium alloys and concluded that the laminated metal sheets showed significant increase in fatigue life compared to monolithic aluminium alloy sheet. The longer fatigue life in laminated sheet is attributed to the independent crack growth in all layers [43]. Laminated material will restrain the crack growth by lowering the stress intensity factors at the crack tip. But, this phenomenon is not effective if crack growth occurs simultaneously in all the layers in a laminate. To overcome this issue and to further improve the fatigue performance of the metal laminates fibres are introduced in the bonding adhesive layer and the fibre metal laminate concept was developed [44, 45].

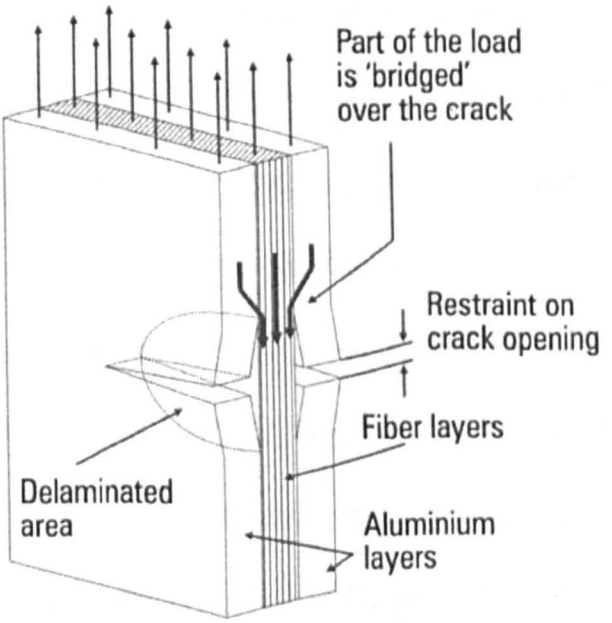

Figure 4.15: Crack bridging in fibre metal laminates [46]

The concept of the fibre metal laminate is to bridge a growing crack by unbroken fibres in the adhesive. Fibres between the metal sheets are insensitive to the fatigue loading. They transfer the fatigue loads and restrain the crack opening. As a result, there will be significant reduction in stress intensity factor at the crack tip. This phenomenon is called fibre bridging and is illustrated in figure 4.15 [46-48]. For structural fibre-metal laminates

the crack growth behaviour and the delamination between the fibres and adhesive are the two important criteria. During loading, shear stresses will be induced between the interface of the fibre layers and metal sheets due to crack bridging. Shear stresses cause delamination along the crack edges. These shear stresses can be reduced by increasing the number of fibre/metal interfaces [49].

Another important aspect in the development of structural fibre metal laminates for cyclic loading is to minimise or eliminate the fibre failure during delamination of the fibre/metal interface. This can be achieved by increasing the number of fibres in the adhesive layers or by increasing the tensile strength of the fibres. However, experiments have shown that the delamination is limited and acceptable for a well-balanced fibre volume ratio and sufficient interfaces [47, 48]. In chapter 2 we discussed different fibre metal laminates and their applications and advantages. It was concluded that glass laminated aluminium reinforced (GLARE) fibre metal laminates possess better mechanical properties than aramid and carbon fibre reinforced laminates. Furthermore, all the fatigue tests performed in this dissertation use GLARE as a bonded crack retarder. Therefore, only fatigue behaviour of GLARE is presented here.

Extensive research [43-66] has been performed by both experiment and computation to study the fatigue performance of fibre metal laminates. It has been found that the linear elastic fracture mechanics can be used to study the crack growth behaviour in GLARE [52, 65]. The difference between the crack growth behaviour of GLARE and monolithic aluminium is due to the presence of glass fibres in the GLARE. However, the influence of glass fibres in crack initiation and propagation is different. During fatigue crack initiation, fibres will not contribute to bridge the crack but the fibre layers and residual stresses resulting from laminate bonding determine the actual stress in the aluminium layers. Due to this, the actual stresses in the GLARE are higher than the

applied stresses and result in slower crack initiation compared to monolithic aluminium. As mentioned earlier, as there will be no fibre bridging contribution during the crack nucleation it is suggested that the minimum crack length at which the fibres become effective for crack bridging is 2 mm. At a same stress state fatigue initiation mechanism or fatigue life of aluminium layers in GLARE can be compared to the monolithic aluminium [61, 66].

Fatigue crack geometries in GLARE can be classified into three groups: through crack, surface cracks and part-through cracks. The type of crack generated in the GLARE is dependent on the type of laminate and load experienced. The crack is fully constrained by bridging effects. If a specimen with a through crack is subjected to pure tension load, the outer aluminium layers of the GLARE will experience slightly faster crack growths compared to the inner layers. This is due to the fact that the inner layers have a higher bridging effect than the outer layers. Surface cracks will grow only on the outer layers of the GLARE provided a crack initiation site. Part through cracks can be observed only in the first few layers of the GLARE when different layers experience different loads. This type of crack can be observed during combined tension and bending loading [47].

Fatigue crack resistance in GLARE can be enhanced by reducing the stress intensity factors at the crack tip by optimising the laminate. The stress intensity factors can be reduced by:

- Increasing the fibre volume fraction in the adhesive or by increasing the tensile strength of the fibres. Either of these optimisations will increase fibre bridging.
- Reducing the thickness of aluminium layers and increasing the number of layers.
- Increasing the adhesive shear stiffness this restrains the crack opening.

4.4 Summary

In this chapter, theoretical principles related to fatigue and fracture mechanics have been summarised. Linear elastic fracture mechanics are discussed in detail. Fatigue testing performed in this research is limited to Mode I loading. Stress intensity factor is an important criterion in this investigation. Plane stress and plane strain conditions and crack tip plasticity were also discussed. Later, fatigue crack growth mechanisms, parameters influencing the fatigue crack growth and effect of stress ratio and residual stresses on fatigue crack growth were presented. Finally, fatigue in fibre metal laminates was presented. The detailed theoretical framework on fracture mechanics is necessary to understand the experimental results. Experimental results on fatigue crack growth are presented in chapter 7.

4.5 References

[1]. F. Liu, *Mechanics, and Mechanisms of Fracture: An Introduction* (Google eBook). ASM International, 2005.

[2]. T. L. Anderson, *Fracture Mechanics: Fundamentals and Applications*, Third Edition. CRC Press, 2005.

[3]. E. E. Gdoutos, *Fracture Mechanics: An Introduction* (Google eBook). Springer, 2006.

[4]. A. Griffith, *The Phenomena of Rupture and Flow in Solids*, Philosophical Transactions of the Royal Society A: Mathematical, Physical and Engineering Sciences, vol. 221, no. 582-593, pp. 163–198, 1921.

[5]. G. R. Irwin, *Onset of fast crack propagation in high strength steel and aluminum alloys,* Sagamore Research Conference Proceedings 2, pp. 289-305, 1956.

[6]. G. R. Irwin, *Analysis of stresses and strains near the end of cracking traversing a plate,* Journal of Applied Mechanics, vol. 24, pp. 361-364, 1957.

[7]. H. M. Westergaard, *Bearing Pressures and Cracks*, Journal of Applied Mechanics, vol. 6, 1939.

[8]. M. L. Williams, *On a stress distribution at the base of a stationary crack,* Journal of Applied Mechanics, pp. 109 -114, 1957.

[9]. A. A. Wells, *The Condition of Fast Fracture in Aluminum Alloys with Particular Reference to Comet Failures*, British Welding Research Association Report, NRB 129, 1955

[10]. D. H. Winne and B. M. Wundt, *Application of the Griffith-Irwin theory of crack propagation to the bursting behavior of disks including analytical and experimental studies,* in Transactions of the American Society of Mechanical Engineers 80, pp. 1643–1655, 1958.

[11]. P. Paris, *A rational analytic theory of fatigue*, The Trend in Engineering, vol. 13, pp. 9-14, 1961.

[12]. C. H. Wang, *Introduction to fracture mechanics*, Report number DSTO-GD-0103, 1996.

[13]. Y. Murakami, *Metal Fatigue: Effects of Small Defects and Non-metallic Inclusions*, Elsevier, 2002.

[14]. M. Janssen, J. Zuidema, and R. J. H. Wanhill, *Fracture Mechanics*. Spon Press, 2004.

[15]. D. Gross and T. Seelig, *Fracture Mechanics: With an Introduction to Micromechanics* (Google eBook). Springer, 2011.

[16]. N. E. Dowling, *Mechanical behavior of materials: engineering methods for deformation, fracture, and fatigue*, Prentice Hall, 1993.

[17]. http://www.afgrow.net/applications/DTDHandbook/default.aspx, Accessed on 11th March, 2014.

[18]. R. W. Hertzberg, *Deformation and fracture mechanics of engineering materials*. John Wiley & Sons, 1996.

[19]. D. Broek, *Elementary engineering fracture mechanics*. Springer, 1986.

[20]. ASM handbook, Fatigue and Fracture, Volume 19. ASM International, 1996.

[21]. S. Suresh, *Fatigue of Materials*. Cambridge University Press, 1998.

[22]. J. Schijve, *Fatigue of Structures and Materials*, 2nd edition. Springer, 2009.

[23]. C. Y. Kung and M. E. Fine, *Fatigue Crack initiation and microcrack growth in 2024-T4 and 2124-T4 aluminum alloys*, Metallurgical Transactions A, vol. 10, no. 5, pp. 603–610, 1979.

[24]. D. Sigler, M. C. Montpetit, and W. L. Haworth, *Metallography of fatigue crack initiation in an overaged high-strength aluminum alloy*, Metallurgical Transactions A, vol. 14, no. 4, pp. 931-938, 1983.

[25]. T. Kvackaj, *Aluminium Alloys, Theory, and Applications*. InTech, 2011.

[26]. P. Paris and F. Erdogan, *A Critical Analysis of Crack Propagation Laws*, Journal of Basic Engineering, vol. 85, no. 4, p. 528-533, 1963.

[27]. R. G. Forman, V. E. Kearney, and R. M. Engle, *Numerical Analysis of Crack Propagation in Cyclic-Loaded Structures*, Journal of Basic Engineering, vol. 89, no. 3, p. 459-463, 1967.

[28]. J. Weertman, *Rate of growth of fatigue cracks calculated from the theory of infinitesimal dislocations distributed on a plane*, International Journal of Fracture Mechanics, vol. 2, no. 2, pp. 460-467, 1966.

[29]. M. Klesnil and P. Lukas, *Influence of strength and stress history on growth and stabilisation of fatigue cracks*, Engineering Fracture Mechanics, vol. 4, no. 1, pp. 77-92, 1972.

[30]. R. J. Donahue, H. M. Clark, P. Atanmo, R. Kumble, and A. J. McEvily, *Crack opening displacement and the rate of fatigue crack growth*, International Journal of Fracture Mechanics, vol. 8, no. 2, pp. 209-219, 1972.

[31]. A. J. McEvily, *On Closure in Fatigue Crack Growth*, ASTM STP 982, American Society for Testing and Materials, pp. 35-43, 1988.

[32]. K. Walker, *The effect of stress ratio during crack propagation and fatigue for 2024-t3 and 7075-t6 aluminum* in *Effects of environment and complex load history on fatigue life*, ASTM STP 462, pp. 1–14, 1970.

[33]. R. G. Forman, *Behavior of Surface and Corner Cracks Subjected to Tensile and Bending Loads in Ti-6Al-4V Alloy*. NASA technical memorandum 102165, 1990.

[34]. R. R. Cervay and J. V. Kumar, *Effects of humidity on the fatigue crack growth rate in aluminum alloy 8090-T8771 thick plate*, Report, UDR-TR-95-01, University of Dayton Research Institute, 1995.

[35]. S. E. Stanzl, H. R. Mayer, and E. K. Tschegg, *The influence of air humidity on near-threshold fatigue crack growth of 2024-T3 aluminum alloy*, Materials Science and Engineering: A, vol. 147, no. 1, pp. 45-54, 1991.

[36]. M. Dorman, M. B. Toparli, N. Smyth, A. Cini, M. E. Fitzpatrick, and P. E. Irving, *Effect of laser shock peening on residual stress and fatigue life of clad 2024 aluminium sheet containing scribe defects*, Materials Science and Engineering: A, vol. 548, pp. 142-151, 2012.

[37]. G. Ratti, U. Mariani, M. Giglio, and M. Guagliano, *Effect Of Residual Stresses From Shot Peening On Fatigue Strength And Threshold To Crack Propagation Of Al 7475 Alloy Components*," ICAF 2009, Bridging the Gap between Theory and Operational Practice, pp. 859-870, 2009.

[38]. E. Wolf, *Fatigue crack closure under cyclic tension*, Engineering Fracture Mechanics, vol. 2, no. 1, pp. 37-45, 1970.

[39]. D. L. Davidson, "Fatigue crack closure," Engineering Fracture Mechanics, vol. 38, no. 6, pp. 393–402, Jan. 1991.

[40]. R. M. J. Kemp, *Fatigue crack closure-A review*, Technical report TR-900046, Royal Aerospace establishment, 1990.

[41]. A. K. Vasudeven, K. Sadananda, and N. Louat, *A review of crack closure, fatigue crack threshold and related phenomena*, Materials Science and Engineering: A, vol. 188, no. 1-2, pp. 1-22, 1994.

[42]. H. L. Ewalds and R. T. Furnée, *Crack closure measurement along the fatigue crack front of center cracked specimens*, International Journal of Fracture, vol. 14, no. 2, pp. R53–R55, 1978.

[43]. J. Schijve, H. T. M. Van Lipzig, G. F. J. A. Van Gestel, and A. H. W. Hoeymakers, *Fatigue properties of adhesive-bonded laminated sheet material of aluminum alloys*, Engineering Fracture Mechanics, vol. 12, no. 4, pp. 561-579, 1979.

[44]. A. Vlot. and G. J. Willem, *Fibre Metal Laminates: An Introduction*. Kluwer academic publishers, 2001.

[45]. A.Vlot, *Glare, history of the development of new aircraft material*. Kulwer academic publishers, 2001.

[46]. A. Vlot, L. Vogelesang, and T. J. de Vries, *Towards application of fibre metal laminates in large aircraft*, Aircraft Engineering and Aerospace Technology, vol. 71, no. 6, pp. 558-570, 1999.

[47]. R. C. Alderliesten, *Fatigue Crack Propagation and Delamination Growth in Glare*, Ph.D. thesis, Delft University of Technology, 2005.

[48]. H. Plokker, *Crack closure in fibre metal laminates*, Fatigue and Fracture of Engineering Materials and Structures, vol. 30, no. 7, pp. 608–620, 2007.

[49]. R. Marissen, *Fatigue crack growth in ARALL-A hybrid aluminium-aramid composite material; Crack growth mechanisms and quantitative predictions of the crack growth rates*, Ph.D. thesis, Delft University of Technology, 1988.

[50]. A. Chlupová, J. Heger, and A. Vašek, *Fatigue Crack Initiation and Early Growth in GLARE 3 Fiber-metal Laminate Subjected to Mixed Tensile and Bending Loading*, Acta Polytechnica, vol. 41, no. 4, pp. 5-8, 2001.

[51]. A. Vašek, J. Polak, and V. Kozak, *Fatigue crack initiation in fibre-metal laminate GLARE 2*, Materials Science and Engineering: A, vol. 236, pp. 621-624, 1997.

[52]. J. Homan, *Fatigue initiation in fibre metal laminates*, International Journal of Fatigue, vol. 28, no. 4, pp. 366-374, 2006.

[53]. M. Papakyriacou, J. Schijve, and S. E. Stanzl-Tschegg, *Fatigue Crack Growth Behaviour of Fibre-Metal Laminate Glare-1 and Metal Laminate 7475 With Different Blunt Notches*, Fatigue and Fracture of Engineering Materials and Structures, vol. 20, no. 11, pp. 1573-1584, 1997.

[54]. S. U. Khan, R. C. Alderliesten, and R. Benedictus, *Post-stretching induced stress redistribution in Fibre Metal Laminates for increased fatigue crack growth resistance*, Composites Science and Technology, vol. 69, no. 3-4, pp. 396-405, 2009.

[55]. S. U. Khan, R. C. Alderliesten, and R. Benedictus, *Delamination in Fiber Metal Laminates (GLARE) during fatigue crack growth under variable amplitude loading*, International Journal of Fatigue, vol. 33, no. 9, pp. 1292-1303, 2011.

[56]. J. J. Remmers and R. de Borst, *Delamination buckling of fibre–metal laminates*, Composites Science and Technology, vol. 61, no. 15, pp. 2207-2213, 2001.

[57]. J. Schut and R. Alderliesten, *Delamination growth rate at low and elevated temperatures in Glare*, 25th International congress of the Aeronautical Sciences, Hamburg, Germany, pp. 1-7, 2006.

[58]. T. Takamatsu, T. Shimokawa, T. Matsumura, Y. Miyoshi, and Y. Tanabe, *Evaluation of fatigue crack growth behavior of GLARE3 fiber/metal laminates using a compliance method*, Engineering Fracture Mechanics, vol. 70, no. 18, pp. 2603-2616, 2003.

[59]. R. Alderliesten and J. Homan, *Fatigue and damage tolerance issues of Glare in aircraft structures*, International Journal of Fatigue, vol. 28, no. 10, pp. 1116-1123, 2006.

[60]. P. Chang, P. Yeh, and J. Yang, *Fatigue crack growth in fibre metal laminates with multiple open holes*, Fatigue and Fracture of Engineering Materials and Structures, vol. 35, no. 2, pp. 93-107, 2012.

[61]. M. Papakyriacou and S. Stanzl-Tschegg, *Fatigue crack growth in Glare, role of glass fibers*, ECF10, Berlin, 2013.

[62]. D. J. Shim, R. C. Alderliesten, S. M. Spearing, and D. A. Burianek, *Fatigue crack growth prediction in GLARE hybrid laminates*, Composites Science and Technology, vol. 63, no. 12, pp. 1759-1767, 2003.

[63]. T. Takamatsu and T. Matsumura, *Fatigue crack growth properties of a GLARE3-5/4 fiber/metal laminate*, Engineering Fracture Mechanics, vol. 63, no. 3, pp. 253-272, 1999.

[64]. R. Alderliesten and C. Rans, *The meaning of threshold fatigue in fibre metal laminates*, International Journal of Fatigue, vol. 31, no. 2, pp. 213-222, 2009.

[65]. T. Beumler, *Flying Glare*, Delft University of Technology, 2005.

[66]. R. Alderliesten, *Development of an empirical fatigue crack growth prediction method for the Fibre Metal Laminate Glare*, Master thesis, Delft University of Technology, 1999.

Chapter 5 : Experimental materials and procedures

In previous chapters, the necessary background on residual stress measurements and fracture mechanics and fatigue was introduced in detail. In this chapter the experimental materials and experimental methods used to investigate the durability of bonded crack retarders will be discussed. The primary objective of this research is to investigate the fatigue durability of bonded crack retarders and to investigate thermal residual stresses developed during GLARE bonding. The experimental outcomes of this investigation will be used to predict and design mock-up aircraft panels for further research. Hence, it is very important that all the sample preparation and experiments carried out should be according to the appropriate standards and be fully repeatable.

5.1 Experimental materials

Aluminium is the world's most abundant metal and the third most common element, comprising 8% of the Earth's crust. The versatility of aluminium makes it the most widely used metal after steel. The major advantages of using aluminium are to its remarkable properties such as high strength to weight ratio, corrosion resistance, electrical and thermal conductivity, and it is recyclable. Aluminium is one of the lightest engineering materials, having strength to weight ratio superior to steel. However, pure aluminium is soft and ductile and cannot be used in many engineering applications due to its low yield strength. Therefore, in order to achieve the desired mechanical and physical properties, aluminium is used in alloy form. Adding different alloying elements results in different mechanical properties of the alloy. For example:

- The addition of copper increases the strength and hardness and makes the alloy heat treatable.

- The addition of magnesium causes increased tensile strength, resistance to corrosion and makes it weldable.
- The other common alloying elements are manganese to increase strength and corrosion, silicon to lower the melting point and improve castability, and zinc will increase the strength and the hardness.

Aluminium is available mainly in two forms, alloys for casting, and alloys for the manufacturing of wrought products. Aluminium alloys specified as cast alloys contain one or more alloying elements. They are directly produced in their final form and are preferred for the manufacturing of complex shapes. Aluminium casting alloys are usually designated by two or three digit numbers. Wrought alloys generally cast into large ingots and the final mechanical and physical properties will be achieved by various heat treatment and working processes. Wrought alloys can be produced in both heat-treatable and non-heat-treatable form. Quenching and suitable aging processes can improve the mechanical properties of the heat treatable aluminium alloys. The mechanical properties of the non-heat-treatable aluminium alloys can be varied by strain hardening or strain hardening followed by partial annealing. Table 5.1 shows common alloying elements and different grades in aluminium alloys.

Wrought alloys			**Cast alloys(Non heat-treatable)**	
Major alloying element	**Series**	**Condition**	**Major alloying element**	**Series**
None (99.9% pure aluminium)	1XXX	Non-heat-treatable alloys	None (99.9% pure aluminium)	1XX0
Mn	3XXX		Cu	2XX0
Si	4XXX		Si	3XX0
Mg	5XXX		Si	4XX0
Cu	2XXX	Heat-treatable alloys	Mg	5XX0
Mg+Si	6XXX		Zn	7XX0
Zn	7XXX		Sn	8XX0
Other	8XXX		Other	9XX0

Table 5.1: Different series of aluminum alloys with major alloying elements [1]

All the aluminium substrate specimens used in this research were sectioned from wrought aluminium alloy 2624-T351 of 5 mm thickness. The term T351 in the alloy designation represents that the alloy is solution heat-treated, cold worked, and naturally aged to a substantially stable condition. The mechanical properties of Al 2624-T351 are shown in table 5.2. High damage tolerance, fatigue durability, and good resistance to stress corrosion cracking are some of its prime features. The alloy has good machinability and surface finish characteristics. The alloy was developed and supplied by Alcoa, USA [2].

As seen from table 5.1, for aluminium alloys of 2XXX series copper is the main alloying element. In addition to this, a small amount of magnesium is also added to this series of alloys. These two alloying elements increase the strength of the material by precipitation hardening. The alloy is quenched and cold worked which increases the dislocation density and subsequently refines the size of intermediate precipitates which inhibits dislocation motion and thereby increasing the strength of the material. The two intermetallic precipitates that form in this alloy are Al_2Cu and Al_2CuMg. However, these precipitates tend to sit at the grain boundaries leading to a decrease in the stress corrosion performance.

Al 2624-T351		GLARE constituents	
		Al 2024-T3	FM94/S2-prepreg
E_1 / GPa	73	72	50.3
E_2, E_3 / GPa	71	72	5.5
G_{12}/GPa	28	28	1.995
G_{23}/GPa	28	28	2.099
ν_{21}	0.33	0.30	0.034
α_1 / °C^{-1}	2.32×10^{-5}	2.32×10^{-5}	2.88×10^{-6}
α_2 / °C^{-1}	2.32×10^{-5}	2.32×10^{-5}	4.03×10^{-5}
Density /kg m^{-3}	2770	2770	1972

Table 5.2: Mechanical properties of Al 2624-T351 [2]

Al 2624-T351 substrates were surface treated to improve adhesion properties following ASTM-D2651 standard. The procedure included degreasing and chemical etching or phosphoric acid anodising (ASTM D3933). The primer BR 127 was applied on both sides of the substrate to improve the adhesion characteristics. These primers offer superior durability and resistance to hostile environments within the bond line and may be used as a protective coating outside of the bonded areas. The recommended procedure for applying the primer is as follows [3]:

1. Allow the primer to equilibrate at room temperature prior to opening the container.
2. Thoroughly mix before and agitate during application.
3. Spray or brush coat to a dry primer thickness of 0.0025 mm nominal with a 0.005 mm maximum thickness. For protective coatings, increase primer thickness to 0.0102 to 0.025 mm.
4. Air-dry a minimum of 30 minutes prior to oven cure.
5. Oven cure at 121°C ± 6°C for 60 minutes.

GLARE 2 (6/5) was chosen as the strap material. It consists of two constituents, alternate layers of six-aluminium alloy 0.4 mm thick 2024-T351 sheets and five double layers of unidirectional glass fibres impregnated in epoxy resin of 0.26 mm thick. The thickness of the strap was 3.7 mm. The mechanical and thermal characteristics of GLARE constituents are different. Table 5.2 shows the mechanical properties of GLARE constituents. The unidirectional glass fibre epoxy is an anisotropic material, whereas aluminium sheet is an isotropic material that shows plasticity. Specimens were bonded using an elevated temperature cure adhesive FM 94® supplied by Cytec Ltd. The thickness of the adhesive layer is approximately 0.13 mm.

5.2 Material characterisation

Prior to discussing the test sample preparation, it is important to discuss the characterisation of the material used in this research, such as grain size and texture, of the Al 2624-T351. The grain size and the material texture play an important role in the residual stress measurements [4].

5.2.1 Grain size measurements

As mentioned earlier, all the fatigue crack growth test specimens were prepared by using 5 mm thick Al 2624-T351. The chemical composition of the Al 2624-T351 was supplied by Alcoa, USA and is listed in table 5.3.

Si	Fe	Cu	Mn	Mg	Cr	Zn	Ti	Other, each	Other, total
0.08	0.08	3.8-4.3	0.45-0.7	1.2-1.6	0.05	0.15	0.10	0.05	0.15

Table 5.3: Chemical composition of aluminium alloy 2624 (wt%)

The specimens were prepared from large ingots. The ingots are rolled to the desired dimensions resulting in severe deformation of the metal. The deformation leads to different grain sizes and texture in the rolled, transverse, and normal directions of the specimen. Grain size distribution plays a major role in the macrostress determination by diffraction since enough grains must contribute to the diffracted intensity to obtain good statistics. Optical microscopy was carried out to determine the grain size distribution across the thickness of the specimen. Samples for optical microscopy were extracted from a 5 mm thick plate in the rolling direction (longitudinal direction), in the transverse direction, and in the normal direction as shown in figure 5.1.

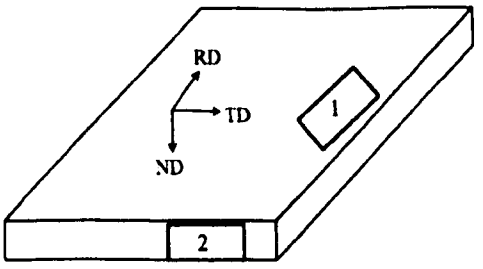

Figure 5.1: Schematic representation of specimens extracted for grain size measurements showing RD (rolling direction), TD (transverse direction) and ND (normal direction)

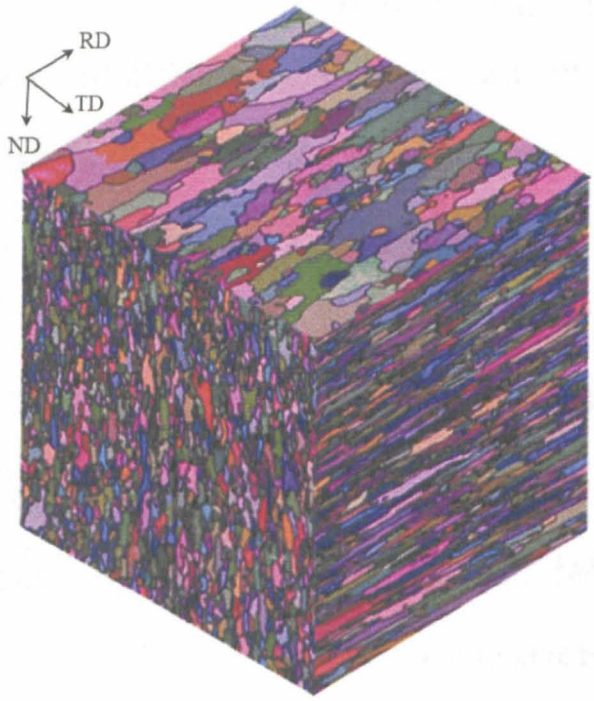

Figure 5.2: 3-dimensional grain distribution of Al 2024-T351

Specimens were extracted with an automatic high precision cutting machine which enables very smooth cutting with the least mechanical deformation. Extracted specimens were prepared for optical microscopy and etching was performed by immersing the specimen in Keller's Reagent for 12 seconds [5, 6]. Figure 5.2 shows the 3-dimensional image of Al 2624-T351 grain distribution in all three directions. The grain structure is a "pancake" structure. The grain size measurements were performed by using ASTM E112. In the rolling direction the grain size is found to be 113-134 μm, in the transverse direction 33-40 μm and in the normal direction 28-33 μm.

5.2.2 Texture analysis

As the substrate material used in this investigation is deformed by rolling, a strong preferred grain orientation or crystallographic texture will be developed in the specimen. When the material passes through the rollers, the interaction with the roll affects the homogeneity and through-thickness deformations of the material, being higher near the rollers. Texture combines the crystallographic feature of lattice orientation with the microstructural feature of grain structure. The degree of grain orientation is often of

interest in materials used for diffraction measurements. This is particularly important for samples manufactured by rolling where the orientation of grains may evolve to some preferred crystallographic direction [6]. The crystallographic texture was characterised by the electron backscatter diffraction (EBSD) facility in the scanning electron microscope (SEM) [7]. The electron backscatter diffraction technique reveals the micro-texture pattern with high spatial resolution.

The texture pattern was determined and represented in terms of pole figures. A pole figure is a means of displaying a stereographic projection of the crystallographic directions present in the grains onto a sphere and then onto a circle. For texture studies of rolled materials, the axes of the projection sphere can be aligned with the axes of the sample. The directions of crystal plane normals (poles) are usually plotted as an (hkl) pole figure which shows the distribution of the {hkl} poles in the sample.

A specimen of 10 × 10 × 5 mm^3 was used to study the through thickness texture pattern. A step size of 5μm over a grid of 2 × 1 mm was used and the measurement was repeated by moving the specimen until the whole sample is measured. Figure 5.3 shows the measurement locations in the specimen. A total of 5 measurements were performed to investigate the change in crystallographic texture at different thickness locations.

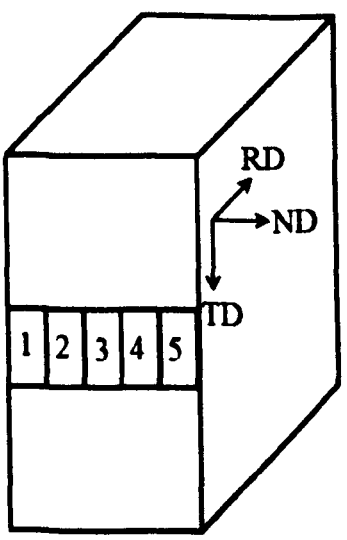

Figure 5.3: Texture measurement location in the specimen

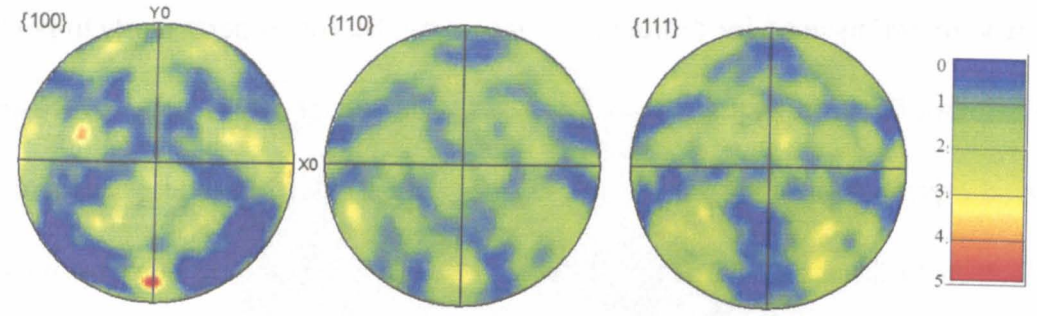

At 1 mm, Maximum experimental density (MUD) = 3.57

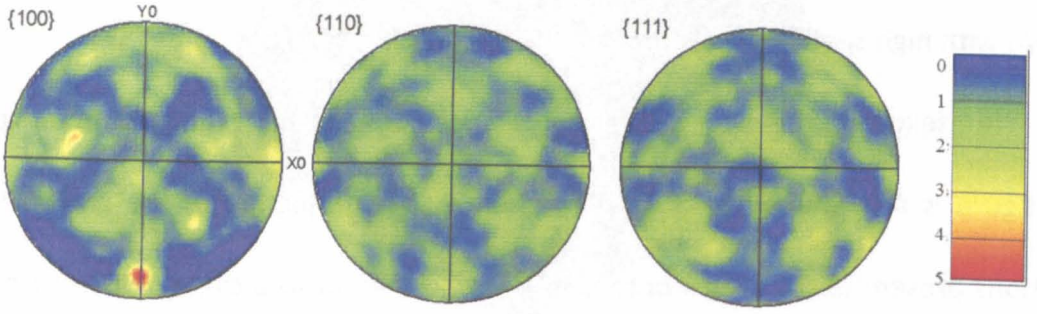

At 2 mm, maximum experimental density (MUD) = 4.19

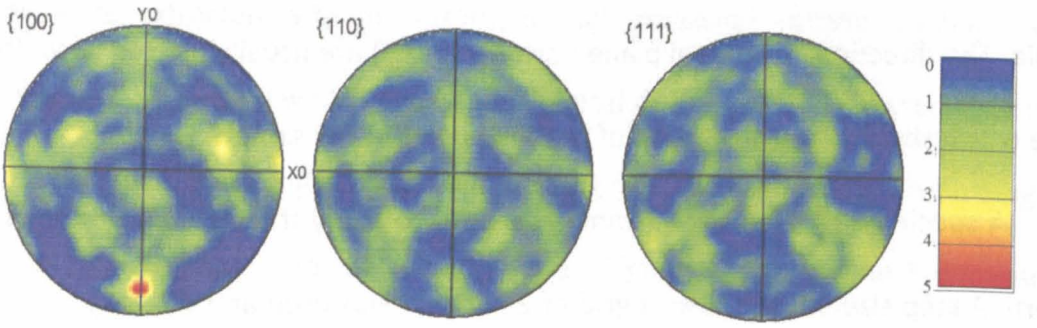

At 3 mm, maximum experimental density (MUD) = 5.06

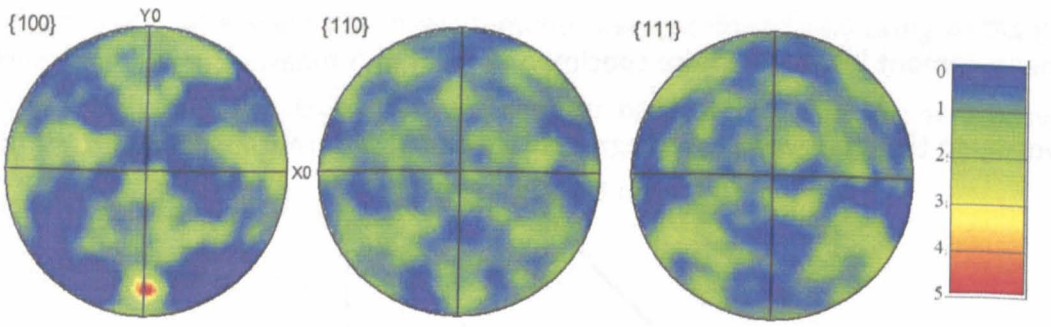

At 4 mm, maximum experimental density (MUD) = 4.29

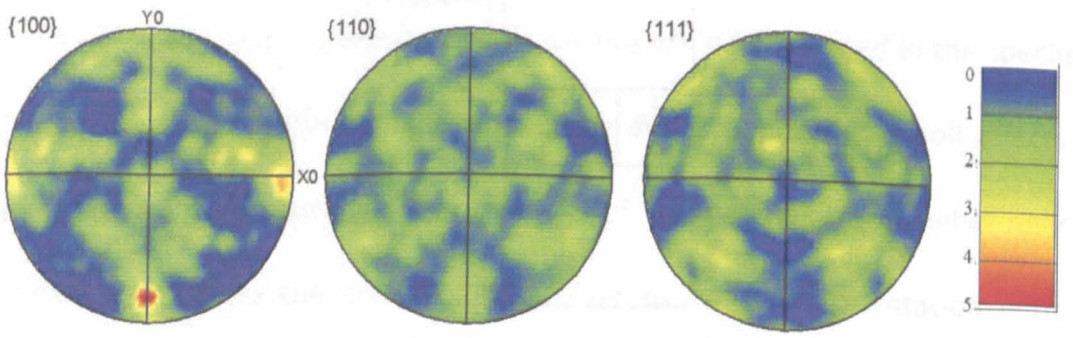

At 5 mm, maximum experimental density (MUD) = 3.69

Figure 5.4: Crystallographic texture measurements of Al 2624-T351

Figure 5.4 shows five crystallographic texture measurements at 1 mm, 2 mm, 3 mm, 4 mm and 5 mm from top to bottom respectively. The pole figures shown are obtained by a contour plot of the experimental densities obtained from the diffraction pattern. The colour contours show a scale from blue to red with blue the minimum and red the maximum texture. The absolute values of densities observed are shown in every figure on the right hand scale. It can be observed that the material is textured in the {100} direction and there a small variation in the texture at 3 mm compared to other thickness locations.

5.2.3 Characterisation of GLARE

GLARE consists of alternate layers of an aluminium sheet and double layers of glass fibres impregnated in epoxy. Figure 5.5 shows the cross-sectional view of the GLARE strap bonded onto the substrate.

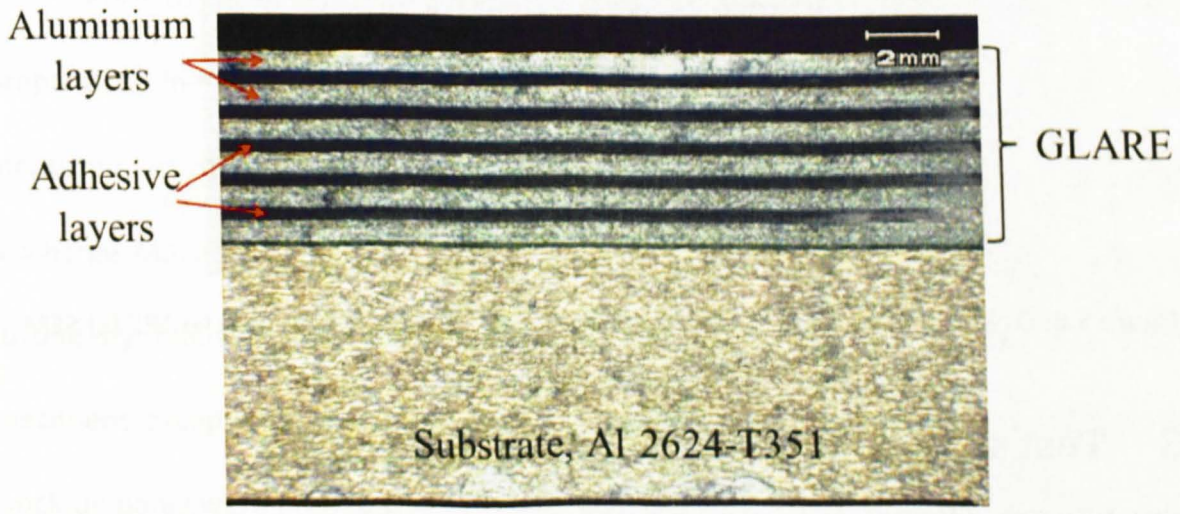

Figure 5.5: Optical image showing GLARE and substrate assembly

Figure 5.6 shows the cross-sectional view of the adhesive layer in the GLARE. It can be seen that the glass fibres are randomly distributed with diameters ranging from 60 to 80 μm. The optical image in figure 5.6 (b) shows pores in the adhesive which might be a result of air entrapped during the manufacturing process.

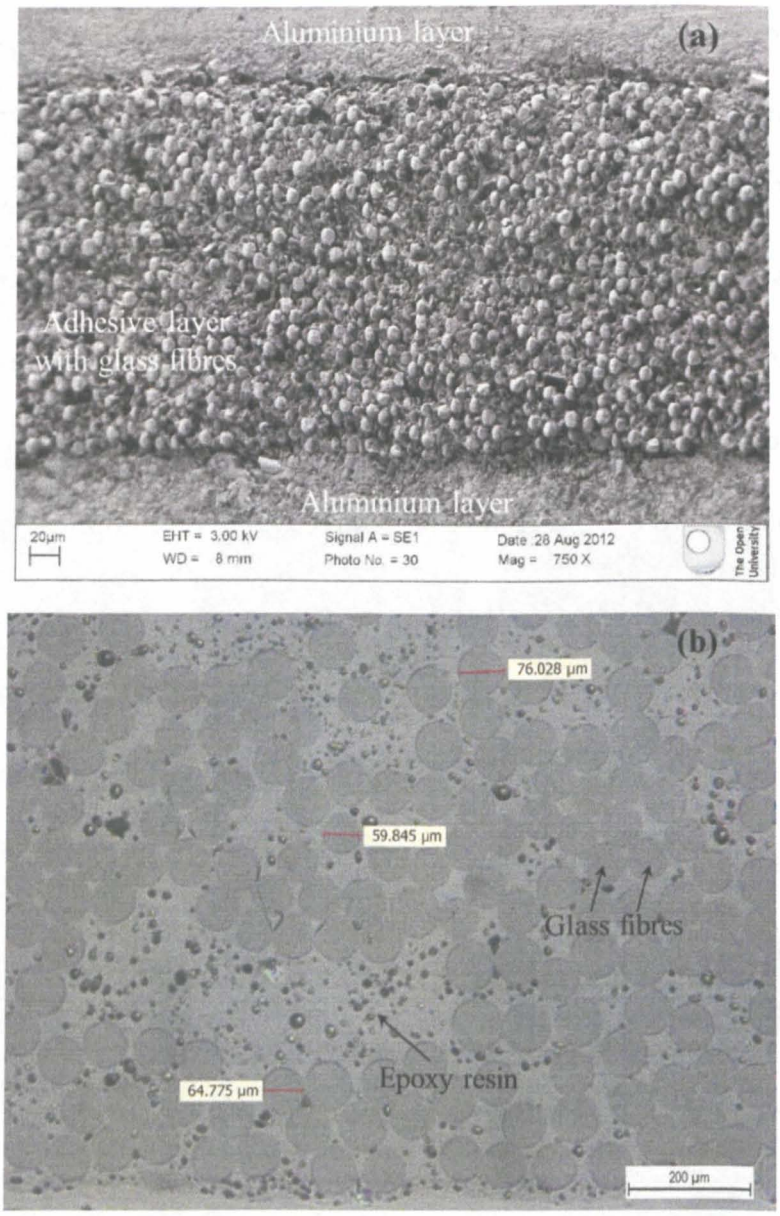

Figure 5.6: Cross sectional view of glass fibre impregnated adhesive layer in GLARE (a) SEM image and (b) optical image

5.3 Test specimen preparation and geometry

In this research different specimen geometries were used to characterise the fatigue durability and residual stresses developed in the reinforced coupon specimens. For constant amplitude fatigue crack growth tests, mainly two specimen configurations are used:

1. Middle crack Tension (M(T)) or Centre Cracked Tension (CC(T)) specimens with and without a reinforcing strap,
2. Single Edge Notch Tension (SEN(T)) specimen with and without a reinforcing strap.

Residual stress measurements were performed on various coupon specimens and structural joints:

1. Cold expanded and bolted hole coupon specimens with and without a reinforcing strap,
2. Middle crack Tension or Centre Cracked Tension specimen,
3. Impact damage specimen,
4. Manhole coupon specimen,
5. Single strap butt joint and
6. Mock-up aircraft panel with reinforcing straps.

In addition to this, Double Cantilever Beam (DCB) specimens were used to investigate the critical strain energy release rate of the FM94 adhesive.

Prior to discussing specimen geometry, it is important to discuss the specimen preparation in detail. All the substrates for fatigue crack growth and residual stress measurement specimens were machined at The Open University using an Electro Discharge Machine (EDM). Straps were machined to required dimensions by water jet cutting by following the instruction manual supplied by the manufacturer. All the specimens except cold expanded and bolted hole, manhole, single strap butt joint, and mock-up panel were prepared at Cranfield University.

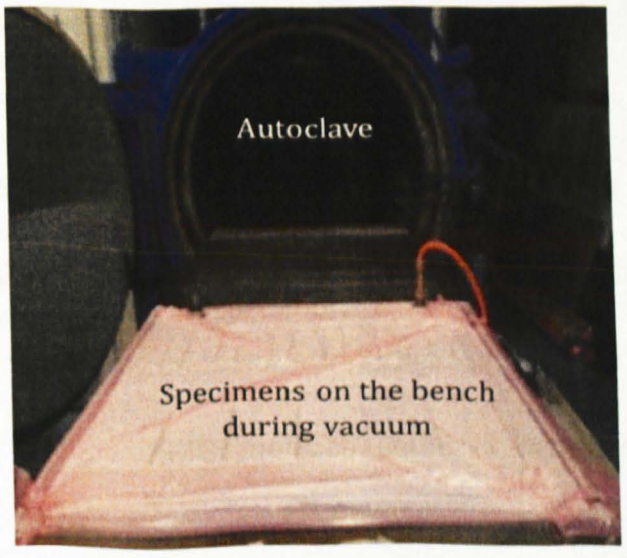

Figure 5.7: Sample preparation at Cranfield University

The substrate and GLARE straps were cleaned thoroughly using alcohol prior to assembly. The FM 94 prepreg was cut from the roll to the desired strap size. Once the samples had been assembled, they were de-bulked via vacuum using a Bosch R5 vacuum pump for 20 minutes. The next stage in the bonding process is to cure the specimen assembly in an autoclave. Figure 5.7 shows the Autoclave at Cranfield University. The curing process is performed according to the procedure supplied by the adhesive manufacturer Cytec Ltd.

- Apply vacuum at ambient temperature for a minimum of 15 minutes and increase the temperature at a rate of 3°C/min from ambient to 125 ± 5°C, and increase pressure in autoclave to 520 kPa.
- Vent vacuum when the pressure reached 415 kPa, or when the temperature reached 60°C, then a pressure of 520 kPa and the temperature of 125°C for 90 minutes is maintained.
- After 90 minutes, turn off the heat and allow the autoclave to cool to below 60°C, whilst maintaining the pressure prior to removing the samples from the autoclave.

After curing, samples are removed from the autoclave and non-destructively inspected by using an Olympus Omniscan MX with a Phased Array (PA) to ensure the bond quality, as the presence of voids in the bond line may lead to premature failure of the specimen.

5.3.1 Middle crack tension (M(T)) specimen

M(T) specimens were used for constant amplitude fatigue crack growth testing and evaluation of residual stresses during fatigue crack growth. Substrates were sectioned from Al 2624-T351 alloy plates to dimensions 400 mm long, 140 mm wide and 5 mm thick. Figure 5.8 shows the geometrical details of the M(T) specimens with a reinforcing strap. A 16 mm slot was cut through the thickness at the center of the specimen with a 0.5 mm wire using an electro discharge machine (EDM).

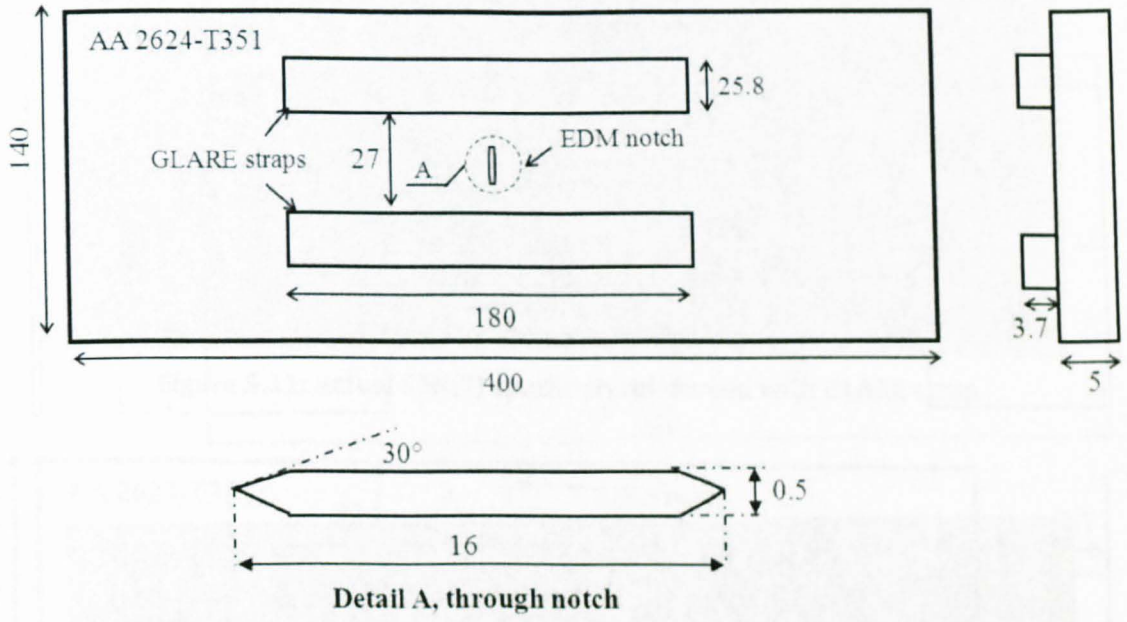

Figure 5.8: Geometrical details of M(T) specimen reinforced with strap

Geometrical details of the notch are shown in figure 5.8, detail A. The sharp edge of the slot will ensure stress concentration at the slot tip induce a crack during loading.

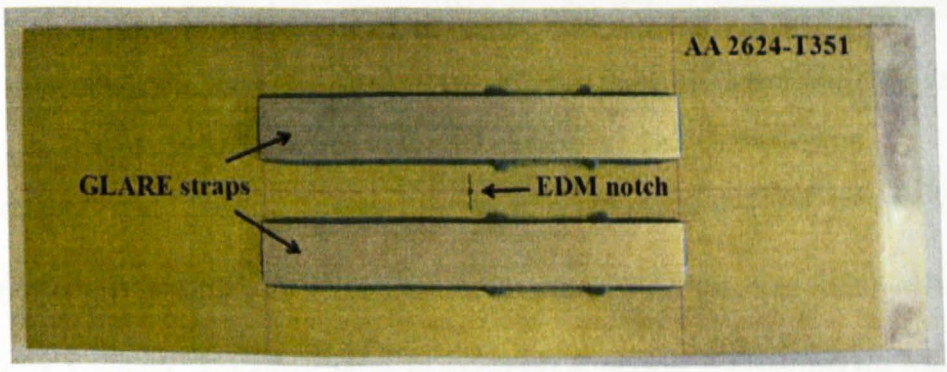

Figure 5.9: Actual M(T) specimen reinforced with GLARE straps

The specimens were tested according to ASTM E647. A global stiffness ratio (μ) of 0.2 is selected for this research, which results in individual strap dimensions of 180 mm long, 25.8 mm wide and 3.7 mm thick for M(T) coupons. Two straps are placed on each side of the slot at a distance of 13.5 mm from the center of the substrate (see figure 5.9). Specimens were prepared both with and without straps. The geometrical details of the specimen without strap are not shown because the only difference is the absence of the strap.

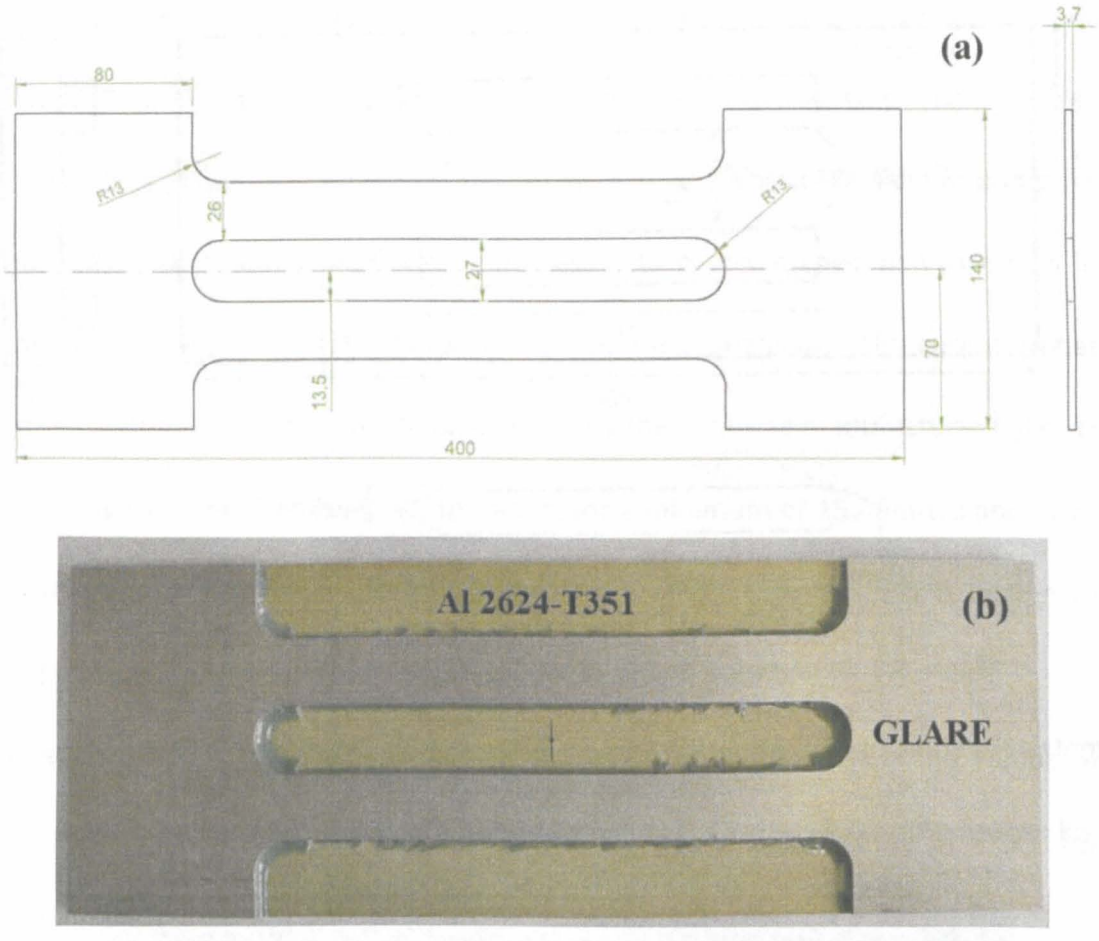

Figure 5.10: M(T) specimen with load carrying GLARE strap (a) geometrical details of the strap and (b) actual M(T) specimen with load carrying GLARE strap

In addition to the M(T) specimens with strap (regular straps), two specimens were prepared with load carrying GLARE straps in order to investigate the effect of load carrying straps on the fatigue durability of bonded crack retarders. Figure 5.10 shows the geometrical details of the load carrying GLARE strap and the actual M(T) specimens with load carrying GLARE strap.

5.3.2 Single Edge Notch Tension (SEN(T)) specimen

SEN(T) specimens were used for constant amplitude fatigue crack growth testing and evaluation of residual stresses after impact damage on the GLARE. The actual specimen is shown in figure 5.11 and the geometrical details of the SEN(T) specimen with strap are shown in figure 5.12.

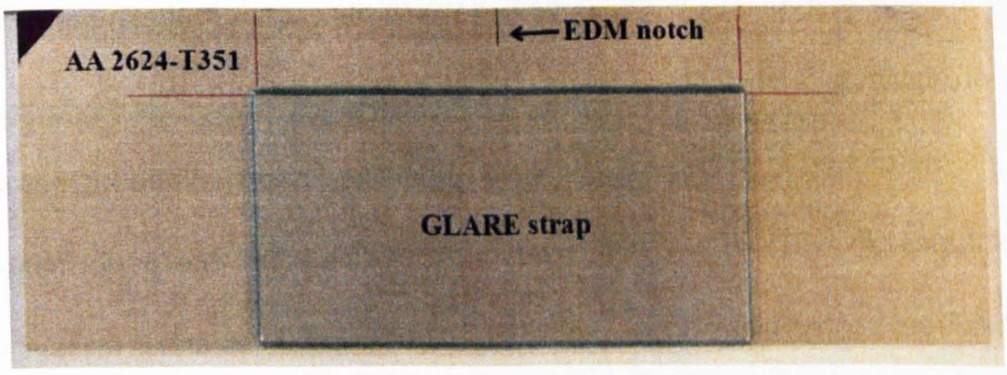

Figure 5.11: Actual SEN(T) specimen reinforced with GLARE strap

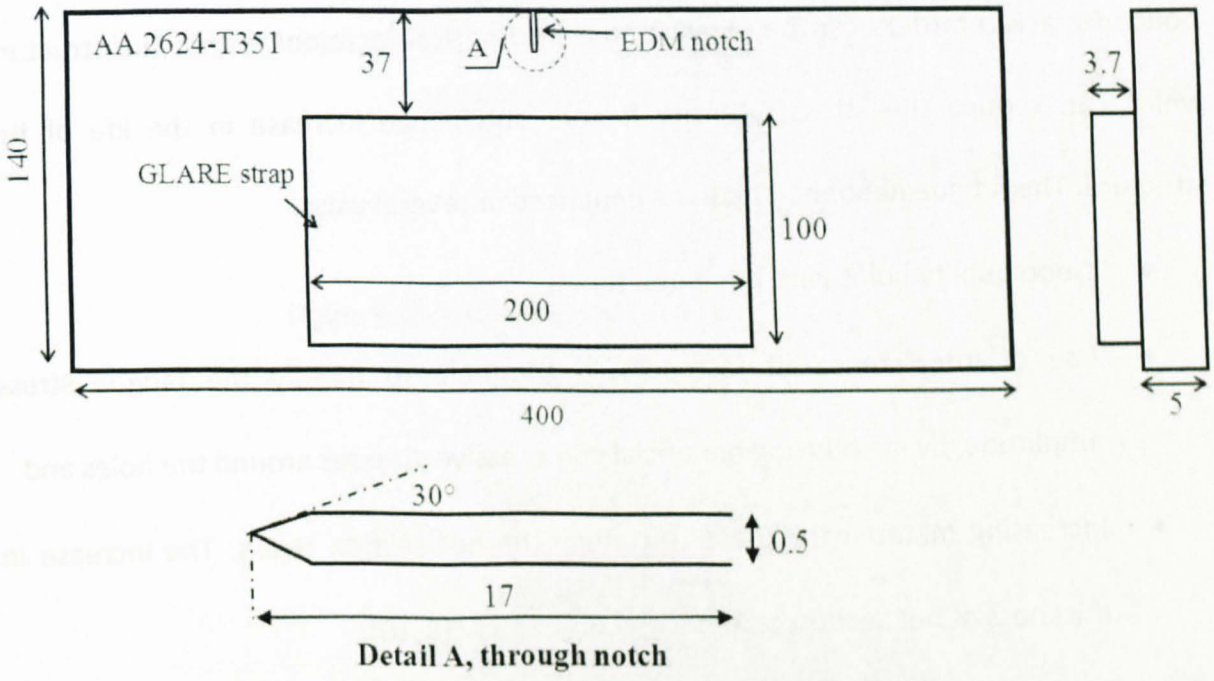

Figure 5.12: Geometrical details of SEN(T) specimen reinforced with strap

Substrates were sectioned from Al 2624-T351 alloy plates of 400 mm long, 140 mm wide and 5 mm thick. A 17 mm slot was cut through the thickness at the edge of the specimen with a 0.5 mm wire using an electrical discharge machine (see figure 5.11 and 5.12). A GLARE strap of 200 mm long, 100 mm wide and 3.7 mm thick were placed at a distance of 37 mm from the edge of the specimen.

5.3.3 Cold expanded and bolted hole specimen

Prior to discussing the geometrical details of the cold expanded and bolted hole specimen, it is important to explore the concept of cold expansion and its significance in aircraft structural joints. Structural joints that incorporate bolts and rivets are extensively used in aircraft structures. These joints become fatigue critical locations. During service,

these joints are vulnerable to fatigue loading which may result in the initiation of fatigue cracks, propagation, and eventual structural failure.

As mentioned in chapter 4, the stress intensity factors will be high at structural discontinuities. Increase in stress intensity factors can affect the performance of the structure. From an economic point of view, the fundamental demand is for longer service life. In order to improve the damage tolerance and avoid large penalising safety factors, bonded crack retarders can be incorporated into critical locations within the structure which can reduce the stress intensity factors and hence increase in the life of the structure. The fatigue life of holes can be enhanced in several ways:

- Good quality holes with minimum flaws
- Use of interference fit fasteners in the hole to modify the fatigue stress amplitude, by introducing beneficial compressive stresses around the holes and
- Increasing material thickness to reduce the net section stress. The increase in thickness of net section carries a weight penalty [8-10].

Among the remainder, introducing compressive residual stresses around the hole is the most popular and effective method in enhancing the fatigue life of a hole. This method complements other methods and carries no weight penalty. Fatigue life improvement from the cold expansion process usually ranges from 3 to 10 times for typical aircraft structures [11-24]. Of the methods available to induce compressive residual stresses around holes the split sleeve cold expansion method is the most commonly used by aerospace and other industries.

Fatigue Technology Inc (FTI) has developed the split sleeve cold expansion. The cold expansion process is accomplished by pulling an oversize tapered mandrel pre-fitted with an internally lubricated stainless steel sleeve through the hole. The function of the split sleeve is to reduce the mandrel pull force, protect the hole from damage, and ensure

the correct radial expansion of the hole. The sleeve also allows the process to be a one-sided operation. Figure 5.13 illustrates the split sleeve cold expansion process.

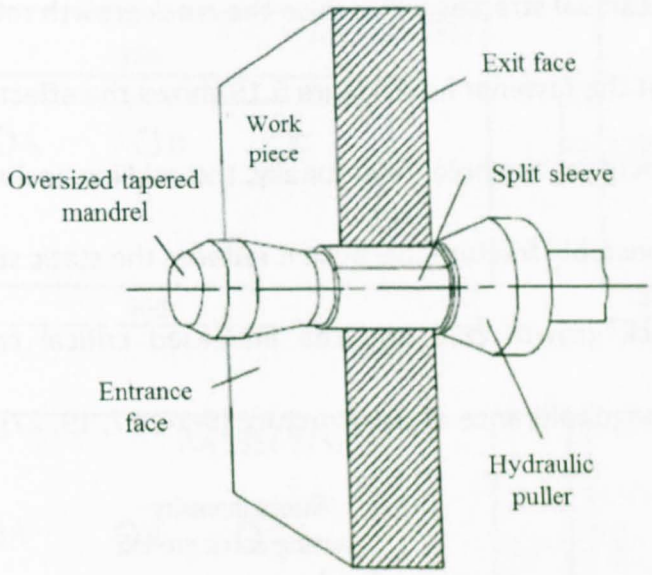

Figure 5.13: Split sleeve cold expansion process [25]

Residual Stress

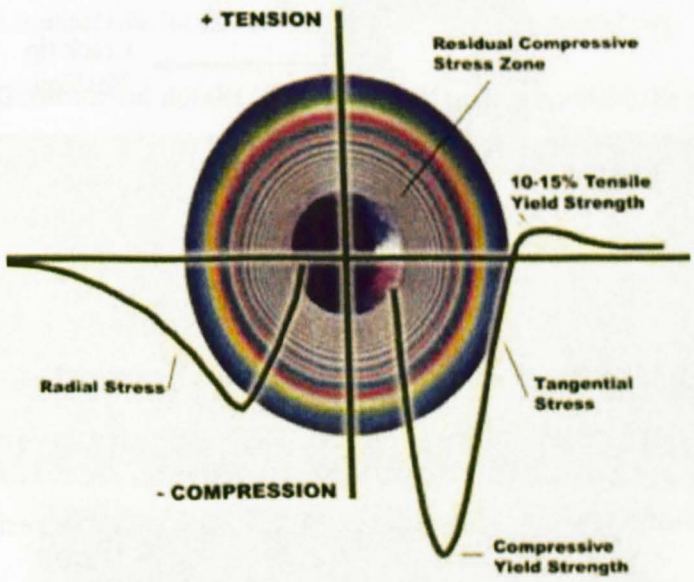

Figure 5.14: Typical radial compressive stresses around a cold expanded hole [26]

Typical radial residual stresses generated by cold expansion are illustrated in Figure 5.14. The action of drawing the mandrel through the hole causes a radial plastic flow of material and results in an annular zone of residual compressive stresses that extends up to one diameter beyond the edge of the hole. The peak magnitude of compressive stresses is roughly equal to the compressive yield strength of the material. A balancing tensile stress lies just beyond the compressive stress region which varies between 10 to

15% of the material tensile yield strength. As discussed earlier, the major contributor affecting the fatigue life of a fastener holes is the stress intensity factor. The presence of cold expansion residual stresses will reduce the crack growth rates by lowering the stress intensity factor at the fastener hole. Figure 5.15 shows the effect of cold expansion on the stress intensity factor at the hole. Additionally, the cold expansion may change the critical crack length for unstable fracture, because it reduces the static stress intensity factor. The reduction in crack growth rate and the increased critical crack length significantly improves the damage tolerance of the structure [9-14, 17, 19, 27].

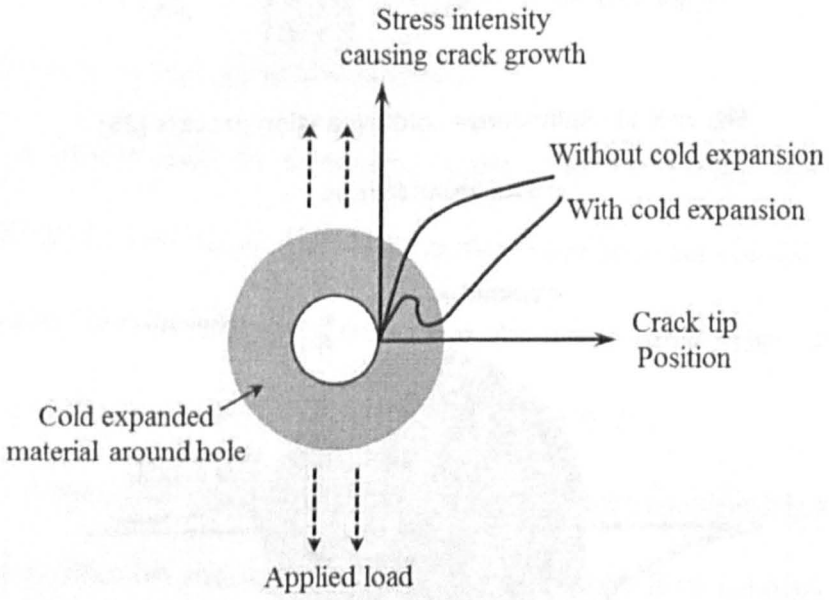

Figure 5.15: effect of cold expansion on stress intensity factor [9]

Several investigators have observed that the cold expansion stresses may not be uniform through the thickness of the plate. It has been determined that the residual stresses near the mandrel exit (outlet) face of the hole are greater than the stresses near the mandrel entrance (inlet) face [17, 18, 20, 24, 28]. The amount of cold expansion is expressed in terms of a percentage and depends on the type of material to be cold expanded. Optimal fatigue performance can be achieved when the hole is expanded by 3% in aluminium alloys and at least 4.5% in high strength materials such as steel and titanium [9, 30].

Cold expanded and bolted hole specimens were used to investigate the effect of thermal residual stresses generated during the GLARE bonding process on the cold

expansion stresses. Two specimens were prepared, one without a strap and the second with a strap. The geometrical details of the two specimens are shown in figure 5.16.

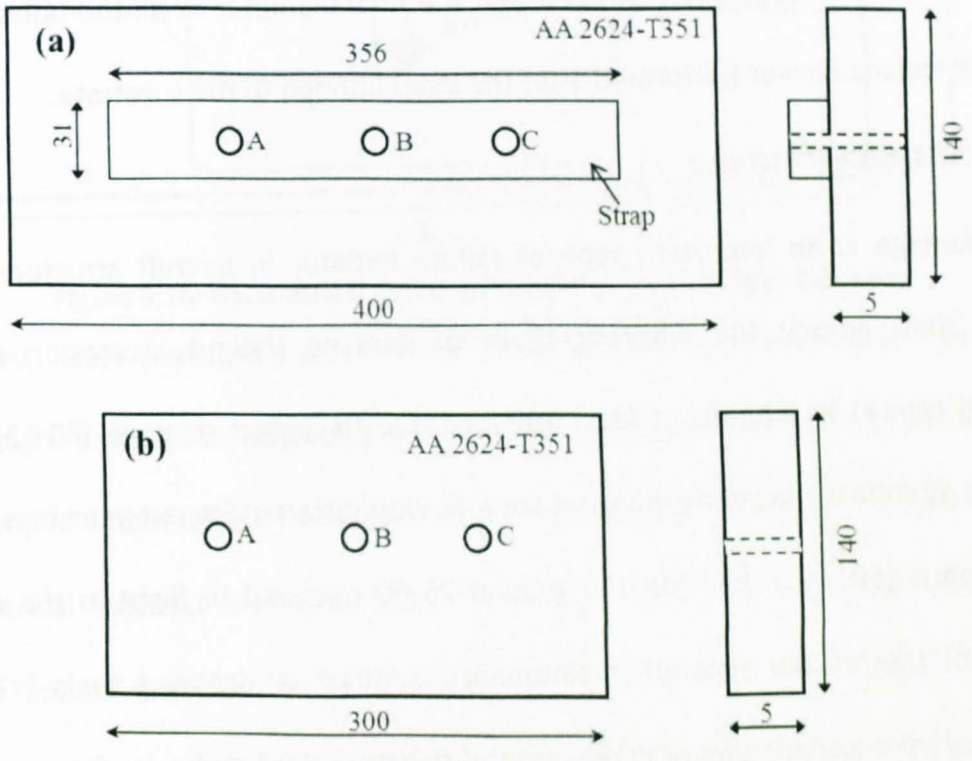

A-Cold expanded hole, B-Drilled hole and C- Cold expanded and bolted hole

Figure 5.16: Geometrical details of cold expanded and bolted hole specimens

A-Cold expanded hole, B-Drilled hole and C-Cold expanded and bolted hole

Figure 5.17: Actual cold expanded and bolted hole specimens

Both the specimens were extracted from a 5-mm-thick plate of Al 2624-T351. Both the specimens contain a cold expanded hole, a drilled hole and a bolted hole represented by A, B and C respectively as shown in figure 5.16. Figure 5.17 shows the actual cold

expanded and bolted hole specimens. The bolted hole was cold expanded prior to installing the bolt. Both of the specimens were 3% cold worked by using a split sleeve mandrel of 5.66 mm nominal diameter and the final diameter of all the holes was 6.27 mm. Cold expansion was performed after the strap bonded to the substrate.

5.3.4 Impact damage

Impact damage is an important type of failure initiator in aircraft structures. It was reported that, among the different types of damage (fatigue, corrosion etc.) and associated repairs in aircraft, at least 13% are due to impact damage [30-32]. Impact damage in aircraft is caused by different sources with different impact velocities such as: runway debris (60 m/s), hail (on the ground 25-60 m/s and in flight in the order of hundreds of metres per second), maintenance damage or dropped tools (<10 m/s), collisions between service cars or cargo and the structure, bird strike, ice from propellers striking the fuselage, engine debris, and tyre shrapnel from tread separation and tyre rupture. However, different impact regimes are possible in aircraft which should be considered during the design process for reasons of safety. It is also important for economic reasons, because the damage has to be detected and repaired during maintenance [31, 32].

Impact damage specimens were used to ascertain the effect of impact damage on GLARE residual stresses and fatigue durability of the bonded crack retarder. Figure 5.18 shows the geometrical details of the specimen which is identical to the SEN(T) specimen used for fatigue crack growth testing. The additional feature in this specimen is the impact damage on the GLARE.

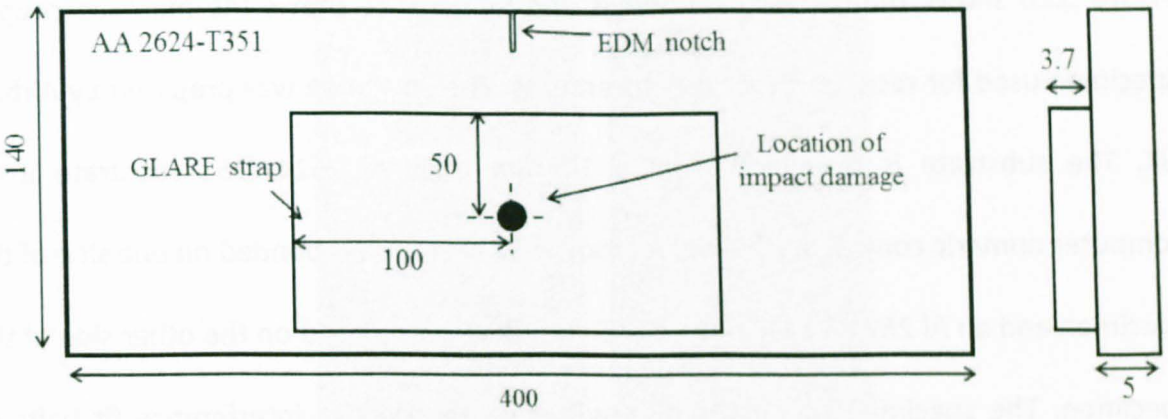

Figure 5.18: Geometrical details of impact damage SEN(T) specimen

Impact tests were performed at Cranfield University with a low velocity instrumented falling weight machine fitted with a second strike preventer. For impact, the specimens were clamped within a steel frame fitted with a rectangular aperture. A 20 mm diameter hemispherical indenter was used and the total mass of the impactor was 2.54 kg. Different impact energies can be achieved by changing the drop height. The impact damage resistance was characterized by investigating the indent depth and width of the damaged area using a Laser Co-ordinate Measurement Machine.

5.3.5 Manhole specimen

The openings in aircraft skins are usually referred to as manholes. Manholes provide access to aircraft wings, fuel tank, and stabilizers. Generally, any structure of the aircraft, comprising a hole, or opening requires reinforcement to enhance its service life. A typical image of a manhole in an aircraft wing is shown in figure 5.19.

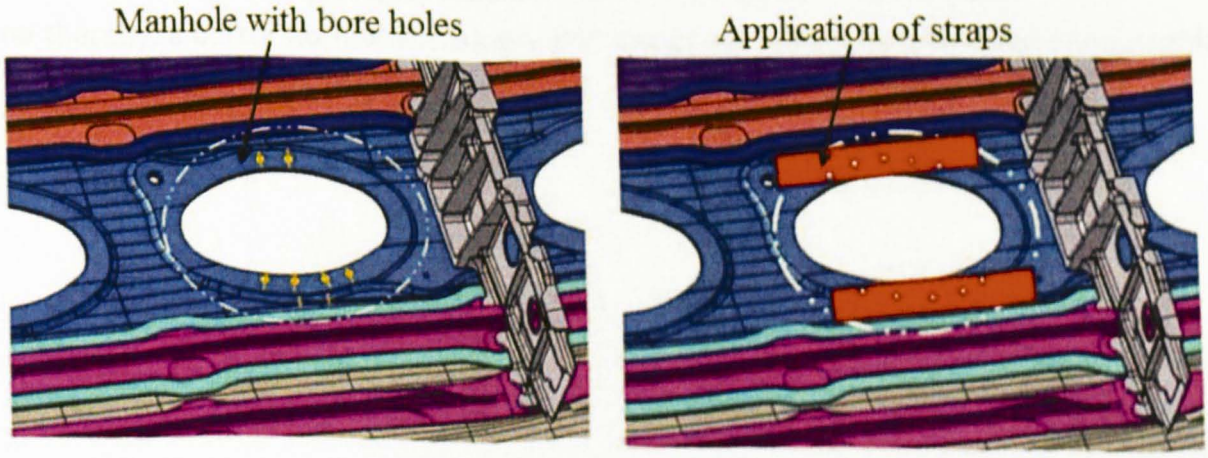

Figure 5.19: Manhole in an aircraft wing and bonded crack retarder application

Figure 5.20 shows the geometrical details and figure 5.21 shows the manhole coupon specimen used for residual stress measurements. The specimen was prepared by Airbus, UK. The substrate is machined from a 10 mm thick Al 2624-T351 substrate using computer numeric control machining. A strap of 37 mm wide is bonded on one side of the specimen and an Al 2624 metallic strap of 5 mm thick was placed on the other side of the specimen. The specimen was assembled with five countersink interference fit bolts of 7.28 mm nominal diameter. Prior to assembly, the fastener holes for the bolts were 3% cold expanded.

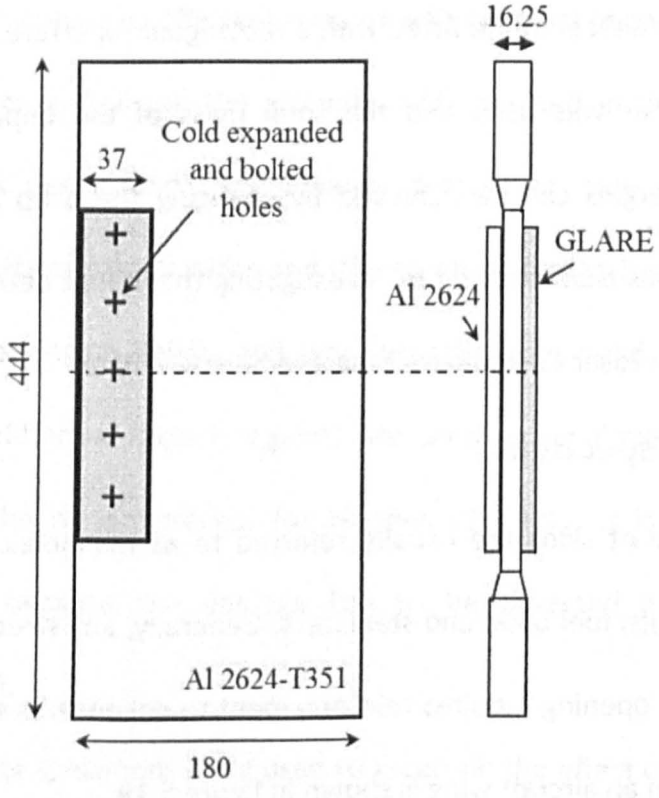

Figure 5.20: Geometrical details of manhole coupon specimen

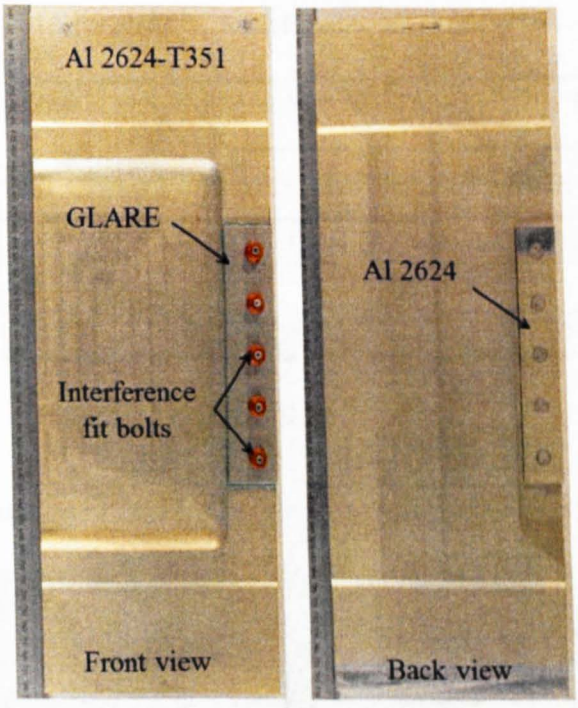

Figure 5.21: Actual manhole coupon specimen

5.3.6 Single strap butt-joint specimen

The single strap butt joint is one of the most critical locations in an aircraft structure. Due to the critical fastener row and the eccentric load path, butt joints in aircraft structures are susceptible to fatigue crack nucleation and subsequent crack growth. Under nominal tensile loading, the eccentric load path results in secondary bending of the structure. The maximum moment due to secondary bending is induced primarily at the fastener rows which are structural critical locations. The damage tolerance of the single strap butt joint can be improved by the application of a single reinforcement to the butt joint. The reinforcement strap will have an overall effect of increasing the rigidity of the butt joint and thereby, a better normal stressing alignment of the joint structure should be possible [33, 34].

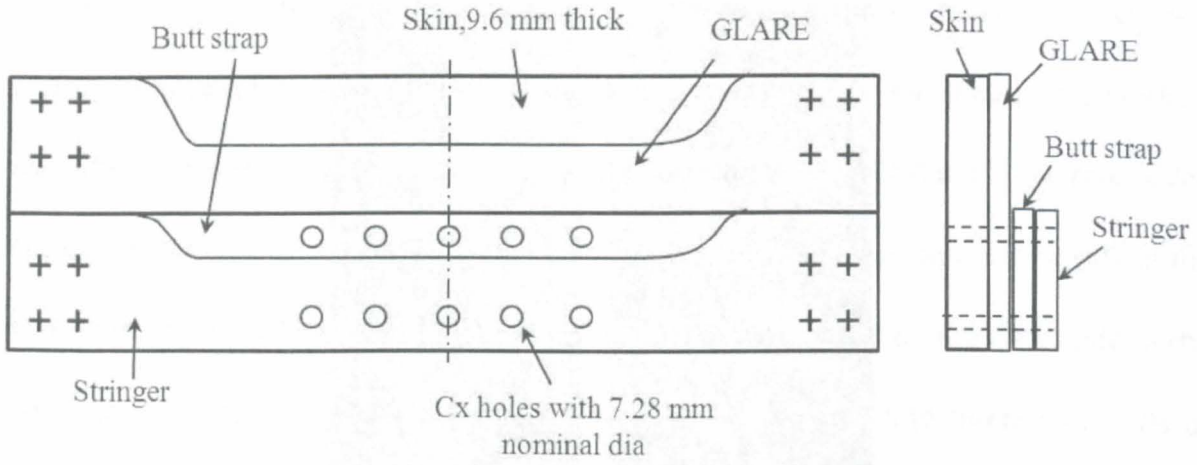

Figure 5.22: Geometrical details of single strap butt joint coupon specimen

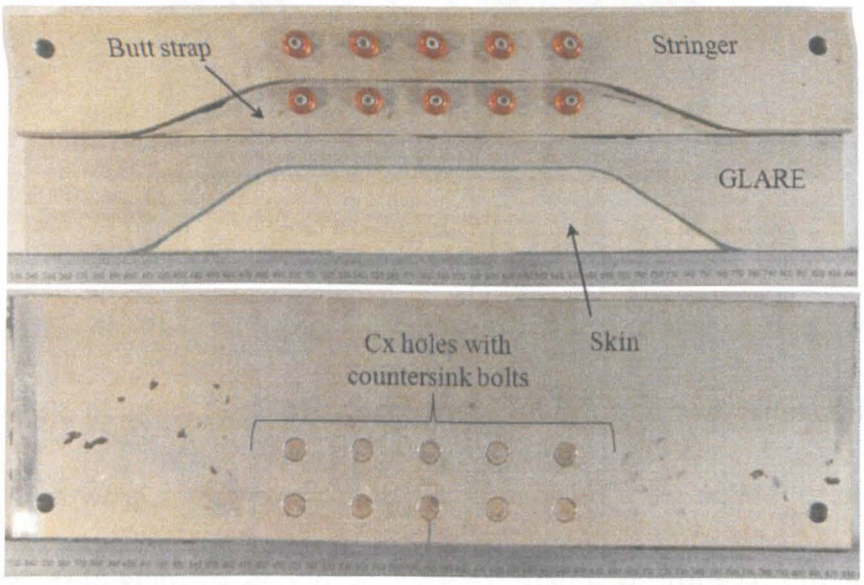

Figure 5.23: Actual single strap butt joint coupon specimen

Figure 5.22 shows the geometrical details of the single strap butt joint coupon specimen. It consists of skin, stringer, and butt strap. GLARE is bonded onto the 9.6 mm thick skin plate. The specimen was assembled with ten countersink interference fit bolts of 7.28 mm nominal diameter. Prior to assembly, the fastener holes for the bolts were 3% cold expanded. Figure 5.23 shows the actual single strap butt joint coupon specimen used for residual stress measurements.

5.3.7 Mock-up aircraft panel assembly

To further investigate the application of bonded crack retarders at a larger scale than the coupon samples, a skin-stringer panel representing the upper wing skin of a transport aircraft was designed and manufactured. Alcoa and Airbus, UK performed all the finite

element stress analysis, material supply, and panel manufacturing. Similar to the coupon specimens, the mock-up panel is also designed to have a stiffness ratio of 0.2. Figure 5.24 shows the application of GLARE as a bonded crack retarder in an aircraft mock-up panel.

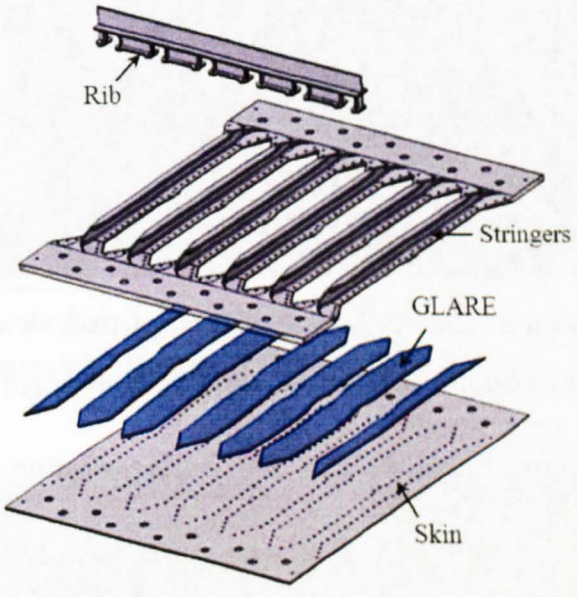

Figure 5.24: Application of GLARE as a bonded crack retarder in aircraft mock-up panel

The panel is about 1200 mm long and 780 mm wide, containing 5 stringers. The central stringer on the centre line was cut and a defect of 92 mm of total length was machined with a width of 2 mm through the stringer and skin plate. Figure 5.25 and figure 5.26 shows the mock-up panel front and back view respectively.

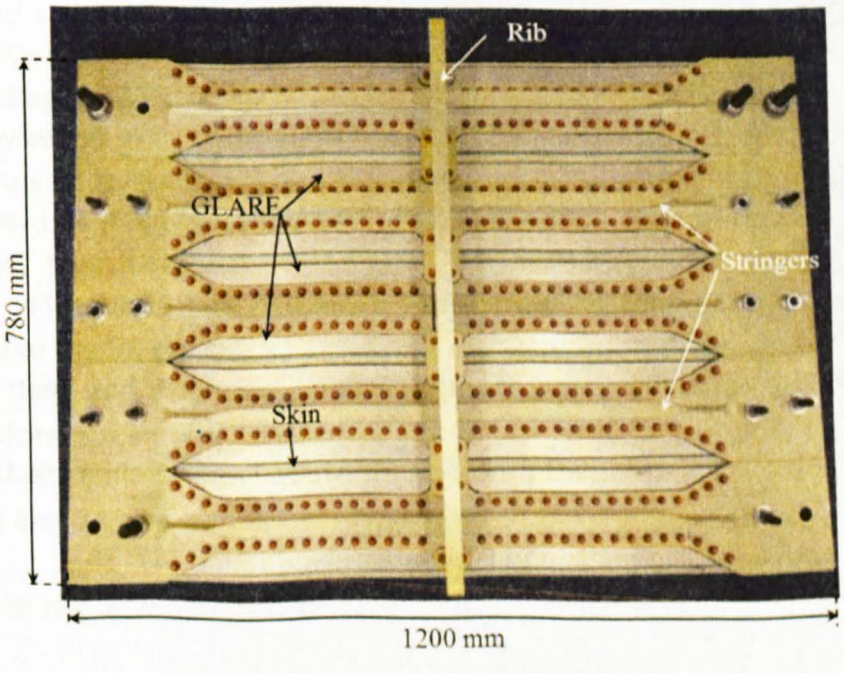

Figure 5.25: Mock-up aircraft panel, front view

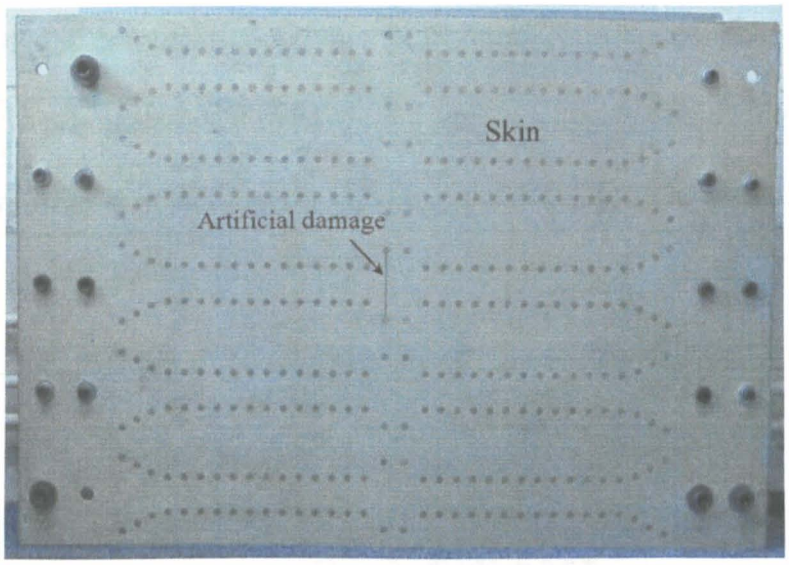

Figure 5.26: Mock-up aircraft panel, Back view

In this research, structural coupon specimens, manhole and single strap butt joint and the mock-up aircraft panel were studied only for the characterisation of the residual stresses. After residual stress measurements, the structural coupons were tested at Airbus, UK and the aircraft mock-up panel was delivered to Cranfield University to assess the fatigue durability of bonded crack retarders. Hence, the fatigue test results of manhole, single strap butt joint, and mock-up panel specimens are not included in this dissertation.

5.3.8 Double Cantilever Beam (DCB) specimen

In the case of fatigue loading, fatigue cracks will propagate along the path of least resistance, i.e. through the aluminium substrate and GLARE strap interface. The GLARE is bonded onto the substrate by using FM94 high temperature cure adhesive. A material's resistance to crack propagation depends on the fracture toughness, and several standard methods exist for testing metals, composites, adhesives, and plastics. For adhesive joint studies, the double cantilever beam (DCB) specimen geometry has been most popular [35, 36]. There are existing standard protocols for Mode I interlaminar fracture toughness (G_{IC}) testing of both adhesive joints and laminate delamination [37, 38].

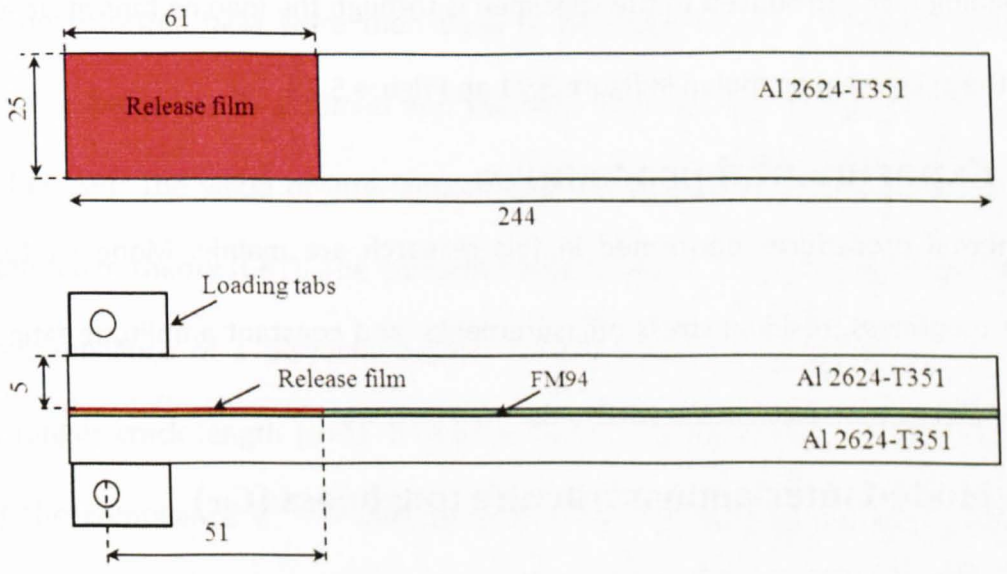

Figure 5.27: Geometrical details of DCB specimen

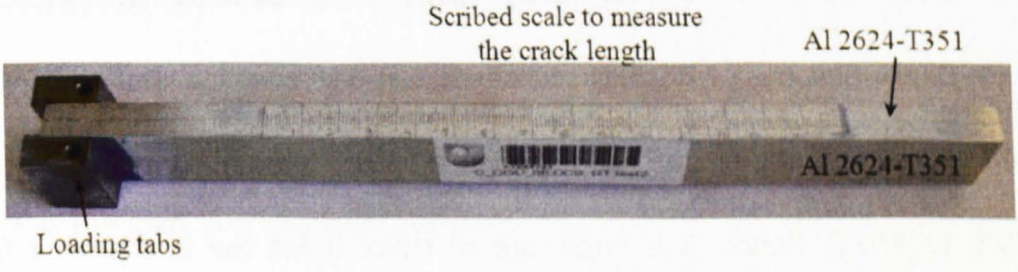

Figure 5.28: Actual DCB specimen

The DCB specimen geometry consists of a uniform thickness rectangular specimen with a crack starter at one end. Figure 5.27 and figure 5.28 shows the geometrical details of the DCB specimens and the actual DCB specimens used in this investigation. The specimen can be visualized as two cantilevered beams, bonded along their length. Specimens were prepared according to ASTM-5528 standard.

Two plates of 244 mm long, 25 mm width and 5 mm thick were extracted from Al 2624-T351 alloy. Specimens were bonded using FM94 adhesive. An adhesive film is extracted equal to the length and width of the specimen and placed on the first plate (see figure 5.27). Before placing the second plate onto the adhesive for bonding, a release film of 61 mm long and 25 mm width was placed on the adhesive. The release film acts as a barrier and does not allow the adhesive to stick to the second plate in the release film area. This area acts as a crack starter for Mode I interlaminar fracture toughness testing.

The opening load introduced to the specimen is through the loading tabs attached at the end of the specimen, as shown in figure 5.21 and figure 5.28.

5.4 Experimental procedures

Experimental procedures performed in this research are mainly: Mode I interlaminar fracture toughness, residual stress measurements, and constant amplitude fatigue crack growth tests.

5.4.1 Mode-I interlaminar fracture toughness (G_{IC})

Double cantilever beam static tests were performed according to ASTM-5528. The resistance to both crack initiation and crack propagation can be determined by DCB tests. Tests were performed on a MTS 5kN servohydraulic test machine. During service, the reinforced structures in the aircraft will experience service temperatures typically ranging from −60°C to +70°C. Hence, it is important to characterise the interlaminar fracture toughness of FM 94 at realistic temperatures. For this, DCB static tests were performed at Room Temperature (RT), −60°C and +70°C. At-temperature DCB static tests were performed using an Instron (3119-407) environmental chamber capable of temperature range of −150°C to +370°C was used. The temperature in the chamber and on the specimen was monitored by using an N-type thermocouple with an accuracy of ±0.5°C. For DCB tests at −60°C, liquid nitrogen was used as a cooling medium.

The crack length was measured along the edge of the specimen with an accuracy of ±0.5 mm by using a high-resolution camera with a scale marked on the specimen (see figure 5.28). The specimen was loaded with a constant displacement of 1 mm/min. The load, displacement and the crack lengths were recorded until the crack reaches 150 mm length. The specimen was loaded with pins inserted into the loading tabs. After mounting the specimen in the loading tabs, the end of the specimen was supported in order to keep the specimen orthogonal to the direction of the applied load.

The recorded data were then used to evaluate the G_{IC}. During G_{IC} evaluation, linear elastic behaviour is assumed and the data is processed by using corrected beam theory [38, 39]. The value of interlaminar fracture toughness can be ascertained from corrected beam theory (CBT). The corrected beam theory is the most popular expression for the compliance of a perfectly built-in DCB specimen. It assumes the beam has a slightly longer crack length ($a+\Delta$). Δ may be found experimentally by plotting the cube root of the compliance $C^{1/3}$. If loading tabs or blocks are used, the cube root of the normalised compliance $(C/N)^{1/3}$ can be used to calculate Δ. The adhesive fracture energy G_{IC} is given by [38, 39]

$$G_{IC} = \frac{3p\delta}{2B(a+|\Delta|)} \qquad \text{Equation 5.1}$$

Where P is the load, δ is the displacement, B is the width of the specimen and a is the crack length.

5.4.2 Residual stress measurements

Residual stress measurements were performed using neutron diffraction techniques. Diffractometers based at both spallation and reactor sources were utilised in this research. A detailed description of each instrument was given in chapter 3. Table 5.4 shows the list of instruments used for residual stress measurements on different coupon specimens used in this research.

Instrument	Specimens
ENGIN-X, ISIS, UK	Cold expanded and bolted hole without strap, M(T) specimen, Butt strap coupon and Mock-up panel.
SALSA, ILL, France	Cold expanded and bolted hole with strap, Impact damage SEN(T)coupon , Manhole coupon, and Mock-up panel.
POLDI, PSI, Switzerland	Impact damage coupon SEN(T) coupon
STRESS-SPEC, FRM-II, Germany	M(T) specimen

Table 5.4: List of specimens and instruments used for residual stress measurements

5.4.2.1 Residual stress measurements on cold expanded and bolted hole specimens

Residual stress measurements were performed at SALSA, ILL, and ENGIN-X, ISIS. Measurements were performed from the edge of the hole to the far end of the specimen in the width direction in two different thickness locations, z = 1.5 and 3.5 mm from the reinforced side, though owing to time constrains measurements were performed only at z = 1.5 mm at the bolted hole in both specimens. Measurements were not carried out at the drilled hole on the specimen without strap as there will be no residual stresses. Table 5.5 shows the details of the measurements and the instrument used.

Specimen	Location	Z (mm)	Instrument
Specimen with strap	Cold expanded hole	1.5	ENGIN-X
		3.5	SALSA
	Drilled hole	1.5	SALSA
		3.5	SALSA
	Bolted hole	1.5	SALSA
Specimen without strap	Cold expanded hole	1.5	ENGIN-X
		3.5	SALSA
	Bolted hole	1.5	ENGIN-X

Table 5.5: Details of the measurement locations and the instrument used

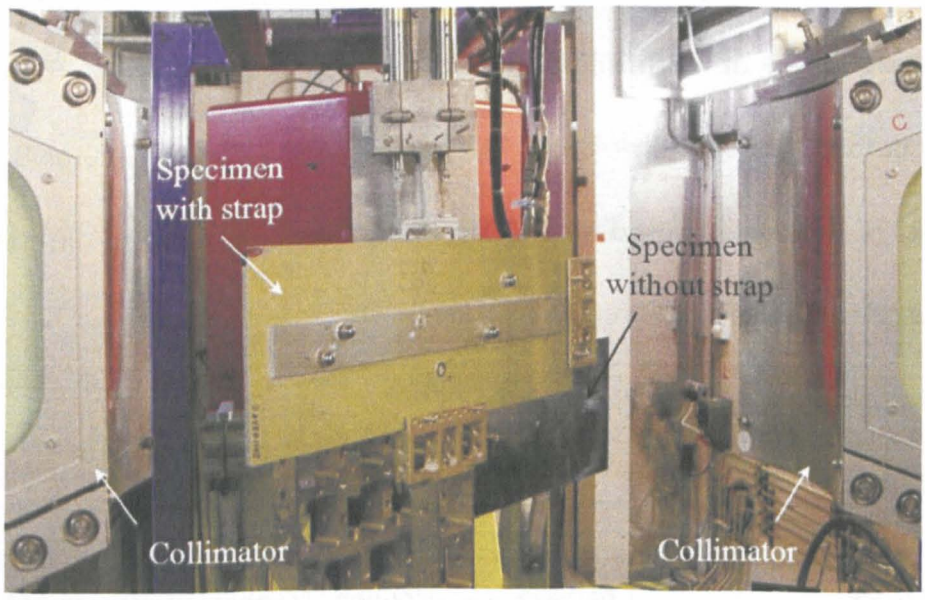

Figure 5.29: Experimental setup at ENGIN-X

Figure 5.29 shows the experimental setup for residual stress measurements on specimens with and without strap. Measurements were carried out in three principal strain directions, which were inferred from the geometry and symmetry around the holes. All

the measurements were made by using a gauge volume of 2 × 2 × 2 mm^3. Stress free reference (d_0) measurements were performed in three principal directions on 3 × 3 × 3 mm^3 specimen which was extracted from the edge of the specimen.

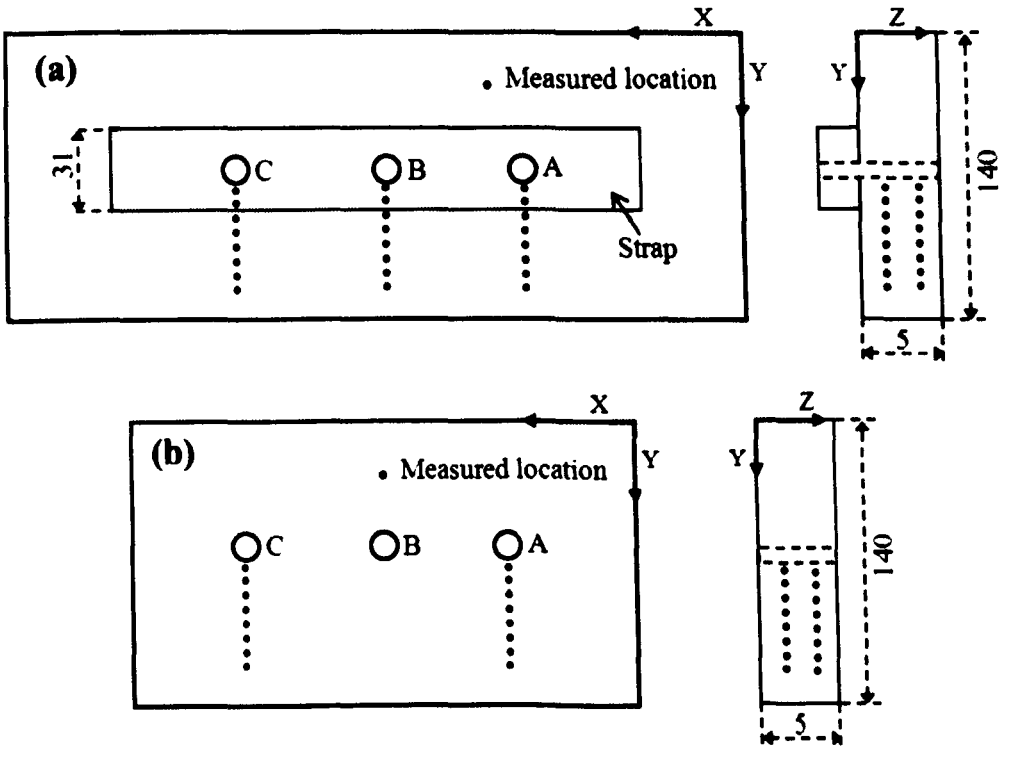

A-Cold expanded hole, B-Drilled hole and C-Cold expanded and bolted hole

Figure 5.30: Measurement locations in the cold expanded and bolted hole specimens (a) with strap and (b) without strap

Figure 5.30 shows measurement locations in the cold expanded and bolted hole specimen with and without strap respectively. In figure 5.30, X, Y, and Z are representing the hoop, radial and axial directions of the holes respectively.

5.4.2.2 Residual stress measurements on M(T) specimen

Thermal residual stresses arise due to thermal expansion co-efficient mismatch between the substrate and strap, and the asymmetric configuration of the single-sided bonding on M(T) specimen may have a significant effect on the fatigue durability of the bonded crack retarder assembly. Furthermore, single sided reinforcing can also result in out-of-plane distortion of the structure which can also affect the fatigue performance.

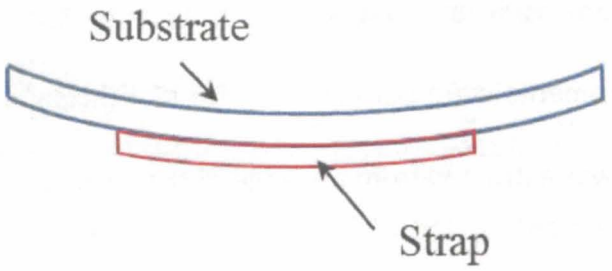

Figure 5.31: Possible out-plane-deflections observed in this research due to a single side strap bonding process

Prior to residual stress measurements and after specimen preparation an out-of-plane deflection was observed in the specimen. In the M(T) specimen, the out-of-plane deflection was observed similar to as shown in figure 5.31. This deflection may have a detrimental effect on the delamination behaviour of the specimen, and therefore it was important to quantify it. Out-of-plane deflection measurements were performed using a laser co-ordinate measurement machine on the non-reinforced side along the longitudinal direction, with a measurement pitch of 1 mm. Figure 5.32 shows the out-of-plane deflection resulting from the bonding process, and it can be clearly seen that a deflection of approximately 0.9 mm was observed in the non-reinforced side.

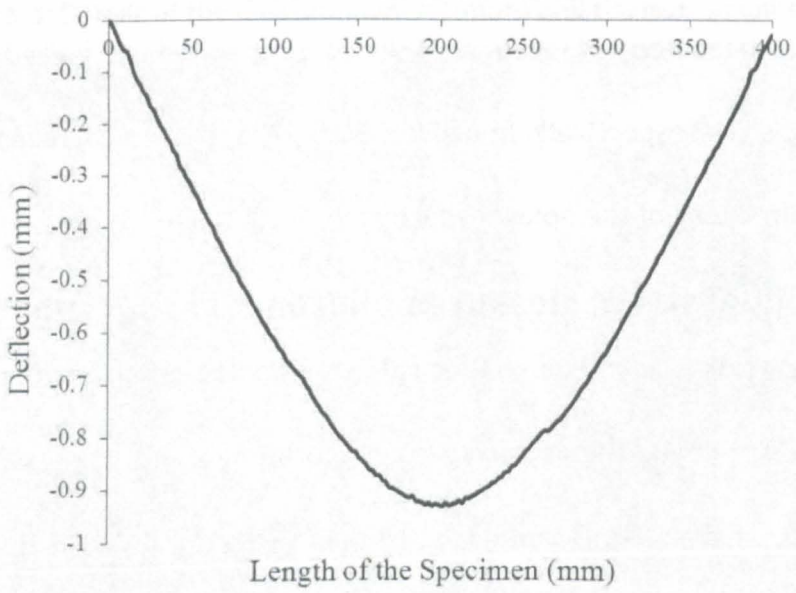

Figure 5.32: Out-of-plane deflection in M(T) specimen on the non-reinforced side

Figure 5.33 shows a schematic representation of the measurement locations on the M(T) specimen reinforced with a strap. Measurements were performed at ENGIN-X, ISIS, UK. Figure 5.34 shows the residual stress measurement experimental setup at ENGIN-X. The

direction along the longest dimension is hereafter referred to as the longitudinal direction (X), the direction along the width dimension is referred to as the transverse direction (Y) and the distance through the thickness is referred to as the normal direction (Z) as shown in figure 6.10.

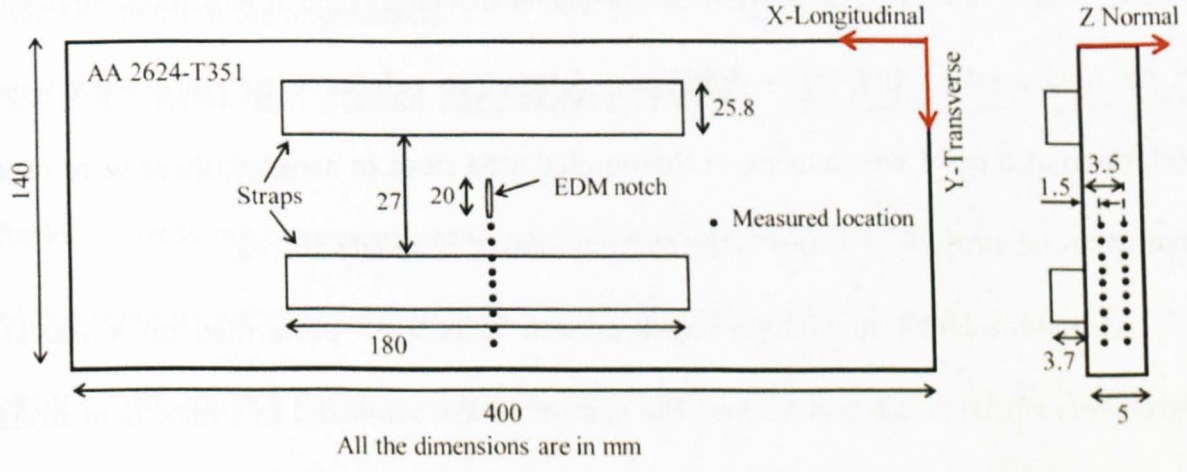

Figure 5.33: Residual stress measurement location on M(T) specimen

All the residual stress measurements were performed in the substrate along the crack growth direction (y-direction) in two different thickness locations, z = 1.5 and z = 3.5 mm from the reinforced side as shown in figure 5.33. Measurements were performed at four crack lengths: 10, 17, 26.5, and 48 mm from the centre of the specimen (10 mm corresponds to the initial condition with a starter notch before a fatigue crack is grown). Owing to time constraints, measurements of the 48 mm crack length were made only at z =1.5 mm.

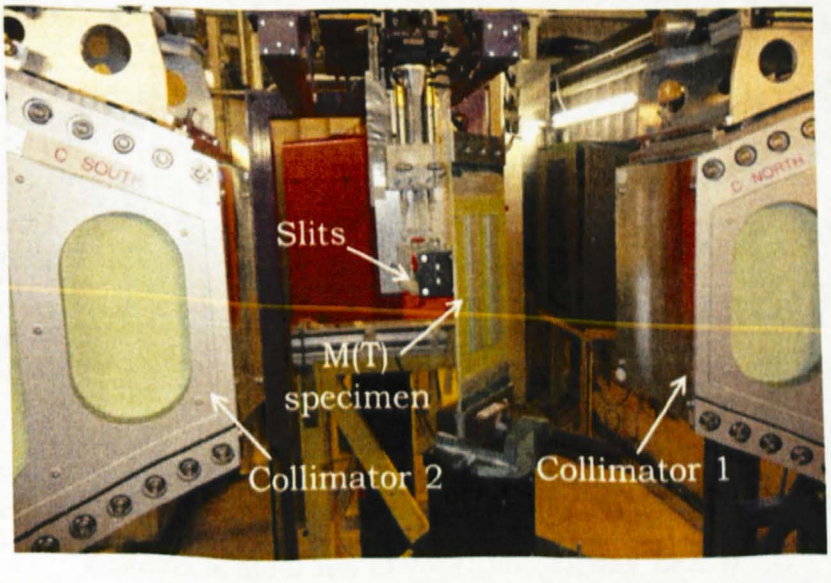

Figure 5.34: Experiment setup for residual stress measurements at ENGIN-X, ISIS

A gauge volume, defined by the intersection of the incident and scattered beams of the neutrons, of $2 \times 2 \times 2$ mm^3 was used for all the measurements. As the substrate is rolled in the longitudinal direction, texture and plastic anisotropy will be present which results in significant variation in the lattice parameters in all three directions (longitudinal, transverse and normal). Therefore the inter-planar distance in the stress-free sample had to be measured in the three directions. Stress-free reference measurements were performed at a point well outside of the bonded area close to an edge; these were used to provide the stress-free values in the computation of residual stresses.

Constant amplitude fatigue crack growth tests were performed on a 100 kN Instron servo-hydraulic test machine. The specimen was subjected to a maximum stress of 60 MPa at 10 Hz and with a load ratio of $R = 0.1$. Prior to fatigue tests the desired crack lengths were marked on the specimen using a Vernier height gauge with an accuracy of ± 0.01 mm. The crack length was monitored with a high resolution camera placed in front of the specimen and close to the growing crack as shown in figure 5.35. Tests were performed according to the ASTM E647 standard. The test procedure was performed in two phases: the first phase was to carry out pre-cracking of the sample and the second phase involves crack growth until specimen failure.

Figure 5.35: Fatigue crack growth test setup at ENGIN-X

During the in-situ residual stress measurements care was taken to measure a point at the crack tip for each crack length in the three principal directions. As mentioned earlier, residual stress measurements were performed at different crack lengths and the number of cycles for each crack length were 86 000, 128 000 and 204 000 cycles for 17, 26.5 and 48 mm crack lengths respectively.

5.4.2.3 Residual stress measurements on impact damaged SEN(T) specimen

Residual stress measurements were carried at POLDI and at the SALSA diffractometers. Measurements were performed in two specimens, one without impact damage and the second with impact damage, along the crack growth direction (y-direction) from the notch tip, as shown in figure 5.36.

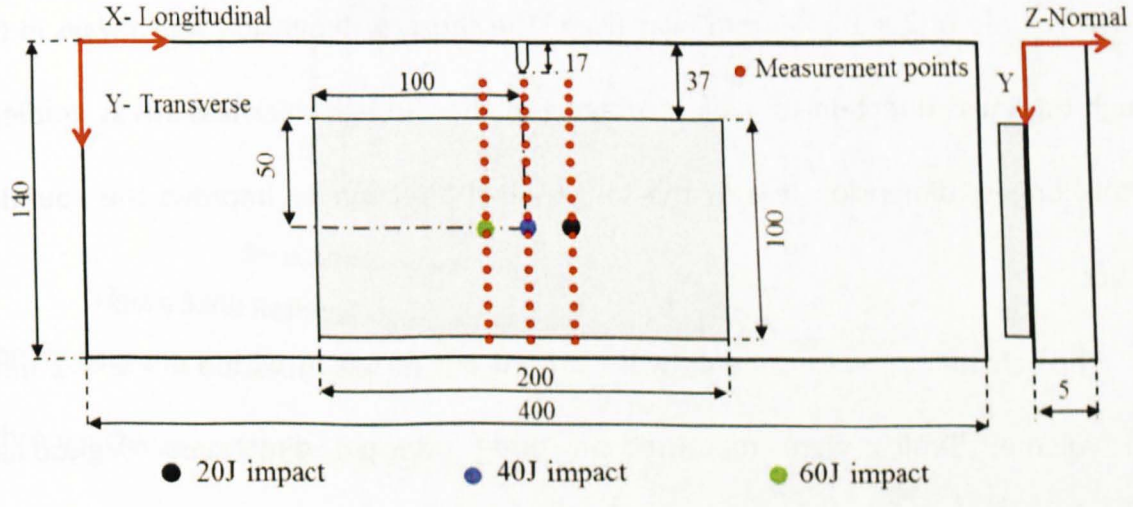

Figure 5.36: Residual stress measurement locations in the impact damage specimen

Impact damage was performed in three different locations on the GLARE with three different energies 20 J, 40 J and 60 J, to quantify the residual stresses developed during the bonding process and the change in the stresses due to impact damage. The centre of the impact location was 90 mm from the edge of the specimen for both 20 J and 40 J impacts, and 86 mm for the 60 J impact. The slight variation in the impact location is a result of positioning error of the specimen during impact.

All the measurements, except for the 20 J impact, were performed at two different thickness locations, at z =1.5 and 3.5 mm from the reinforced side in the

substrate. Owing to time constraints the region impacted with 20 J was measured only at z =1.5 mm. The specimen without impact damage and impact damaged with 60 J were measured at POLDI. Figure 5.37 shows the experimental setup at POLDI.

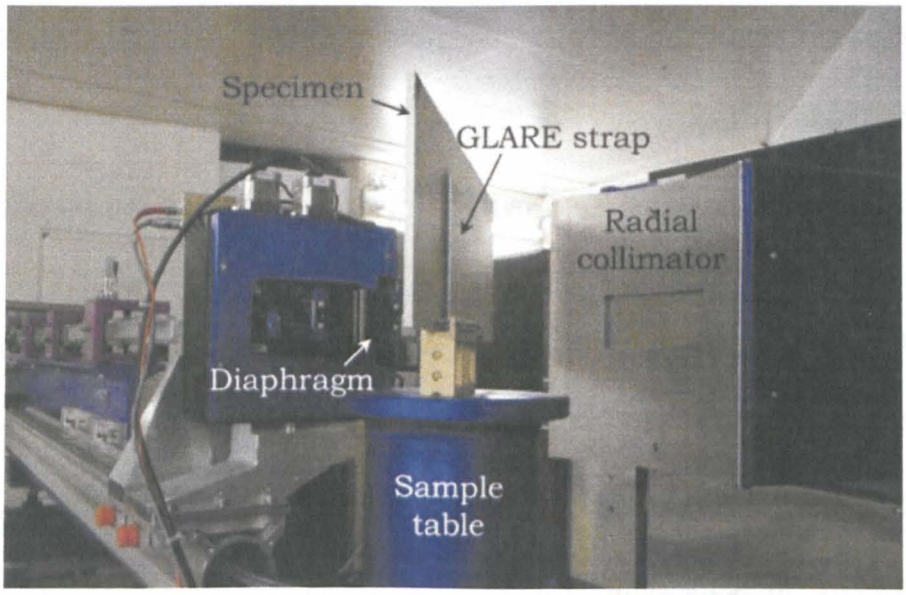

Figure 5.37: Experimental setup at POLDI

A gauge volume of 2 × 1.5 × 5 mm^3 was used. The shortest dimension was always in the through-thickness direction to avoid averaging of the through-thickness stress gradient, and the longest dimension was in the longitudinal direction to improve the counting statistics.

The remaining measurements were carried out at SALSA with a 2 × 2 × 2 mm^3 gauge volume. Strains were measured in three principal directions, longitudinal, transverse, and normal. As mentioned earlier, SALSA is a monochromatic strain diffractometer where single lattice reflections are measured. Aluminium is face-centered cubic and measurements were made using the {311} lattice plane as this has been found to give the best approximation to the macroscopic strain response. The wavelength used was 1.648 Å. For stress free reference measurements, data from a point well outside of the bonded area close to an edge were obtained in all three principal directions and were used to provide the stress-free values in the computation of residual stresses.

5.4.2.4 Residual stress measurements on the manhole specimen

Residual stress measurements on the manhole specimen were carried out at SALSA using a 2 × 2 × 2 mm^3 gauge volume using the {311} lattice plane. Measurements were performed, in three principal strain directions, which were inferred from the geometry and symmetry around the holes, in two different locations, i.e. line 1 and line 2 as shown in figure 5.38.

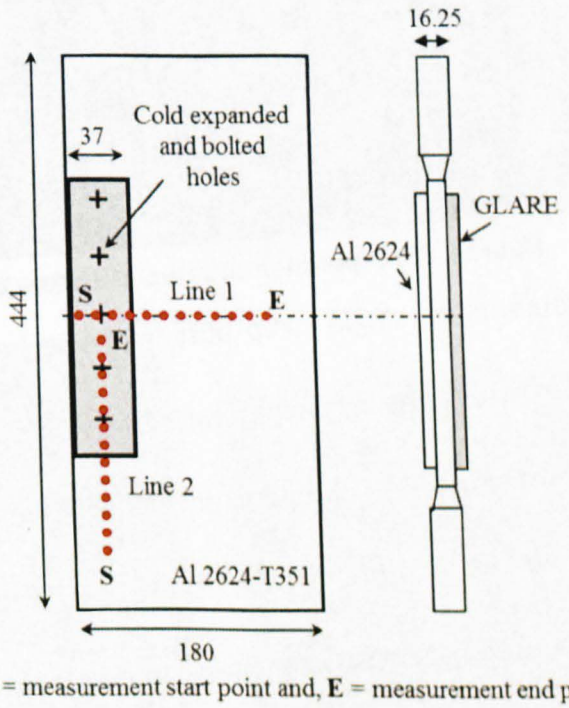

Figure 5.38: Residual stress measurement location in manhole specimen

All the measurements were carried in the substrate at 1.5 mm from the reinforced side in the through thickness direction. The wavelength used was 1.648 Å. During production the substrate is rolled and due to this, texture and plastic anisotropy will be induced in the material which results in variation in the lattice parameters in all three principal directions (hoop, radial and axial). Therefore, stress-free reference measurements were performed in three directions at a point well outside of the bonded area close to an edge and were used in computation of residual stresses.

5.4.2.5 Residual stress measurements on single strap butt-joint specimen

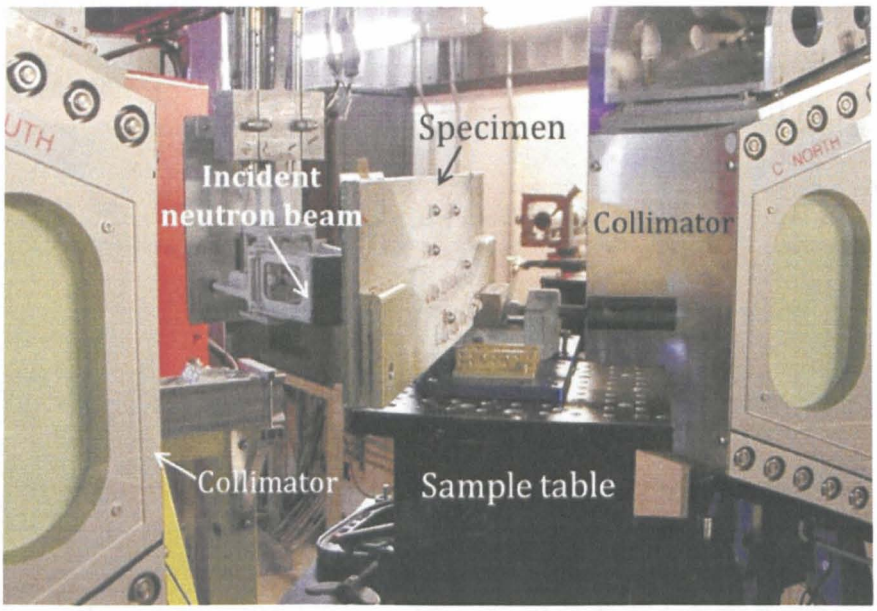

Figure 5.39: Experimental setup at ENGIN-X

Residual stress measurements on single strap butt joint specimens were performed at ENGIN-X and figure 5.39 shows the experimental setup. All the measurements were carried out on the skin plate along the y-direction at two different thickness locations, i.e. at z = 2.5 and 6 mm from the reinforced side. Figure 5.40 shows the measurement locations in the single strap butt joint specimen. In figure 5.40, X, Y, and Z are representing the hoop, radial and axial directions of the holes respectively

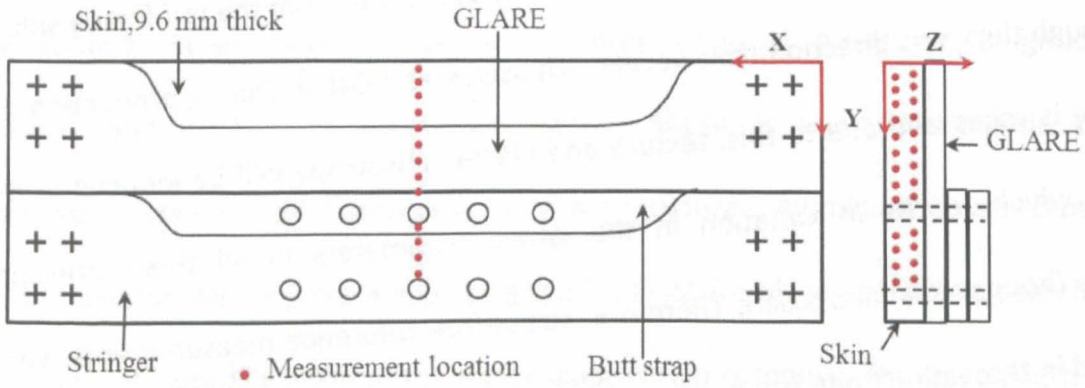

Figure 5.40: Measurement locations in single strap butt joint specimen

A gauge volume of 2 × 2 × 2 $mm^3$was used and the stress free reference measurement was performed in the skin plate in three principal directions at a point well outside of the bonded area close to an edge

5.4.2.6 Residual stress measurements on mock-up panel

So far, residual stress measurements in coupon specimens reinforced with bonded crack retarder have been presented. Residual stress measurements in the mock-up panel will take the investigation further and investigate the residual stresses associated with bonded crack retarders when incorporated into a typical structural application. The geometrical details of the mock-up panel were presented in chapter 5. The GLARE strap is bonded to the skin plate, therefore, residual stress measurements were performed only in skin plate at three different locations as shown in figure 5.41. The skin plate is of 4 mm thickness and the measurements were performed at 1.5 mm and 2.5 mm through the thickness from the reinforced side.

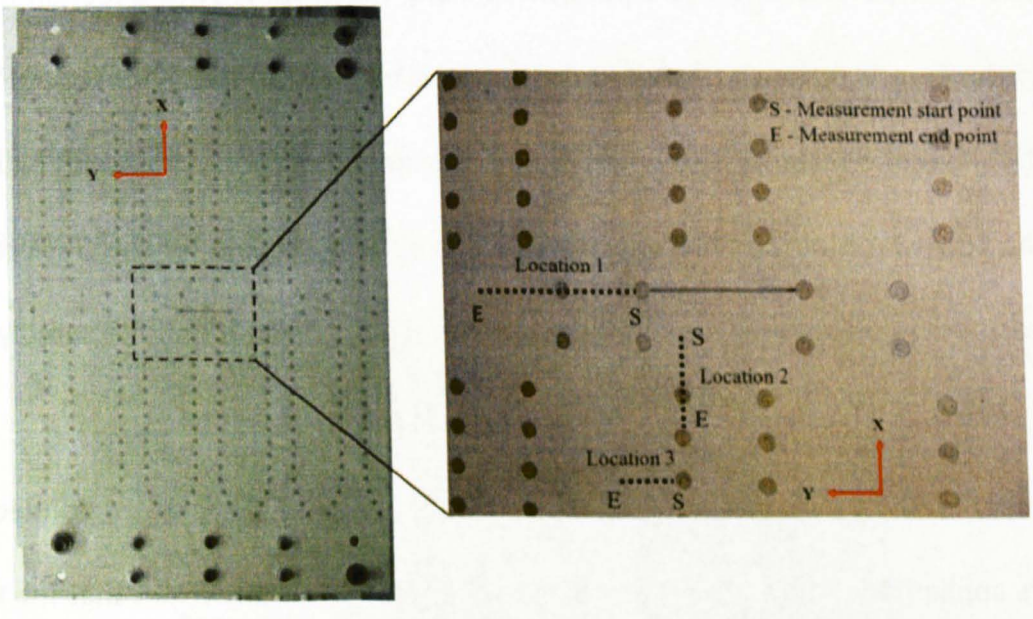

Figure 5.41: Residual stress measurement locations on the skin plate showing the back view of the mock-up panel on the left side and a close-up view of the measurement locations on the right side

Three measurement locations were chosen in different sections in the mock-up panel and the measurements were carried out at ENGIN-X with $2 \times 2 \times 2$ mm^3 gauge volume. Figure 5.42 shows the experimental setup at ENGIN-X. Measurements were performed, in three principal strain directions, which were inferred from the geometry and symmetry around the holes. Six stress-free lattice parameter measurements were made in the three principal directions from a point well outside the bonded area, close to an edge of the

specimen and the average was used to provide a stress free reference value in the computations of residual stresses.

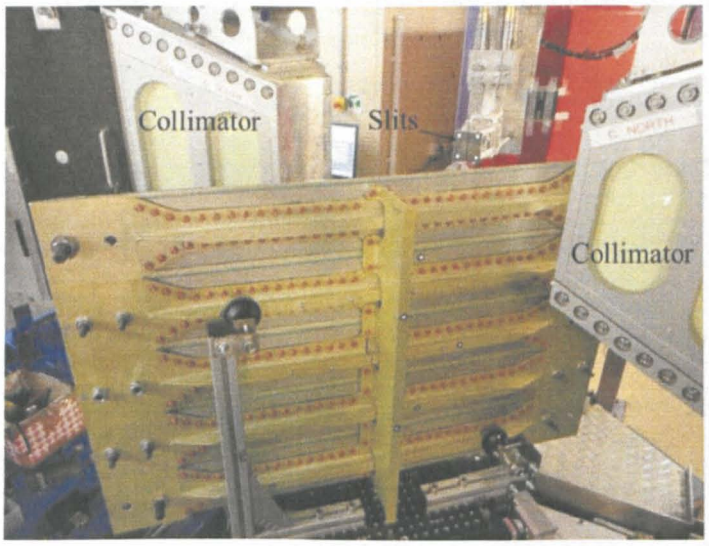

Figure 5.42: Experimental setup at ENGIN-X

At location 1, measurements were performed along the crack growth direction from the edge of the centre fastener of the rib towards the second stringer (y-direction) passing through the second fastener of the rib. The measurement location is shown in figure 5.41 where an EDM slot is also visible, which will act as a starting notch for the crack to grow. This measurement location contains all the structural parts present in the assembly.

5.4.3 Constant amplitude fatigue crack growth testing

The primary focus of this research is to investigate the fatigue durability of bonded crack retarders applied on different M(T) and SEN(T) specimens. It is important that the testing carried out should be repeatable with a standard procedure. For this, all the constant amplitude fatigue crack growth testing and data analysis was performed according to ASTM E647. Fatigue crack growth testing was performed on an MTS servo hydraulic test machine which has a static loading capacity of 200 kN and a dynamic loading capacity of 100kN. Crack length measurements were performed optically by using a scaled travelling microscope with an accuracy of ±0.01 mm. Crack length measurements were performed only on the non-reinforced side of the specimen as the crack growth on the reinforced is not visible due to the presence of the straps.

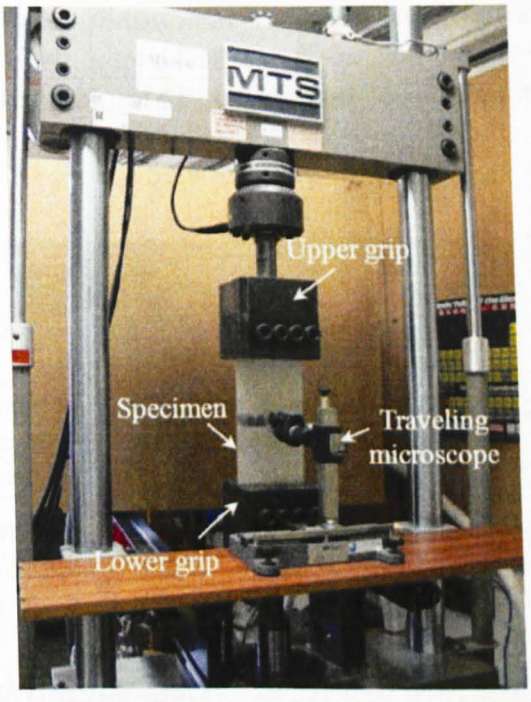

Figure 5.43: Experimental set-up for room temperature fatigue crack growth test

Figure 5.43 shows the experimental setup for a room temperature constant amplitude fatigue crack growth test. In order to ensure accurate crack length measurements, as recommended by ASTM-E647, the crack growth area on the substrate is polished to a mirror surface in order to measure the crack tip position precisely.

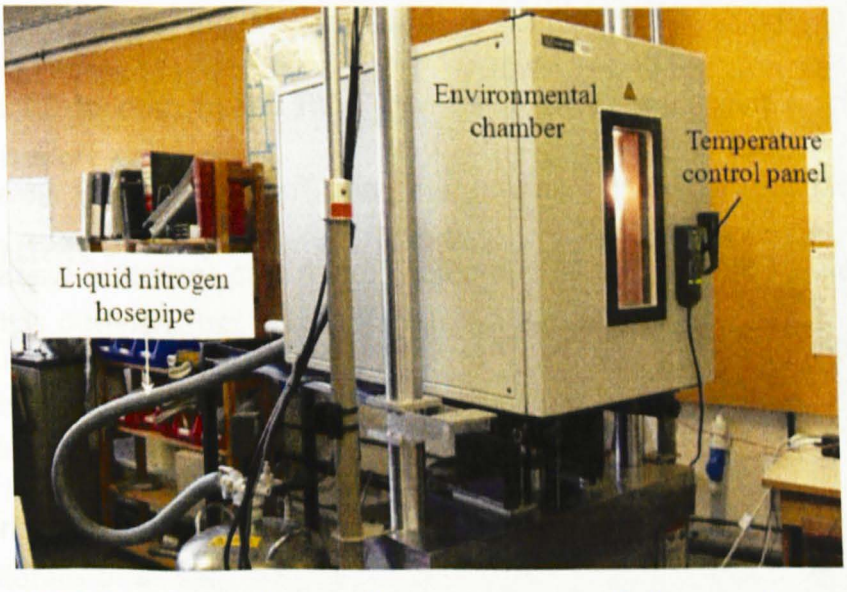

Figure 5.44: Experimental set-up for at temperature fatigue crack growth test

At temperature fatigue crack growth tests were performed using an Instron (3119-407) environmental chamber. The temperature of the specimen was monitored by using an N-type thermocouple attached at the center of the specimen with an accuracy of ±0.5°C on the specimen. Figure 5.44 shows the experimental setup for at temperature fatigue. The

temperature of the environmental chamber was monitored and controlled by a control panel mounted on the chamber. For tests at −60°C, liquid nitrogen was used as a cooling medium.

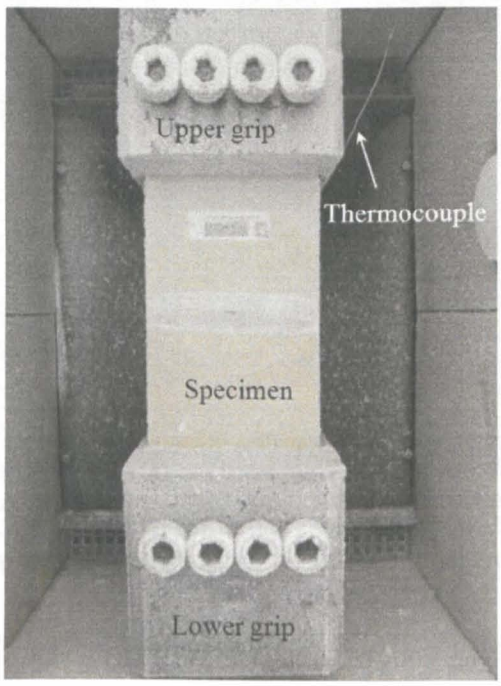

Figure 5.45: Specimen in the environmental chamber during fatigue crack growth test at −60°C

Figure.5.45 shows the specimen in the environmental chamber during fatigue crack growth tests at −60°C. All the constant amplitude fatigue crack growth tests were performed using a maximum stress of 60 MPa with a load ratio of 0.1 and at 10 Hz frequency. Table 5.6 shows the parameters used for fatigue crack growth tests on different coupon specimens. The fatigue crack growth test procedure was split into two phases. In the first phase pre-cracking of the specimen was carried out and in the second phase, crack growth was continuous until the specimen failed. According to fracture mechanics the specimen with a saw cut instead of a fatigue crack does not have a plastic wake field [40, 41]. In order to meet the fracture mechanics requirements according to ASTM E647, a pre-crack of length of 2 mm was initiated in each specimen. The pre-cracking was performed using the similar loading conditions used for crack growth measurements.

Specimen	Minimum load (kN)	Maximum load (kN)	Load ratio and frequency	K_{min} (MPa.mm$^{1/2}$)	K_{max} (MPa.mm$^{1/2}$)
M(T) without strap	4.2	42	0.1 and 10Hz	1.062	10.629
M(T) with strap	5.34	53.4	0.1 and 10Hz	1.062*	10.629*
SEN(T) without strap	4.2	42	0.1 and 10Hz	1.800*	18.009*
SEN(T) with strap	6.42	64.2	0.1 and 10Hz	1.800*	18.009*

* All the fatigue crack growth testing in this research was performed with constant stress. Therefore, maximum (60MPa) and minimum (6MPa) applied stresses (equal for both with and without strap specimens) and first crack length i.e. 10 mm were used to calculate the K_{max} and K_{min}.

Table 5.6: Test parameters used for constant amplitude fatigue crack growth test

In the first phase, once a pre-crack was achieved approximately 2 mm in the specimen, the number of fatigue cycles was recorded and the second phase was commenced. During the second phase, crack length measurements were recorded at intervals such that da/dN data are nearly evenly distributed with respect to ΔK. According to ASTM-E647, suggested intervals are

$$\Delta a \leq 0.03W \text{ for } 2a/W < 0.60$$

$$\Delta a \leq 0.02W \text{ for } 2a/W > 0.60$$

Where Δa is the change in crack length, W is the width of the specimen and $2a$ is the total crack length after pre-cracking.

5.5 Summary

This chapter has outlined the materials and the methodologies used to investigate the durability of bonded crack retarders. Also, characterisation of the materials used in the research has been discussed in detail. A brief description of sample preparation and the geometrical details of all the specimens used in this research are presented. In order to have repeatability, all the constant amplitude fatigue testing was performed according to ASTM standards. Overall, this chapter provides a sound understanding of the sample materials, preparation, experimental procedures for both residual stress measurements and constant amplitude fatigue crack growth testing and the data analysis.

5.6 References

[1]. ASM handbook, Properties, and selection: Non-ferrous alloys and special-purpose materials, Volume 2. ASM International, 1990

[2]. *http://www.alcoa.com/mill_products/catalog/pdf/alloy2024techsheet.pdf*, Accessed on 15th March, 2014.

[3]. *http://www.cemselectorguide.com/pdf/FM_94_032910.pdf*, Accessed on 18th April, 2013.

[4]. M. E. Fitzpatrick, A. Lodini, *Analysis of Residual Stress by Diffraction using Neutron and Synchrotron Radiation*. CRC Press, 2003.

[5]. G. F. Vander Voort, *Metallography, Principles, and Practice* (Google eBook). ASM International, 1984.

[6]. *ASM handbook, Metallography and Microstructures*. ASM International, 1992.

[7]. O. Engler and V. Randle, *Introduction to Texture Analysis: Macrotexture, Microtexture, and Orientation Mapping*, Second Edition (Google eBook). CRC Press, 2009.

[8]. X. Zhang and Y. Li, *Damage Tolerance and Fail Safety of Welded Aircraft Wing Panels*, AIAA Journal, vol. 43, no. 7, pp. 1613-1623, 2005.

[9]. Len Reid, *Sustaining an Aging Aircraft Fleet with Practical Life Enhancement Methods*, Paper presented at the Meeting on Life Management Techniques for Ageing Air Vehicles, and published in RTO-MP-079 (II), Manchester, United Kingdom, 2011.

[10]. X. Zhang, *Fatigue life improvement in fatigue-aged fastener holes using the cold expansion technique*, International Journal of Fatigue, vol. 25, no. 9-11, pp. 1249-1257, 2003.

[11]. Len Reid, *Enhanced repair durability with cold expansion techniques*, 41st International SAMPE Symposium, pp. 951–961. 1986.

[12]. D. Stefanescu, *Measurement and prediction of fatigue crack growth from cold expanded holes Part 2: Prediction of fatigue crack growth from cold expanded holes*, The Journal of Strain Analysis for Engineering Design, vol. 39, no. 1, pp. 41-52, 2004.

[13]. J. M. Mínguez and J. Vogwell, *Fatigue life of an aerospace aluminium alloy subjected to cold expansion and a cyclic temperature regime*, Engineering Failure Analysis, vol. 13, no. 6, pp. 997-1004, 2006.

[14]. V. Lacarac, D. Smith, M. Pavier, and M. Priest, *Fatigue crack growth from plain and cold expanded holes in aluminium alloys*, International Journal of Fatigue, vol. 22, pp. 189-203, 2000.

[15]. V. Lacarac, *Prediction of the growth rate for fatigue cracks emanating from cold expanded holes*, International Journal of Fatigue, vol. 26, no. 6, pp. 585-595, 2004.

[16]. T. N. Chakherlou, Y. Alvandi-Tabrizi, and a. Kiani, *On the fatigue behavior of cold expanded fastener holes subjected to bolt tightening*, International Journal of Fatigue, vol. 33, no. 6, pp. 800-810, 2011.

[17]. S. Pasta, *Fatigue crack propagation from a cold-worked hole*, Engineering Fracture Mechanics, vol. 74, no. 9, pp. 1525-1538, 2007.

[18]. B. Nadri, L. Edwards, M. E. Fitzpatrick, and A. Lodini, *Analysis of Residual Stresses Following Overloading of Cold Expanded Holes Using the X-ray Diffraction Technique and Finite Element Method*, Journal of Neutron Research, vol. 12, no. 1-3, pp. 219-224, 2004.

[19]. J. Liu, X. J. Shao, Y. S. Liu, and Z. F. Yue, *Effect of cold expansion on fatigue performance of open holes*, Materials Science and Engineering: A, vol. 477, no. 1-2, pp. 271-276, 2008.

[20]. Y. Zhang, M. E. Fitzpatrick, and L. Edwards, *Analysis of the Residual Stress around a Cold-expanded Fastener Hole in a Finite Plate*, Strain, vol. 41, no. 2, pp. 59-70, 2005.

[21]. D. Ball and D. Lowry, *Experimental investigation on the effects of cold expansion of fastener holes*, Fatigue and Fracture of Engineering Materials and Structures, vol. 21, no. 1, pp. 17-34, 1998.

[22]. M. S. Rana, C. Makabe, and G. Fujiwara, *The effect of hole shape on the extent of fatigue life improvement by cold expansions*, Engineering Failure Analysis, vol. 16, no. 7, pp. 2081-2090, 2009.

[23]. G. Clark, *Modelling residual stresses and fatigue crack growth at cold-expanded fastener holes*, Fatigue and Fracture of Engineering Materials and Structures, vol. 14, no. 5, pp. 579-589, 1991.

[24]. R. A. Pell, P. W. Beaver, J. Y. Mann, and J. G. Sparrow, *Fatigue of thick-section cold-expanded holes with and without cracks*, Fatigue and Fracture of Engineering Materials and Structures, vol. 12, no. 6, pp. 553-567, 1989.

[25]. M. Pavier, C. Poussard, and D. Smith, *Finite element modelling of the interaction of residual stress with mechanical load for a crack emanating from a cold worked fastener hole*, Journal of strain analysis for engineering design, vol. 33, no. 4, pp. 275-289, 1998.

[26]. *http://www.fatiguetech.com/coldEX_Split_sleeve.html*, Accessed on 20th March, 2014.

[27]. V. Lacarac, D. Smith, and M. Pavier, *The effect of cold expansion on fatigue crack growth from open holes at room and high temperature*, International Journal of Fatigue, vol. 23, pp. 161-170, 2001.

[28]. T. Ozdemir and L. Edwards, *Through-Thickness Residual Stress Distribution After the Cold Expansion of Fastener Holes and Its Effect on Fracturing*, Journal of Engineering Materials and Technology, vol. 126, no. 1, p. 129-135, 2004.

[29]. J. L. Phillips, *Sleeve Cold working Fastener Holes*, Vol. I, Air Force Materials Laboratory report AFML-TR-74-10, 1974.

[30]. A. Vlot, *Impact loading on fibre metal laminates*, International Journal of Impact Engineering, vol. 18, no. 3, pp. 291-307, 1996.

[31]. M. Sadighi, R. C. Alderliesten, and R. Benedictus, *Impact resistance of fiber-metal laminates: A review*, International Journal of Impact Engineering, vol. 49, pp. 77-90, 2012.

[32]. A. Vlot, *Low velocity impact loading on fiber reinforced aluminium laminates (Arall and Glare) and other aircraft sheet materials*. Report number-LR-718, Delft University of Technology, The Netherlands, 1993.

[33]. J. D. Minford, *Handbook of Aluminum Bonding Technology and Data*. CRC Press, 1993.

[34]. S. Andrzej and S. Malgorzata, *Riveted Lap Joints in Aircraft Fuselage: Design, Analysis and Properties* (Google eBook). Springer, 2012.

[35]. E. J. Ripling, S. Mostovoy, and H. T. Corten, *Fracture Mechanics: A Tool for Evaluating Structural Adhesives*, The Journal of Adhesion, vol. 3, no. 2, pp. 107-123, 1971.

[36]. S. Mostovoy, E. J. Ripling, and C. F. Bersch, *Fracture Toughness of Adhesive Joints*, The Journal of Adhesion, vol. 3, no. 2, pp. 125-144, 1971.

[37]. *ASTM D3433-99, Standard Test Method for Fracture Strength in Cleavage of Adhesives in Bonded Metal Joints*, 2012.

[38]. *ASTM D5528-94a Standard Test Method for Mode I Interlaminar Fracture Toughness of Unidirectional Fiber Reinforced Polymer Matrix Composites*, 2007.

[39]. *BS 7991:2001-Determination of the mode I adhesive fracture energy, GIC, of structural adhesives using the double cantilever beam (DCB) and tapered double cantilever beam (TDCB) specimens,"* 2001.

[40]. T. L. Anderson, *Fracture Mechanics: Fundamentals and Applications*, Third Edition. CRC Press, 2005.

[41]. J. Schijve, *Fatigue of Structures and Materials*, 2nd edition. Springer, 2009.

Chapter 6 : Residual stress measurements

In previous chapters, residual stress, residual stress measurement techniques, and the specimens used for residual stress measurements were discussed in detail. In this chapter, the extensive research performed on the thermal residual stresses that arise from GLARE bonding on to the different coupon specimens will be presented. Thermal residual stresses arise from the coefficient of thermal expansion difference between the substrate and the adhesive. These stresses can have a deleterious effect on the performance of the strap. Hence, quantification of these stresses is essential to improve the fatigue life of reinforced structures and thereby the damage tolerance of aircraft.

6.1 Residual stress measurements on cold expanded and bolted hole specimens

Residual stress measurements were performed at SALSA, ILL, and ENGIN-X, ISIS. The experimental procedure and measurement locations are described in detail in chapter 5. The data obtained were analysed in depth and the thermal residual stresses induced in the specimen with a strap at drilled hole are shown in figure 6.1.

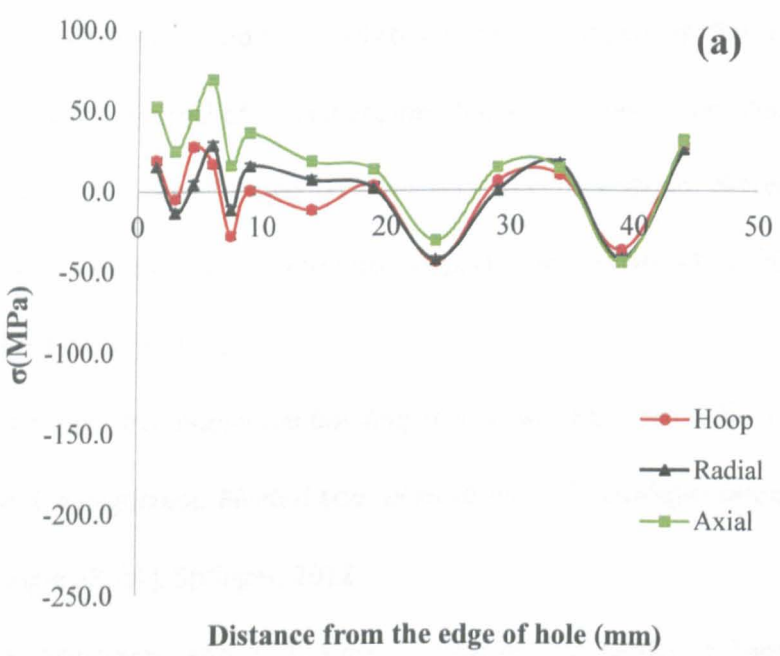

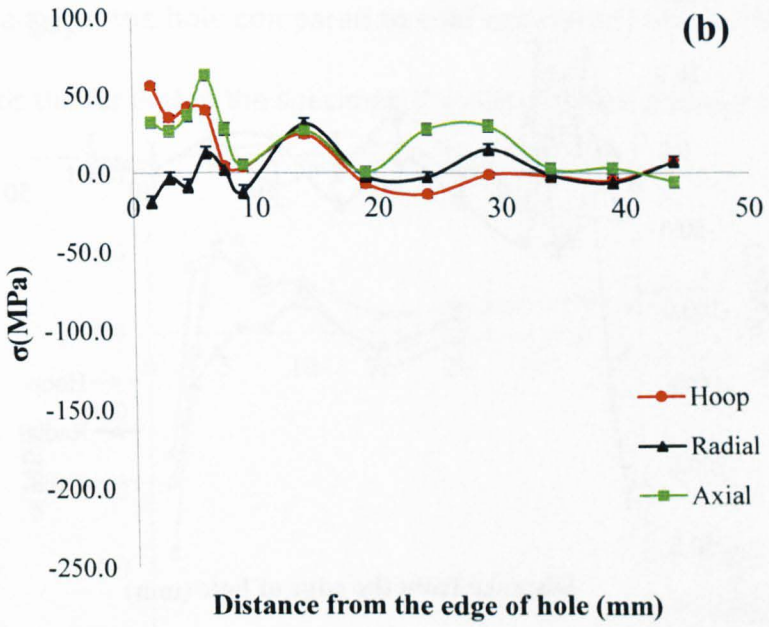

Figure 6.1: Residual stresses at drilled hole with strap specimen at (a) z = 1.5 and (b) z = 3.5

From figure 6.1 it can be seen that the measurements performed under the strap area show tensile stresses up to 50 MPa. There is no significant variation in stresses through the thickness. The small scatter in the measurement might be attributed to the texture and directional micro-stress in the material as a consequence of which the noise to signal ratio will be high. Also, the adhesive layers present in the complete assembly contain hydrogen, which causes inelastic scattering of the neutrons and results in fewer neutrons collected by the detector and higher scatter in the measurements.

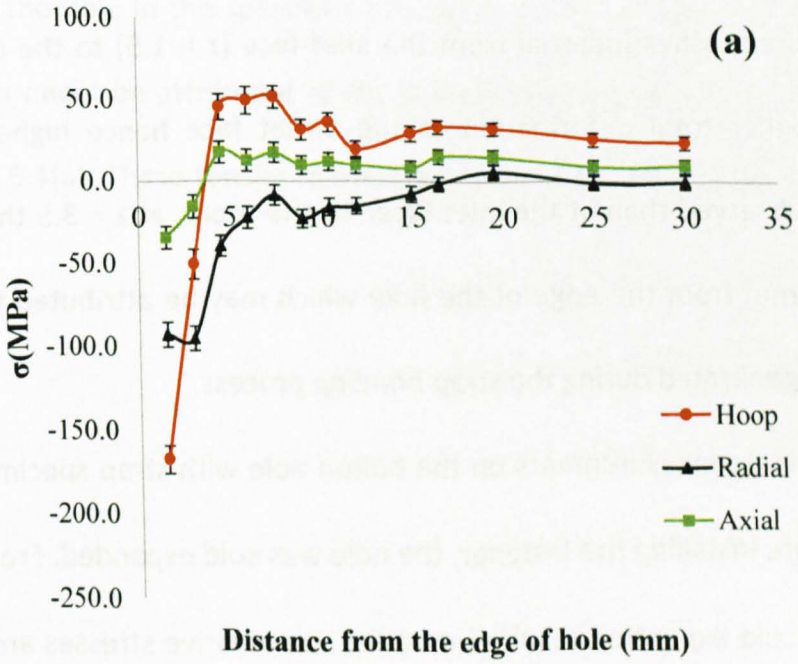

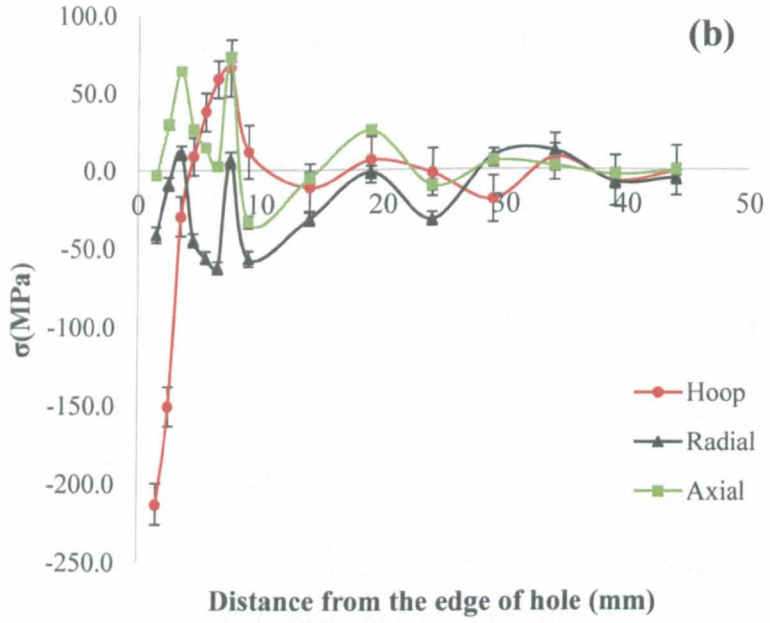

Figure 6.2: Residual stresses at cold expanded hole with strap specimen at (a) z = 1.5 and (b) z = 3.5

Residual stress measurements on the cold expanded hole with strap specimen are shown in figure 6.2. The cold expansion resulted in radial compressive stresses around the hole up to 3-4 mm from the edge of the hole. As the measurements progressed towards the far end of the specimen the compressive stresses diminish. Thermal residual stresses do not have a significant effect on the cold expansion stresses.

Measurements performed at z = 3.5 mm show higher compressive stresses at the edge of the hole compared to z = 1.5 mm. This is attributed to the cold expansion process where the mandrel pushes material from the inlet face (z = 1.5) to the outlet face (z = 3.5): there is higher total deformation at the outlet face hence higher compressive stresses can be observed than at the inlet face. Furthermore, at z = 3.5 there are tensile stresses at 5-10 mm from the edge of the hole which may be attributed to the thermal residual stresses generated during the strap bonding process.

Residual stress measurements on the bolted hole with strap specimen are shown in figure 6.3. Before installing the fastener, the hole was cold expanded. From figure 6.3 it can be seen that cold expansion resulted in radial compressive stresses around the hole up to 4 mm from the edge of the hole. There is no significant variation of bolted hole

stresses at the edge of the hole compared to cold expanded hole. As the measurements progress towards the far end of the specimen the compressive stresses diminish.

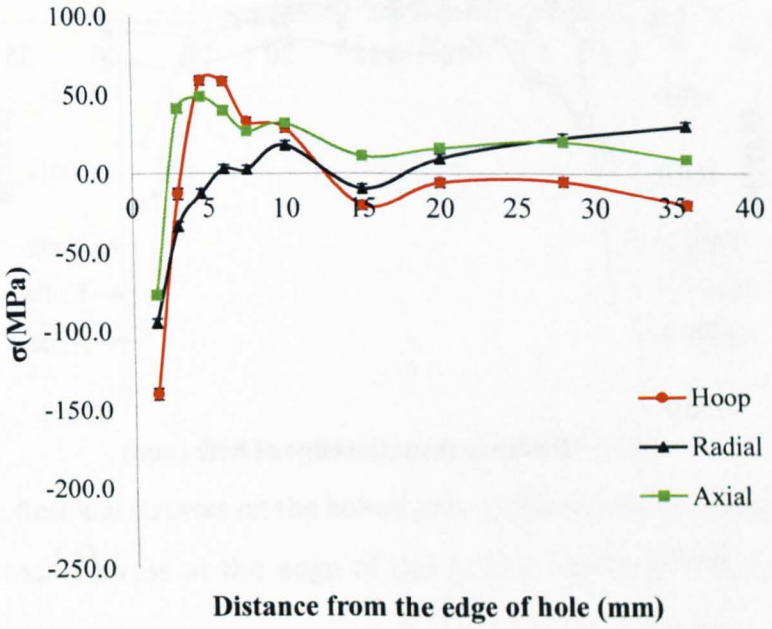

Figure 6.3: Residual stresses at bolted hole with strap specimen at z = 1.5

Figure 6.4 shows the evolution of the residual stresses for a cold expanded hole without strap at z = 1.5 and 3.5 mm. Cold expansion resulted in radial compressive stresses around the hole, being higher at the cold expanded mandrel outlet face (z = 3.5) compared to the inlet face (z = 1.5). There is no significant variation in the cold expansion stresses of the specimens with and without strap. However, measurements performed remotely from the hole in the specimen with strap showed small tensile stresses under the strap which might be attributed to the stresses developed during the strap bonding process, figure 6.4(a). These tensile stresses were not observed in the specimen without strap.

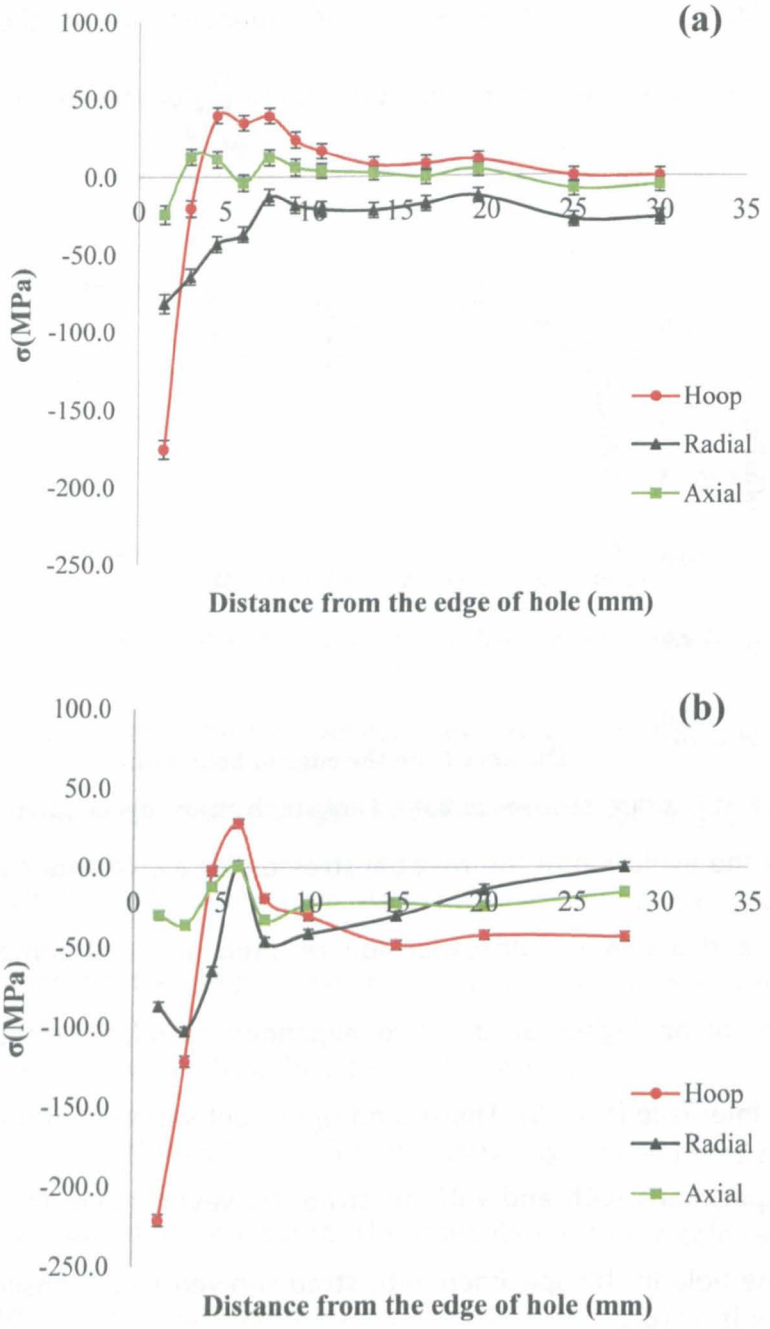

Figure 6.4: Residual stresses on the cold expanded hole without strap specimen at (a) z = 1.5 and (b) z = 3.5

Residual stresses at the bolted hole without strap specimen are shown in figure 6.5. Before installing the fastener, the hole was cold expanded. Radial compressive stresses resulting from the cold expansion can be observed around the hole up to 5 mm from the edge of the hole.

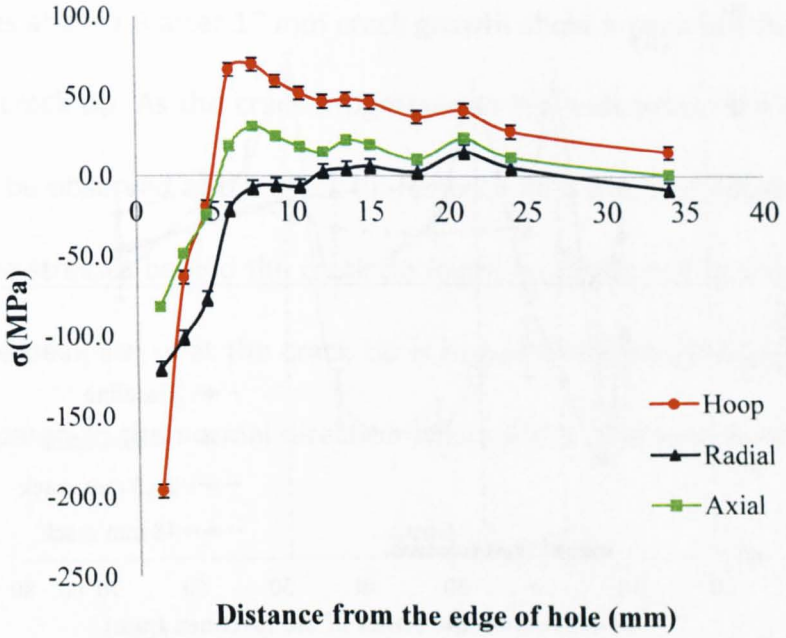

Figure 6.5: Residual stresses on the bolted hole without strap specimen at z = 1.5

The peak compressive stress at the edge of the hole is higher for the specimen without strap. This might be attributed to the effect of additional compressive stresses developed during the fastener installation, whereas there was no effect of fastener stresses observed in the specimen with a strap. As the measurements progressed towards the edge of the specimen compressive stresses are seen to diminish and balancing tensile stresses are observed.

6.2 Residual stress measurements on M(T) specimen

The measurements were performed at ENGIN-X, ISIS and the experimental details are given in chapter 5. Figure 6.6 and figure 6.7 shows the residual stress measurements at different crack lengths in the M(T) specimen at z = 1.5 and 3.5 mm respectively. The crack tip locations are marked in vertical dashed lines, in red for 17 mm, in black for 26.5 mm and in blue for 48 mm crack lengths respectively. Baseline measurements performed at two different thickness locations shows that residual stresses from the strap bonding process are tensile in nature and relatively low (20 MPa) and there is little variation in the stresses across the specimen.

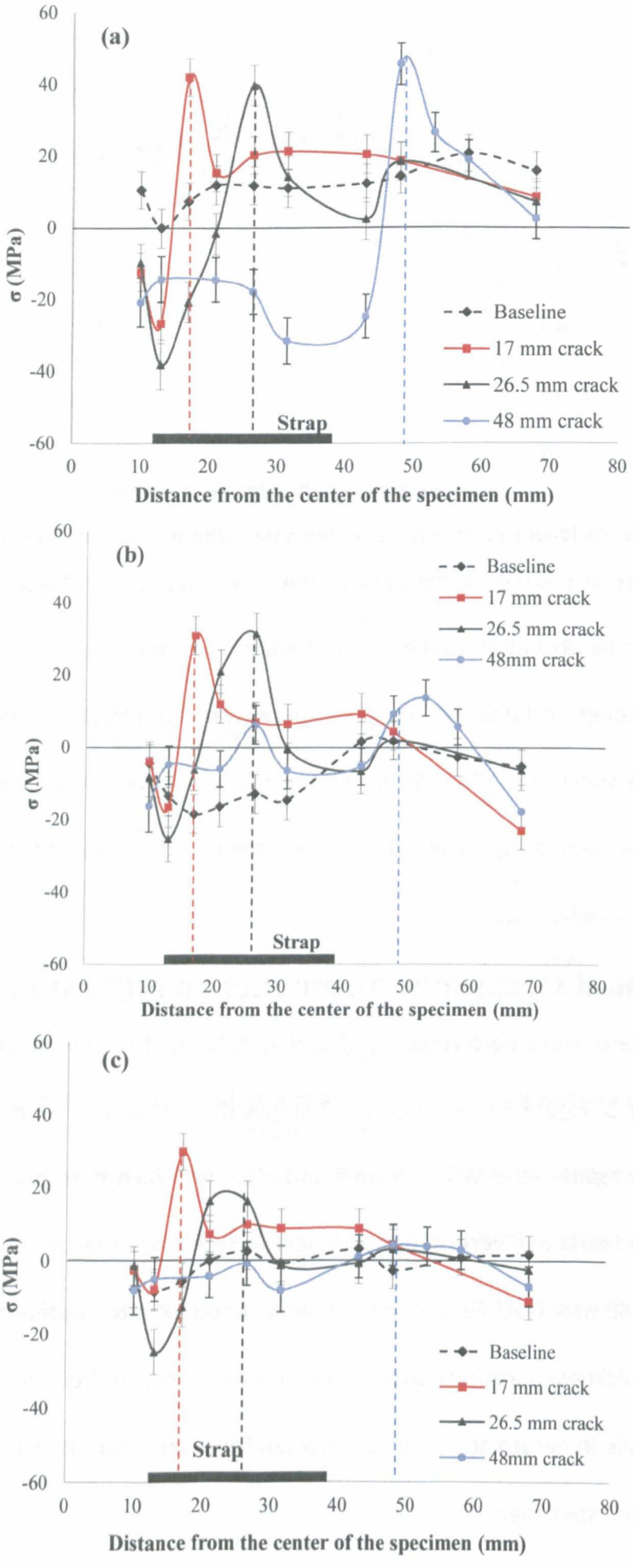

Figure 6.6: Residual stress measurements on the M(T) specimen at z = 1.5 mm (a) longitudinal (b) transverse and (c) normal direction

Residual stresses at z = 1.5 after 17 mm crack growth show a peak tensile stress of about 40 MPa at the crack tip. As the crack progressed in the y-direction the peak stress also moves and can be observed at the crack tip for both 26.5 mm and 40 mm crack lengths. The compressive stresses behind the crack tip might be attributed to crack closure in the crack wake. The peak stress at the crack tip is higher in the longitudinal and transverse directions compared to the normal direction because the specimen is not constrained in this direction.

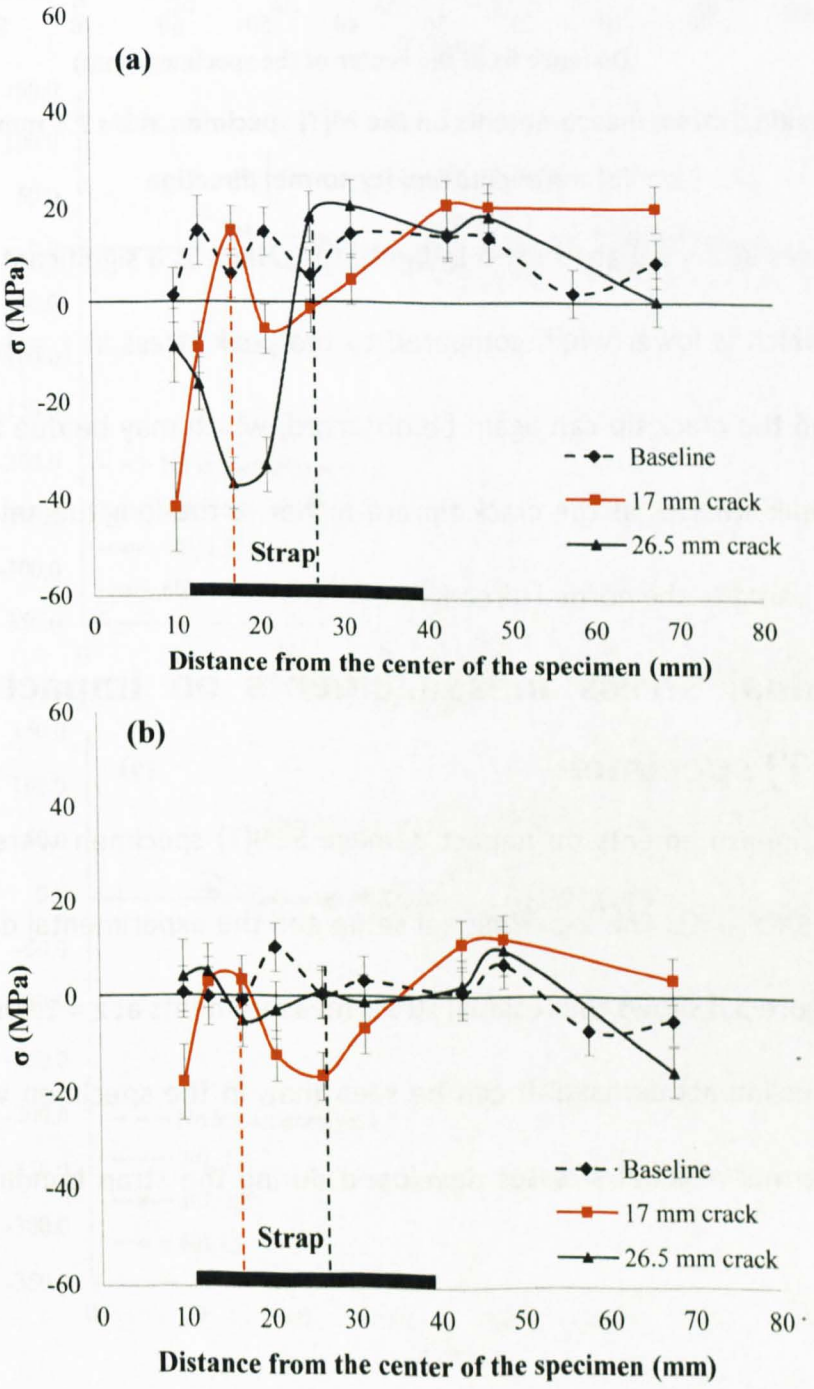

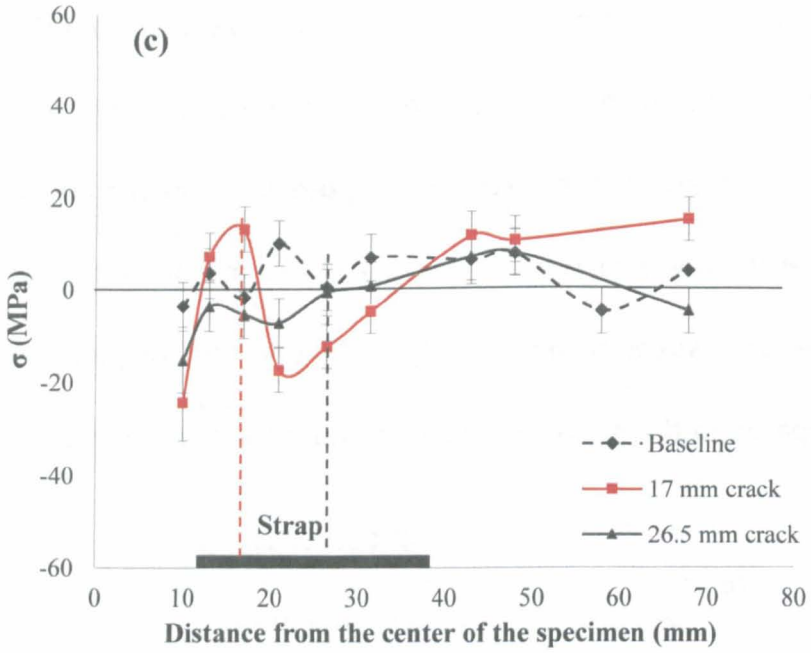

Figure 6.7: Residual stress measurements on the M(T) specimen at z = 3.5 mm (a) longitudinal (b) transverse and (c) normal direction

Residual stresses at z = 3.5 are shown in figure 6.7. There is a significant variation in the peak stress, which is lower when compared to the peak stress at z = 1.5. Compressive stresses behind the crack tip can again be observed, which may be due to crack closure effects. The peak stresses at the crack tip are higher in the longitudinal and transverse directions compared to the normal direction.

6.3 Residual stress measurements on impact damaged SEN(T) specimen

Residual stress measurements on impact damage SEN(T) specimen were performed at POLDI, PSI and SALSA, ILL. The experimental setup and the experimental details are given in chapter 5. Figure 6.8 shows the residual stress measurements at z = 1.5 in the specimen with and without impact damage. It can be seen that, in the specimen without impact damage the thermal residual stresses developed during the strap bonding process are relatively low.

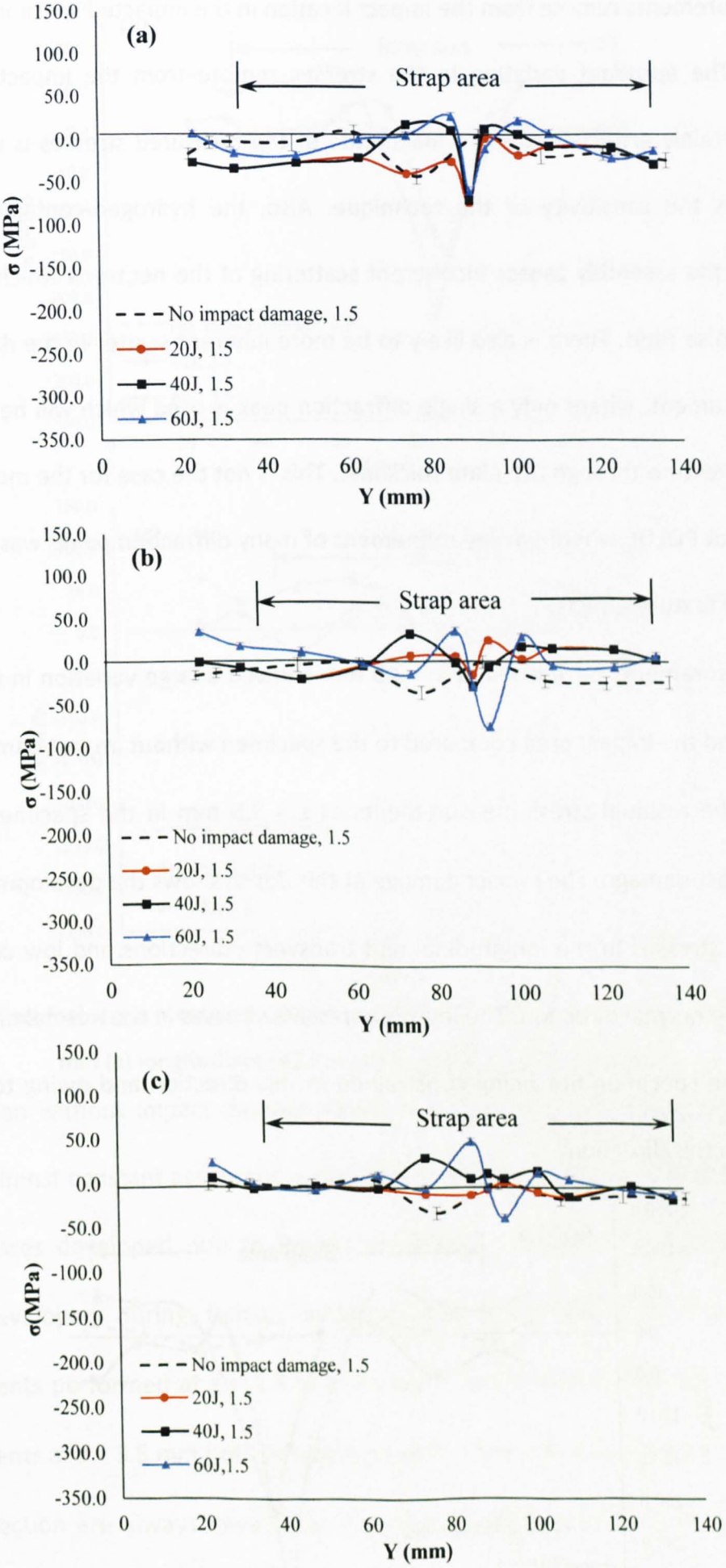

Figure 6.8: Residual stress measurements on baseline and impact damage specimen at z = 1.5 mm (a) longitudinal (b) transverse and (c) normal direction

The measurements remote from the impact location in the impacted specimens show low stresses. The apparent variation in the stresses remote from the impact locations is almost certainly artificial since the magnitude of the measured stresses is very low and approaches the sensitivity of the technique. Also, the hydrogen-containing adhesive present in the assembly causes incoherent scattering of the neutrons which impairs the signal-to-noise ratio. There is also likely to be more inherent scatter in the data from the SALSA instrument, where only a single diffraction peak is used which will be sensitive to changes in texture through the plate thickness. This is not the case for the measurements performed at POLDI, where Pawley refinement of many diffraction peaks was used which reduces any texture effects.

Measurements performed at z = 3.5 mm showed a large variation in the stresses at and around the impact area compared to the specimen without impact damage. Figure 6.9 shows the residual stress measurements at z = 3.5 mm in the specimen with and without impact damage. The impact damage at this depth shows the development of high compressive stresses in the longitudinal and transverse directions and low compressive stresses in the normal direction. The low compressive stresses in the normal direction are a result of the specimen not being constrained in this direction and owing to Poisson's contraction in this direction.

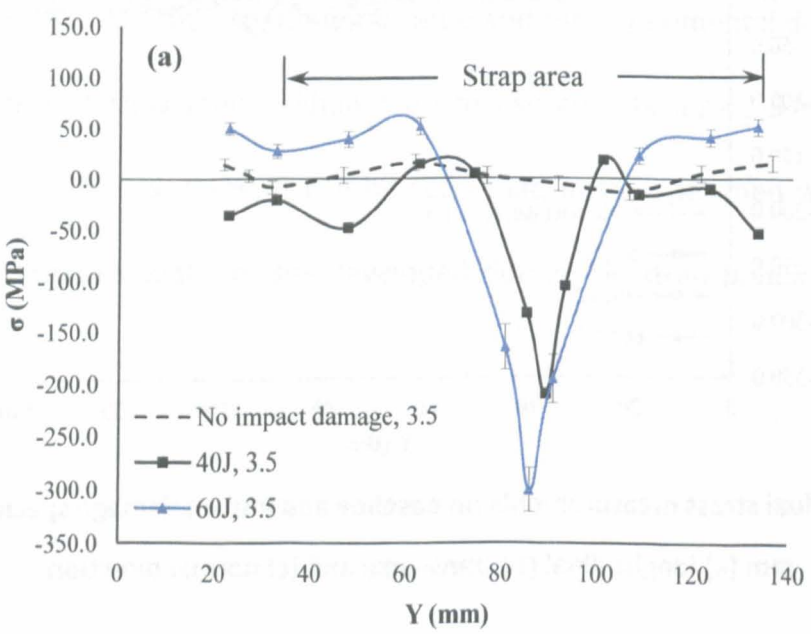

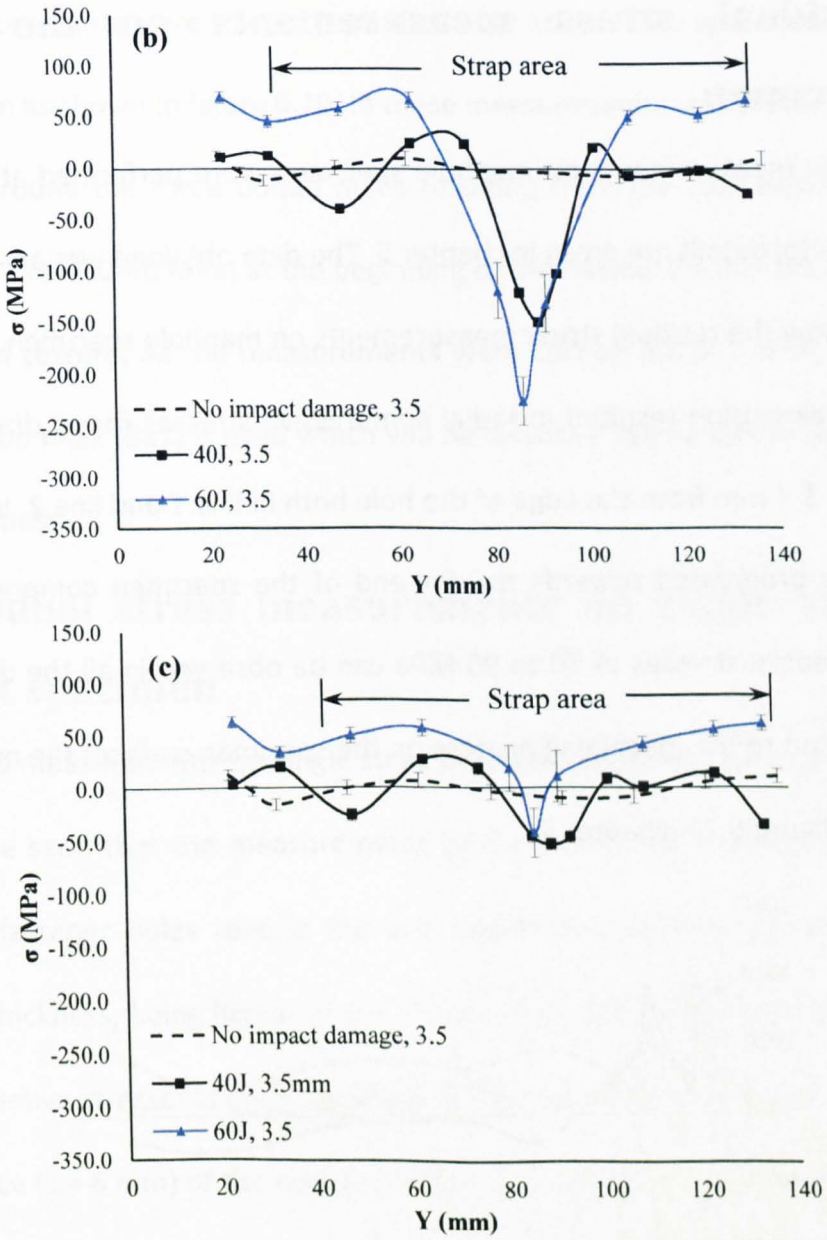

Figure 6.9: Residual stress measurements on baseline and impact damage specimen at z = 3.5 mm (a) longitudinal, (b) transverse and (c) normal direction

The specimen without impact damage shows very low stresses through the thickness which are almost constant across the width of the specimen. There is significant variation in the stresses developed due to impact at different energies. Compressive residual stresses developed during impact increase with the increase in impact energy. Measurements performed at z = 1.5 mm results in low stresses when compared to the measurements at z = 3.5 mm both in longitudinal and transverse direction. Stresses in the normal direction are always lower than the stresses in the longitudinal and transverse directions.

6.4 Residual stress measurements on the manhole specimen

Residual stress measurements on manhole specimen were performed at ENGIN-X, ISIS. The experimental details are given in chapter 5. The data obtained was analysed in depth. Figure 6.10 show the residual stress measurements on manhole specimen. It can be seen that the cold expansion resulted in radial compressive stresses (hoop direction) around the hole up to 3-4 mm from the edge of the hole both in line 1 and line 2. In line 1, as the measurements progressed towards the far end of the specimen compressive stresses diminish and tensile stresses of 50 to 90 MPa can be observed in all the directions. This may be attributed to the machining process on the specimen surface: the machining lines can be seen in figure 5.21, chapter 5.

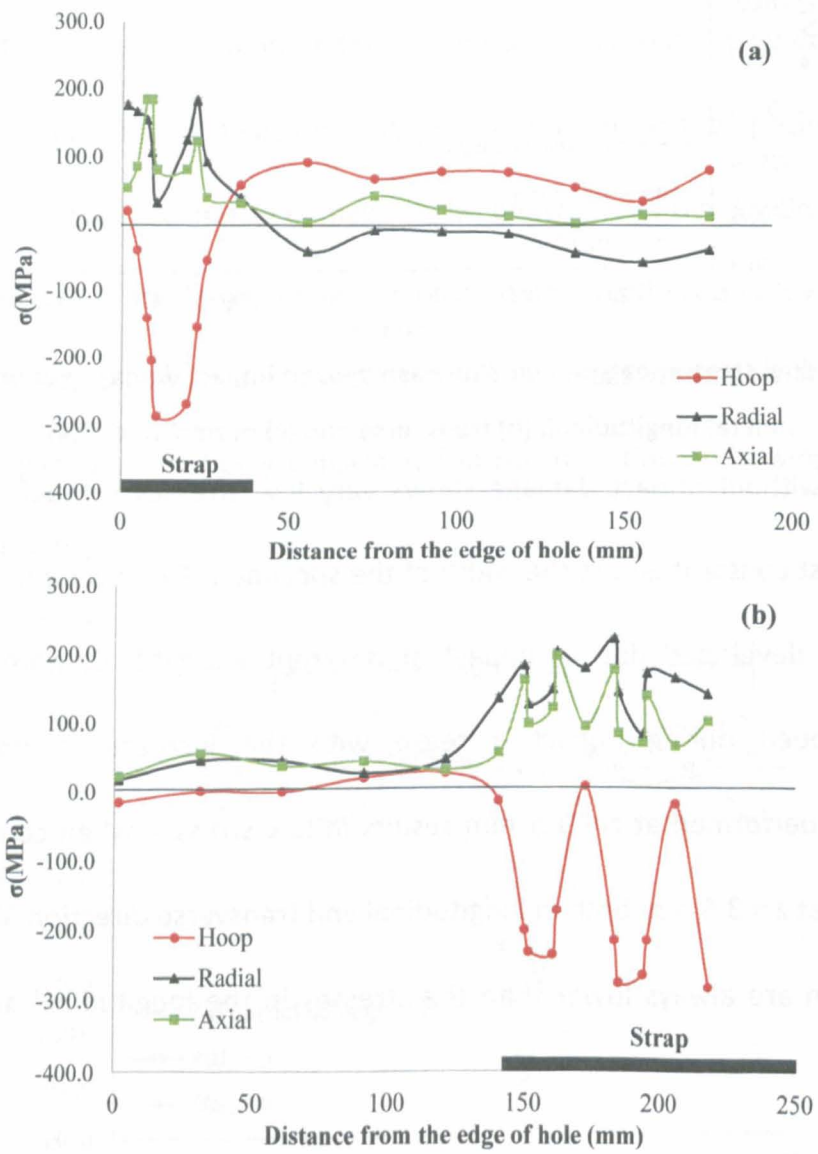

Figure 6.10: Residual stress measurements on manhole specimen (a) line 1 and (b) line 2

In line 2, measurements were started from the lower edge of the specimen to the centre of the specimen as shown in figure 6.10. In these measurements compressive stresses can be observed around the three bolted holes resulting from the cold expansion process. The tensile stresses (30-40 MPa) at the beginning of the measurements may be attributed to the material texture. As the measurements were carried out at SALSA, where only a single diffraction peak (311) is used which will be sensitive to changes in texture through the plate thickness.

6.5 Residual stress measurements on single strap butt-joint specimen

Residual stress measurements on single strap butt-joint specimen are presented in figure 6.11. It can be seen that the measurements performed in the hoop direction near the edge of the fastener holes reveals the cold expansion residual stresses which varies through the thickness, being higher at z = 2.5 mm from the reinforced side. This variation in the compressive stresses is corresponding to the variation from the outlet (z = 2.5 mm) & the inlet face (z = 6 mm) of the cold expanded tool. Measurements performed remotely from the fastener holes result in very low stresses and are fairly constant.

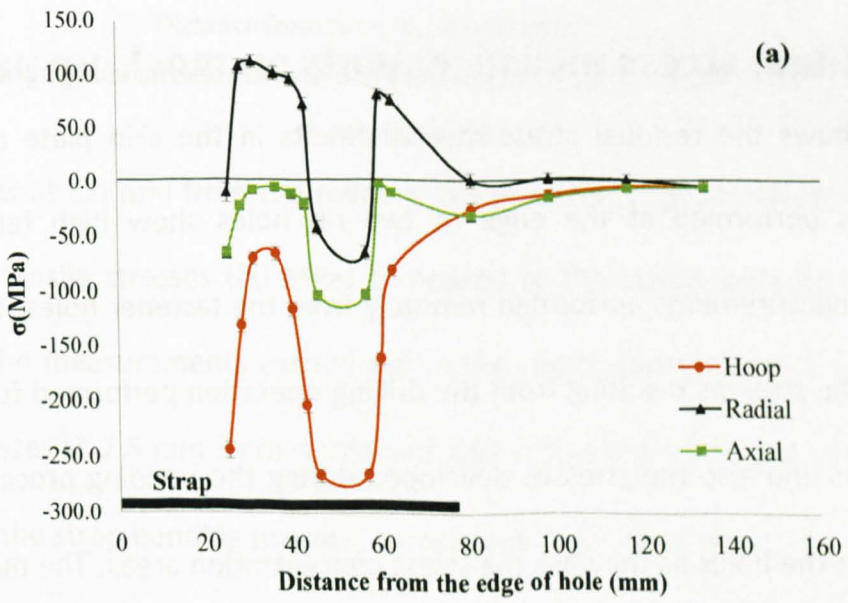

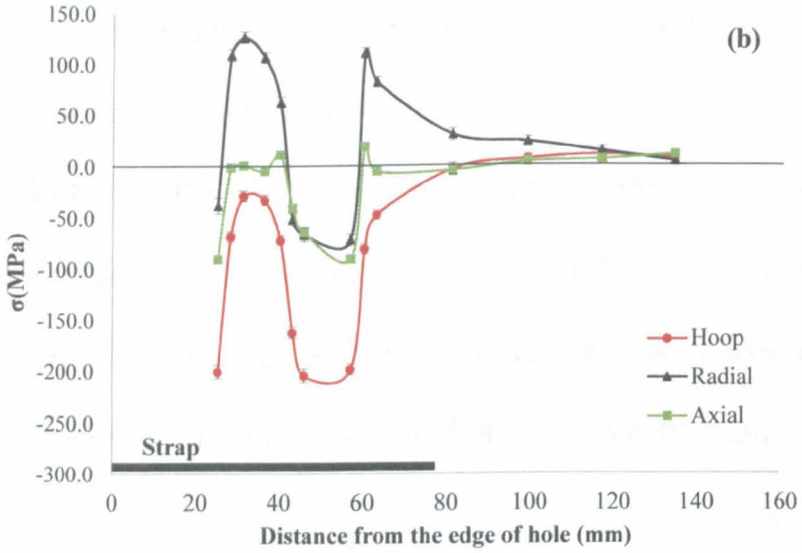

Figure 6.11: Residual stress measurements in the single strap butt joint, skin plate (a) z = 2.5 mm and (b) z = 6 mm from reinforced side

Measurements performed near the edge of the fastener in the radial direction show lower compressive stresses. As measurements progress in the y-direction, tensile stresses can be observed which are dominant in the radial direction and reach a maximum value of 125 MPa at 31 mm from the edge of the plate. Furthermore, as the measurements progress in the radial direction towards the far field from the fastener hole, tensile stresses can be observed reaching approximately 30 MPa at z = 2.5 mm. This might be attributed to the stresses generated due to the strap bonding. In contrast, very low tensile stresses were observed at z = 6.5 mm.

6.6 Residual stress measurements on mock-up panel

Figure 6.12 shows the residual stress measurements in the skin plate at location 1. Measurements performed at the edge of two rib holes show high tensile stresses compared to measurements performed remotely from the fastener holes. This might be attributed to the stresses resulting from the drilling operation performed for installation of the fasteners and also the stresses developed during the bonding process which are concentrated at the holes as they are the stress concentration areas. The measurements performed in between the holes and towards the second stringer show low tensile stresses, which resulted from the strap bonding process.

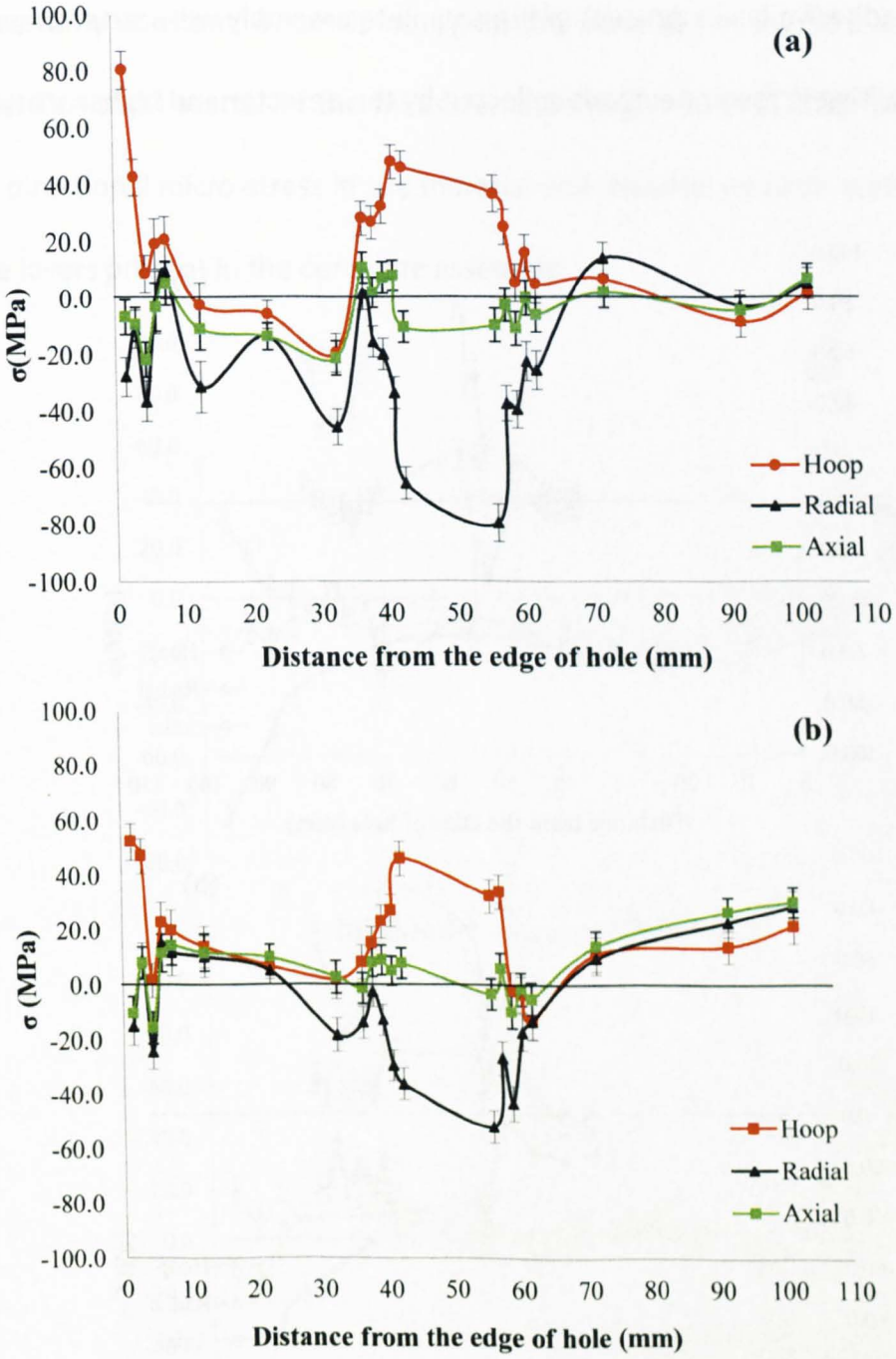

Figure 6.12: Residual stresses in skin plate at location 1 (a) 1. 5 mm and (b) 2.5 mm from reinforced side

Measurements at 1.5 mm from the reinforced side at the edge of the first fastener hole show higher tensile stresses (80 MPa) compared to the measurements at 2.5 mm (60 MPa). Also, the measurements carried out in the radial direction at 1.5 mm are higher than the stresses at 2.5 mm from reinforced side. This variation in the stresses might be attributed to the strap bonding process, being higher near the strap.

The small scatter in the measurement might be attributed to the degree of texture and directional micro-stress in the material due to which the noise to signal ratio will be

high. Also, the adhesive layers present in the complete assembly will scatter the neutrons inelastically resulting in fewer neutrons collected by the detector and higher scatter in the measurements.

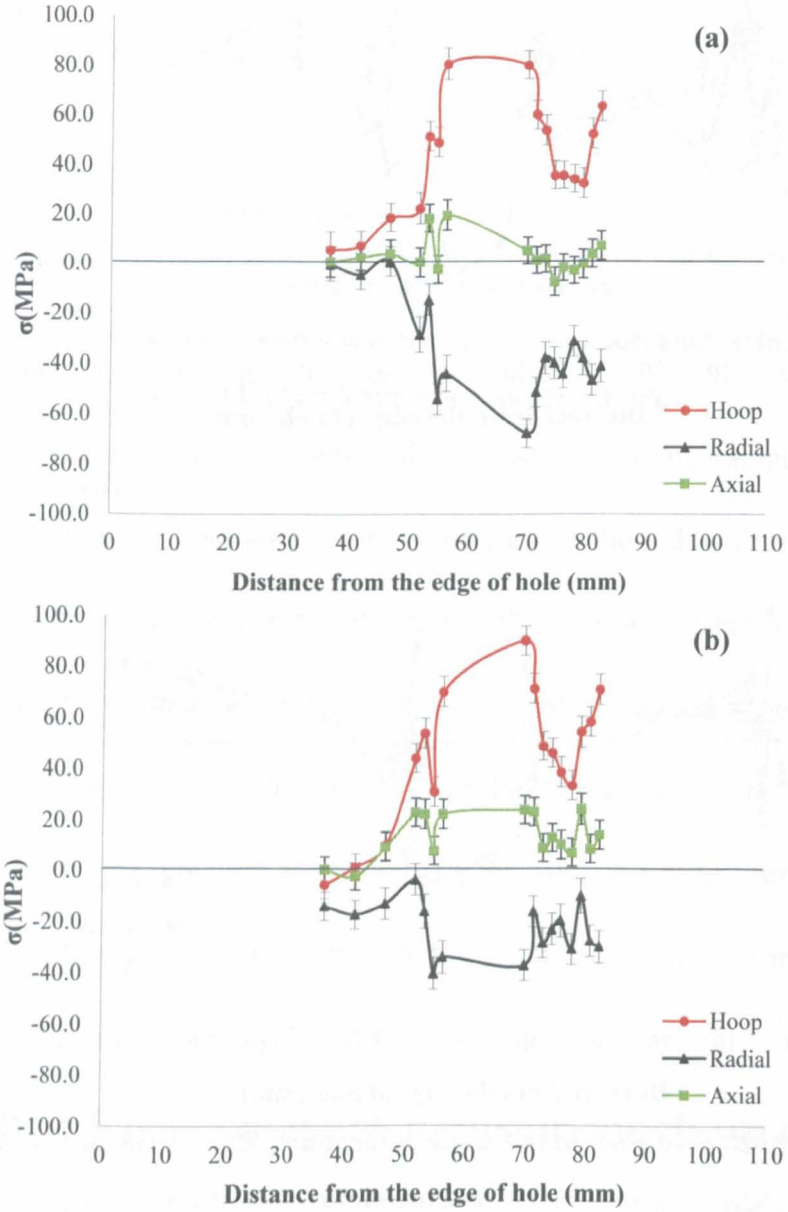

Figure 6.13: Residual stresses in skin plate at location 2 (a) 1. 5 mm and (b) 2.5 mm from reinforced side

Residual stress measurements in the skin plate at location 2 are shown in figure 6.13. Measurements were performed in the x-direction along the centre stringer as shown in figure 5.41, chapter 5. From figure 6.13, high tensile stresses (approximately 80 MPa) can be observed at the edge of the fastener holes in the measurements at thickness 1.5 and 2.5 mm from the reinforced side. Measurements performed remotely from the fastener holes (between 30 to 50 mm in figure 6.13), near the EDM slot, show very low stresses

which are fairly constant. There is no significant variation in the stresses through the thickness. The small scatter in the measurements might be attributed to the degree of texture, directional micro-stress in the material and inelastic neutron scattering from the adhesive layers present in the complete assembly.

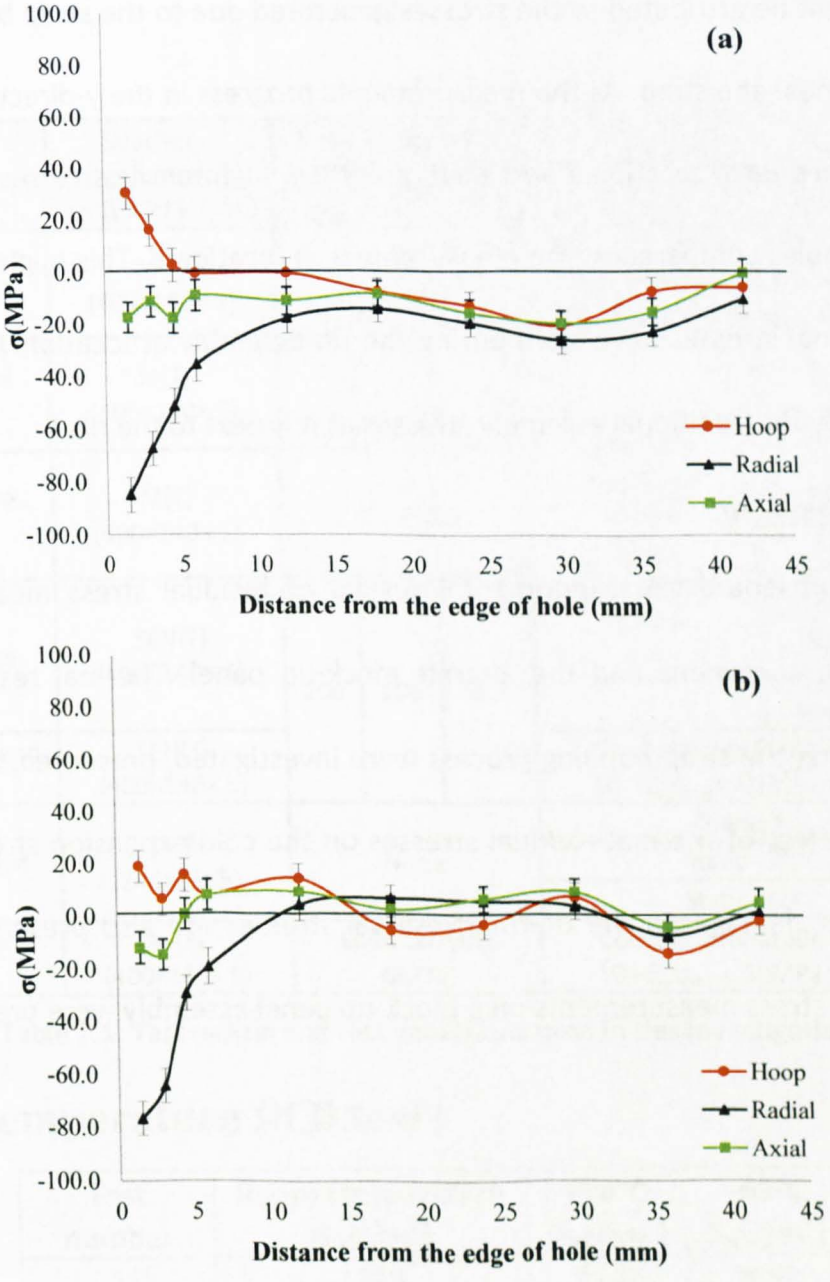

Figure 6.14: Residual stresses in the skin plate at location 3 (a) 1. 5 mm and (b) 2.5 mm from reinforced side

Figure 6.14 shows the residual stress measurements in the skin plate at location 3. The measurements were performed starting from the edge of the fastener in the centre stringer, and progressed towards the edge of the next stringer. Similar to the measurements at location 1 and 2, tensile stresses can be observed at the edge of the

fastener hole. Tensile stresses can be observed in the hoop direction and compressive stress in the radial direction, whereas the axial stresses are very low and fairly constant. Measurements performed at the edge of the fastener hole, at 2.5 mm from the reinforced side, showed lower tensile stresses compared to the measurements at 1.5 mm. This might be attributed to the stresses generated due to the strap bonding process being higher near the strap. As the measurements progress in the y-direction, the tensile stresses reaches zero. Location 1 and location 2 show high tensile stresses at the edge of the fastener holes compared to the measurement at location 3. This might be attributed to the additional stresses developed during the rib assembly at location 1. Location 2 is also affected by the additional assembly stresses as it is next to the rib.

6.7 Summary

This chapter presented the experimental results of residual stress measurements in various coupon specimens and the aircraft mock-up panel. Thermal residual stresses developed during the strap bonding process were investigated, presented, and discussed in detail. The effect of thermal residual stresses on the cold expansion stresses and the effect of impact damage on the thermal residual stresses are also presented in detail. Finally, residual stress measurements on a mock-up panel assembly were presented.

Chapter 7 : Fatigue crack growth testing

The fatigue durability of bonded crack retarders was investigated with constant amplitude (CA) fatigue crack growth testing of M(T) and SEN(T) coupon specimens with and without GLARE straps. Table 4.1 shows the test matrix for fatigue crack growth testing.

Task	Specimen geometry (L x W x T)	Strap dimensions (GLARE 6/5), mm			Loading		No Off
		L	W	T			
Thermal cycling	M(T) (400×140× 5)	180	25.8	3.7	Thermal Cycling (+70°C to −60°C), followed by constant amplitude fatigue crack growth testing		12
At-temperature fatigue	M(T) (400×140× 5)				Constant amplitude fatigue 10 HZ σ_{max}= 60MPa R = 0.1	RT	2
						+70°C	2
						−60°C	2
At-temperature fatigue	M(T) (400×140× 5)	No strap				RT	3
						+70°C	3
						−60°C	2
Impact damage	SEN(T) (400×140× 5)	200	100	3.7		Without strap	3
						With strap	2
						Impact 20 J	2
						Impact 35 J	3
Cold expanded and bolted hole	SEN(T) (400×140× 5)				Constant amplitude fatigue 10 HZ, σ_{max}= 60MPa, R = 0.1		3
DCB testing (Substrate/FM94 interface)	DCB (244×25×5)	None			Static, RT		3
					Static +70°C		3
					Static −60°C		3
Fatigue crack growth	M(T) (400×140× 5)	Load carrying GLARE			Constant amplitude fatigue 10 HZ, σ_{max}= 60MPa, R = 0.1		2

Table 7.1: Test matrix and test conditions used in this investigation

7.1 At temperature DCB tests

Test number	Room temperature G_{Ic}(J/m^2)	+70°C G_{Ic}(J/m^2)	−60°C G_{Ic}(J/m^2)
1	1529	2167	1858
2	2085	2126	1882
3	1947	2042	1869
Average	**1853**	**2111**	**1869**

Table 7.2: summary of DCB test results

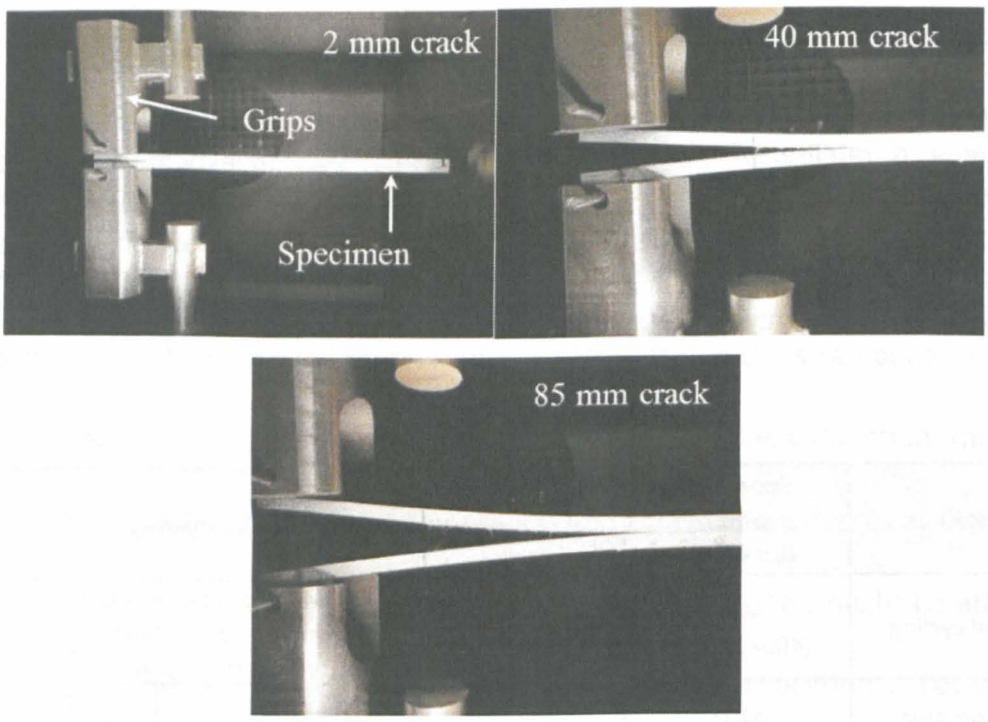

Figure 7.1: Images taken during the DCB test in progress

A total of 9 specimens were tested 3 each at room temperature, +70°C and −60°C. Table 7.2 shows the summary of DCB test results and figure 7.1 shows the images taken during the room temperature DCB test. Tests at −60°C show lower critical strain energy release rate compared to room temperature and +70°C.

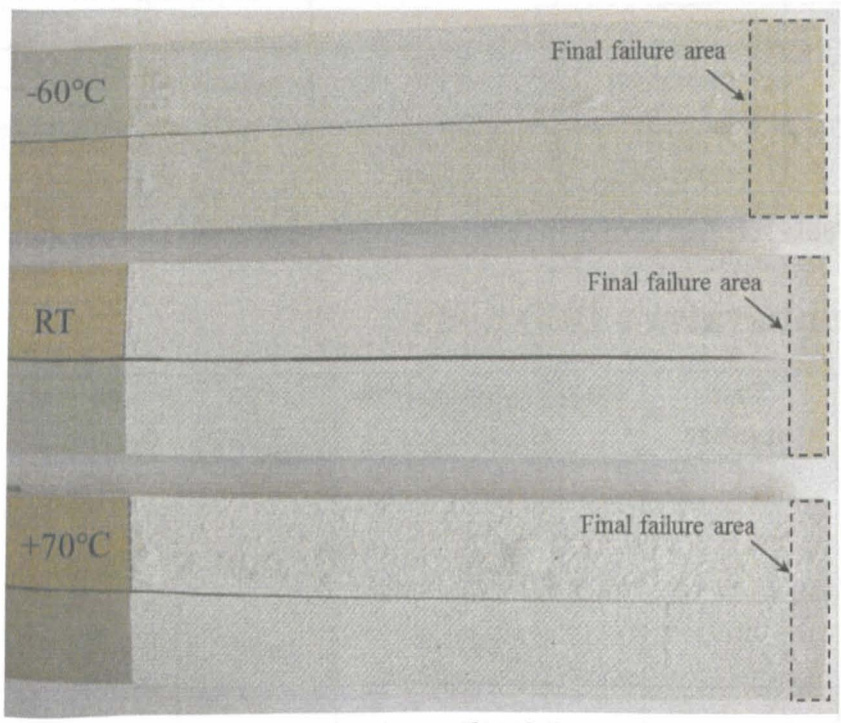

Figure 7.2: DCB specimen after failure surfaces

Figure 7.2 shows specimens after the test and it is clearly seen that the specimen has failed due to cohesive delamination. The adhesive can be observed on both the surfaces

of the DCB specimens and there are no signs of absence of adhesive. It can also be observed that the final failure area is higher for tests performed at −60°C compared to room temperature and +70°C tests.

7.2 At temperature fatigue crack growth tests on M(T) specimens with strap

The geometrical details of the M(T) specimens were presented in Chapter 5. A total of 8 M(T) tests without strap were performed: three specimens each at room temperature and at +70°C and two specimens at −60°C. Figure 7.3 (a-c) shows at-temperature fatigue tests results for the M(T) specimens without a strap.

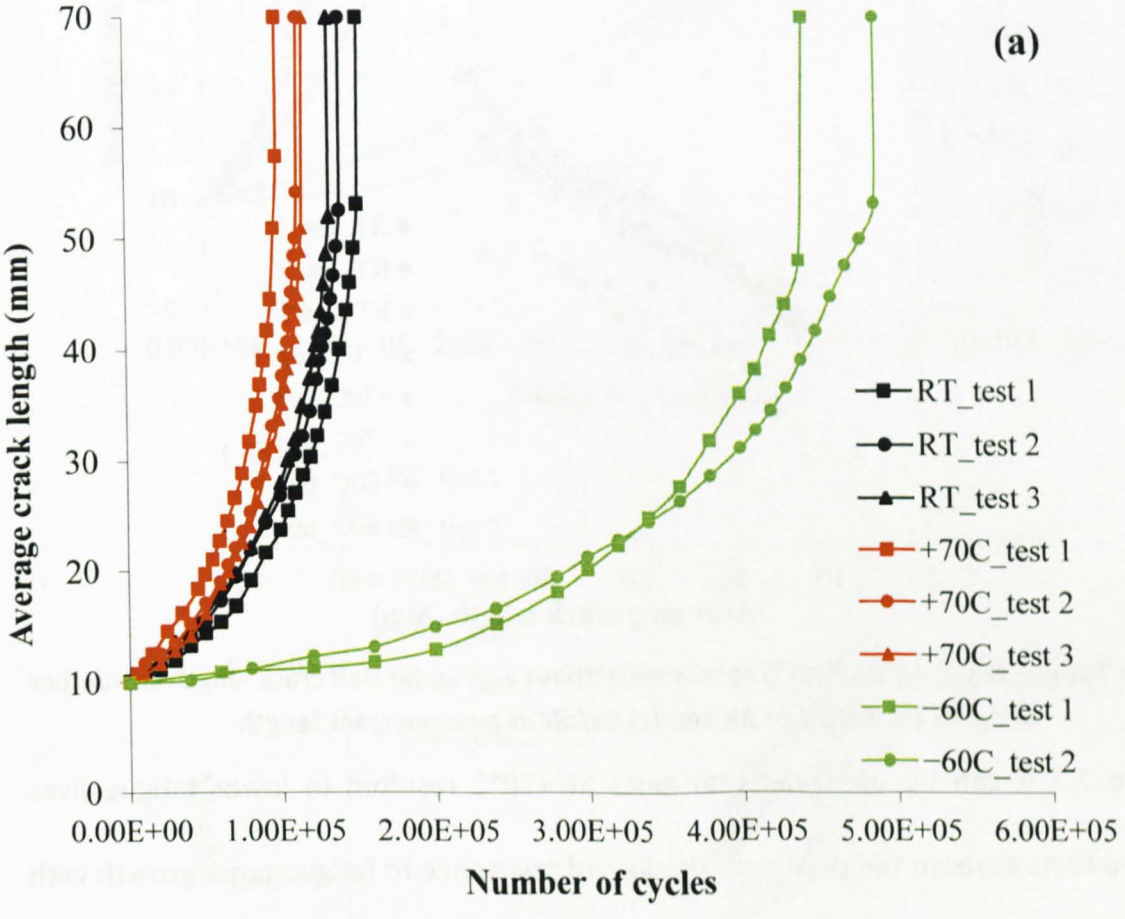

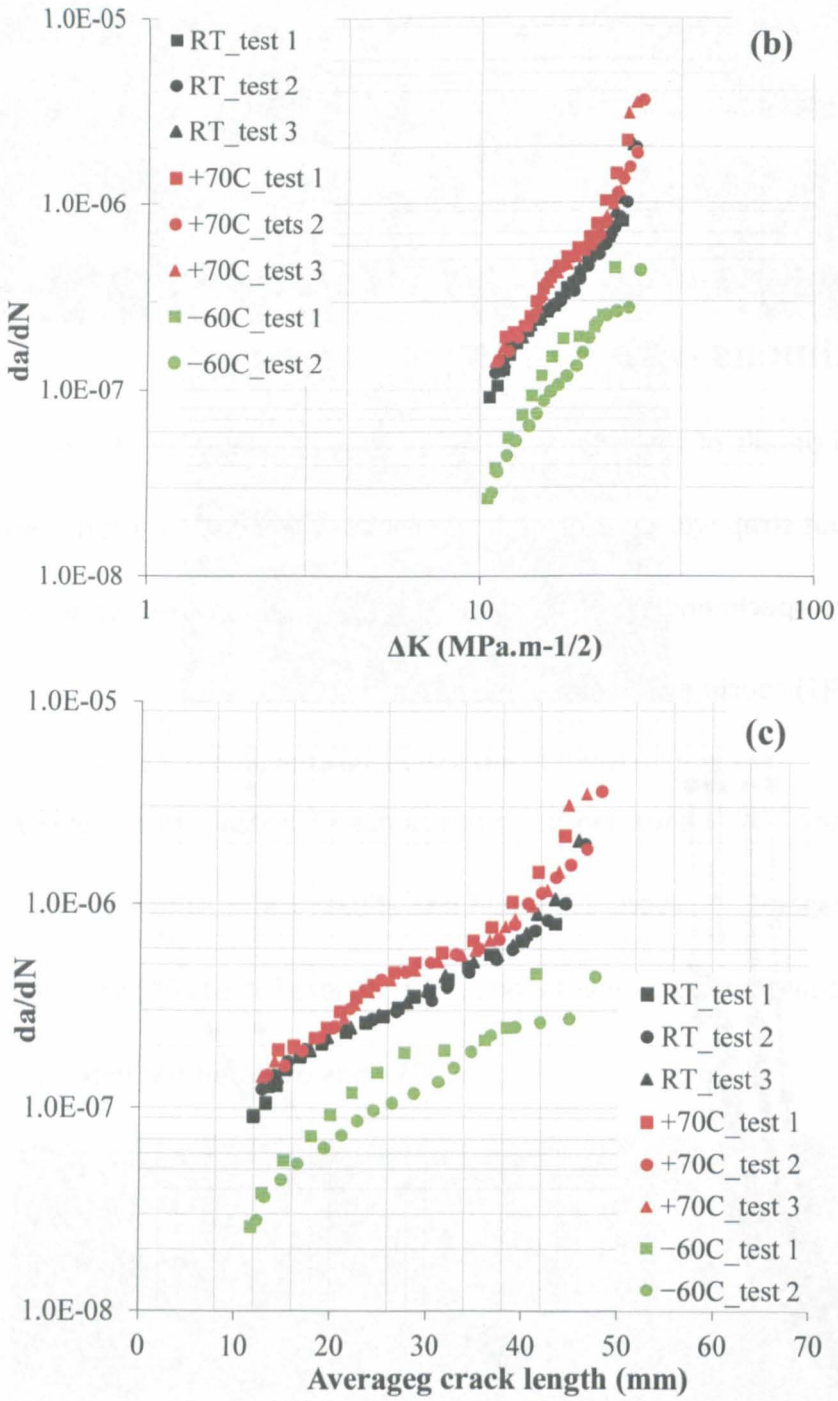

Figure 7.3: Fatigue test results of M(T) specimen without a strap (a) Half crack length vs number of cycles (b) da/dN vs ΔK and (c) da/dN vs average crack length

From figure 7.3 it can be observed that tests at +70°C resulted in lower fatigue lives compared to tests at room temperature. The loss of resistance to fatigue crack growth with increasing temperature may be attributed to the deterioration of properties when the temperature is increased. In contrast, tests at −60°C resulted in higher fatigue lives compared to both room temperature and +70°C tests. This significant increase in fatigue life is attributed to the increase in mechanical properties of the substrate material with decrease in temperature.

7.3 At temperature fatigue crack growth tests on M(T) specimens with strap

Figure 7.4 (a-c) shows fatigue crack growth test results of M(T) with strap specimens. A total of 6 specimens were tested: two each at room temperature, +70°C and −60°C.

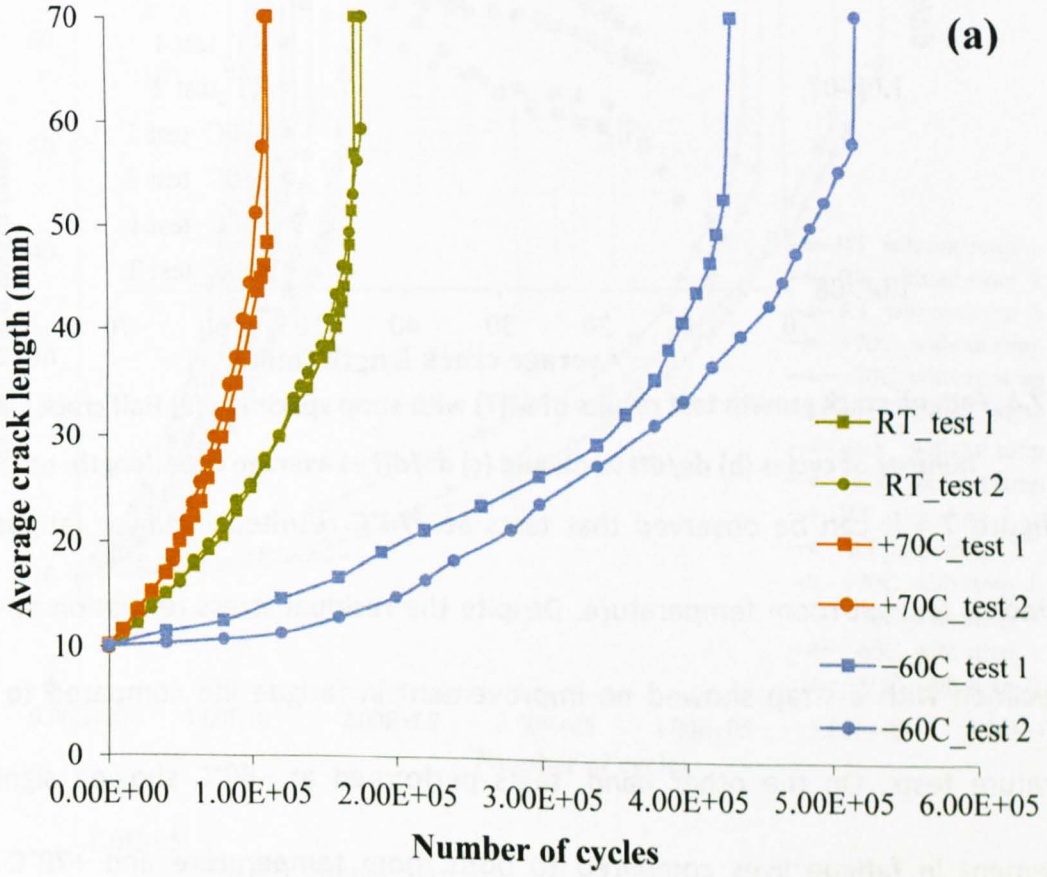

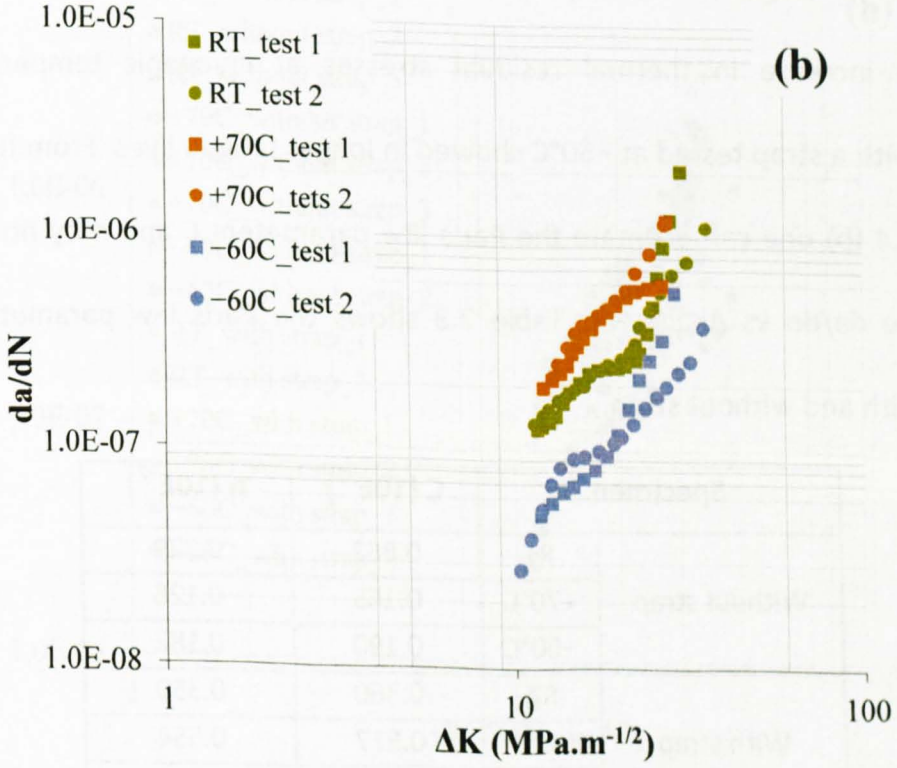

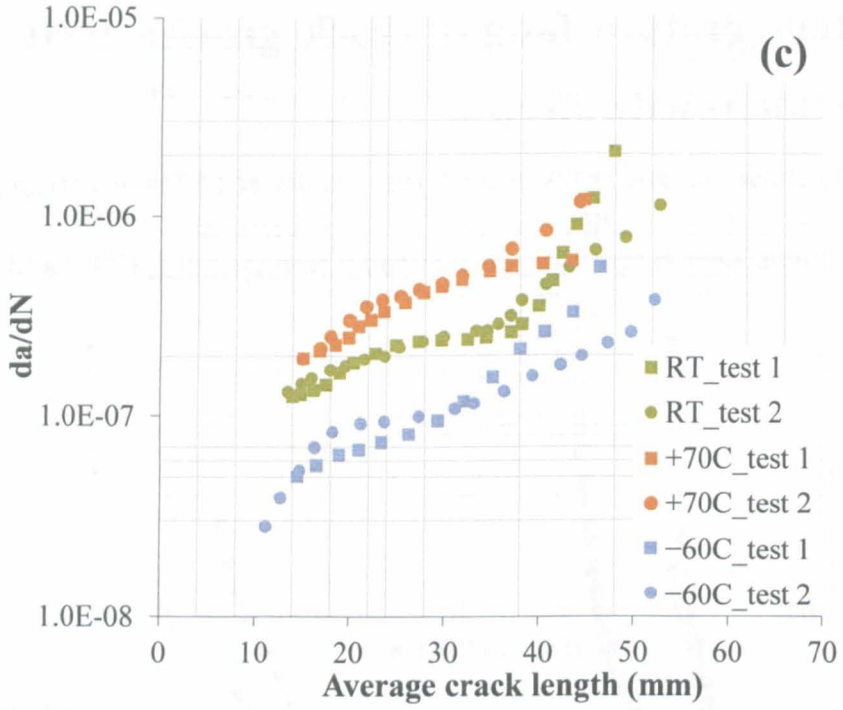

Figure 7.4: Fatigue crack growth test results of M(T) with strap specimen (a) Half crack length vs number of cycles (b) da/dN vs ΔK and (c) da/dN vs average crack length

From figure 7.4 it can be observed that tests at +70°C resulted in lower fatigue lives compared to tests at room temperature. Despite the residual stress relaxation at +70°C, the specimen with a strap showed no improvement in fatigue life compared to room temperature tests. On the other hand, tests performed at −60°C showed significant improvement in fatigue lives compared to both room temperature and +70°C tests. Despite the increase in thermal residual stresses at cryogenic temperatures, the specimens with a strap tested at −60°C showed in longer fatigue lives. From figure 7.3 (b) and figure 7.4 (b) one can estimate the Paris law parameters *C* and *n* by fitting a linear curve for the da/dn vs ΔK curves. Table 7.3 shows the Paris law parameters for the specimens with and without strap.

Specimen		C ($10E^{-6}$)	n ($10E^{-7}$)
Without strap	RT	0.862	0.729
	+70°C	0.165	0.126
	−60°C	0.190	0.182
With strap	RT	0.360	0.350
	+70°C	0.517	0.554
	−60°C	0.089	0.111

Table 7.3: Calculated Paris law parameters

The fatigue crack growth improvement associated with bonded crack retarders and the life improvement factor can be determined by comparing the at temperature fatigue crack growth results of M(T) specimens with and without strap.

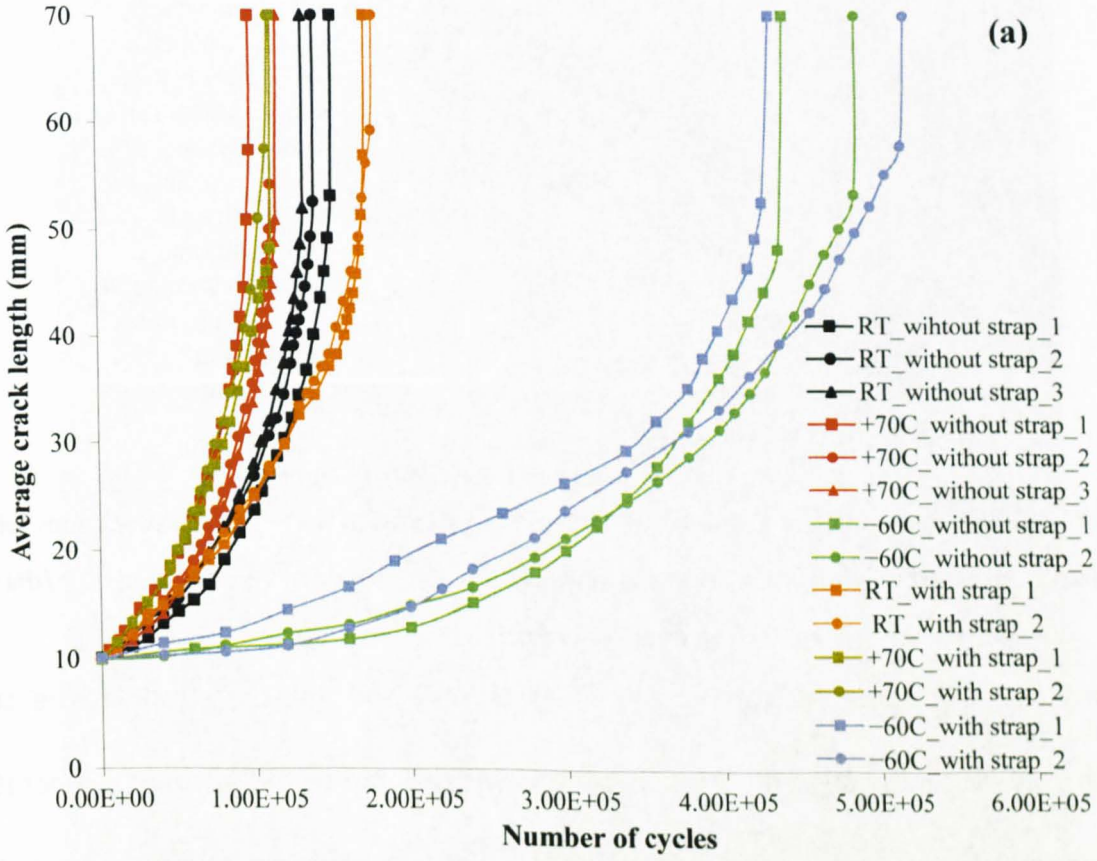

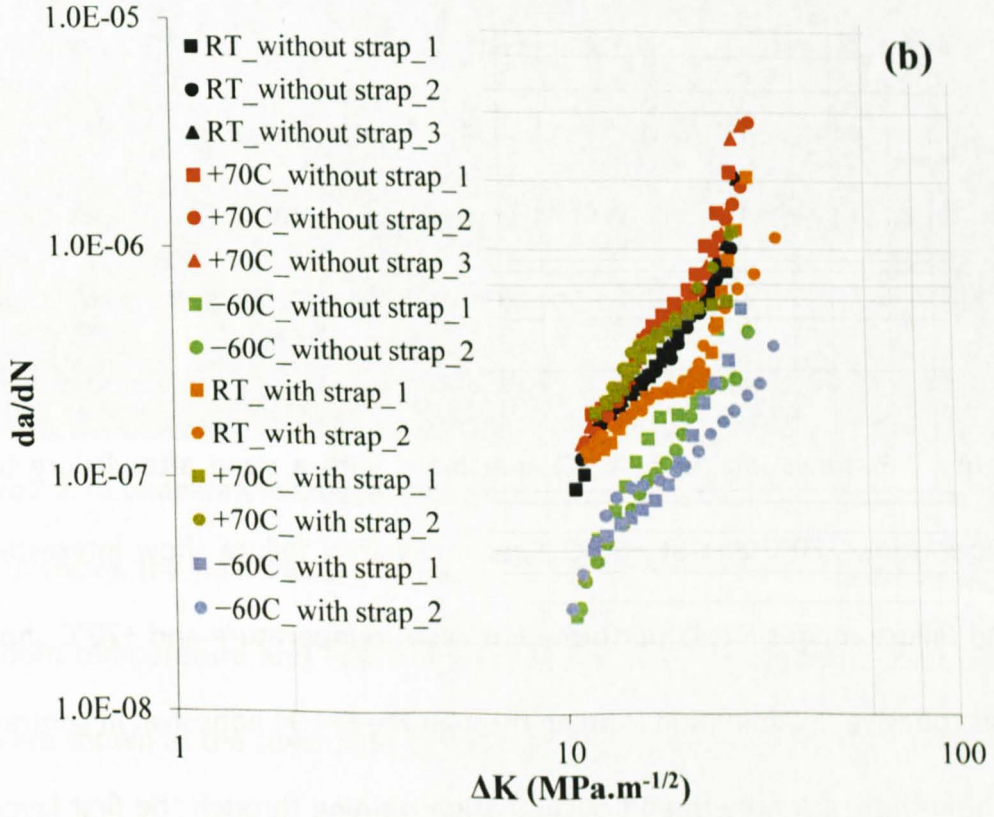

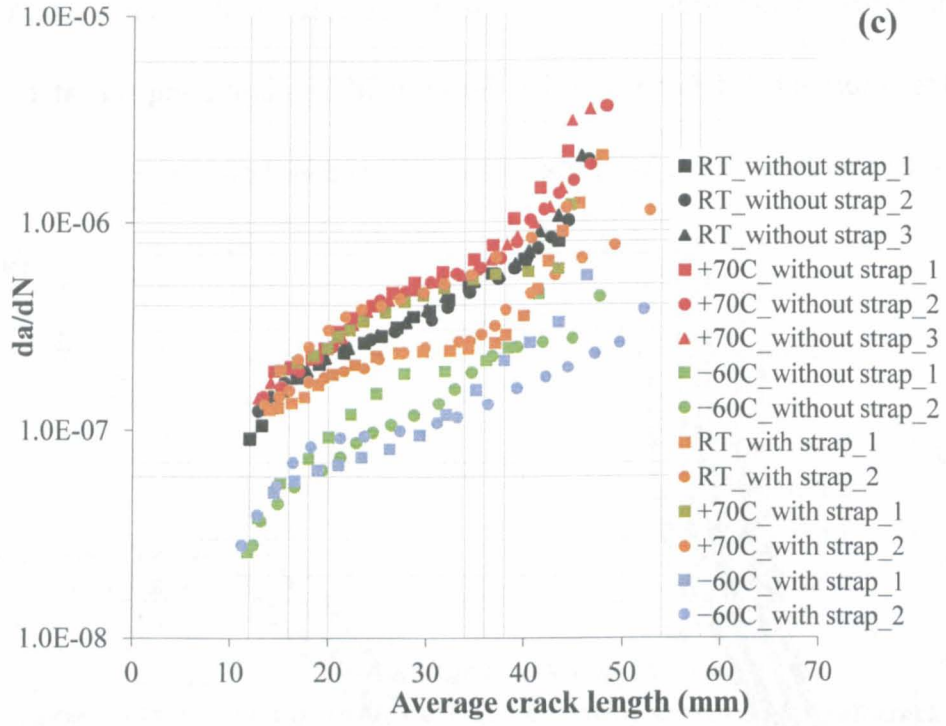

Figure 7.5: Comparison of at temperature fatigue crack growth tests of M(T) specimens with and without strap (a) Half crack length vs number of cycles (b) da/dN vs ΔK and (c) da/dN vs average crack length

Figure 7.5 (a-c) shows the comparison of M(T) with and without strap fatigue crack growth tests. It can be seen that the specimens with a strap tested at room temperature show an average life improvement factor of 1.2 compared to specimens without a strap tested at room temperature. The life improvement factor at room temperature tests is the ratio of average number of cycles for failure of M(T) specimens with a strap to the average number of cycles for failure of M(T) specimens without strap. Specimens with a strap tested at +70°C and −60°C show no significant life improvement when compared to the specimens without a strap tested at +70°C and −60°C.

Figure 7.6 shows images of M(T) specimens with a strap after failure tested at room temperature, +70°C and at −60°C. Specimens after failure show interesting crack growth and failure modes. Tests performed at room temperature and +70°C show crack growth and cohesive delamination running through the FM 94 adhesive. In contrast, tests at −60°C show the crack growth and delamination running through the first layer of the GLARE. This might be attributed to the increase in thermal residual stresses at −60°C

which results in a change in the stress intensity factors at the bond line of the strap and the substrate.

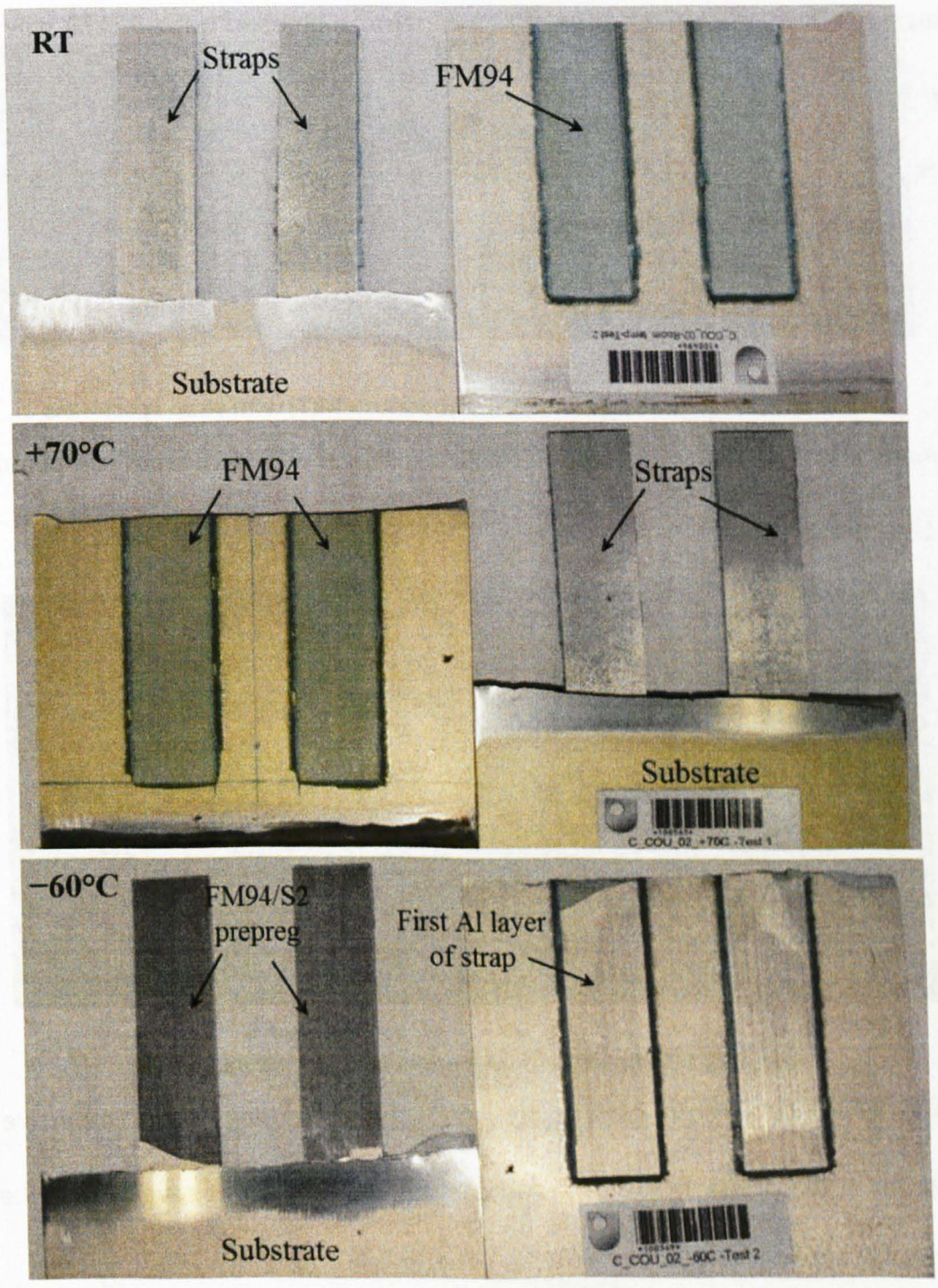

Figure 7.6: At temperature fatigue crack growth M(T) specimens with strap after failure

Figure 7.7 shows the half fracture surfaces of the M(T) with strap specimens tested at +70°C, room temperature and −60°C from top to bottom respectively. Only half facture surfaces are shown as the specimens are symmetric about the vertical axis. Fatigue beach marks are visible on the fracture surfaces of the specimens tested at room temperature, whereas the fracture surface of specimens tested at +70°C are relatively smooth and

show no fatigue beach marks. This might be the reason that the specimen tested at +70°C showed faster crack growth rates which resulted in a lower number of cycles to failure.

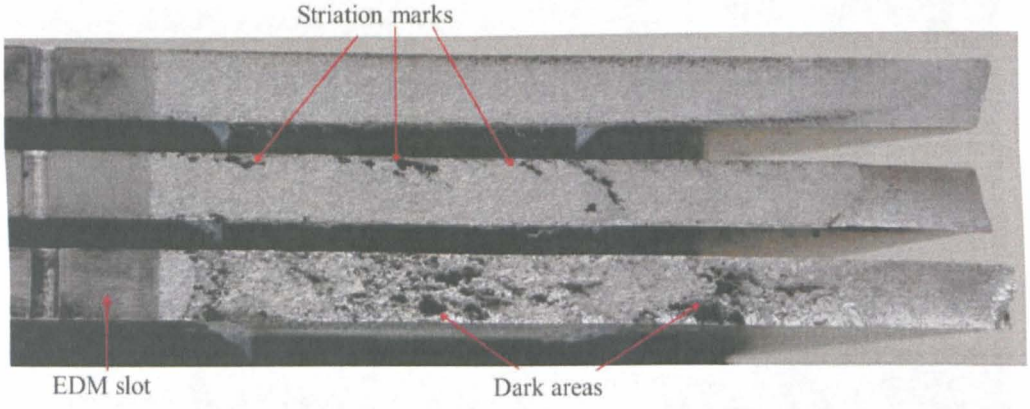

Figure 7.7: Fracture surface of at-temperature M(T) with strap specimens

Specimens tested at −60°C show rough fracture surfaces with dark areas compared to the room temperature tests.

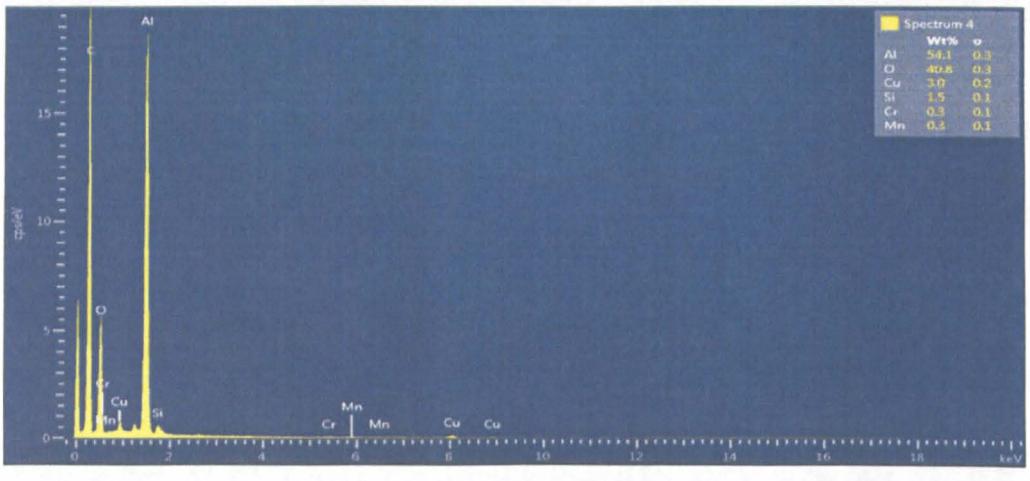

Figure 7.8: EDX analysis of dark areas on the fracture surface

The dark areas on the fracture surface were investigated by using Energy Dispersive X-ray spectroscopy (EDX). Figure 7.8 shows the results from EDX and it reveals that the dark areas are aluminium oxides.

7.4 Fatigue crack growth tests on M(T) specimens with load carrying GLARE straps

The design of the GLARE straps used to reinforce the M(T) specimens may have a significant effect on the performance of the bonded crack retarders. The load carrying capacity of the GLARE straps can be increased by extending the GLARE straps into the loading area of the specimen. The geometrical details and actual specimen is shown in

figure 5.4. Two M(T) specimens reinforced with load carrying GLARE straps were tested at constant amplitude by using the loading parameters mentioned in table 7.1. After the load carrying GLARE strap bonding process, an out-of-plane deflection was observed in the specimens similar to the M(T) specimen with a regular strap. Measurements were performed on the specimens and resulted in an out-of-plane deflection of about 1 mm.

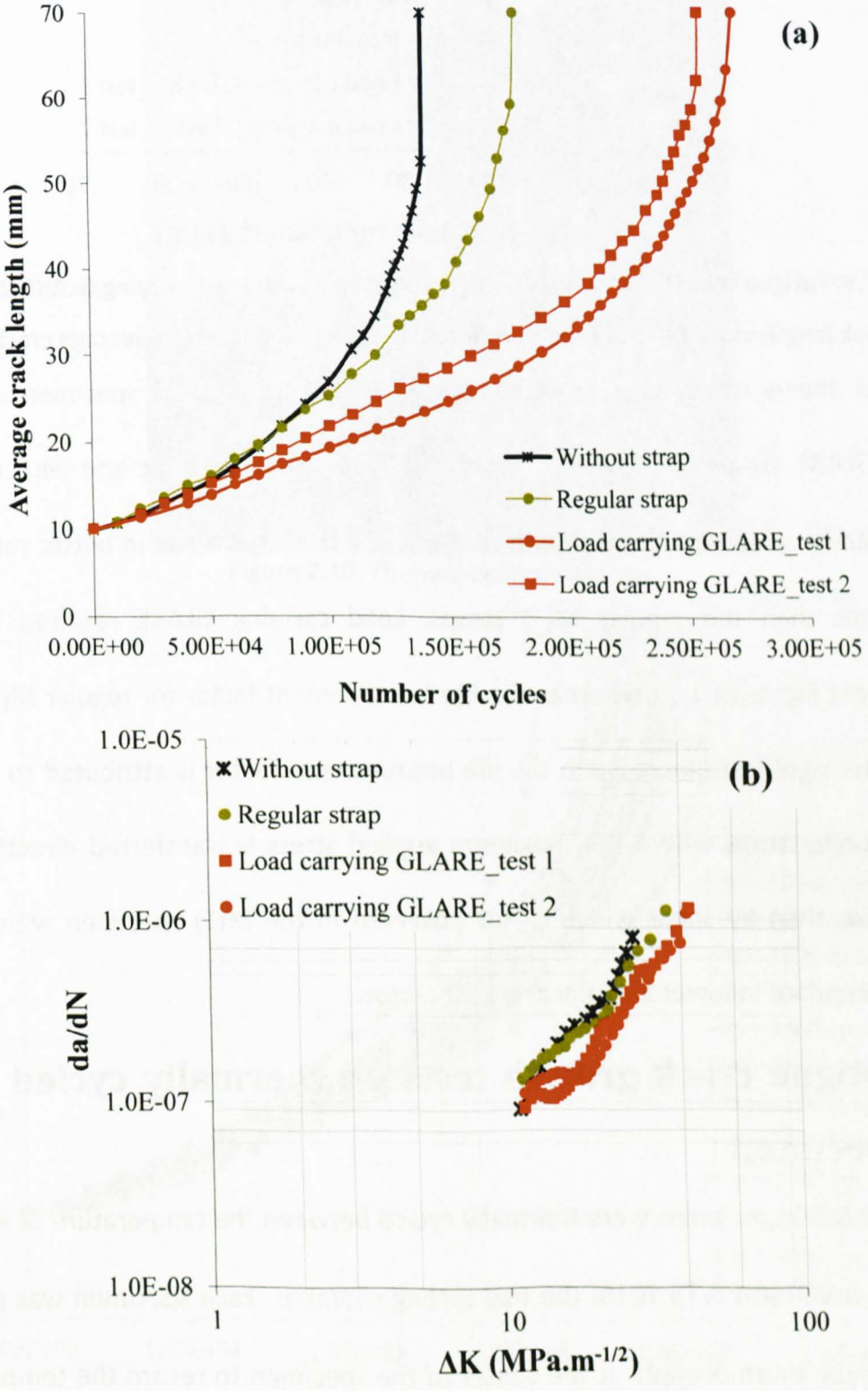

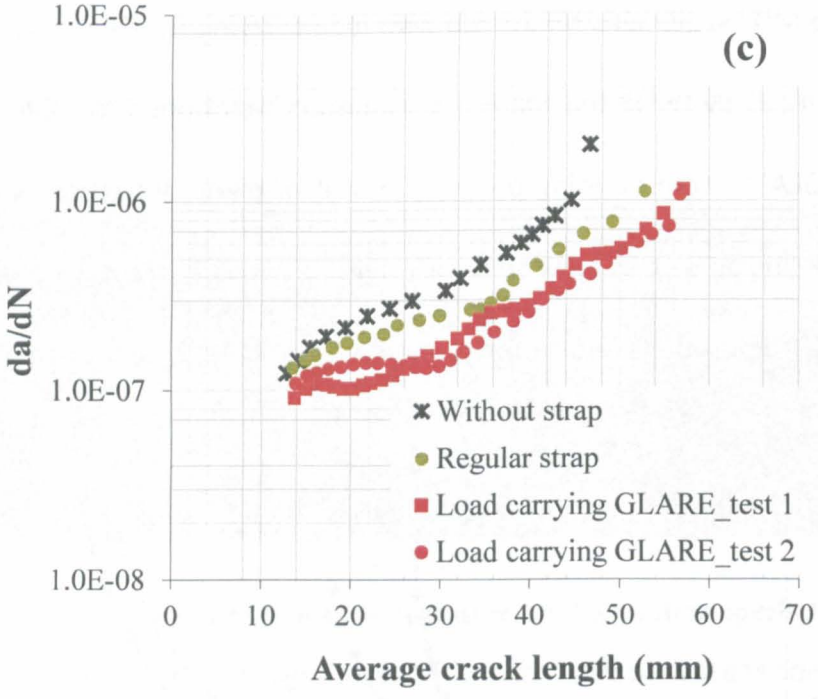

Figure 7.9: Fatigue crack growth tests of M(T) specimens with load carrying GLARE straps (a) Half crack length vs number of cycles (b) da/dN vs ΔK and (c) da/dN vs average crack length

Figure 7.9 shows the fatigue crack growth tests results of M(T) specimen with load carrying GLARE straps in comparison with M(T) specimen without and with a regular strap. It can be observed that the load carrying GLARE straps result in better retardation performance than the regular M(T) straps. Load carrying GLARE resulted in a life improvement factor of 1.72 whereas the life improvement factor for regular M(T) straps was 1.2. The significant increase in the life improvement factor is attributed to the load carrying GLARE straps where the maximum applied stress is transferred directly to the straps rather than by shear which is not observed in the M(T) specimen with regular straps and resulted in lower life improvement factor.

7.5 Fatigue crack growth tests on thermally cycled M(T) specimen

A total of 12 M(T) specimens were thermally cycled between the temperature of −60°C to +70°C using a VOTSCH (VTS 7010) thermal cycling chamber. Each specimen was coupled with one N-type thermocouple at the center of the specimen to record the temperature with an accuracy of ±0.5°C. A holding time of 40 minutes at each temperature (i.e. 40

minutes each at −60°C and +70°C) was maintained. Figure 7.10 shows the thermal cycling test chamber. Thermal cycling was performed from June 2012 to April 2014 followed by fatigue crack growth tests. Fatigue crack growth tests were performed at room temperature with two specimens each after 500, 1000, 1500, 2000, 3000 and 4500 thermal cycles.

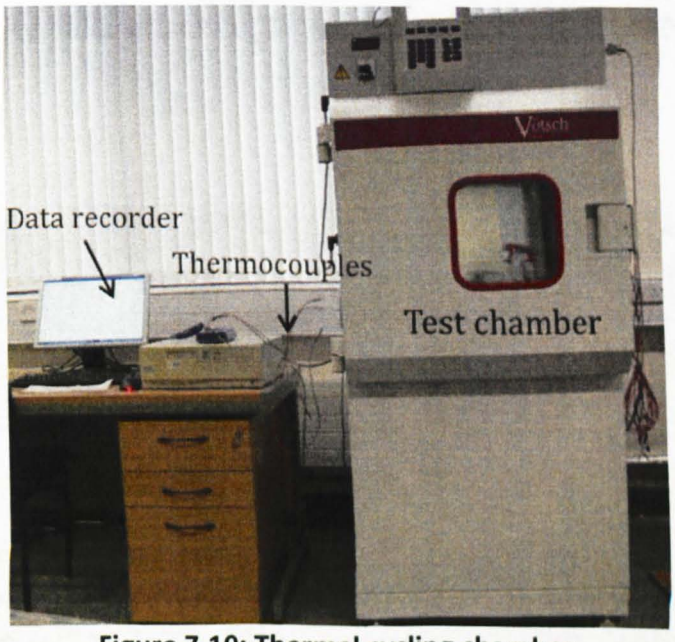

Figure 7.10: Thermal cycling chamber

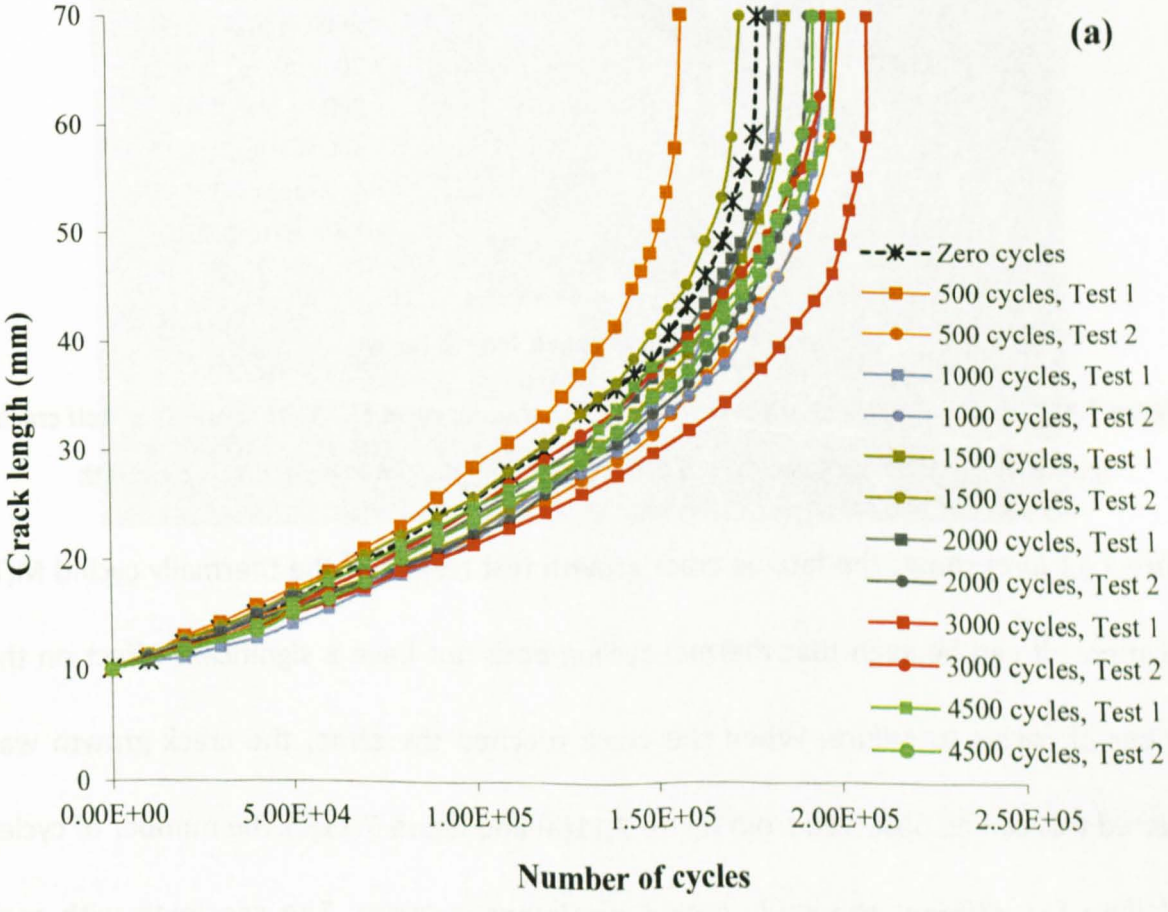

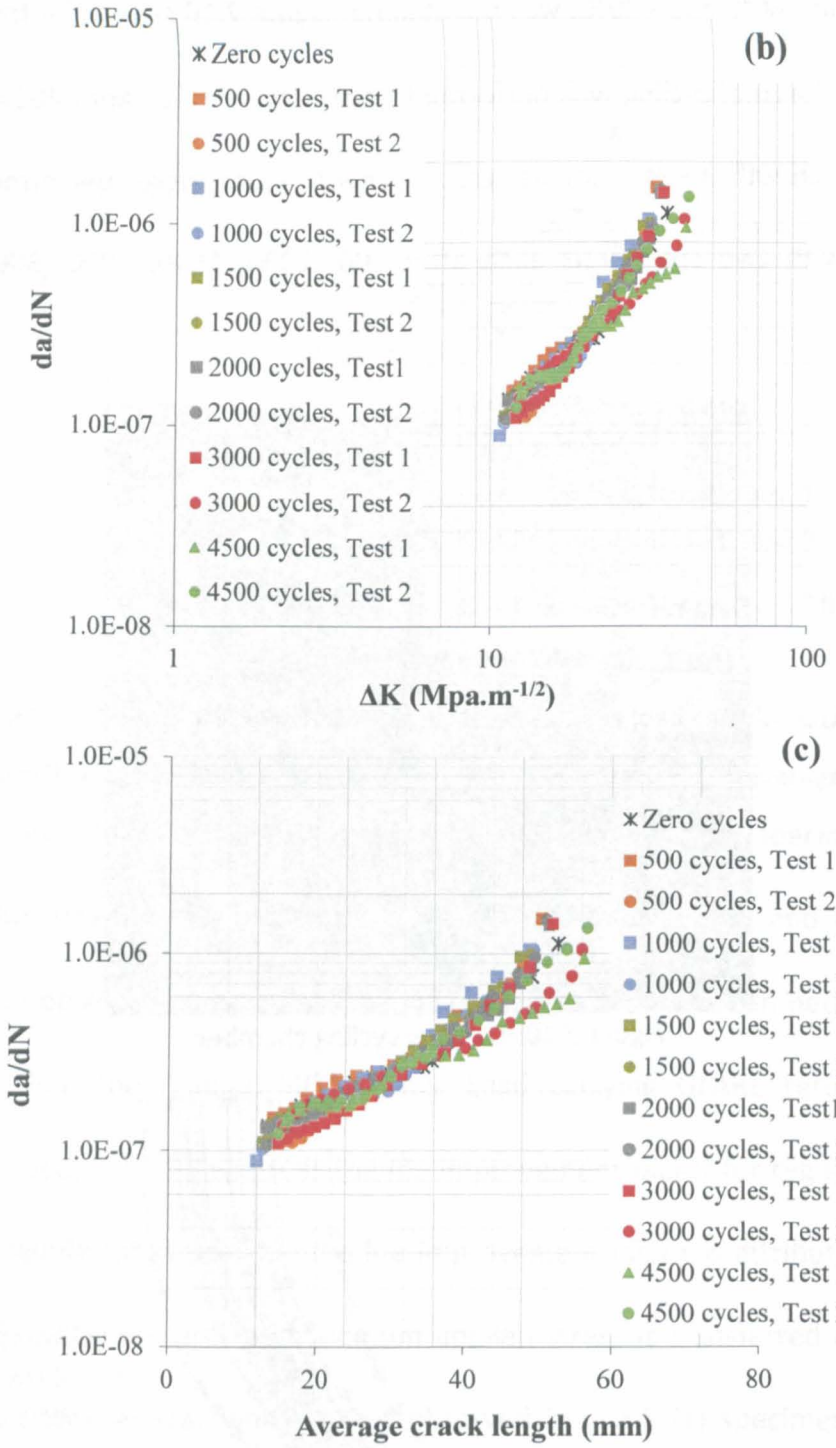

Figure 7.11: Fatigue crack growth test results of thermally cycled M(T) specimen (a) Half crack length vs number of cycles (b) da/dN vs ΔK and (c) da/dN vs average crack length

Figure 7.11 (a-c) shows the fatigue crack growth test results of the thermally cycled M(T) specimens. It can be seen that thermal cycling does not have a significant effect on the number of cycles to failure. When the crack reached the strap, the crack growth was hindered this can be observed from figure 7.11(a) and figure 7.11(c).The number of cycles for failure for different thermally cycled specimens is varies. The specimen with zero

thermal cycles failed at 175659 cycles whereas the average number of cycles for failure at the different thermal cycles is 181433, 194236, 181886, 189250, 204673, and 198494 for 500, 1000, 1500, 2000, 3000 and 4500 thermal cycles respectively. The scatter in the data is acceptable (not more than 10%) which might be attributed to changes in humidity and temperature during the test. Figure 7.12 shows the thermal cycled specimen after failure. It is clear that cohesive failure causes the delamination of the GLARE straps from the substrate.

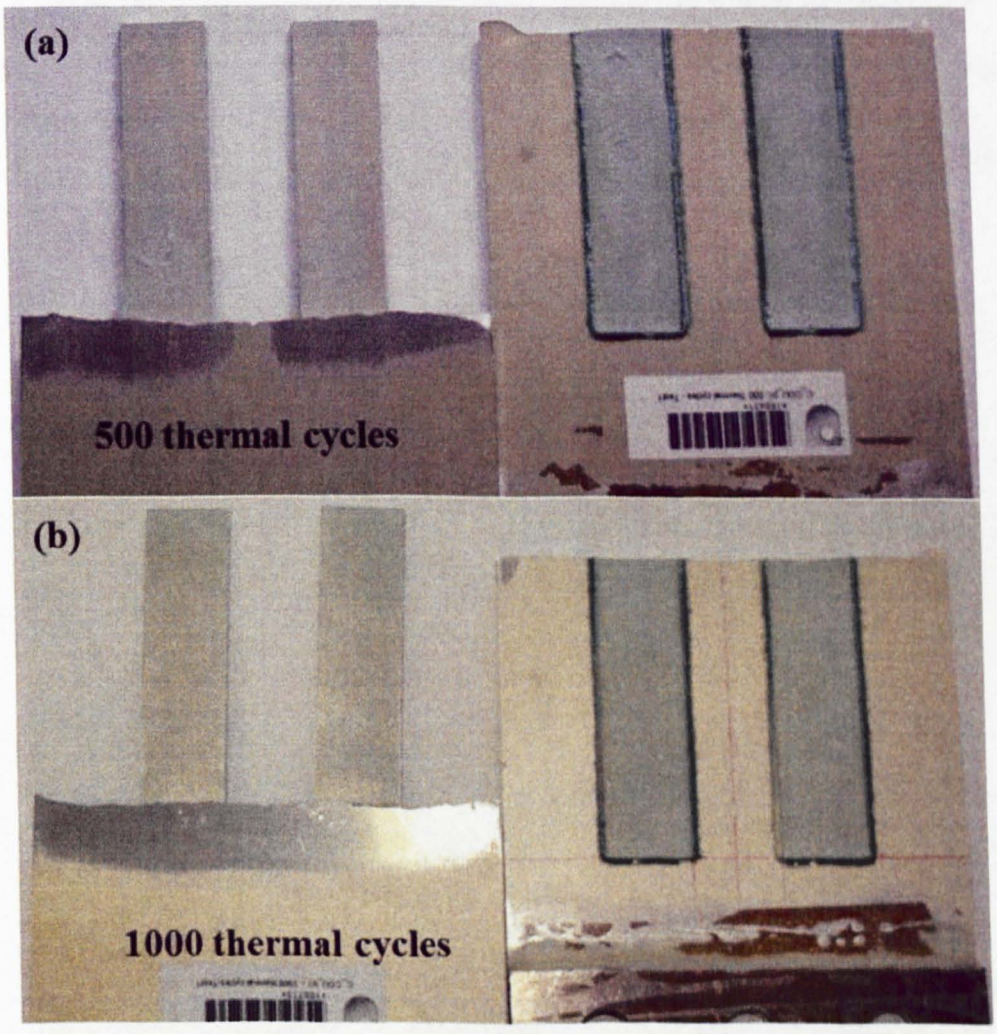

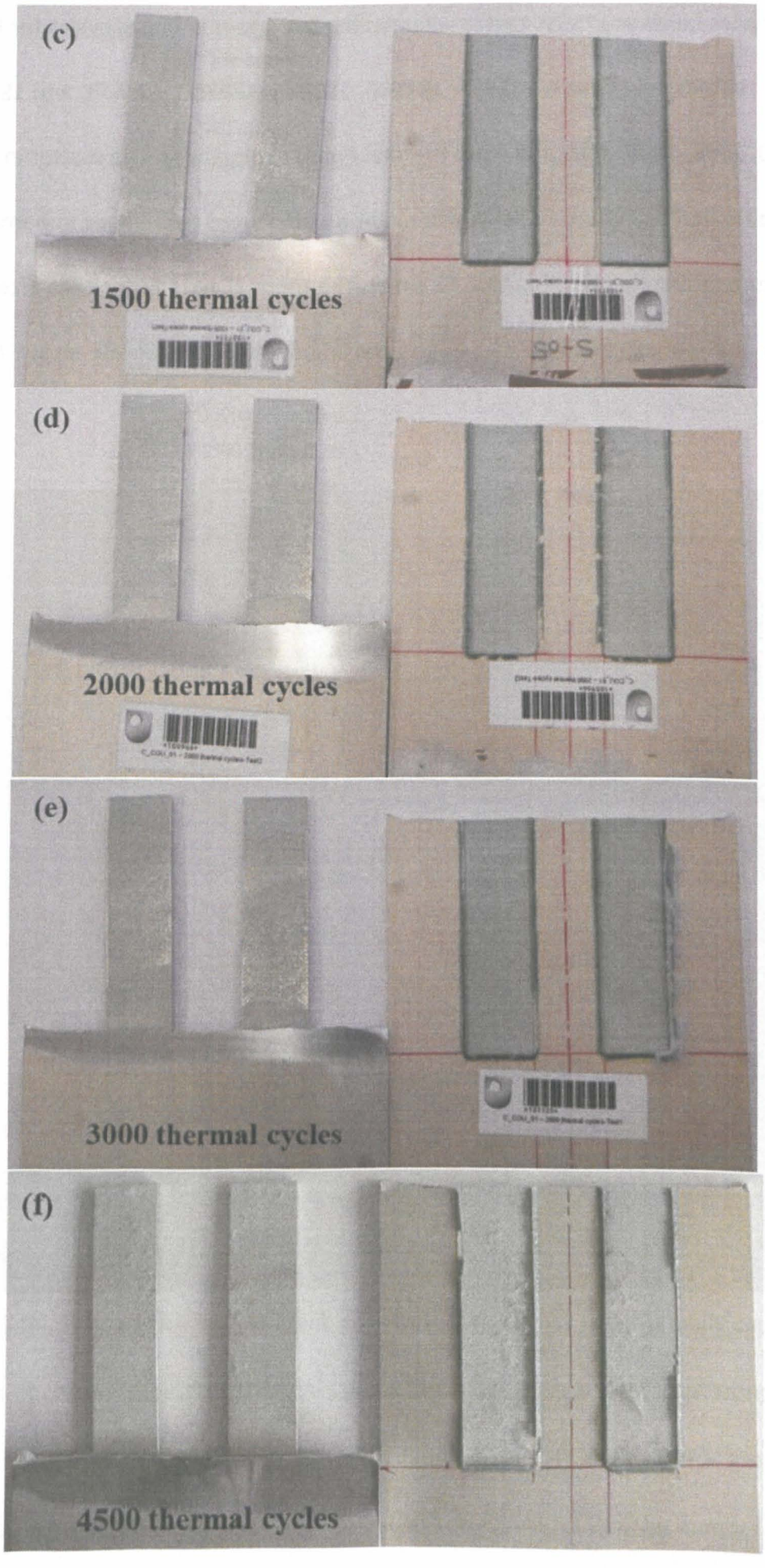

Figure 7.12: Thermally cycled M(T) specimens after failure

7.6 Fatigue crack growth tests on impact damage SEN(T) specimens

The geometrical details of the impact damage specimens and the impact damage procedure was discussed in detailed in chapter 5. Prior to impacting the specimens, the damage depth and damage width resulting from different impact energies were investigated to determine the required impact energy to produce 0.3 mm barely visible impact damage (BVID). For this, a series of impacts ranging from 10 J to 60 J were made on a small coupon specimen and the damage depth and width were measured using a laser co-ordinate measurement machine. Figure 7.13 shows impact damage analysis and table 7.4 summarizes the depth and width of the damage resulting from the impact on GLARE.

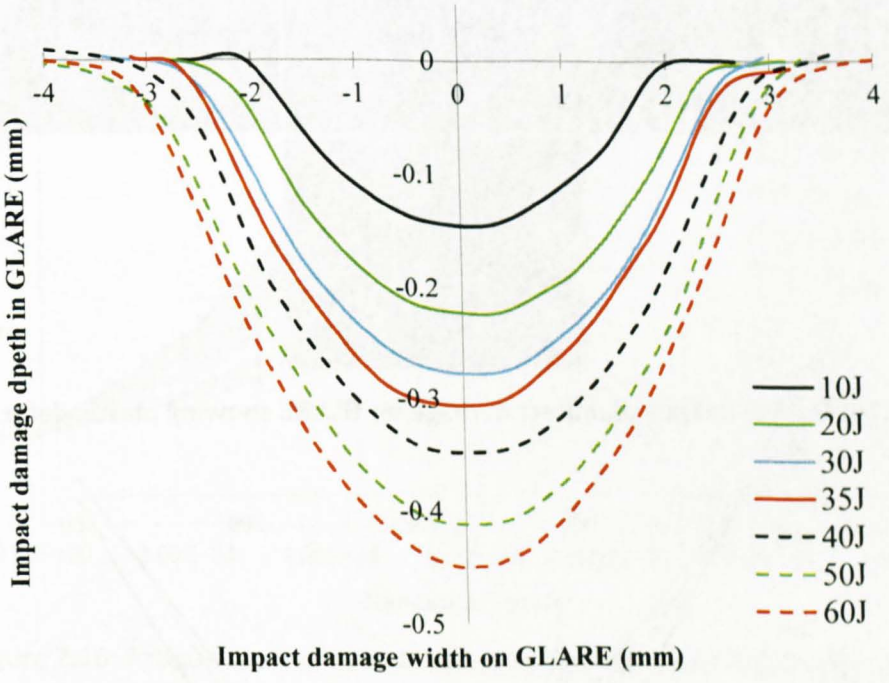

Figure 7.13: Impact damage analysis

Impact energy/J	10	20	30	35	40	50	60
Damage depth/mm	0.14	0.22	0.27	0.31	0.35	0.41	0.45
Damage width/mm	4	5.2	5.6	6	6.4	7.04	7.52

Table 7.4: Summary of post-impact damage analysis

The low velocity impact performed on the GLARE resulted in visible damage on the GLARE strap in the form of plastic deformation. Figure 7.14 shows the plastic deformation on

GLARE after impact damage. Impact damage depth and width are directly proportional to the impact energy. To select the optimum level of damage, from figure 7.13 and table 7.4 it can be seen that barely visible impact damage of 0.3 mm can be caused by 35 J and was selected as the impact energy to impact the specimens to be fatigued. In addition, two fatigue tests with the specimens impacted at 20 J were also conducted. Therefore, a total of 10 specimens were fatigue tested: three without strap, two with strap and no damage, two with strap after 20 J impact and three with strap after 35 J impact.

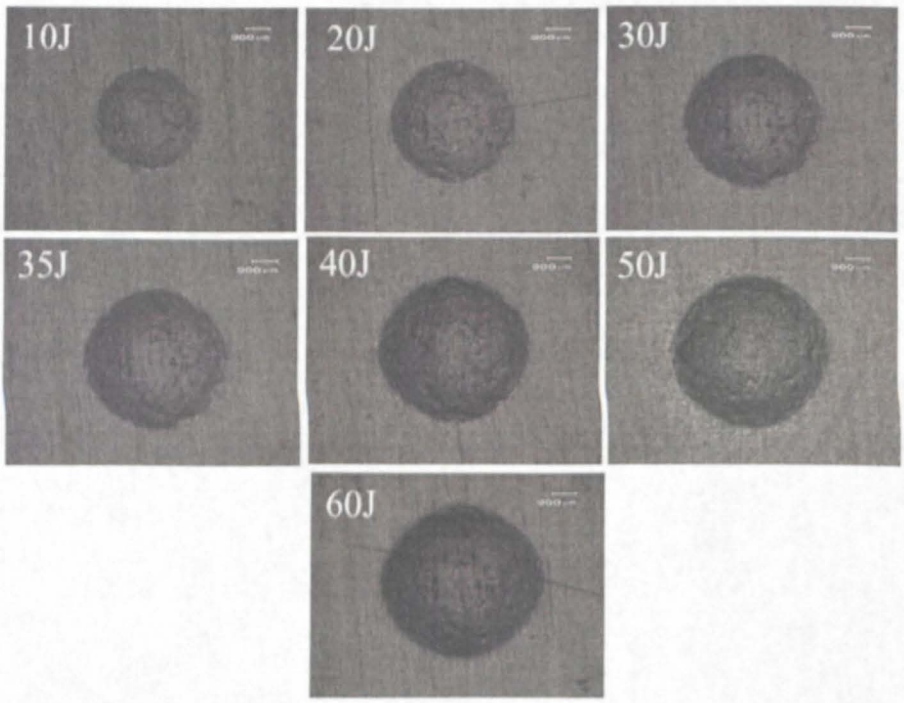

Figure 7.14: Optical images of impact damage on GLARE showing plastic deformation

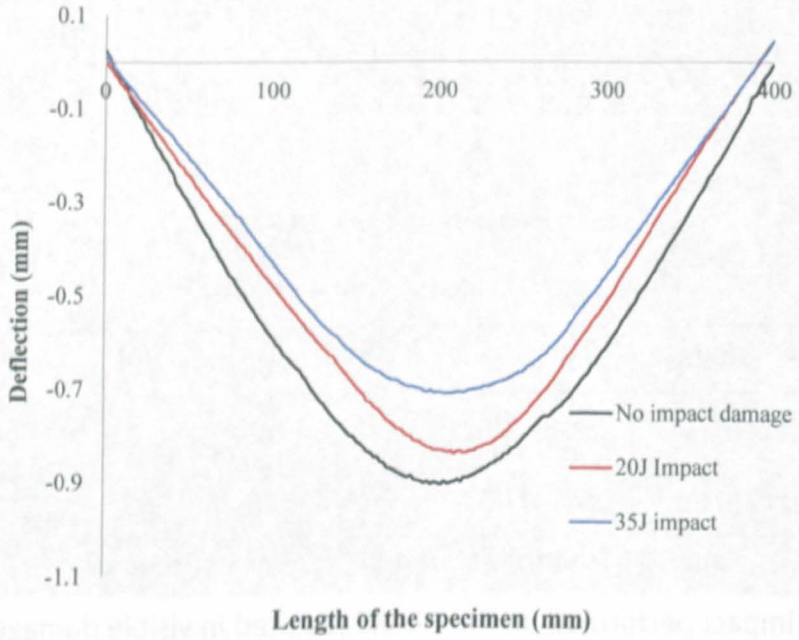

Figure 7.15: Average distortion measurements of the impact damaged specimens before and after impact

Prior to fatigue testing, the out of plane distortion of the specimens after bonding with and without impact damage was measured by using a laser co-ordinate measurement machine. The measurements were performed on the substrate on the non-reinforced side along the length of the specimen. A total of two specimens were measured to obtain the baseline distortion measurements and two specimens each at 20 J and 35 J. The average distortion measurements are shown in figure 7.15 and it can be seen that the impact damage on the GLARE resulted in a change in the specimen distortion. The impacting has overlaid a new distortion that acts in the opposite sense to that resulting from the high temperature adhesive curing.

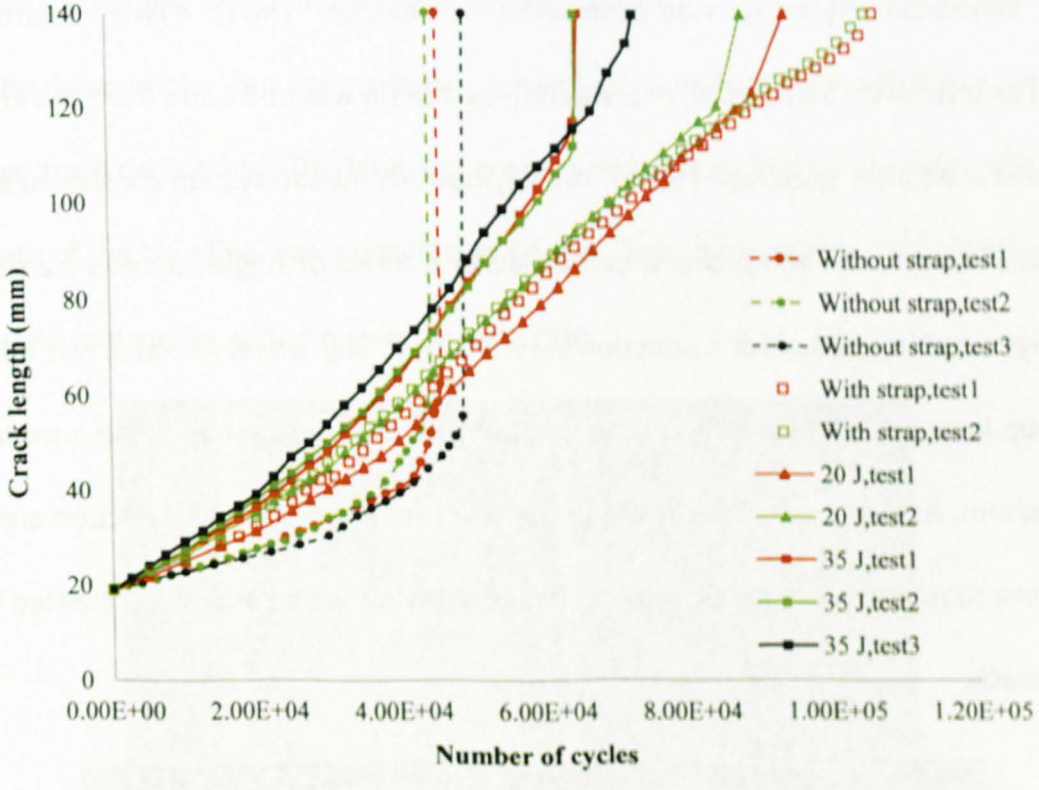

Figure 7.16: Fatigue crack growth tests on impact damage SEN(T) specimens

Figure 7.16 shows constant amplitude fatigue crack growth tests on the SEN(T) specimens. It shows that the specimens with a strap have a longer life when compared to specimens without a strap, confirming the efficacy of the bonded crack retarder concept. The specimens with a strap produced a fatigue life more than double that of the fatigue life of an unstrapped specimen and the life improvement factor for the strapped specimens was 2.26. Specimens impacted with 20 J and 35 J have a shorter fatigue life

than the strapped specimen without damage, but had longer life when compared to an unstrapped specimen. Specimens impacted with 20 J showed a 16% reduction in the fatigue life whereas the specimens impacted with 35 J showed a 55% reduction in the fatigue life when compared to the fatigue life of the undamaged strapped specimen.

One interesting aspect of the bonded crack retarders is to study the delamination shape and growth between the strap and the substrate when the crack propagates through the specimen. Better understanding of the delamination behaviour when the crack propagates can help to optimise the design of the coupon specimens. For this, a specimen with no impact damage was inspected with the help of ultrasound (a phased array Omniscan system) non-destructive technique (NDT). Two delamination measurements were performed, one when the crack tip was at 85 mm from the EDM slot and the second after specimen failure. The Olympus Omniscan system consists of a probe designated as 5L64-I1. The probe is composed of a series of single element transducers. The ultrasound frequency for inspection was 5Hz. A rolling wheel encoder was added to the probe in order to measure the scanning distance. The resolution of the encoder was 12 steps/mm. As the dimensions of the probe were smaller than the inspection area, two scans were required to create a complete image showing the delamination created by the fatigue crack.

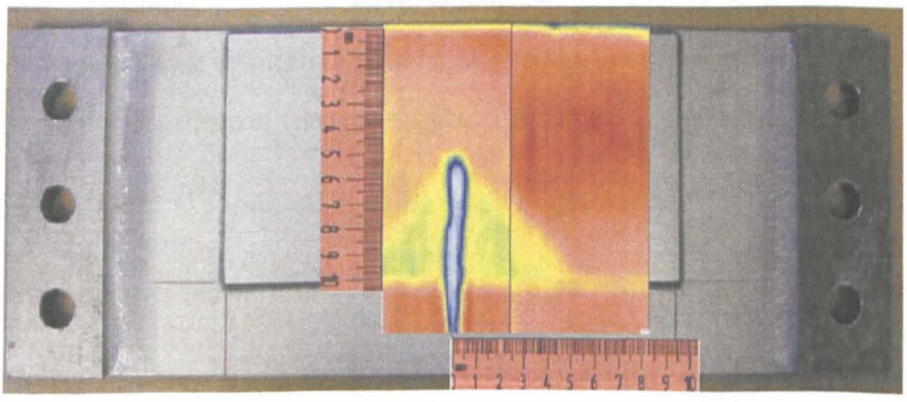

Figure 7.17: Delamination growth when the crack tip is at 85 mm

Figure 7.17 shows the non-destructive analysis to study the delamination growth between the strap and substrate when the crack is at 85 mm. Measurements were performed from the non-reinforced side. The image obtained from the Ominscan has been overlaid onto the specimen photograph to facilitate the comprehension of the results. An image obtained from Omniscan shows different features in different colours. The delamination between the strap and substrate can be seen in yellow and green and the crack is shown in white and blue.

The delamination found is roughly triangular in shape with an angle of approximately 45 degrees. The longest side extends along the edge of the bonded strap parallel to the loading direction up to a distance of 50 mm (figure 7.17). The green region within the delamination represents the area where the strap and the substrate are more separated from each other. The blue line corresponds to the line of the substrate crack. The length of the blue line was measured as 84 mm. This can be compared with the crack length of 85 mm visible on the non-reinforced side.

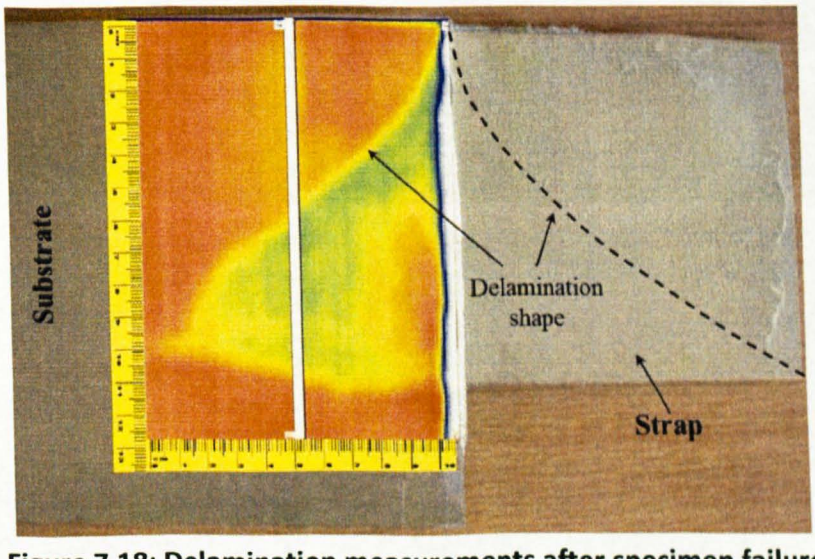

Figure 7.18: Delamination measurements after specimen failure

Figure 7.18 shows the delamination measurements performed after specimen failure. The shape of the delamination area can be compared to the delamination seen with the naked eye on the specimen after failure. The Omniscan image is overlaid on the left hand side on the top of the specimen. The dotted line shows the delamination shape which

resembles the delamination shape in the Omniscan image. The longest side extends along the edge of the bonded strap parallel to the loading direction for a distance of 100 mm. From figures 7.17 and 7.18, it is clear that the delamination shape is triangular with the longest side extending along the edge of the bonded strap.

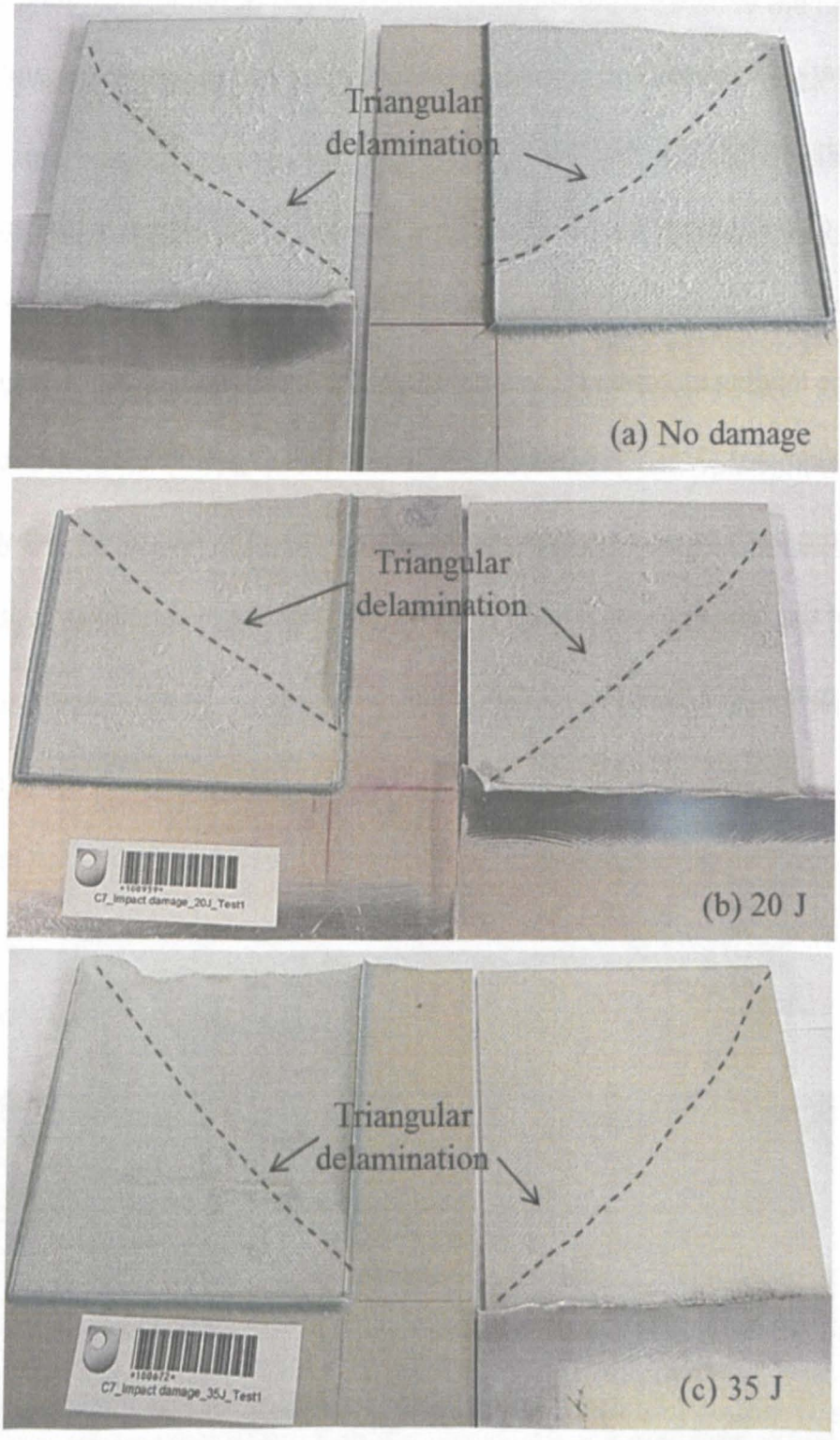

Figure 7.19: Specimens after failure with and without impact damage

The triangular delamination was observed in all SEN(T) specimens reinforced with a strap. SEN(T) specimens with and without impact damage after failure are shown in figure 7.19. There is clear evidence that the delamination between the strap and the substrate was cohesive.

7.7 Fatigue crack growth tests on bolted SEN(T) specimens

A total of three specimens were tested at room temperature. The loading parameters are shown in table 7.1. Figure 7.20 shows the fatigue crack growth results and table 7.4 shows the summary of the results.

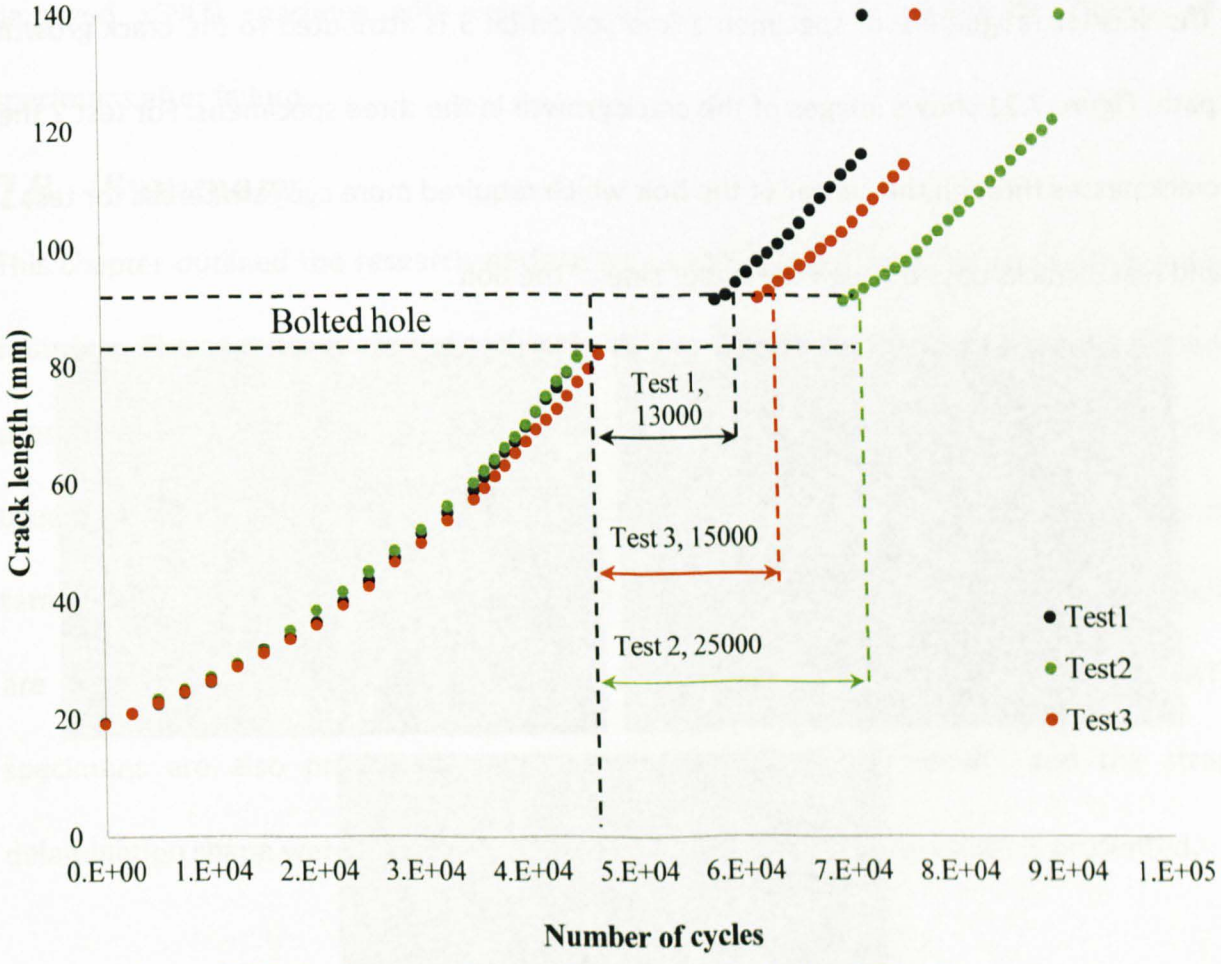

Figure 7.20: Fatigue crack growth tests on the bolted SEN(T) specimens

From figure 7.20, it can be observed that the number of cycles to failure is different for the three specimens. The number of cycles required for the crack to reach the fastener/bolt is approximately equal for all the specimens whereas the number of cycles required for the crack to leave the fastener is different for all the specimens (table 7.5)

being higher for the specimen 2 which resulted in a higher number of cycles to specimen failure.

Test 1	Crack reached the bolt	45000 cycles
	Crack left the bolt	58000 cycles
	Failure	72406 cycles
Test 2	Crack reached the bolt	45000 cycles
	Crack left the bolt	70000 cycles
	Failure	90946 cycles
Test 3	Crack reached the bolt	47000 cycles
	Crack left the bolt	62000 cycles
	Failure	77371 cycles

Table 7.5: Summary of fatigue crack growth tests on the bolted SEN(T) specimens

The shorter fatigue life of specimen 1 and specimen 3 is attributed to the crack growth path. Figure 7.21 shows images of the crack growth in the three specimens. For test 2 the crack passes through the center of the bolt which required more cycles whereas for test 1 and test 3 cracks pass through the upper side of the bolt.

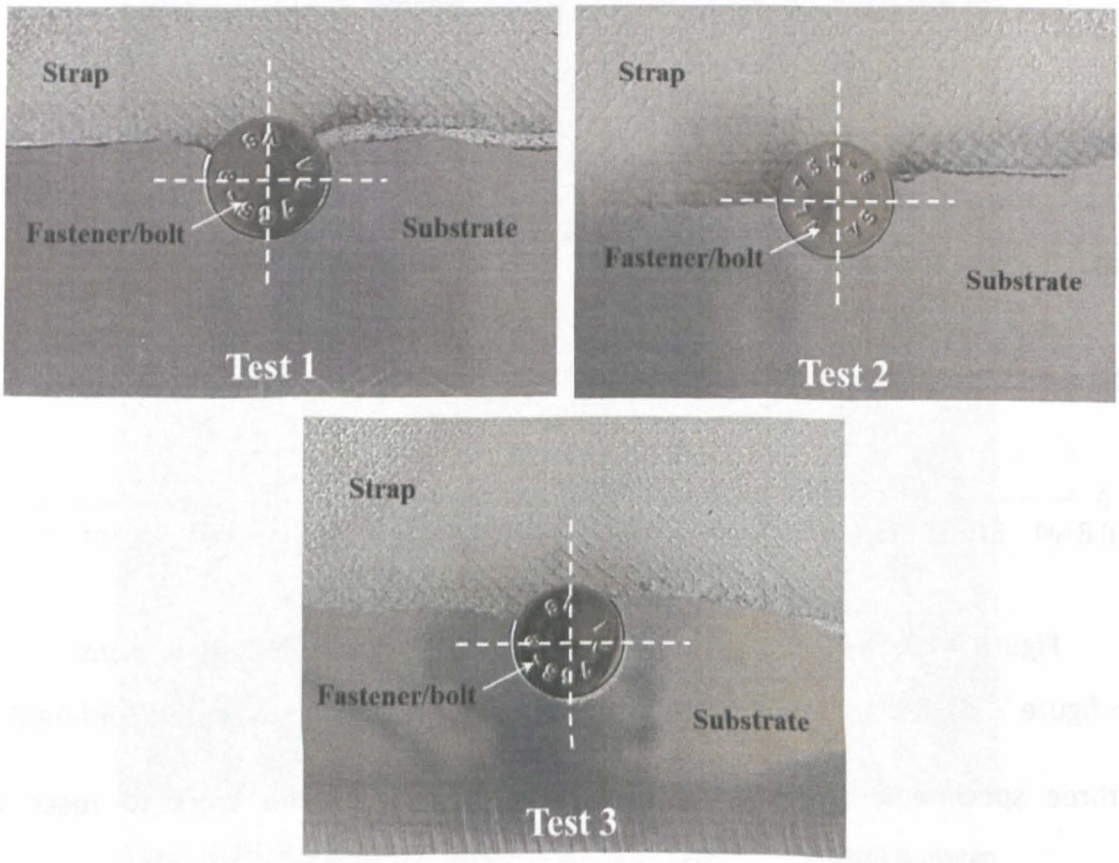

Figure 7.21: Crack growth direction in bolted SEN(T) specimens

Figure 7.22: Bolted SEN(T) specimens after failure

Specimens after failure showed a similar triangular delamination behaviour as the impact damaged SEN(T) specimen with cohesive failure. Figure 7.22 shows the images of specimens after failure.

7.8 Summary

This chapter outlined the research performed on the fatigue durability of bonded crack retarders. The experimental results of both M(T) and SEN(T) with and without straps are presented. Also, the at-temperature critical strain energy release rate of the adhesive used to bond the strap was investigated and the results are summarised. The effects of temperature and thermal cycling on fatigue crack growth behaviour of M(T) specimens are presented in detail. Fatigue durability of impact damaged and bolted hole SEN(T) specimens are also presented. Finally, the delamination mechanism and the strap delamination shape were investigated by using NDT and a brief discussion is presented.

Chapter 8 : Conclusions and future work

The conclusions of this research will provide important information for the researchers to improve the life of aircraft critical structures. Based on the study conducted in this research, the following conclusions can be drawn

1. The application of bonded crack retarders in the initial design and fabrication of aircraft critical structures has been investigated. A new high-damage-tolerance aluminium alloy 2624-T351 and GLARE6/5 have been used as substrate and strap materials respectively. GLARE straps are bonded onto the structural coupons by using a high temperature cure adhesive.
2. The asymmetric configuration of the GLARE strap resulted in an out-of-plane deflection of the substrate, because of the mismatch in coefficient of thermal expansion between the strap and the substrate.
3. Thermal residual stresses associated with GLARE bonded crack retarders on structural coupons and aircraft mock-up panels have been determined using neutron diffraction. The strap bonding process resulted in the development of thermal residual stresses in the substrate, which are very low, because of the mismatch in coefficient of thermal expansion between the GLARE and the aluminium.
4. Cold expansion resulted in the development of radial compressive residual stresses around the hole that were higher at the outlet face and lower at the inlet face. Thermal residual stresses have no significant effect on the cold expansion stresses and bolted stresses.
5. The application of bonded crack retarders in aircraft mock-up panel resulted in low thermal residual stresses. Tensile residual stresses are developed at the edge of the bolted hole which is attributed to the machining process during the drilling of holes and the additional stresses developed due to the ribs and stringer assembly.

6. The fatigue durability of bonded crack retarders was studied by constant amplitude fatigue crack growth tests on M(T) and SEN(T) specimens. The inclusion of a bonded crack retarder on M(T) specimens resulted 20% fatigue life improvement in specimens tested at room temperature. There is no significant effect of thermal cycling on the fatigue lives of M(T) specimens with crack retarders.
7. M(T) specimens tested at −60°C showed fatigue crack growth in the first layer of the GLARE whereas the M(T) specimens tested at room temperature and +70°C showed the crack growth through the adhesive layer in FM94.
8. The inclusion of a bonded crack retarder on SEN(T) specimens resulted 214% fatigue life improvement and the crack growth was observed to progress through the adhesive layer in FM94.
9. Impact damage on the GLARE resulted in the development of compressive residual stresses in and around the damage location, with lower stresses close to the bonded strap side and higher compressive stresses further from it.
10. Impact damage on the GLARE resulted in lower fatigue life when compared to specimens without impact damage. There was a greater decrease in fatigue life as the impact energy was increased, with a 35 J impact giving a 55% decrease in fatigue life.
11. Inclusion of bonded crack retarders in bolted hole specimens resulted in fatigue life improvement of 186% compared the specimen without strap and bolted hole. The life improvement factor of the bolted hole specimen is depend on the crack growth path. Crack growth through the centre of the bolt resulted in higher fatigue life.

8.1 Future work

Based on the conclusions, the following recommendations are made for further research to advance the current understanding on the application of bonded crack retarders.

1. Strap and substrate geometry plays a vital role on the fatigue durability of bonded crack retarders and this has to be further investigated by optimising the strap and substrate geometry and the stiffness ratio.
2. Comparative studies can be performed between damage tolerance, weight saving and increase in section stress of the reinforced structure.
3. Different strap and substrate geometries result in different out-of-plane deflection and residual stresses which will affect the performance of the bonded crack retarders and have to be investigated further
4. Adhesive optimising studies can be performed by using fibre reinforced adhesive (FM94/S2 prepreg) to bond the strap to the substrate. The presence of glass fibres in FM94/S2 prepreg may improve the fatigue performance of the bonded crack retarders.
5. At temperature fatigue crack growth testing has shown no significant effect on the M(T) specimens with strap compared to without strap. This has to be further investigated with different strap and substrate geometry, with different loading condition and testing at different temperatures.
6. Relative humidity also plays an important role in the performance of the bonded crack retarders, hence it is suggested to record the relative humidity and temperature for future testing, and testing should be performed with various humidity leads to investigate the effect of humidity on the fatigue crack growth behaviour.

7. From the results it can be observed that the load carrying GLARE strap has resulted better fatigue crack performance compared regular M(T) strap, this has to be further investigated by performing constant amplitude and variable amplitude testing at aircraft service temperatures.